Università degli Studi di Napoli *Federico II*

DOTTORATO DI RICERCA IN
FISICA

Ciclo: XXXI

Coordinatore: prof. Salvatore Capozziello

Quantum walks and topological phenomena with structured light

Settore Scientifico Disciplinare FIS/03

Dottorando
Alessio D'Errico

Tutori
Prof. Lorenzo Marrucci
Dott. Filippo Cardano

Anni 2015/2018

Acknowledgements

At the end of my PhD, I would like to thank my tutors, Lorenzo Marrucci and Filippo Cardano, for allowing me to take part in experiments on fascinating topics. Special thanks go also to the people in Barcelona, Maria Maffei, Alexandre Dauphin and Pietro Massignan, that helped us understanding the theory behind our work, in particular to Maria that helped also in some of the experiments. I would like also to thank Bruno Piccirillo for the help in the fabrication of g-plates, and the rest of the SLAM group: Raouf Barboza, Andrea Rubano, Domenico Paparo and Sen Mou. Finally I express my gratitude to my friends and family who helped me going through these years.

Published articles related to my thesis

1.F. Cardano, **A. D'Errico**, A. Dauphin, M. Maffei, B. Piccirillo, C. De Lisio, G. De Filippis,V. Cataudella, E. Santamato, L. Marrucci, M. Lewenstein, P. Massignan. **Detection of Zak phases and topological invariants in a chiral quantum walk of twisted photons.** *Nature Communications*, **8**:15516, (2017)

2. **A. D'Errico**, M. Maffei, B. Piccirillo, C. De Lisio, F. Cardano, L. Marrucci. **Topological features of vector vortex beams perturbed with uniformly polarized light.** *Scientific Reports*, **7**:1-11, (2017)

3. **A. D'Errico**, R. D'Amelio, B. Piccirillo, F. Cardano, L. Marrucci. **Measuring the complex orbital angular momentum spectrum and spatial mode decomposition of structured light beams** *Optica*, **4**:11, (2017)

4. **A. D'Errico**, F. Cardano, M. Maffei, A. Dauphin, R. Barboza, C. Esposito, B. Piccirillo, M. Lewenstein, P. Massignan, L. Marrucci. **Two dimensional topological quantum walks in the momentum space of structured light.** arXiv:1811.04001v2

I will explicitly mention in a footnote when a section contains paragraphs, figures or tables that are adapted or copied “verbatim” from one of these articles.

Abstract

Prototypes of quantum simulators have been realized in many different physical setups, employing atoms, ions, Bose-Einstein condensates, superconducting cavities and photons. In particular, many quantum simulators realize a specific class of processes, known as Quantum Walks (QWs). Quantum walks consist in evolutions over discrete spaces often conditioned by some internal degree of freedom. These processes have revealed themselves as a powerful tool for studying solid state systems, and, in particular, topological phases of matter.

This Thesis work is mainly devoted to the implementation of Quantum Walks within coherent light beams. We explore the possibility to associate the lattice space with some structural feature of light, e.g. its phase distribution. One possibility is to implement Quantum Walks in the Orbital Angular Momentum (OAM) space of light, a quantized quantity (a single photon can carry an OAM that is an integer multiple of $\hbar$), which can be used to emulate a one dimensional discrete space. By exploiting devices, called q-plates, that change the OAM in a way that is conditioned by the polarization, it is possible to realize QWs on one dimensional lattices. In this Thesis we explore the topological phases associated to this system. In particular we demonstrate a new method of detecting the topological invariant, the signature of the topological phase of a system, in one dimensional systems with chiral symmetry.

Topological phases of matter are an hot topic due to the possibility of employing topologically protected states for quantum computation. In particular two dimensional topological insulators exhibit interesting features, like edge spin or charge currents that propagate without experiencing back-scattering or being absorbed in the bulk. This motivated us to look for photonic implementations of QWs on two dimensional lattices. In order to do this we switched to another degree of freedom: the transverse component of light wave vector. We devised patterned waveplates, called g-plates, that allow to perform polarization conditioned discrete translations in the transverse momentum space. The transverse wave vector allows to implement QWs in one and two dimensional lattices. We give examples of dynamics in 1D, with and without an applied external force, investigating ballistic spreading and refocusing phenomena. Then we propose a 2D protocol

that simulates a periodically driven Chern insulator and perform a first investigation of the nontrivial topology looking at center of mass displacements. Future investigations of topological features of quantum walks can exploit our capability of directly explore the reciprocal lattice space and study the evolution of the polarization distribution in this space. As a preliminary study we investigated the behavior of polarization singularities produced by a q-plate. During our studies on the implementation of QW with structured light, we also investigated a new approach for measuring the OAM power spectrum of a light beam. Indeed we developed an interferometric technique that allows to retrieve, from a small number of recorded images (three or four), the full OAM spectrum of an unknown beam. Moreover our approach allows to reconstruct also the radial phase and amplitude profile of each OAM mode.
The Thesis is structured as follows:

- **Chapter 1: Structured Light** This introductory Chapter aims to review the fundamental physics of structured light beams. Some space is dedicated to the Orbital and Spin angular momenta of light. The transverse momentum space is reviewed focusing on the possibility of treating it as a useful degree of freedom for experiments on large Hilbert spaces. Some of the techniques used to generate structured light beams are introduced, focusing in particular on the properties of q-plates and g-plates.
- **Chapter 2: Measurement of structured light beams** This chapter continues the discourse on structured light, discussing the methods for measuring the features of these beams. It is focused in particular on the reconstruction of the OAM power spectrum. A new interferometric technique is introduced that allows also to characterize the radial structure of the electric field.
- **Chapter 3: Topology and dynamics of polarization singularities in optical beams** Structured light is a physical phenomenon that allows to illustrate some basic concepts in topology that will be essential in the last chapter. Here we present an experiment in which we study the topological singularities in polarization patterns produced by q-plates with variable optical retardation.
- **Chapter 4: Photonic quantum walks employing light's spatial degrees of freedom** We introduce the concept of Quantum Walks and briefly review the most important photonic implementations. Then we introduce the 1D protocol implemented in the OAM space of light. Finally the new architecture performing QWs in the transverse wave vector space is described in detail together with some experimental results.

- **Chapter 5: Exploring topological phases with structured light** The concept of topological insulators is introduced by defining the topological invariants related to the energy band structure. We describe the topological features of the 1D and 2D protocols that we implemented. In the 1D case, we experimentally characterized the topological phases of the system by measuring the so called *mean chiral displacement*, which can be related to the Zak phase. In the 2D case we explore experimentally the effects of the topology on the displacements of ground state center of mass under an external force.

Contents

Chapter 1

Structured light

1.1 Introduction

Light is among the most familiar natural phenomena that a human being experiences. Through its perception we receive the largest amount of information about the surrounding world. Indeed, most of the knowledge of a single individual, achieved from direct experience, or from reading books and watching videos, is due to the interaction of electromagnetic radiation with the eye and with the objects that we perceive. Despite this, the nature of light, together with the plethora of different features that a single light ray can possess, has been the subject of long investigations and debates. Some of the most relevant changes of paradigm in the history of Physics have been strictly related to new discoveries and ideas on the theory of light. The debate on the wave or particle description of luminous phenomena flowed into the identification of light with electromagnetic waves, a result that, put into the form of the Maxwell equations, set one of the first challenges to the Newtonian mechanics, resulting as the starting point of the Special Theory of Relativity. At the same time, the discovery of the photoelectric effect showed that light can still behave, in some situations, as a particle. This was at the beginning of the formulation of the wave-particle duality, one of the pillars of the Quantum Theory.

Today, the theory of light can be considered extremely solid, in the sense that the known phenomena concerning light and its interaction with matter can be described with the set of equation and models developed hitherto. Nowadays, intense research activities are focused on the study, characterization and manipulation of the variety of features that a light beam can possess. Indeed, one can be surprised by the complexity of this everyday phenomenon. To a light beam one can associate a large number of physical properties: frequency, intensity, phase, linear and angular momentum. A light beam can thus transfer energy, exert pressure and even torque. All these properties can be exploited for studying light matter interactions, micro-manipulation, communication and computation. In particular some optical degrees of freedom are of interest for realizing large Hilbert spaces. These can be used in turn to perform quantum simulations, communications or computation, or even to enlarge the capabilities of optical communication channels. For these (and many other) applications, a growing number of researches has concerned the spatial structure of a light beam.

This chapter is devoted to the description of the main features of these "structured light beams" and the principal technologies used for their generation and manipulation. In particular we will focus on those degrees of freedom that can be used to simulate infinite and discrete Hilbert spaces, due to their interest in Quantum Walks, one of the main topics of this thesis work.

We will start reviewing the balance equations for linear and angular momentum of the electromagnetic field and then focusing on the description of paraxial light beams. It is indeed in the paraxial approximation that one can treat separately the spin and orbital angular momentum degrees of freedom. The first will be associated to the polarization, i.e. to the behavior of the electric field vector in the transverse plane. The second is related to the wavefront shape of the light beam and, being quantized, will represent an infinite dimensional, but discrete, degree of freedom, with many potentialities in quantum applications. This chapter will be mainly devoted into the description of the Orbital Angular Momentum (OAM) of light, on the beams that transport OAM and their generation technique. In a separate chapter we will discuss also the methods for detecting the OAM of an unknown light beam. Moreover we will also give some remarks on a more familiar feature of a light beam, that is its wavevector, and in particular its projection on the plane transverse to a "nominal" propagation direction. We will do this motivated by the possibility of using this degree of freedom for the implementation of multidimensional quantum walks exploiting a liquid crystal based polarization grating, that will be described at the end of this chapter.

1.2 Linear and angular momentum of electromagnetic fields

Light can be described as an electromagnetic wave, thus it can be characterized in terms of propagation of an electric **E** and magnetic induction **B** field. Their evolution in space and time is given by the Maxwell equations:

$$\mathrm{div}\mathbf{D} = \rho, \tag{1.1}$$

$$\mathrm{div}\mathbf{B} = 0, \tag{1.2}$$

$$\mathrm{curl}\mathbf{E} = -\frac{\partial \mathbf{B}}{\partial t}, \tag{1.3}$$

$$\mathrm{curl}\mathbf{H} = \mathbf{i} + \frac{\partial \mathbf{D}}{\partial t}, \tag{1.4}$$

where ρ and $\mathbf{i}$ represents, respectively, free charge and current densities, while $\mathbf{D}$ and $\mathbf{H}$, respectively called the electric displacement field and magnetic field, are related to $\mathbf{E}$ and $\mathbf{B}$ by constitutive relations. We will consider the simple case of propagation in homogeneous, isotropic, dispersionless and non dissipative media, where: $\mathbf{D} = \epsilon\mathbf{E}$ and $\mathbf{B} = \mu\mathbf{H}$. The constants ϵ and μ are, respectively, the electric and magnetic permittivity. Starting from these relations one can derive the balance equations for the linear and angular momentum.

To obtain the balance equations of the linear momentum, we recall that the force density applied by an electromagnetic field on a distribution of charges is: $\mathbf{f} = \rho\mathbf{E} + \mathbf{i} \times \mathbf{B}$. By vector multiplying Eq. 1.4 with $\mathbf{B}$ and using the other Maxwell equations one gets (see e.g. [1]):

$$\frac{\partial}{\partial t}\mathbf{g} = -\mathbf{f} + \mathrm{div}\mathbf{T}, \tag{1.5}$$

where $\mathbf{T}$ is a second rank tensor, known as the Maxwell stress tensor, whose components are (c is the light speed in the medium):

$$T_{i,j} = \epsilon\big(E_iE_j + c^2B_iB_j - \frac{1}{2}(\mathbf{E}\cdot\mathbf{E} + c^2\mathbf{E}\cdot\mathbf{E})\big),$$

and

$$\mathbf{g} = \frac{1}{c^2}\mathbf{E} \times \mathbf{H} = \frac{\mathbf{S}}{c^2}, \tag{1.6}$$

where we have introduced the Poynting vector $\mathbf{S} = \mathbf{E} \times \mathbf{H}$. In absence of charges and currents it follows from Eq. 1.5 the conservation of the quantity: $\mathbf{G} = \int \mathbf{g}dV$ (the integral is carried over all the three-dimensional space). $\mathbf{G}$ is identified with the total linear momentum of the electromagnetic field. Using the Planck relation for the energy $E = n\hbar\omega$ for a light beam with n photons and frequency ω, one can easly find that the linear momentum carried by a photon is $\mathbf{G} = \hbar\mathbf{k}$, where $\mathbf{k}$ is the wavevector.

From the balance equation of the linear momentum one can derive the analog for the angular momentum by taking the vector product of the position vector $\mathbf{r}$ with Eq. 1.5 and observing that $\mathbf{T}$ is symmetric:

$$\frac{\partial}{\partial t}(\mathbf{r} \times \mathbf{g}) = -\mathbf{r} \times \mathbf{f} + \mathrm{div}(\mathbf{r} \times \mathbf{T}). \tag{1.7}$$

From this result it follows that, in absence of matter, the total angular momentum of light,

$$\mathbf{J} = \int (\mathbf{r} \times \mathbf{g}) dV,$$

is a conserved quantity. It is customary to write $\mathbf{J}$ in terms of the vector potential $\mathbf{A}$ defined by the relation $\mathbf{B} = \mathrm{curl}\mathbf{A}$. This leads to:

$$\mathbf{J} = \epsilon \int \big(\sum_j E_j (\mathbf{r} \times \nabla) A_j - \mathbf{r} \times \partial_j (E_j \mathbf{A}) \big) dV. \tag{1.8}$$

Integration by parts of the second term of the above equation and neglecting the resulting surface integral (i.e. assuming zero fields at infinity) one obtains:

$$\mathbf{J} = \epsilon \int \big(\sum_j E_j (\mathbf{r} \times \nabla) A_j + \mathbf{E} \times \mathbf{A} \big) dV. \tag{1.9}$$

Observing that the term $\mathbf{r} \times \nabla$ is reminiscent of the orbital angular momentum operator in quantum mechanics, it is possible to separate $\mathbf{J}$ into two contributions:

$$\mathbf{J} = \mathbf{L} + \mathbf{S}, \tag{1.10}$$

$$\mathbf{L} = \frac{1}{\mu c^2} \int \big(\sum_j E_j (\mathbf{r} \times \nabla) A_j \big) dV, \tag{1.11}$$

$$\mathbf{S} = \frac{1}{\mu c^2} \int \big(\mathbf{E} \times \mathbf{A} \big) dV, \tag{1.12}$$

where one can be tempted to interpret $\mathbf{L}$ as the orbital angular momentum and $\mathbf{S}$ as the spin angular momentum. However this identification is unlawful, since both $\mathbf{L}$ and $\mathbf{S}$ are gauge dependent (while $\mathbf{J}$ is not). This issue can be circumvented by substituting in Eq. 1.9 the vector potential $\mathbf{A}$ with its projection on the plane perpendicular to the wavevector (that we will define as the transverse plane) $\mathbf{A}_t$. The new formulas thus obtained satisfy correctly all the symmetries required by the electromagnetic theory. But this does not guarantee a true physical significance to $\mathbf{L}$ and $\mathbf{S}$. For example, it was shown by van Enk and Nienhuis [2] that the quantum operators corresponding to $\mathbf{L}$ and $\mathbf{S}$ do not satisfy the correct commutation relations expected by the generators of rotations. In this sense they cannot be regarded as "true angular momenta".

The issue was made clearer by Barnett [3] who looked at the possible rotations of the electromagnetic field. The author observed that $\mathbf{L}$, seen as a true angular momentum, should be associated to a rotation of the amplitude of the fields that leaves their orientation (the polarization) unchanged. Similarly $\mathbf{S}$ should be related to rotations in the field orientation without rotating the amplitude distribution. Surprisingly, these transformation are not compatible with the Maxwell equations, since they violate the transversality conditions. Nevertheless, Barnett observed that the expressions of $\mathbf{L}$ and

$\mathbf{S}$ with $A \to \mathbf{A}_t$ actually generate the transformations:

$$\mathbf{E} \to \mathbf{E} - (\theta \cdot (\mathbf{r} \times \nabla)\mathbf{E})_t, \tag{1.13}$$

$$\mathbf{E} \to \mathbf{E} + (\theta \times \mathbf{E})_t, \tag{1.14}$$

where θ is an vector whose direction gives the rotation axis and whose (infinitesimal) modulus gives the angle of rotation. These transformations are actually the closest to the expected rotation that satisfy the transversality conditions. They are a good approximation of real rotations when the components of $\mathbf{E}$ and $\mathbf{B}$ along the propagation direction are small. Light beams satisfying this requirement are called paraxial beams. For these beams the separation of the total angular momentum in a spin and orbital part can be considered licit and physically meaningful. We will turn now to a detailed description of these realization of electromagnetic fields. All the works presented in this Thesis have been done using laser beams well described by the paraxial approximation. A recent and detailed discussion on the separation of orbital and spin angular momentum can be found in Ref. [4].

1.3 Paraxial light beams

Let us consider a monochromatic electromagnetic wave described by the electric field: $\mathbf{E}(\mathbf{r}, t) = \mathbf{U}(\mathbf{r}) \exp(-i\omega t)$. It is well known that from the Maxwell equations the field $\mathbf{U}(\mathbf{r})$ must satisfy the Helmholtz equation:

$$\triangle \mathbf{U}(\mathbf{r}) + k^2 \mathbf{U}(\mathbf{r}) = 0, \tag{1.15}$$

where $k = \omega/c = 2\pi/\lambda$ is the wavenumber, λ the wavelength and $\triangle$ is the Laplace operator, that in Cartesian coordinates reads: $\triangle = \partial_x^2 + \partial_y^2 + \partial_z^2$. We want to look for (at least approximate) solutions of Eq. 1.15 which are strongly directional, as it happens for a common laser beam. A plane wave is a trivial example, however we will search also for solutions that carry an infinite energy and thus have an intensity that decays fast at infinity. Thus we multiply the pane wave contribution $\exp(ikz)$ for a complex field $\mathbf{F}(\mathbf{r})$, called *slowly varying envelope*, whose amplitude changes slowly along the z axis. Indeed we require that:

$$\frac{\partial^2 \mathbf{F}}{\partial z^2} \ll \frac{1}{\lambda} \frac{\partial \mathbf{F}}{\partial z} \ll \frac{\mathbf{F}}{\lambda^2}.$$

With these approximations we can neglect the term $\partial^2 \mathbf{F}/\partial z^2$ appearing in the Helmholtz equation obtaining:

$$(\triangle_t + 2ik\partial_z)\mathbf{F} = 0, \tag{1.16}$$

where $\partial_z = \partial/\partial z$ and $\triangle_t = \partial_x^2 + \partial_y^2$. This is the *paraxial wave equation.* It has the form of a Schrodinger equation with the temporal variable replaced by the z coordinate. This result is of great interest since, in many applications, laser beams are well described by solutions of the paraxial equation [5].
We will give now a brief review of the best known solution of Eq. 1.16, the Gaussian Beam, highlighting the features which will be used in the following chapters.

1.3.1 Gaussian Beams

A plane wave is an object infinitely extended in space and time. Such a solution of the wave equation is thus unphysical, even if useful for understanding fundamental properties of the physics of electromagnetic waves. A more realistic solution would be such that its amplitude in the plane transverse to the propagation direction z is a rapidly decaying function of the distance $r = \sqrt{x^2 + y^2}$ from the propagation axis. A simple example would be given by a beam whose intensity distribution is a Gaussian: $I(r) = I_0 \exp(-2r^2/w^2)$, where w is in general a function of z. This parameter is known as the beam width. At $r = w$ the beam intensity is decreased as I_0/e^2. One can thus search for a solution of the paraxial equation in the form:

$$\mathbf{F}(r, z) = F(r, z)\mathbf{s} = F_0(z) \exp(-r^2/a(z)^2)\mathbf{s},$$

where $a(z)$ can be in general a complex function such that $\Re(1/a(z)^2) = 1/w(z)^2$ and $\mathbf{s}$ is a complex vector representing the polarization of the electric field. The corresponding electric field will be given by: $\mathbf{E}(r, z, t) = \mathbf{F}(r, z) \exp(ik_z z - i\omega t)$. Substituting this *ansatz* in the paraxial equation one obtains the two following differential equations for $F_0(z)$ and $a(z)$:

$$\frac{1}{a(z)} - ik\partial_z a(z) = 0, \tag{1.17}$$

$$ik\partial_z F_0(z) + \frac{2}{a(z)^2} F_0(z) = 0. \tag{1.18}$$

The solution of the two equations is straightforward and leads to:

$$F(r, z) = A\frac{w_0}{w(z)} \exp\left(- \frac{r^2}{w(z)^2}\right) \exp\left(- ik\frac{r^2}{R(z)} - i\arctan(z/z_0)\right), \tag{1.19}$$

where we have used the following standard definitions of the *beam parameters*:

$$w(z) = w_0\sqrt{1+\left(\frac{z}{z_0}\right)^2} \quad \textit{beam width}, \tag{1.20}$$

$$R(z) = z + \frac{z_0^2}{z} \quad \textit{wavefront curvature radius}, \tag{1.21}$$

$$z_0 = \frac{\pi w_0^2}{\lambda} \quad \textit{Rayleigh range}. \tag{1.22}$$

The parameter w_0 is the beam width at $z = 0$ and it is denoted as *waist radius*. The Rayleigh range z_0 gives a measure of the distance in which the beam width is smaller than $\sqrt{2}w_0$. This distance, equal to $2z_0$, is known as *depth of focus* or *confocal parameter*. $R(z)$ gives the curvature radius of the wavefront. The ratio $\theta_0 = w_0/z_0$ is the beam divergence.

It is often useful to introduce a parameter $q(z)$ that contains all the information on the Gaussian beam. This parameter is defined by:

$$\frac{1}{q(z)} = \frac{1}{R(z)} - i\frac{\lambda}{\pi w(z)^2} = z + iz_0. \tag{1.23}$$

The evolution of a Gaussian beam through a paraxial optical system can be expressed as a transformation of this *q-parameter*. In geometrical optics the action of a succession of paraxial optical elements on an arbitrary (but paraxial) input ray can be described in terms of the so called ABCD matrix (see e.g Ref. [6] or [7]). The same matrix can be used to calculate the evolution of paraxial beams in an optical system. Let $q_1(z)$ the q-parameter of a Gaussian beam impinging on a paraxial optical system. The outgoing beam is still a Gaussian beam with q-parameter $q_2(z)$ given by:

$$q_2(z_2) = \frac{A\, q_1(z_1) + B}{C\, q_1(z_1) + D}, \tag{1.24}$$

where z_1 and z_2 are the positions of the input and output transverse planes. For a proof we refer to Ref. [6].

1.4 Angular momentum of paraxial beams

We now turn again our attention to the angular momentum of light, focusing on the case of paraxial beams. Indeed we have seen that, in this approximation, the separation of **J** in an orbital and spin component is physically meaningful.

Consider a monochromatic field, that, in complex representation can be written as:

$$\mathbf{E} = (\boldsymbol{E}e^{-i\omega t} + c.c)/2, \tag{1.25}$$

$$\mathbf{B} = (\boldsymbol{B}e^{-i\omega t} + c.c)/2. \tag{1.26}$$

Using $i\omega\boldsymbol{B} = \mathrm{curl}\boldsymbol{E}$ we can rewrite the total angular momentum $\mathbf{J} = \epsilon\int\big(\mathbf{r}\times(\mathbf{E}\times\mathbf{B})\big)dV$:

$$\mathbf{J} = \Re\,\frac{\epsilon}{2i\omega}\int\Big[\sum_j E_j^*(\mathbf{r}\times\nabla)E_j + \boldsymbol{E}^*\times\boldsymbol{E}\Big]dV. \tag{1.27}$$

For a paraxial beam propagating in the z direction we can focus on the J_z component, given by [8]:

$$J_z = L_z + S_z \tag{1.28}$$

$$L_z = \frac{\epsilon}{2i\omega}\int\sum_j E_j^*(x\partial_y - y\partial_x)E_j dV \tag{1.29}$$

$$S_z = \frac{\epsilon}{2i\omega}\int(E_x^*E_y - E_y^*E_x)]dV. \tag{1.30}$$

Let us consider some special cases. First, we can evaluate the total angular momentum of a Gaussian beam that is circularly polarized. The electric field is given by: $E = Ae^{ikz}F(r,z)(\hat{\mathbf{x}} \pm i\hat{\mathbf{y}})/\sqrt{2}$ where the ± sign refers to left or right circular polarization, respectively, and $F(r)$ is given by Eq. 1.19. Using the identity: $(x\partial_y - y\partial_x) = \partial_\phi$ ($\phi = \arctan(y/x)$) it is immediate to check that $L_z = 0$. Assuming the normalization condition:

$$\int\int_{-\infty}^{\infty} F^*(x,y,z)F(x,y,z)dxdy = 1$$

we obtain:

$$J_z = S_z = \pm\frac{\epsilon\,|A|^2}{2\omega}.$$

Using the relation: $I = \epsilon\,|A|^2/2 = N\hbar\omega$, where N is the average number of photon per unit area, one gets:

$$S_z = \pm N\hbar \tag{1.31}$$

which means that each photon carries a spin equal in modulus to $\hbar$ and with sign determined by the polarization handedness. This relation between circular polarization and angular momentum of light was demonstrated experimentally by the famous work of Beth [9] in 1936. There a circularly polarized light was shined on a birefringent plate with half optical retardation. Such a medium inverts the handedness of the circular polarization, thus the light spin is expected to be flipped leading to an angular momentum transfer to the plate equal to $2\hbar$ per photon. The torque exerted on the plate was measured and shown to be compatible with the prediction. It follows that S_z is maximum in modulus for circular polarizations while it is zero for linear polarization (see also the next section).

We now look for fields carrying a non zero value of L_z. To this aim, it is worth nothing that the expression of L_z resembles the quantum mechanical average of the operator $\hat{l}_z = -i\partial_\phi$, where ϕ is the azimuthal angle. Hence a beam carrying a well defined orbital angular momentum is described by an electric field proportional to an eigenfunction of l_z, that is, in cylindrical coordinates:

$$\boldsymbol{E}(r, \phi, z) = A\, u(r, z) \exp(il\phi)\mathbf{s}, \tag{1.32}$$

where $\mathbf{s}$ is the polarization unit vector, $u(r, z)$ a normalized complex function, and l is an integer (since one should have looked for monotonic solutions of the eigenvalue equation for l_z). For such a beam the orbital angular momentum is:

$$L_z = N\hbar l. \tag{1.33}$$

Free space propagating beams described by Eq. 1.32 are called Circular Beams (CiB) [10]. These beams are characterized by helical wavefronts and annular shaped intensity patterns. Indeed the point $r = 0$ is a phase singularity that induces an "hole" in the beam amplitude. That a Circular Beam exerts a torque even if linearly polarized (i.e. $S_z = 0$) has been demonstrated in experiments with particles trapped by a CiB. If the particle is trapped on the axis of the beam it will rotate around itself. More interestingly, due to the particular intensity distribution of these beam, one can trap a particle at a given distance from the beam axis, corresponding approximately to the distance at which the beam has the maximum intensity. If the particle is small enough it will be possible to observe the particle rotate around the beam axis. Moreover, making the beam circularly polarized, will allow to observe both the rotation of the particle around itself and the revolution around the beam axis. Experiments of this kind are reviewed in Ref.[11].

1.4.1 The polarization of light

We have seen how the z component of light spin angular momentum is directly related to the polarization. In this section we will review the description of polarized light using a formalism adapted from quantum physics. Indeed we will see how the polarization states of light can be used to encode single qubits.

Light polarization describes how the electric field of an electromagnetic wave evolves in time. For a paraxial beam we can consider the electric field as lying in the plane transverse to the propagation direction z. Therefore it can be written in the following form, known as Jones vector:

$$\boldsymbol{E} = E_0(a\hat{\mathbf{x}} + b\hat{\mathbf{y}}) = E_0 \begin{pmatrix} a \\ b \end{pmatrix}, \tag{1.34}$$

where we defined the complex coefficients a and b such that $|a|^2 + |b|^2$ and E_0 is the total amplitude of the field. In the following we will impose for simplicity $E_0 = 1$. The electric field is linearly polarized when its direction does not change during the propagation. Circular polarization, on the other hand, is observed when the tip of the electric field vector describes a circle in the transverse plane. If the rotation in time of the electric field is counterclockwise (with respect to the positive z axis) one refers to left handed polarization, that will be labeled in Dirac's notation as $|L\rangle$ (see Fig. 1.1 (a)). This correspond to the receiver-point-of-view handedness convention. This polarization state, as we have seen in the previous section, is associated with a positive spin $S_z = \hbar$ per photon. Similarly, the clockwise rotation of the electric field is identified with right handed polarization (labeled as $|R\rangle$), for which $S_z = -\hbar$ per photon. In the Jones vector formalism one has:

$$|L\rangle = \frac{1}{\sqrt{2}} \begin{pmatrix} 1 \\ i \end{pmatrix}, \; |R\rangle = \frac{1}{\sqrt{2}} \begin{pmatrix} 1 \\ -i \end{pmatrix}, \tag{1.35}$$

that is, one has circularly polarized light where the x and y components of the electric field have a relative phase $\pm\pi/2$, respectively. In the following we will often choose to write formulas in the circular polarization basis, i.e. we will assign $|L\rangle = (1\,0)^T$ and $|R\rangle = (0\,1)^T$, which is equivalent to write the general Jones vector in the form $\boldsymbol{E} = c_L\hat{\mathbf{e}}_L + c_R\hat{\mathbf{e}}_R$ with $\hat{\mathbf{e}}_{L,\,R} = (\hat{\mathbf{x}} \pm i\hat{\mathbf{y}})/\sqrt{2}$ and $c_{R,L}$ complex numbers. This description highlights the analogy with the quantum state of an electron spin: $|\psi\rangle = c_\uparrow|\uparrow\rangle + c_\downarrow|\downarrow\rangle$, where $|\uparrow\rangle$ and $|\downarrow\rangle$ are electron states with spin $S_z = \pm\hbar/2$, respectively. Similarly, in the circular polarization basis, $|L\rangle$ and $|R\rangle$ are eigenstates of the Pauli matrix σ_3 while $|H\rangle$ and $|V\rangle$ are eigenstates of σ_1. We recall that the Pauli matrices $\{\sigma_1, \sigma_2, \sigma_3\}$ are defined by:

$$\sigma_1 = \begin{pmatrix} 0 & 1 \\ 1 & 0 \end{pmatrix}, \tag{1.36}$$

$$\sigma_2 = \begin{pmatrix} 0 & -i \\ i & 0 \end{pmatrix}, \tag{1.37}$$

$$\sigma_3 = \begin{pmatrix} 1 & 0 \\ 0 & -1 \end{pmatrix}. \tag{1.38}$$

The eigenstates of σ_x are linear polarization states given by:

$$|H\rangle = \frac{|L\rangle + |R\rangle}{\sqrt{2}},\ |V\rangle = \frac{|L\rangle - |R\rangle}{\sqrt{2}}, \tag{1.39}$$

The eigenstates of σ_y are still linear polarization states oriented at 45 degrees with respect to $|H\rangle$ and $|V\rangle$:

$$|D\rangle = \frac{|L\rangle + i|R\rangle}{\sqrt{2}},\ |A\rangle = \frac{|L\rangle - i|R\rangle}{\sqrt{2}}, \tag{1.40}$$

that are called, respectively, *diagonal* and *antidiagonal* polarization states. Polarization states can be visualized by means of a beautiful geometrical description as points on the so called Poincarè sphere (equivalent to the Bloch sphere describing two level systems in quantum mechanics). To introduce it, we first rewrite the Jones vector (that we will label as a ket vector $|E\rangle$) in the form:

$$|E\rangle = \cos\left(\frac{\theta}{2}\right)|L\rangle + e^{i\phi}\sin\left(\frac{\theta}{2}\right)|R\rangle. \tag{1.41}$$

This expression keeps all the essential properties of a polarized state: the relative phase between the two polarizations and the relative amplitudes of the basis states. The parameters θ and ϕ can be considered as, respectively, a polar and azimuthal angle determining the position of a point on the unit sphere as shown in Fig. 1.1 (b). For example circular polarization states will be localized on the two poles of the sphere while linear polarization states, being characterized by an equal superposition of left and right handed polarization, will be displaced along the equatorial circle ($\theta = \pi/2$).
It is easy to show that the coordinates of a polarization state on the Poincarè sphere can be calculated as the mean values of the Pauli matrices, $S_i = \langle E|\sigma_i|E\rangle$ where $i = 1, 2, 3$, also called *Stokes parameters*. Indeed one gets that the Stokes parameters give the parametric equations of the Poincarè sphere:

$$S_1 = \sin(\theta)\cos(\phi), \tag{1.42}$$

$$S_2 = \sin(\theta)\sin(\phi), \tag{1.43}$$

$$S_3 = \cos(\theta). \tag{1.44}$$

The Stokes parameters are useful for obtaining a complete characterization of the polarization state of a light beam. They can be used to go beyond the Jones formalism, i.e. to describe partially polarized light. A partially polarized beam is indeed an incoherent ensemble of different polarization states, as such it can be described using the density

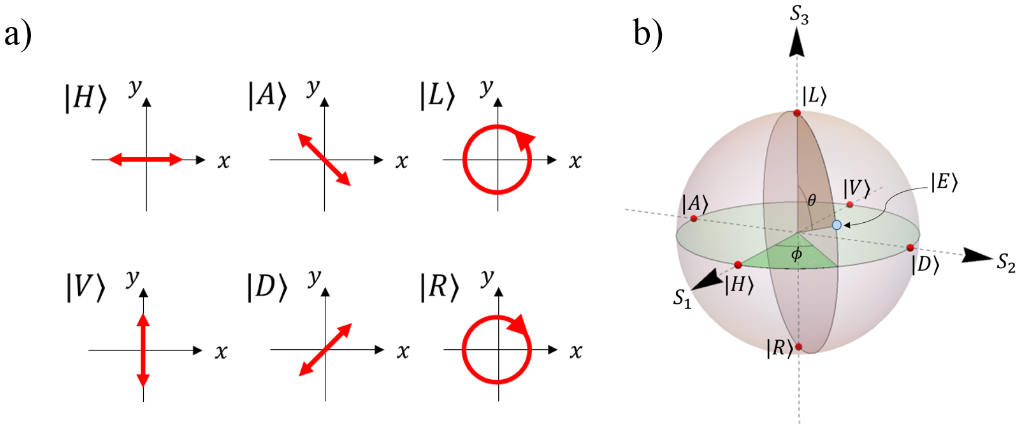

FIGURE 1.1: **Polarization states of light.** Inset a) shows the trajectories of the tip of the electric field vector at a fixed z for the different polarization states that are eigenstates of the Pauli matrices. In inset b) the Poincarè sphere is illustrated. A generic polarization state $|E\rangle$ is identified by the polar θ and azimuthal ϕ angles on this sphere. The Cartesian coordinates of the points on the Poincarè sphere can be identified with the Stokes parameters $S_i = \langle E|\sigma_i|E\rangle$ where $i = 1, 2, 3$. Red dots on the figure individuate the points on the sphere corresponding to the Pauli matrices eigenstates.

matrix formalism, which describes the polarization state in the form of an operator:

$$\rho = (1/2) \sum_{i=0,1,2,3} S_i \, \sigma_i,$$

where σ_0 is the 2×2 Identity matrix, $S_0 = 1$ and $S_{1,2,3}$ are the Stokes parameters here redefined as real coefficients. For completely polarized light one has $S_1^2 + S_2^2 + S_3^2 = 1$, while for incoherent mixtures of polarization states one has $S_1^2 + S_2^2 + S_3^2 < 1$. Indeed such states can be visualized as points lying *inside* the Poincarè sphere.

The polarization of a light beam can be manipulated and analyzed by using essentially two kinds of devices: polarizers and birefringent plates. A polarizer acts as a projector on some linearly polarized state, for example it can be represented by the operator $P = |H\rangle\langle H|$. On the other hand, birefringent plates act as unitary operators in the polarization space. They are based on optically anisotropic devices, whose orientation and thickness determine how light polarization is transformed. More precisely, in anisotropic media the dielectric permittivity is a 3×3 positive (and symmetric) matrix $\boldsymbol{\epsilon}$. Birefringent plates are uniaxial materials, which means that two of the three eigenvalues of the dielectric tensor are equal. Thus one has two eigenvalues of $\boldsymbol{\epsilon}$: ϵ_e with multiplicity one, and ϵ_o with multiplicity two. This allows to define two different refractive indexes: the *ordinary index* $n_o = \sqrt{\epsilon_o}$ and the *extraordinary index* $n_e = \sqrt{\epsilon_e}$. It follows that, if light is linearly polarized along the *optic axis*, defined as the eigendirection associated to ϵ_e, then it will propagate with speed c/n_e, while it will propagate with speed c/n_o if polarized along any direction orthogonal to the optic axis. It is thus easy to derive the action of such a material on an arbitrary input polarization. Let us consider z as the propagation axis, x as the optic axis and let d be the thickness. This means that a $|H\rangle$ polarized input will acquire a phase $\exp(i2\pi n_e d/\lambda)$, while the phase acquired for a $|V\rangle$ input will be $\exp(i2\pi n_o d/\lambda)$. Thus the action of the birefringent material in the space of Jones vectors (in linear polarization basis) is given by the unitary matrix:

$$W(\delta) = \begin{pmatrix} e^{i\delta/2} & 0 \\ 0 & e^{-i\delta/2} \end{pmatrix} \tag{1.45}$$

where we have neglected a global phase factor $e^{i\Delta/2}$ (with $\Delta = 2\pi(n_e + n_o)d/\lambda$), and defined the *optical retardation*:

$$\delta = \frac{2\pi}{\lambda}(n_e - n_o)d. \tag{1.46}$$

The waveplate operator, $W(\delta, \alpha)$ in the case of an optic axis rotated at an angle α can be obtained by simply applying a rotation:

$$R(\alpha) = \begin{pmatrix} \cos\alpha & -\sin\alpha \\ \sin\alpha & \cos\alpha \end{pmatrix},$$

that gives:

$$W(\delta, \alpha) = R(\alpha)W(\delta)R^{-1}(\alpha).$$

The result takes a simple form in the circular polarization basis:

$$W_{cp}(\delta, \alpha) = \cos\left(\frac{\delta}{2}\right)1 + i\sin\left(\frac{\delta}{2}\right)\begin{pmatrix} 0 & e^{-2i\alpha} \\ e^{2i\alpha} & 0 \end{pmatrix} \tag{1.47}$$

where the subscript *cp* was used to remind that this expression is valid in the $\{L, R\}$ basis and 1 is the identity matrix. This result will be important in the following sections, where we will introduce waveplates with space variant optic axis $\alpha = \alpha(x, y)$, which are a powerful tool for manipulating structured light and implementing spin-orbit coupling in light beams.

There are two specific kinds of waveplates of particular interest: the case $\delta = \pi$, which refers to a so called *half wave plate* (HWP) and the case $\delta = \pi/2$ in which the material is called *quarter wave plate* (QWP).

An half wave plate flips the handedness of circular polarization. On the other hand, a beam linearly polarized along a direction making an angle α with the optic axis of the

HWP remains linearly polarized but the oscillation direction is rotated by 2α towards the optic axis of the plate.

A quarter wave plate can be used to convert linear into circular polarization, and vice versa. Indeed if the optic axis is rotated by $\alpha = \pm\pi/4$ with respect to an input linearly polarized light (the angle is positive for counterclockwise rotations as seen from the observer) then the outgoing light will be, respectively, L or R polarized.

Combining these two devices, one can generate an arbitrary polarization state starting from a linear one, say $|H\rangle$. Indeed, from straightforward calculations, it is possible to show that, in order to generate the generic state $|E\rangle = \cos(\theta/2)|L\rangle + \exp(i\phi)\sin(\theta/2)|R\rangle$ it suffices to apply to the initial $|H\rangle$ state the sequence: $QWP(\beta) \cdot HWP(\alpha)$, provided that the angles β and α satisfy the relations:

$$\alpha = \frac{1}{4}(\phi + \theta - \frac{\pi}{2}) \tag{1.48}$$

$$\beta = \frac{\phi}{2}. \tag{1.49}$$

We conclude this section with a remark. In deriving the expression for the waveplate operators we have considered the optic axis as perpendicular to the z axis. If the optic axis makes an angle γ with the propagation direction of the light beam, all the previous formulas are still correct, provided that one replaces the extraordinary index n_e with an effective index $n(\gamma)$ given by [6]:

$$\frac{1}{n^2(\gamma)} = \frac{\cos^2(\gamma)}{n_o^2} + \frac{\sin^2(\gamma)}{n_e^2}. \tag{1.50}$$

This result allows to tune the optical retardation of a device by simply rotating its optic axis towards the propagation direction.

1.4.2 The Orbital Angular Momentum (OAM)

We have seen that Circular Beams, i.e. paraxial beams characterized by a phase which is a linear function of the azimuthal angle, carry a quantized value of the Orbital Angular Momentum (OAM), equal to $l\hbar$ per photon (l is an integer number). The wavefront of a CiB, i.e. the surface of constant phase, consists in $|l|$ intertwined helices with handedness given by the sign of l, as shown in Fig. 1.2. The characteristic wavefronts of CiBs are singular on the beam axis, $r = 0$. As a consequence the intensity on the beam axis is zero. This manifests in a peculiar transverse intensity profile that presents a ”donut” shape. We will give specific examples in the following subsections where particular classes of CiBs will be introduced.

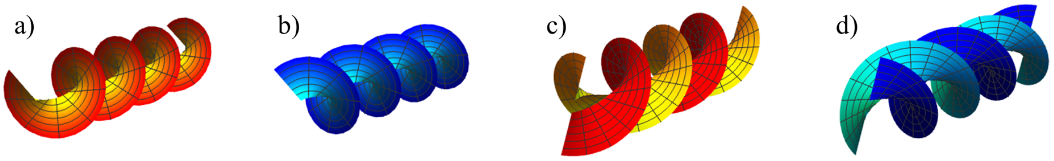

FIGURE 1.2: **Wavefronts of Circular Beams.** Some examples of wavefronts for beams carrying OAM are shown for: a) $l = 1$, b) $l = -1$, c) $l = 2$ and d) $l = -2$.

Since the OAM is an infinite dimensional degree of freedom, one can use it to implement Hilbert spaces of high dimensionality. We can introduce these spaces even remaining in a classical framework. Indeed the functions $\exp(il\phi)$ are vectors $|l\rangle$ that generate an infinite and discrete Hilbert space $\mathcal{H}_o$. A general state $|\psi\rangle \in \mathcal{H}_o$ will be represented as the complex superposition:

$$|\psi\rangle = \sum_l a_l |l\rangle. \tag{1.51}$$

Such a state will correspond to a beam that can be written as a superposition of CBs with different l. We are ignoring for the moment the radial structures of these states, which will be introduced below.

In $\mathcal{H}_o$ is defined the Hermitian scalar product between two vectors $|\psi\rangle = \sum_l a_l |l\rangle$ and $|\zeta\rangle = \sum_l b_l |l\rangle$:

$$\langle\psi|\zeta\rangle = \int_0^{2\pi} \sum_{l,m} a_l^* b_m e^{i(m-l)\phi} \frac{d\phi}{2\pi} = \sum_l a_l^* b_l. \tag{1.52}$$

As a consequence, a general vector $|\psi\rangle \in \mathcal{H}_o$ carries an average OAM given by:

$$\langle\psi|\hat{l}_z|\psi\rangle = \int_0^{2\pi} \psi^*(\phi)(-i\partial_\phi)\psi(\phi) \frac{d\phi}{2\pi} = \sum_l l\, |a_l|^2 . \tag{1.53}$$

where we used $\hbar = 1$.

The OAM can be considered as a quantized observable even in the quantum domain. The use of quantum computational tasks involving single photons is an active research field: for example it has been used for implementing qutrits [12], realizing optimal quantum cloning in high dimensions [13], and can be an useful tool in quantum communications [14–16], and for investigating fundamental aspects of quantum physics [17, 18]. A recent review can be found in Ref. [19].

Until now we have considered only the role of the azimuthal phase factors in CiBs. In fact the slowly varying envelope of a CiB is given by $u(r)\exp(il\phi)$, thus one can deal with CiBs with the same OAM but different radial profiles $u(r)$. Hence, two beams with the same OAM can present a partial overlap due to different radial structures. This is an important consideration for many applications concerning OAM generation and measurement. For example, some techniques for measuring the OAM power spectrum of an unknown beam, based on filtering methods, can suffer of inefficiencies since the filter actually selects also a specific radial shape.

In general the solutions of the paraxial equation can still be considered as vectors of an Hilbert space with scalar product:

$$\langle\psi|\zeta\rangle = \int \psi^*(r,\phi)\zeta(r,\phi)rdrd\phi. \tag{1.54}$$

The basis states of this Hilbert space will be given by: $u_{l,p}(r)\exp(il\phi)$, where p can be an additional discrete index labeling the radial modes. An example of such basis modes is given by the Laguerre-Gaussian beams that we will introduce below.

1.4.2.1 Laguerre-Gaussian beams

Laguerre-Gauss modes where introduced by Zucker in 1970 [20] as higher order modes of optical resonators with Gaussian profiles of the mirror reflectivity. The Gaussian mode, often referred as the $TEM_{0,0}$ mode, arose as the fundamental mode of this family of solutions of the paraxial equation. In 1992, Allen et al. [21], explicitly considered Laguerre-Gaussian beams to show that light can carry OAM. In the work of Allen et al. the relationship between helical wavefronts and Orbital Angular Momentum was recognized for the first time.

Laguerre-Gaussian $LG_{p,m}$ modes have the well known expression:

$$LG_{p,m}(\rho,\zeta,\phi) = \sqrt{\frac{2^{|m|+1}p!}{\pi(p+|m|)!(1+\zeta^2)}}\left(\frac{\rho}{\sqrt{1+\zeta^2}}\right)^{|m|} e^{-\frac{\rho^2}{1+\zeta^2}} \tag{1.55}$$

$$L_p{}^{|m|}(2\rho^2/(1+\zeta^2))e^{i\frac{\rho^2}{\zeta+1/\zeta}}e^{im\phi}e^{-i(2p+|m|+1)\arctan(\zeta)}, \tag{1.56}$$

where we used adimensional coordinates: $\rho = r/w_0$, $\zeta = z/z_0$. $L_p{}^{|m|}(x)$ are generalized Laguerre polynomials, defined by $L_p{}^n = (x^{-p}e^x/n!)\frac{d^n}{dx^n}(x^{p+n}e^{-x})$. The index p is an integer equal or greater than 0.

These beams possess many remarkable features. Their shape does not change during propagation, a property which is not surprising since it follows from the fact that they have been found as stable solutions of the paraxial equation inside an optical resonator. As a consequence, they are eigenfunction of the 2D Fourier transform operator, i.e. the phase and amplitude pattern is unchanged (apart from a global rescaling of the coordinates) in the far field. Moreover, as shown in Ref. [22], $LG_{p,m}$ beams are the CiBs with the smallest possible free space beam divergence, which makes them the best candidate for long distance free space communications based on OAM.

The intensity and phase of some Laguerre Gaussian modes is plotted in Fig. 1.3. The

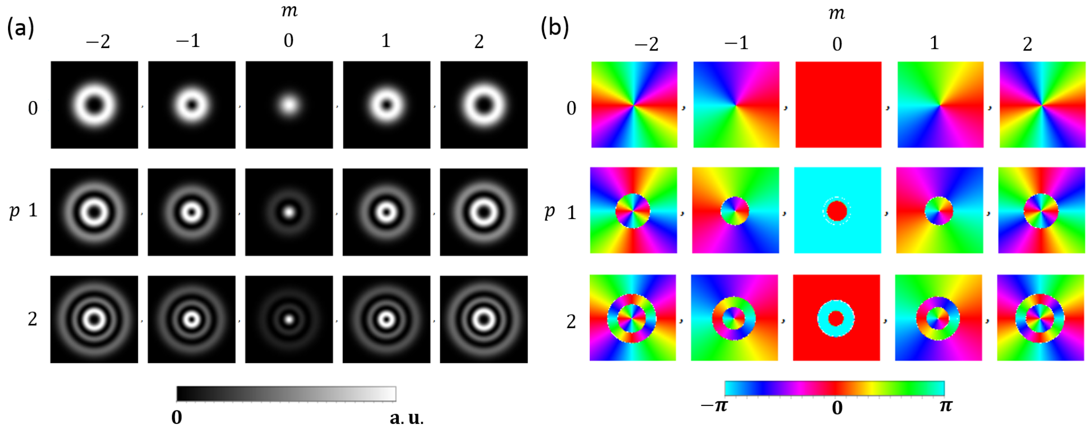

FIGURE 1.3: **Intensity and phase of LG beams.** Some examples of Laguerre-Gaussian beams are shown for $m = -2, \dots, 2$ and $p = 0, 1, 2$. In a) the intensity patterns are displayed. It is evident that with increasing m the central hole becomes larger while the index p gives the number of additional annular rings. The phase patterns are shown in inset (b). The nonzero OAM is associated with the existence of a phase singularity with charge m. For nonzero values of p some phase jumps of π appear in correspondence of the zeros of the Laguerre polynomials.

tipical annular shape associated to the azimuthal phase factor can be appreciated. Moreover the size of the central hole grows with the associated OAM. This is due to the factor $\rho^{|m|}$ in Eq. 1.56. For $p > 0$ the Laguerre polynomials have additional zeros at radii $\rho > 0$. As a consequence additional concentric rings appear, whose number is determined by the radial index p. In correspondence of the intensity zeros there are phase singularities. At $\rho = 0$ there is a point singularity that is common in all the CiBs. The phase of the beam changes of a factor $2\pi m$ when following a closed path, $\mathcal{C}$, around the singularity. Thus one says that m is the *winding number*, or *topological charge* associated to the phase singularity. The concept of winding number is very general and will be considered in many different situations in this Thesis (see in particular Chapters 3 and 5). Additional phase singularities are disclination lines that correspond to the zeros of the Laguerre polynomials. Here the change of sign in the beam amplitude manifests in a phase jump of π.

Laguerre-Gaussian modes are an orthogonal and complete basis. Indeed they satisfy the relation:

$$\langle LG_{p,m}|LG_{q,l}\rangle = \delta_{m,l}\delta_{p,q} \tag{1.57}$$

where the scalar product is the one defined in Eq. 1.54 and the completeness means that every paraxial beam can be expressed as a linear superposition of (in general infinite) LG modes.

1.4.2.2 Hypergeometric-Gaussian Beams

Laguerre-Gaussian modes are the most known examples of Circular Beams, perhaps because of their remarkable features (like small divergence and propagation invariant shapes) and historical interest. However, in many applications involving OAM, the actual beams that are generated in the laboratory can be quite different. Indeed, the majority of techniques for generating OAM modes are based on optical devices whose action consist into multiplying an input Gaussian beam by a phase $\exp(il\phi)$. Thus, on the plane of the transforming device, the beam intensity will be a simple Gaussian. The characteristic hole on the beam center will be generated only during the propagation (in practice it exist already on the device plane because the central singularity "written" on the device has a finite dimension). If we suppose that the beam impinging on this device is collimated (as usual in the experiments), then the slowly varying envelope of the beam on the $\zeta = 0$ plane will be:

$$u(\rho, \phi) \propto \exp(-\rho^2)\exp(-il\phi). \tag{1.58}$$

This expression cannot match with the one of a Laguerre-Gauss mode and thus it will propagate in a different way. The expression of the field on the plane ζ, $u(\rho, \zeta, \phi)$, can be calculated by means of the Fresnel diffraction integral:

$$u(\rho, \zeta, \phi) = \frac{-i}{\pi\zeta}\int \exp\Big(-i\frac{\rho^2 + \rho'^2 - 2\rho\rho'\cos(\phi - \phi')}{\zeta}\Big)u(\rho', 0, \phi')\rho' d\rho'\phi'. \tag{1.59}$$

The solution of this integral can be expressed analytically:

$$u(\rho, \zeta, \phi) = C_{|l|}(\zeta + i)^{-(|l|/2+1)}\zeta^{-|l|/2}\rho^{|l|}e^{-i\frac{\rho^2}{\zeta+i}}e^{i\,l\phi}\,{}_1F_1\big(\frac{|l|}{2}; |l| + 1; \frac{\rho^2}{\zeta(\zeta + i)}\big), \tag{1.60}$$

where $C_{|l|}$ is a normalization constant and ${}_1F_1(a; b; x)$ is the confluent hypergeometric function of the first kind [23]. This mode is a special case of a more general family of modes, called Hypergeometric Gaussian modes, $\mathrm{HyGG}_{p,l}$ [24]. Eq. 1.60 corresponds to the case $p = -|l|$. Modes with different values of p result from the diffraction of a beam whose amplitude in the $\zeta = 0$ plane is $\rho^{p+|l|}\exp(-\rho^2)\exp(-il\phi)$. Their explicit expression, together with the expansion in terms of LG modes, can be found in Ref. [24].

Examples of intensity patterns of $\mathrm{HyGG}_{-|m|,m}$ modes are shown in Fig. 1.4. Since the function ${}_1F_1(|l|/2; |l| + 1; \rho^2/\zeta(\zeta + i))$ does not have zeros for $\rho > 0$, the $\mathrm{HyGG}_{-|m|,m}$ do not present additional annular rings like the Laguerre-Gauss modes, hence the only phase singularity is the one on the beam axis whose topological charge m is related to the OAM carried by these modes. However, since a single Hypergeometric-Gaussian

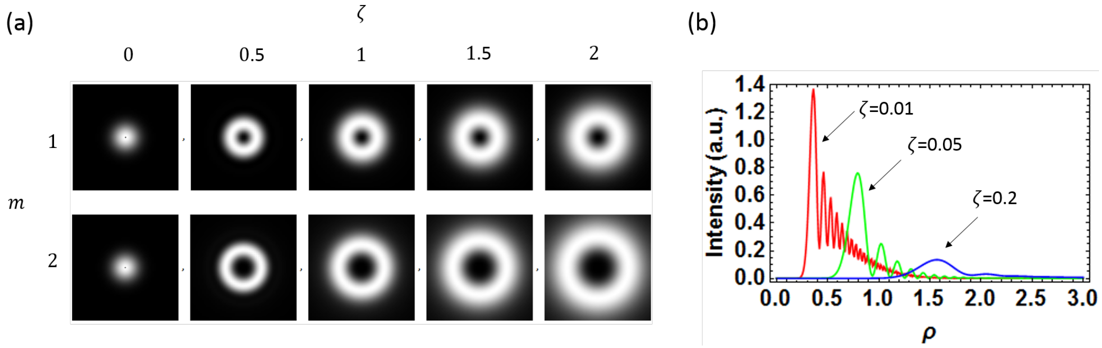

FIGURE 1.4: **Intensity and phase of HyGG beams.** In a) the intensity patterns of some $HyGG_{-|m|,m}$ modes are displayed for $m = 1, 2$ at different ζ. In inset (b) the radial profile for $m = 10$ is plotted for $\zeta = 0.01, 0.05, 0.2$, showing the existence of characteristic "ripples" in the near field arising from the superposition of an infinite number of LG modes

beam is a superposition of an infinite number of LG$_{p,m}$ modes, the multiple rings of these modes can manifest in ripples along the radial shape of the HyGG$_{-|m|,m}$ intensity. These ripples are well visible in the near field, as shown in Fig. 1.4 b).

1.5 The discretized transverse wavevector space

We have seen that the Orbital Angular Momentum of light is a degree of freedom that can be used to emulate high dimensional Hilbert spaces. This makes the OAM a candidate for quantum computation with qudits. We recall that a N dimensional qudit is a quantum state obtained as a linear superposition of N orthogonal states: $|i\rangle$ where $i = 1, \dots, N$. There are other ways to realize qudits states in photonic experiments. Perhaps, the most obvious is to separate a beam (or even a single photon) in N multiple paths, the path i corresponding to the state $|i\rangle$. This is the multidimensional extension of the dual rail logic used in some implementation of photonic quantum gates. Photonic qudits have been implemented using also the time bin encoding of laser pulses, where each ket $|i\rangle$ is associated to a different arrival time of the pulse [25]. Even the radial degree of freedom of LG$_{p,m}$ modes could be in principle exploited. Indeed "quantum features" related to the p index have been demonstrated, like Hong-Ou-Mandel interference effects [18]. However, despite some recent efforts for multiplexing LG modes with different p indexes [26, 27], a complete toolbox for the manipulation of this degree of freedom is still missing.

Here we introduce another implementation of qudit states where each qudit $|i\rangle$ is associated to a tilted plane wave. The idea is to use the linear momentum as the degree of freedom that encodes an infinite dimensional Hilbert space. This space is actually not discrete, thus it should in principle studied in the framework of continous variables.

However, as it will be shown in this Thesis work, one can imagine to consider only a discrete subset of all the possible linear momenta and to use devices whose action is closed within this subspace. This consideration holds true also for implementations using the arrivial times of laser pulses or the optical paths. Moreover, for reasons that will become clear in Chapter 4, we will consider plane waves where the z component of the wavevector k_z is much larger that the transverse components k_x and k_y. k_z will be thus considered to be constant: $k_z \approx 2\pi/\lambda$, and the qudit states will be encoded by the couple (k_x, k_y), where both the transverse components of the wavevector will be integer multiples of a fixed constant p. We are thus dealing with qudits states labeled by two integer indexes $|n, m\rangle$ (that will be associated to a two dimensional lattice over which we can perform quantum walks -see Chapters 4 and 5) encoded in tilted plane waves as follows:

$$|n, m\rangle \rightarrow \exp\bigl(i(nx + my)p\bigr) \exp(ik_z z). \tag{1.61}$$

A geneirc state $|\psi\rangle = \sum_{n,m} c_{n,m}|n, m\rangle$ in this Hilbert space will be a linear superposition of different plane waves:

$$|\psi\rangle \rightarrow e^{ik_z z} \sum_{n,m} c_{n,m} \exp\bigl(i(nx + my)p\bigr), \tag{1.62}$$

where $c_{n,m}$ are complex numbers. Given the condition k_x, $k_y \ll k_z$, these plane waves can be considered, if one works in the near field, as propagating along the z direction but each with a slightly tilted wavefront. The two dimensional Fourier transform of such a beam gives the amplitude distribution of the field in the transverse wavevector space which will be a superposition of Dirac's delta functions:

$$\sum_{n,m} c_{n,m} \delta(k_x - npx,\ ky - npy). \tag{1.63}$$

We note that the intensity of this distribution can be experimentally obtained by looking at the field in the focus of a converging lens, whose action is indeed equivalent to a 2D Fourier transform.

In a real experiment one does not deal with plane waves but with beams that are spatially confined in the transverse plane, like Gaussian beams. As a consequence, the delta functions of Eq. 1.63 will be broadened and eventually overlap. Thus one should take into account the beam parameters in order to reduce as much as possible this overlap. In Chapter 4 these aspects will be discussed in the framework of the implementation of multidimensional Quantum Walks.

1.6 Manipulation of structured light

In this chapter we have seen how a light beam can exhibit a large variety of features related to the spatial variation of its phase, amplitude and oscillation direction of the electric field. A plethora of techniques has been developed so far. Here we will focus only on the technologies used in this thesis work.

1.6.1 Computer Generated Holograms

Let us consider the following problem: given an input Gaussian beam, which is easily produced in the laboratory both as the natural shape of the output of common laser cavities or by suitable spatial filtering techniques, one wants to transform it changing the amplitude and phase distribution. We can imagine to do this with a flat device whose action is to multiply the ingoing field with some transmission function spatially varying along the transverse plane: $t(x, y)$. This is often achieved using holographic techniques. In this case $t(x, y)$ is a real valued function that reproduces the intensity pattern that would result from the interference between the input Gaussian beam (called the reference wave U_r) and the desired output U_o. Let us approximate, for simplicity, U_r with a plane wave: $\exp(i(k_x x + k_z z))$. The transmission function, applied on the plane $z = 0$, is of the form:

$$t(x, y) = t_0 + 2\Re\{U_o(x, y)e^{-i(k_x x)}\}.$$

The resulting beam will be:

$$t(x, y)e^{ik_x x} = t_0 e^{ik_x x} + U_o(x, y) + U_o^*(x, y)e^{2ik_x x}$$

where we excluded the term describing propagation along z, $\exp(ik_z z)$, since it is factored out on both sides of the equation. The second term of the right hand side in the above equation is the beam that we wanted to produce. Notice that the other two terms have different wavevectors and will separate from U_o in the far field. Thus one can select the desired output by filtering the other diffraction orders. This is an example of amplitude modulation that changes also the phase at the expense of losing some light in other diffraction orders.

Beam shaping is often done using phase only holograms, i.e. devices whose transmission function is of the form: $t(x, y) = e^{ig(x,y)}$ and thus does not change the intensity of the beam (this is important especially when using single photons and losses have to be reduced as much as possible). In particular, blazing holograms are often used to get rid of effects due to spatial resolution and to maximize the amount of modulated light. A blazing hologram is of the form:

$$g(x,y) = \mathrm{Mod}\left(\frac{2\pi}{\Lambda_x}x + f(x,y),\ 2\pi\right), \tag{1.64}$$

where $f(x,y)$ is the desired phase modulation and $2\pi/\Lambda$ is the additional wavevector component that gives the propagation direction of the modulated beam.

A phase hologram is sufficient to generate beams carrying Orbital Angular Momentum. Indeed it suffices to choose the phase modulation function in the form $f(x,y) = l\ \arctan(y/x)$ where l will be the OAM of the desired beam. As we have seen in Section 1.4.2.2, such an hologram will generate Hypergeometric-Gaussain beams of the type $\mathrm{HyGG}_{-|l|,l}$. If one wants to control also the radial shape of the beam in general it will be necessary to introduce an amplitude modulation. Interestingly this can still be done by phase only holograms (which are the most widely used, especially the ones whose structure can be dynamically changed by computer control). In principle one should look for the function $\exp(ig(x,y))$ that best approximates the desired field $A(x,y)\exp(i\psi(x,y))$. Several approaches have been demonstrated that achieve this goal, that are reviewed in Ref. [28]. Among these we cite the one in Ref. [29], where the authors consider the transmission function:

$$t(x,y) = \exp\Big(iM(x,y)\mathrm{Mod}(F(x,y) + 2\pi x/\Lambda,\ 2\pi)\Big) \tag{1.65}$$

the action on an impinging plane wave gives, after selecting the first diffraction order, the output mode:

$$E(x,y) = -\mathrm{sinc}(\pi M - \pi)e^{i(F+\pi M)}. \tag{1.66}$$

Thus one can obtain the desired beam by using the relations:

$$M = 1 - \frac{1}{\pi}\mathrm{sinc}^{-1}(A) \tag{1.67}$$

$$F = \psi - \pi M, \tag{1.68}$$

where A and ψ are the amplitude and phase of the desired beam.

Nowadays these holographic techniques are widely used thanks to devices, known as spatial light modulators (SLMs) that allow to remotely control the displayed hologram with the help of a computer. These SLMs are usually based on liquid crystal displays (LC-SLMs) or digital micromirror devices (DMDs). The hologram can be calculated on a computer and then displayed on the SLM. LC-SLMs consist in a layer of aligned liquid crystal molecules behind which a matrix of independent electrodes is used to apply an electric field on the molecules. The orientation of the molecules can be controlled by the applied voltage that can be different for each pixel. As a result the light beam, polarized along the principal axis of the molecules, will acquire at each pixel a different phase. DMDs operate as binary amplitude modulators. They present higher frame rates that LC-SLMs, but at the expense of limited modulation depth and diffraction efficiency. However they are recently emerging as practical SLM, in particular they have been showed to be superior with respect to LC-SLMs for the light control in complex environments, comprising high scattering layers, aberrated optical systems and multimode fibers [30].

1.6.2 Spin-orbit and spin-momentum coupling in liquid crystal based devices

In section 1.4.1 we have introduced wave retarders as devices to manipulate the polarization of light. In that case we focused on the common case of waveplate with uniform optic axis. However, one can also consider a waveplate where some of its properties, i.e. the optic axis orientation or the optical retardation, are spatially inhomogeneous. As a consequence of the spatial modulation, a beam crossing such a device will not only change its polarization but also the phase (and, in general, the amplitude) in a way that depends on the loal properties of the device. The Jones matrix of these space-variant waveplates follows directly from the one in Eq. 1.47:

$$W(\delta,\alpha) = \cos\left(\frac{\delta(x,y)}{2}\right)1 + i\sin\left(\frac{\delta(x,y)}{2}\right)\begin{pmatrix} 0 & e^{-2i\alpha(x,y)} \\ e^{2i\alpha(x,y)} & 0 \end{pmatrix} \tag{1.69}$$

where we have simply introduced a dependence on the transverse coordinates x and y in the optical retardation δ and optic axis angle α. These devices allow to modify the shape of an optical beam in a way that is conditioned by the input polarization. In this sense we refer to these effects as *spin-orbit coupling of light*, where the term "orbit" can be understood in the general sense of the trajectories of the light wavevector. In the specific case of q-plates, as we will see below, one can actually achieve an exchange of spin and orbital angular momentum. This Thesis work is mainly dedicated to exploit spin-orbit photonics in classical and quantum applications.

In the following we will focus on devices with uniform optical retardation but space-variant optic axis. We only mention here the existence of devices that, by means of applied stresses, use a spatially varying δ to generate inhomogeneous polarization patterns and bottle beams [31][32].

Let us now consider a special case of Eq. 1.69 with $\delta = \pi$ (corresponding to an half wave plate). In this case an input circularly polarized beam will flip its polarization handedness but will also acquire a phase $\exp(\pm i2\alpha(x,y))$, where the sign ± depends on the handedness of the input polarization (+ for input $|L\rangle$ and $-$ for $|R\rangle$). In particular we can think of a device where the optic axis is a linear function of the azimuthal angle ϕ:

$$\alpha(\phi) = \alpha_0 + q\phi. \tag{1.70}$$

Some examples of the resulting pattern are shown in Fig. 1.5. In this case one will obtain a beam with an helical phase factor $\exp(\pm i2q\phi)$ that carries a well defined OAM $l = 2q$ provided that q is an integer or semi-integer. An anisotropic device, with arbitrary uniform retardation δ, characterized by the optic axis given in equation Eq. 1.70 is called a *q-plate* [33]. The q parameter is called the topological charge of the pattern. Indeed it can be identified with the winding number of the field $\alpha(\phi)$ around the origin, which is a singularity for $\alpha(\phi)$.

When $\delta = \pi$ the action of a q-plate consists into a positive (negative) flip of the SAM and negative (positive) change of the OAM by an amount $|2q|$. Interestingly, in the case $q = 1$ there is a perfect balance between the OAM and SAM variations, implying that the total angular momentum of light is unchanged. Hence the q-plate can act as a device that exchanges SAM and OAM. In this particular example ($\delta = \pi$, $q = 1$) there is *total SAM to OAM conversion* (STOC). For $q \neq 1$ one has incomplete STOC, and some of the angular momentum carried by light is transferred to the device. When $\delta \neq \pi$ only a fraction of the light, equal to $\sin^2(\delta/2)$ experiences the STOC.

The concept of q-plates was introduced in 2006 by Marrucci et al. [33], where for the first time the STOC process was demonstrated using q-plates based on nematic liquid crystals. They consist of a 6 μm thick layer of liquid crystal sandwiched between two glasses coated with a dye. The liquid crystal molecules tend to orient along the axis of dye molecules, whose pattern is written through a photoalignment technique that allows to realize geometries wih arbitrary topological charge [34]. Liquid crystal based q-plates are a versatile tool due to the possibility to control the optical retardation δ. This was done originally by means of thermal tuning [35], but then it was made faster by the addition of a conductive ITO substrate on the glasses that allowed to tune δ by changing the applied voltage [36]. The majority of the works presented in this Thesis were based on the use of one or more q-plates and on the exploitation of the tuning of the optical retardation.

As the q-plate implements the coupling between spin and orbital angular momentum of light, it is possible, with similar devices, to couple the SAM and the linear momentum (that is the propagation direction). Phenomena involving coupling between spin and linear momentum of light are at the basis of *chiral optics*. They often arise in nanophotonic devices where variations of the transverse field on the scale of the wavelength lead to the appearence of a strong longitudinal field with a phase of ±$\pi/2$ with respect to the transverse field where the sign, that gives the handedness of the transverse spin component, is determined by the propagation direction [37]. We can implement a similar phenomenon in the framework of paraxial optics by considering again a patterned half-wave plate where, this time, the optic axis results as a linear function of one Cartesian coordinate, say x:

$$\alpha(x) = \alpha_0 + (-1)^s \frac{\pi}{\Lambda} x. \tag{1.71}$$

This device (whose pattern is sketched in Fig. 1.6 (a)) is such that an $L(R)$ polarized input beam acquires a transverse component of the wavevector given by $\mp(-1)^s 2\pi/\Lambda$. In Eq. 1.71 the parameter $s = 0, 1$ takes into account that the angular coefficient of the equation $\alpha(x)$ can be positive or negative. This sign actually depends on the orientation of the device: it can be inverted by a π rotation of the pattern around the x direction. The parameter Λ gives the spatial period of the optical axis pattern. We remark that one period correspond to a π rotation of $\alpha(x)$ (not 2π). The coefficient α_0, differently from its q-plate analogue, does not determine any feature of the pattern shape since it is actually dependent on the choice of the origin of the x axis. However it will acquire importance when considering a stack of these devices.

When based on liquid crystals, devices described by Eq. 1.71 are known in literature as Liquid Crystal Polarization Gratings (LCPG). In general the term polarization grating can refer both to a polarizer (thus a non unitary operator) or to a waveplate. We will focus on the case of waveplates and will choose to call these devices with the term *g-plates*, where ”g” stands for ”grating” [38]. Indeed, when seen between crossed polarizers, these devices appear as gratings with spatial periodicity $\Lambda/2$ (see Fig. 1.6 (b)). The doubled frequency of the grating with respect to the spatial frequency of the optic axis pattern is due to the fact that the light polarization is left unchanged when $\alpha(x) = 0$ or $\pi/2$. The action of g-plates can be interpreted as a ”circular polarizing beam splitter”, in the sense that it separates, at least in the far field, the right and left circular component of light beams. Fig. 1.6 (c) illustrates this concept considering also the case of different δ. The g-plate can be used a a fundamental device for manipulating the transverse momentum of light. The last part of this thesis work will be indeed dedicated to the use of g-plates and uniform waveplates for the implementation of quantum walks on one and two dimensional lattices.

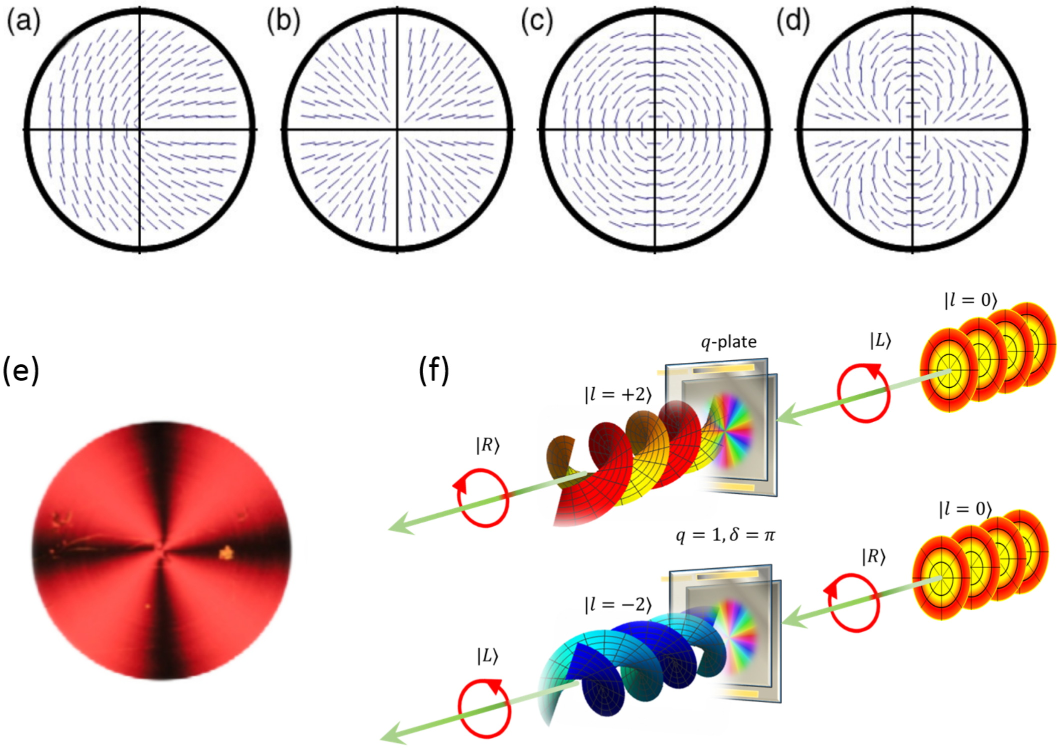

FIGURE 1.5: **SAM to OAM conversion with q-plates.** The basic features of q-plates are illustrated. A q-plate is an anisotropic device whose optic axis α angle is a linear function of the azimuthal angle: $\alpha(\phi) = \alpha_0 + q\phi$. In the top of the figure different examples of q-plate patterns are illustrated: (a) $q = 1/2$, $\alpha_0 = 0$, (b) $q = 1$, $\alpha_0 = 0$, (c) $q = 1$, $\alpha_0 = \pi/2$, (d) $q = 2$, $\alpha_0 = 0$. Inset (e) shows a liquid crystal based $q = 1$ plate between two crossed polarizers under white light illumination. Inset (f) illustrates the STOC process: a plane wave $L(R)$ polarized crosses a $q = 1$ plate at half wave retardation $\delta = \pi$ and is transformed into an helical wave with OAM $l = +2(-2)$ and with inverted circular polarization. Panels (a-e) are adapted from [39].

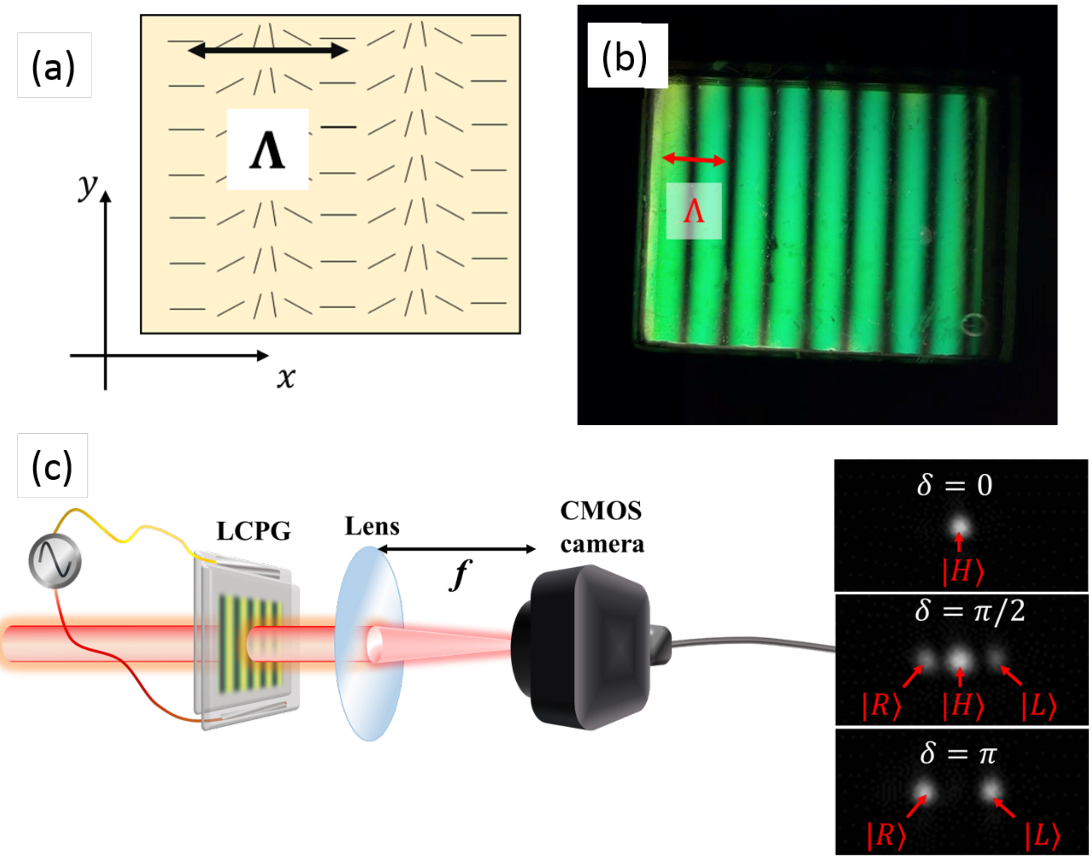

FIGURE 1.6: **Working principle of LCPGs.**(a) Sketch of the liquid crystal pattern in a g-plate. In (b), a g-plate seen between crossed polarizers under white light illumination is shown. It appears as a grating whose pitch is $\Lambda/2$. In panel (c) the working principle of a g-plate is illustrated: a laser beam crosses the electrically controlled device and then is focused by a lens in order to visualize the effect of the g-plate in the far field. The result, depending on the optical retardation of the device, is illustrated on the right: at $\delta = 0$ the device acts as the identity operator and only a single Gaussian spot (in this case linearly polarized) appears on the focal plane, increasing δ two lateral spots appear with opposite circular polarizations. At $\delta = \pi$ the central spot is suppressed.

Chapter 2

Measurement of structured light beams

2.1 Introduction

[1] As we will see in Chapters 4 and 5, a Quantum Walk in the OAM space generates light beams that are complex superpositions of different helical modes. Obtaining the probability distributions resulting from this process will require to experimentally measure the OAM power spectrum of the final beam. In this chapter we will introduce a simple method that achieves this goal by digital analysis of the interference pattern formed by the light beam and a reference field. Our approach allows one to characterize the beam radial distribution also, hence retrieving the entire information contained in the optical field. Setup simplicity and reduced number of measurements could make this approach practical and convenient for the characterization of structured light fields. This technique will provide useful in replacing the more time consuming approach, used hitherto in our QW setup, based on multiple projective measurements.

Light beams carrying orbital angular momentum (OAM) are key resources in modern photonics. In many applications, the ability of measuring the complex spectrum of structured light beams in terms of these fundamental modes is crucial.

The ability to ascertain experimentally the OAM values associated with individual helical modes represents a fundamental requirement for all applications based on twisted light. Hitherto, this has been demonstrated by a variety of methods: exploiting double slit interference [41], diffraction through single apertures [42–45] or through arrays of pinholes [46], interference with a reference wave [47, 48], interferometers [49–51], OAM-dependent Doppler frequency shifts [52, 53], phase flattening and spatial mode projection

---

[1] Some paragraphs and sentences of this section are adapted or copied verbatim from the work [40] which I coauthored

using pitchfork holograms [54–56], q-plates [57, 58], spiral phase plates [59] and volume holograms [60], spatial sorting of helical modes by mapping OAM states into transverse momentum (i.e. propagation direction) [61, 62], quantum weak measurements [63].
General structured fields are however not given by individual helical modes, but can always be obtained as suitable superpositions of multiple helical modes. Accordingly, a full experimental characterization of these structured fields can be based on measuring the complex coefficients (amplitude and phase) associated with each mode appearing in the superposition, for any given choice of the mode basis. In general, this is not a trivial task, but several methods for the reconstruction of the complex spectrum associated with the OAM degree of freedom have been demonstrated thus far [49, 53, 57, 59, 60, 64], possibly including also the radial mode spectrum reconstruction [55, 56, 61–63, 65, 66]. It is worth noting that, once these complex coefficients are known, the complete spatial distribution of the electric field can be obtained and important properties such as beam quality factor M^2, beam width and wavefront are easily computed at any propagation distance [64, 67].
In this chapter we will first review the most important techniques used for the detection of OAM spectra. Then we will describe in detail our new proposal (Ref. [40]).

2.2 Review of the techniques for measuring the OAM of light

A general structured light beam can be written as a superposition of helical modes: $|\psi\rangle = \sum_l a_l |l\rangle$ (we ignore, for the moment, the radial modes). Reconstructing the OAM spectrum means to experimentally measure the complex coefficients a_l. If one is interested only in the moduli of these coefficients then we will talk of OAM *power spectrum* or OAM *probability distribution*. These can be obtained by measuring the intensity of the light passing through a set of devices that implement the projection operator $P_l = |l\rangle\langle l|$.
Suppose that we have at disposal a spatial filter that selects only the $l = 0$ mode. This can be realized by a single mode fiber or by a pinhole placed in the focus of a converging lens. We can then implement P_m by multiplying $|\psi\rangle$ to a phase $\exp(-im\phi)$. Indeed the resulting beam will be: $\sum_l a_l \exp\big(i(l-m)\phi\big)$, and the mode with OAM l will be transformed into the fundamental one, i.e. its phase structure will be "flattened", and selected by the filter. Doing this for all the values of m will allow to reconstruct the full power spectrum (of course, in practice this can be done for a limited number of OAM values). This *phase flattening* technique can be easly implemented using Spatial Light Modulators that implement the transmission functions $g_m(r,\phi) = \exp(-im\phi)$ and filtering the first diffraction order with a single mode fiber. It has been used in Ref.

[54] to demonstrate entanglement in the OAM modes. The same toolbox can be used also for measuring the full OAM state [68, 69] of photons generated in Spontaneous Parametric Down Conversion by means of tomographic measurements. Quantum tomography requires measurements on multiple non-orthogonal bases, hence in this case the set of measurements $\{P_l\}$ is not sufficient. However, with SLMs one can readly realize the projection on superposition of OAM states, like: $|p\rangle = (|j\rangle + |k\rangle)/\sqrt{2}$ and $|q\rangle = (|j\rangle + i|k\rangle)/\sqrt{2}$, where $|j\rangle$ and $|k\rangle$ are OAM eigenstates. The density matrix representing a general quantum state can be written as $\rho = \sum_{j,k} \rho_{j,k} |j\rangle\langle k|$. The coefficients $\rho_{j,k}$ can be obtained experimentally by taking the projections over the states: $|p\rangle, |q\rangle, |j\rangle, |k\rangle$ and making use of the identity [68]:

$$|j\rangle\langle k| = |p\rangle\langle p| + i|q\rangle\langle q| - (1+i)(|j\rangle\langle k| + |k\rangle\langle j|)/2.$$

The phase flattening technique can in principle been used to distinguish between different OAM modes with high accuracy. However it can be unpractical when dealing with a large number of modes. Indeed, single photons projection measurements are limited by a success rate $1/N$, where N is the number of modes of interest. Moreover it was shown in Ref. [70] that the detection efficiency can decrease with l. Indeed the single mode fiber selects not only the modes with $l = 0$ but more precisely the ones with a specific radial shape (usually well approximated by a Gaussian). This means that contributions coming from $\mathrm{LG}_{l=0,p>0}$ modes will be suppressed, too. The phase flattening technique only cancels the helical phase of a specific OAM mode without controlling the radial shape. As a consequence the contributions from high OAM modes will be underestimated. This implies that in experiments that make use of the phase flattening technique a careful calibration procedure is required.

Instead of using projection measurements one can think of spatially separating the different modes contained in an optical beam. A first proposal was given in Ref. [49] where a cascade of interferometers selectively splitting different OAM modes was devised. The basic element is a Mach-Zender interferometer with a Dove prism in each arm. The relative angle α between the prisms is such that, given an input mode with OAM l that is split into the two arms, the beams meeting in the output beam splitter will have a phase difference $2l\alpha$. For $\alpha = \pi/2$ this can be used to sort modes with even and odd OAM. Ref. [49] shows how cascading different interferometers of this kind, with different values of α can allow to measure the Orbital Angular Momentum of a single photon. However this technique is practically challenging in terms of stability and number of resources.

A more efficient and successful ”OAM sorter” was later introduced by Berkhout et al.

[65]. This consists in only two optical phase elements and can in principle be applied to any superposition of modes. The basic idea is to implement a phase transformation that maps the OAM eigenstates in plane waves with a given transverse wavevector. If such a transformation is performed, then one can use a Fourier transforming lens to separate the different wavevector contributions and measure the corresponding intensities. Suppose that we want to image the point (x, y) in the object plane Γ_0 into a point (u, v) in the image plane Γ_1, that we suppose being coincident with the Fourier plane of a lens, given by the relations: $u = u(x, y)$ and $v = v(x, y)$. This can be achieved introducing a space variant phase $\phi_1(x, y)$ on a normally incident plane wave. This phase element introduces transverse wavevector components given by $k_x = \partial_x\phi_1(x, y)$ and $k_y = \partial_y\phi_1(x, y)$ which are focused on the point (u, v) in the Fourier plane provided that the following relations are satisfied:

$$\frac{\partial\phi_1(x,y)}{\partial x} = \frac{k}{f}u(x,y), \tag{2.1}$$

$$\frac{\partial\phi_1(x,y)}{\partial y} = \frac{k}{f}v(x,y), \tag{2.2}$$

where f is the focal length of the lens. For smooth phase elements, i.e. such that $\partial_x\partial_y\phi_1 = \partial_y\partial_x\phi_1$ these relations can be obtained only for conformal transformations, i.e. the functions $u(x, y)$ and $v(x, y)$ must satisfy: $\partial_y u(x, y) = \partial_x v(x, y)$. In particular, for obtaining an OAM sorter, one would map the azimuthal angle $\phi = \arctan(y/x)$ into a Cartesian coordinate u. Posing $u = \arctan(y/x)$ one has that, in order to obtain a conformal transformation, $v = \ln(x^2 + y^2)/2$. The phase $\phi_1(x, y)$ can be calculated from Eq. 2.2 to be:

$$\phi_1(x,y) = \frac{k}{2f}\Big(y\ln(x^2+y^2) - 2x\arctan(y/x) - 2y - (x^2+y^2)\Big). \tag{2.3}$$

where we added a quadratic phase term $-k(x^2 + y^2)/2f$ in order to incorporate the effect of the lens in the optical phase element. If one wants to convert this system into an afocal one, in order that the coordinate-transformed image propagates unchanged, and additional phase element, placed at a distance f from ϕ_1, is required [71]. This is given by the phase varying function:

$$\phi_2(u,v) = \frac{k}{2f}\Big(2e^v\cos(u) - 2y - (u^2+v^2)\Big). \tag{2.4}$$

When implemented with refractive elements this sorter can present a 20% cross talk[72]. However these cross talk effects have been reduced in Ref. [73] by introducing an additional fan-out phase element that generates N coherent copies of the beam that result in narrower spots in the Fourier plane. With this technique it has been possible to lower cross talk effects under 10% [62]. Hitherto the OAM sorter has been used to measure states with up to 50 OAM modes [63, 74].

In the following section we will describe an alternative approach for measuring both the OAM and radial spectrum, based on digital analysis of the unknown beam interfering with a reference [40]. This approach relies on a small set of measurements and can be implemented with ordinary equipment without the need for special devices.

2.3 Measuring the complex orbital angular momentum spectrum and spatial mode decomposition of structured light beams

[2] Inspired by previous works [53, 75–77], here we present an approach to the measurement of light OAM spectrum and, more generally, to spatial mode decomposition of structured light that may prove to be more practical than most alternatives. The OAM complex spectrum information is contained in the intensity pattern resulting from the interference of the light beam with a known reference field (such as a Gaussian beam), and can be hence easily extracted by a suitable processing of the corresponding images recorded on a camera. First, Fourier transform with respect to the azimuthal angle leads to determining the complex coefficients associated with each OAM value, as a function of the radial coordinate. Numerical integration over the latter then allows one to use this information to determine the OAM power spectrum and, eventually, to decompose each OAM component in terms of radial modes, e.g. LG beams. Remarkably, the whole information associated with the spatial mode decomposition, or with the OAM power spectrum, is contained in a few images, whose number does not scale with the dimensionality of the set of detected helical modes. A unique series of data recorded for the characterization of a given field is used for obtaining the decomposition in any basis of spatial modes carrying OAM (LG, HyGG, Bessel,...), as this choice comes into play only at the stage of image analysis.

2.3.1 Description of the technique.

In the following, we limit our attention to the case of scalar optics, as the extension to the full vector field is simply obtained by applying the same analysis to two orthogonal polarization components. Considering cylindrical coordinates (r, ϕ, z), the electric field amplitude associated with a monochromatic paraxial beam propagating along the z

---

[2] Some paragraphs and sentences of this section are adapted or copied verbatim from the work [40] which I coauthored

direction is given by:

$$E_s(r,\phi,z,t) = A_s(r,\phi,z)e^{-i(\omega t - k\,z)}, \tag{2.5}$$

where ω is the optical frequency and k is the wave number. We refer to E_s as the signal field, to distinguish it from the reference beam that will be introduced later on. The information concerning the spatial distribution of the field is contained in the complex envelope $A_s(r,\phi,z)$. Being periodic with respect to the azimuthal coordinate ϕ, such complex function can be expanded into a sum of fundamental helical modes $e^{im\phi}$, carrying $m\hbar$ OAM per photon along the z axis [78]:

$$A_s(r,\phi,z) = \sum_{m=K_1}^{K_2} c_m(r,z)e^{im\phi}, \tag{2.6}$$

where K_1 and K_2 are integer numbers representing the OAM spectrum bounds of the field, respectively (they can also be infinite in the case of unbounded spectra). Coefficients c_m are defined in terms of the angular Fourier transform

$$c_m(r,z) = \frac{1}{2\pi}\int_0^{2\pi} d\phi\, e^{-im\phi}A_s(r,\phi,z). \tag{2.7}$$

The probability $P(m)$ that a photon is found in the m-order OAM state is obtained from the coefficients c_m by integrating their squared modulus along the radial coordinate:

$$P(m) = \frac{1}{S}\int_0^{\infty} dr\, r\, |c_m(r,z)|^2, \tag{2.8}$$

where $S = \sum_m \int_0^\infty dr\, r\, |c_m(r,z)|^2$ is the beam power at any transverse plane. The quantity $P(m)$ is the OAM power spectrum, or spiral spectrum of the beam, and does not depend on the longitudinal coordinate z, because of OAM conservation during propagation. A complete analysis of the field in terms of transverse spatial modes is obtained by replacing $e^{im\phi}$ in Eq. 2.6 with a complete set of modes having a well defined radial dependance, e.g. LG modes:

$$A(r,\phi,z) = \sum_{p=0}^{\infty}\sum_{m=-\infty}^{\infty} b_{p,m}\,\mathrm{LG}_{p,m}(r,\phi,z), \tag{2.9}$$

The link between coefficients c_m and $b_{p,m}$ is then given by:

$$b_{p,m} = \int_0^{\infty} r\,dr\,\mathrm{LG}^*_{p,m}(r,z)\,c_m(r,z), \tag{2.10}$$

where we introduced the radial LG amplitudes $\mathrm{LG}_{p,m}(r,z) = \mathrm{LG}_{p,m}(r,\phi,z)e^{-im\phi}$, for which the ϕ dependence is removed.

The procedure we present here allows one to measure the complex quantities $c_m(r)$, or equivalently the coefficients $b_{p,m}$. We achieve this goal by letting the signal optical field interfere with a reference wave $E_{\text{ref}} = A_{\text{ref}}(r, \phi, z)e^{-i(\omega t - kz)}$, having the same polarization, frequency, wavelength and optical axis of the beam under investigation, and whose spatial distribution is known. The simplest choice for this reference is a Gaussian beam. At any plane transverse to the propagation direction, the intensity pattern I formed by the superposition of signal and reference beams is (we omit the functional dependance on the spatial coordinates)

$$I = I_s + I_{\text{ref}} + \widetilde{I}_\alpha. \tag{2.11}$$

Here I_s and I_{ref} are the intensities corresponding to the sole signal and reference fields, respectively, while the term $\widetilde{I}_\alpha = 2\,\text{Re}(e^{i\alpha} A_s\, A^*_{\text{ref}})$ corresponds to their interference modulation pattern, α being a controllable optical phase between the two. The interference modulation pattern can be experimentally singled out by taking three images, namely I, I_{ref} (blocking the signal beam) and I_s (blocking the reference beam), and then calculating the difference $\widetilde{I}_\alpha = I - I_{\text{ref}} - I_s$.

The interference modulation pattern is linked to the OAM mode decomposition by the following expression:

$$\widetilde{I}_\alpha = 2\sum_m |A_{\text{ref}}||c_m| \cos[m\phi + \alpha + \beta_m], \tag{2.12}$$

where $\beta_m(r, z) = \arg[c_m(r, z)] - \arg[A_{\text{ref}}(r, z)]$. By combining two interference patterns obtained with $\alpha = 0$ and $\alpha = \pi/2$ one then gets:

$$\widetilde{I}_0 - i\,\widetilde{I}_{\pi/2} = 2|A_{\text{ref}}| \sum_m |c_m|\, e^{i[m\phi + \beta_m]}, \tag{2.13}$$

which is proportional to the electric field. Finally, Fourier analysis with respect to the azimuthal coordinate allows one to determine the coefficients $c_m(r)$:

$$c_m(r, z) = \frac{1}{4\pi A^*_{\text{ref}}(r, z)} \int_0^{2\pi} d\phi(\widetilde{I}_0 - i\widetilde{I}_{\pi/2})e^{-im\phi}, \tag{2.14}$$

which contains all the information associated with the spatial distribution of the electric field. Notice that this approach can also be seen as taking the scalar product of the electric field with the OAM eigenmodes

The method just described is required for a full modal decomposition and requires taking a total of four images (that is I with $\alpha = 0$ and $\alpha = \pi/2$, plus I_{ref} and I_s), maintaining also a good interferometric stability between them. However, for applications requiring the measurement of the OAM power spectrum only, that is ignoring the radial structure of the field, and for which the OAM spectrum is bound from below (that is, there is a minimum OAM value) there is a simplified procedure that is even easier and more robust (the case for which the spectrum is limited from above can be treated equivalently). In the case of beams containing helical modes with both positive and negative charges ($K_1 < 0$ and $K_2 > 0$ in Eq. 2), this usually requires to have the signal beam pass first through a spiral optical phase element, described by the transfer factor $e^{iM\phi}$ (this can be achieved with a q-plate or a spiral phase plate with the appropriate topological charge). If $M > |K_1|$, the spiral spectrum of the beam after this optical component will contain only modes associated with positive OAM values. If K_1 and K_2 have the same sign, this preliminary procedure can be skipped. Then, one can extract the associated probabilities $P(m)$ by Fourier analysis of $\widetilde{I}_0$ only (see Eq. 2.12), with no need of measuring also $\widetilde{I}_{\pi/2}$, thus reducing the number of required images to three. We discuss this in more detail in the sections below. In Appendix A we estimate the number of detectable modes for fixed detector area and resolution.

2.3.2 Experimental results

We demonstrate the validity of our technique by determining the OAM spectrum and the radial profile of the associated helical modes for a set of structured light fields. The setup is shown in Fig.2.1 and described in detail in the figure caption. Here, structured light containing multiple OAM components is generated by means of q-plates.

In Figs. 2.2(a-c) and 2.2(d-f) we report the results of our first experiment, consisting in the measurement of both amplitude and phase of coefficients $c_m(r)$ of optical fields having one ($m = 8$) and three ($m = \{-8, 0, 8\}$) different helical modes, respectively, accompanied by the associated OAM power spectrum (see Eq. 2.8). We generate such structured light by shining a q-plate with $q = 4$ with a left-circularly (horizontally) polarized Gaussian beam and setting the plate optical retardation δ to the value π ($\pi/2$), respectively. Our data nicely follow the results from our simulations, with some minor deviations that are due to imperfections in the preparation of the structured fields. In particular, in panel (a), the small peaks centered around $m = -8$ are related to the possible ellipticity of the polarization of the Gaussian beam impinging on the q-plate, while a small contribution at $m = 0$ corresponds to the tiny fraction of the input beam that has not been converted by the q-plate. In panels (b) and (e) the radial profiles used for our simulations are those corresponding to the Hypergeometric-Gaussian modes. Error bars shown in our plots are those associated with the variability in selecting the correct center $r = 0$ in the experimental images, which is identified as one of the main source of uncertainties in the spectral results. They are estimated as three times the

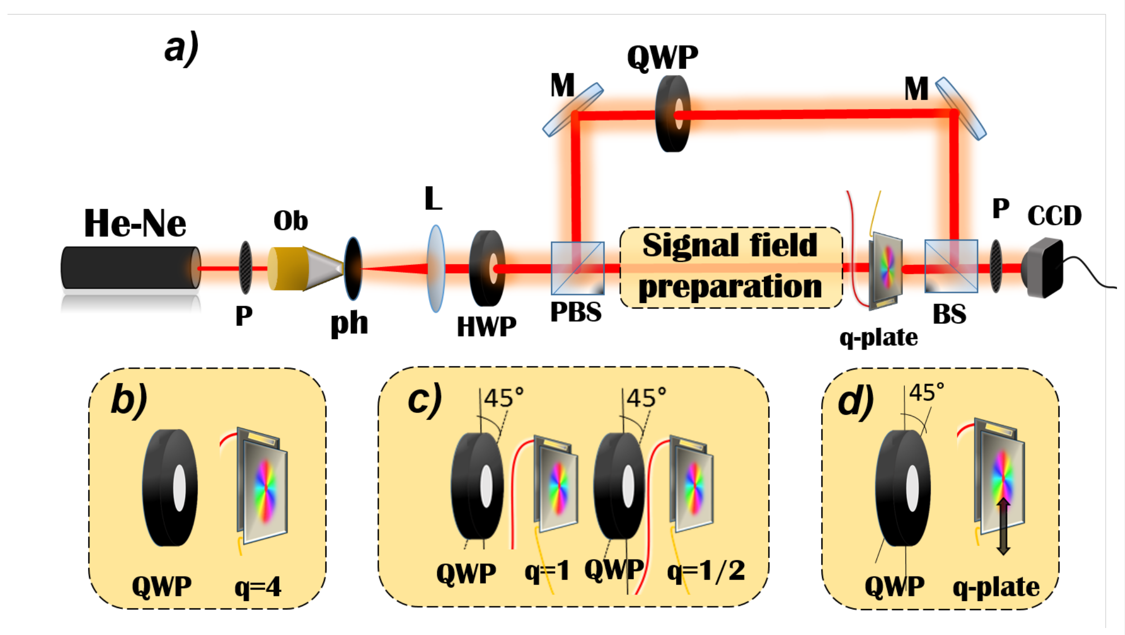

FIGURE 2.1: **Sketch of the experimental apparatus. a)** A He-Ne laser beam passes through a polarizer (P) and is spatially cleaned and collimated by means of an objective (Ob), a pinhole (ph) and a lens (L). A half-wave plate (HWP) and a polarizing beam splitter (PBS) are used in order to split the beam into the signal and reference arms, whose relative intensities can be controlled by HWP rotation. Fields resulting from a complex superposition of multiple helical modes were obtained by using q-plates and quarter-wave plates (QWPs), as shown in panels b-c. After preparing the signal field, we place a further sequence of a QWP and a q-plate in case we need to shift the entire OAM spectrum. The reference field is a $\mathrm{TEM}_{0,0}$ Gaussian mode. In the upper arm of the interferometer, by orienting the QWP at 0 or 90° with respect to the beam polarization we can introduce a $\alpha = 0$ or $\pi/2$ phase delay between the signal and the reference field, respectively. The two beams are superimposed at the exit of a beam splitter (BS) and filtered through a polarizer, so that they share the same polarization state. The emerging intensity pattern is recorded on a CCD camera (with resolution 576×668). **b)** A QWP oriented at 45° or 0, followed by q-plate with $q = 4$ and $\delta = \pi$ or $\delta = \pi/2$, is used for the generation of a light beam containing a single mode ($m = 8$) or three modes ($m = -8, 0, 8$), respectively. **c)** two q-plates with $q = 1$ and $q = 1/2$ are aligned to generate spectra with $m \in [-3, 3]$. **d)** A set of more complex distributions was obtained by displacing laterally the centre of a q-plate ($q = 1$ and $\delta = \pi$) with respect to the axis of the impinging Gaussian beam. Image from Ref. [40]

standard deviation of the data computed after repeating our analysis with the coordinate origin set in one of 25 pixels that surround our optimal choice. Other possible systematic errors, such as for example slight misalignments between the signal and reference fields, are not considered here.

Data reported in Fig. 2.2 prove our ability to measure the complex radial distribution of the field associated with individual helical modes in a superposition. For each of these, we can use our results to obtain a decomposition in terms of a complete set of modes. For a demonstration of this concept, we consider the field obtained when a left-circularly-polarized beam passes through a q-plate with $q = 4$ and $\delta = \pi$. The latter contains only a mode with $m = 8$, as shown in Fig. 2.2(a-c). By evaluating the integrals reported in Eq. 2.10 we determine the coefficients $b_{p,8}$ of a LG decomposition. For our analysis, we use LG beams with an optimal waist parameter $\widetilde{w}_0$ (different from the one of the impinging Gaussian beam), defined so that the probability of the lowest radial index $p = 0$ is maximal [79]. In Fig. 2.3 we plot squared modulus and phase of the coefficients $b_{p,8}$ determined experimentally, matching nicely the results obtained from numerical simulations.

As mentioned above, shifting the OAM spectrum of the signal field may be used to simplify its measurement, when reconstructing the radial profile is not needed. In our case, we let the signal field pass through a q-plate with $q = M/2$ and $\delta = \pi$, after preparing it in a state of left-circular polarization. If M is large enough, i.e. higher than K_1 (see Eq. 2), we have that $c(m) \neq 0$ only if $m > 0$. This allows in turn using Eq. 2.12 to determine the OAM spectrum, instead of Eq. 2.13 that requires the measurement of $I_{\pi/2}$ also. At the same time, this approach is less sensitive to possible noise related to beam imperfections, typically associated with small spatial frequencies, that affect lowest-order helical modes, as reported also in Refs. [53, 76]. Let us note that once the beam passes through an optical element adding the azimuthal phase $e^{iM\phi}$, thanks to the conservation of OAM during free propagation, the associated power OAM spectrum is only shifted by M units, that is $P(m) \to P(m + M)$. The radial distribution of individual helical modes, on the other hand, is altered during propagation, that is $c_m(r, z) \not\to c_{m+M}(r, z)$. For this reason, this alternative procedure proves convenient only when determining the OAM probability distribution but cannot be applied to the reconstruction of the full modal decomposition. In Fig. 2.4, we report the measured power spectrum of different fields containing helical modes with $m \in [-3, 3]$, as determined by shifting the OAM spectrum by $M = 8$ by means of a q-plate with $q = 4$ and $\delta = \pi$.

As a final test, we used our technique for characterizing more complex optical fields, such as those emerging from a q-plate whose central singularity is displaced with respect to the input Gaussian beam axis (Fig.2.1c). In Fig. 2.5 we report the OAM probability distributions obtained when translating a q-plate ($q = 1$, $\delta = \pi$) in a direction that is parallel to the optical table, with steps of $\Delta x = 0.125$ mm. Our data are in excellent agreement with results obtained from numerical simulations. In the same figure we show part of the associated total intensity patterns I_0 (see Eq. 2.11) recorded on the camera. In addition, for each configuration we show in Fig. 2.5 that the first and second order moments of the probability distributions are characterized by Gaussian profiles $\langle m \rangle = 2q \exp(-2x_0^2/w_0^2)$ and $\langle m^2 \rangle = (2q)^2 \exp(-2x_0^2/w_0^2)$ [80]. Fitting our data so that they follow the expected Gaussian distributions (red curves) we obtain $w_0^{\text{fit}} = 1.36 \pm 0.04$

mm from $\langle m \rangle$ (panel g), and $w_0^{\text{fit}} = 1.39 \pm 0.06$ mm from $\langle m^2 \rangle$ (panel h), which are close to the expected value $w_0 = 1.45 \pm 0.18$ mm.

2.4 Conclusions

In this chapter we introduced a new technique for measuring the orbital angular momentum spectrum of a laser beam, accompanied by its complete spatial mode decomposition in terms of an arbitrary set of modes that carry a definite amount of OAM, such as LG beams or others. Based on the azimuthal Fourier analysis of the interference pattern formed by the signal and the reference field, relying on only a few measurements this approach allows one to readily extract the information contained in both the radial and azimuthal degrees of freedom of a structured light beam. Standard interferometric techniques, as reported for instance in Refs. [81, 82], are commonly used for the measurement of the phase profile of optical waves, allowing for the measurement of the complex spatial envelope A_s of the field (see Eq. 1). However, using this information to obtain the decomposition in terms of a complete set of helical modes (using Eqs. 3 and 6), and, in turn, the OAM power spectrum, has not been thoroughly explored before. Furthermore, when interested at the spiral spectrum only, we demonstrated that it is actually possible to retrieve the OAM distribution without measuring the complete field, making use of a reduced number of measurements.

In our approach, the most general method requires taking four images, including the intensity patterns of the signal beam, the reference beam and two interference patterns between them. Information on the modal decomposition of the signal field is then retrieved using a simple dedicated software. Since the spatial mode decomposition is obtained during this post-processing procedure, the same set of images can be used to decompose a beam in different sets of spatial modes. As demonstrated here, the experimental implementation of our approach requires a simple interferometric scheme and minimal equipment. Hence, it may be readily extended to current experiments dealing with the characterization of spatial properties and OAM decomposition of structured light.

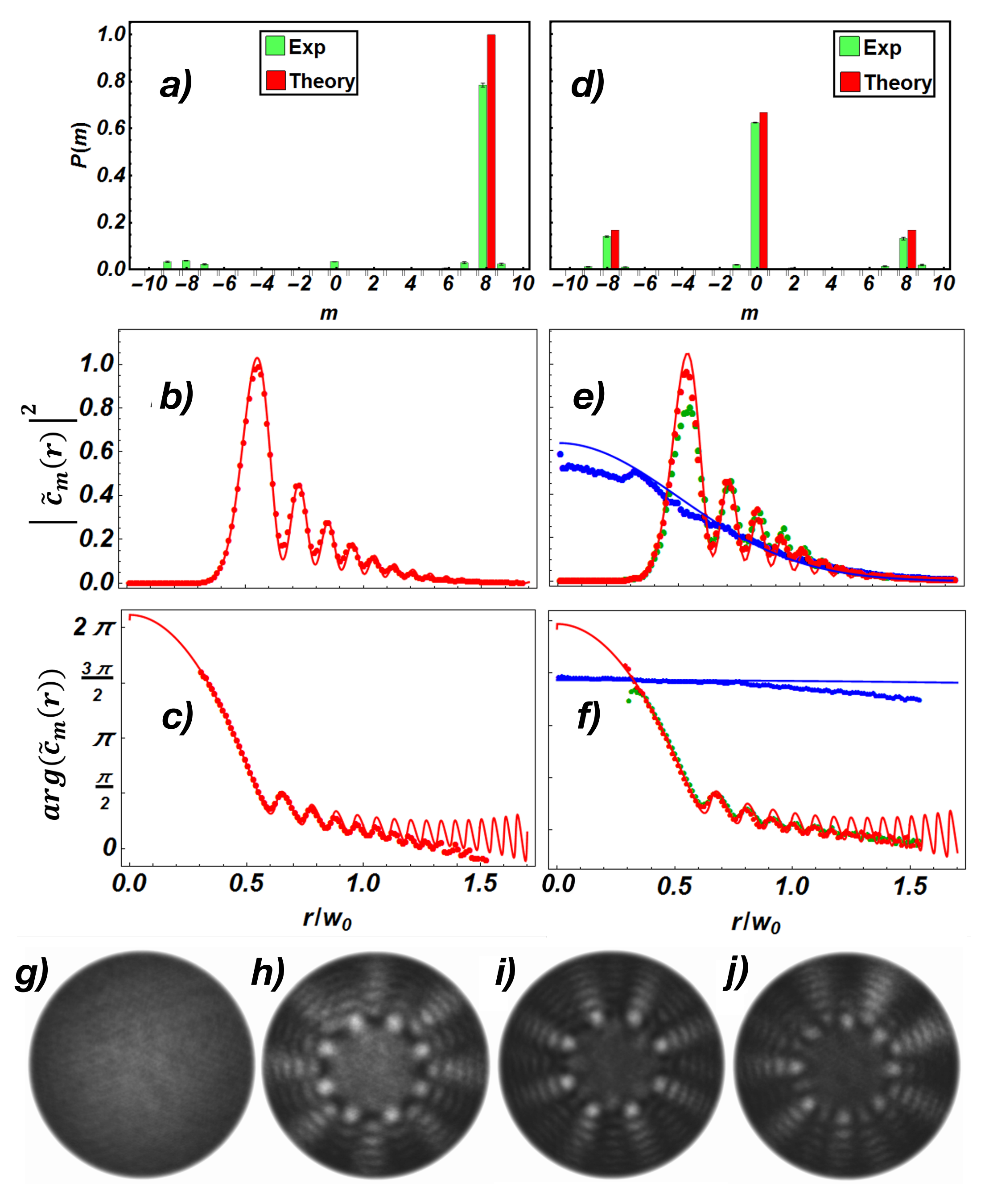

FIGURE 2.2: **Experimental reconstruction of light OAM spectrum**. We report the experimental characterization of optical fields containing one (a-b-c) and three (d-e-f) helical modes, generated using a q-plate with $q = 4$ and $\delta = \pi$ or $\pi/2$, respectively. In panels g-j we report the experimental intensity patterns I_{ref}, I_s, I_0 and $I_{\pi/2}$, respectively, obtained when investigating the field generated by the q-plate with $\delta = \pi/2$. Panels a and d show the OAM distributions in the two cases. Error bars are calculated as three times the standard error. Panels b,c and e,f show the measured amplitude and phase profiles of the non-vanishing helical modes that are present in the beam, where blue, red and green colored points are associated with modes with $m = 0, 8, -8$, respectively. These results are compared with theoretical simulations, represented as continuous curves with the same color scheme adopted for the experimental results. For each value of m, we plot normalized coefficients $\tilde{c}_m = c_m/S_m$, where S_m is the total power associated with the helical mode. As expected from theory, a fraction of the beam is left in the fundamental Gaussian state, while an equal amount of light is converted into helical modes with $m = \pm 8$, both having the radial profile of a HyGG$_{-8,8}$ mode. Simulated profiles of Gaussian and HyGG modes correspond to $w_0 = 1.45$ mm and $z = 30$ cm, the latter being the distance between the q-plate and the camera. Error bars are smaller than experimental points. Image from Ref. [40]

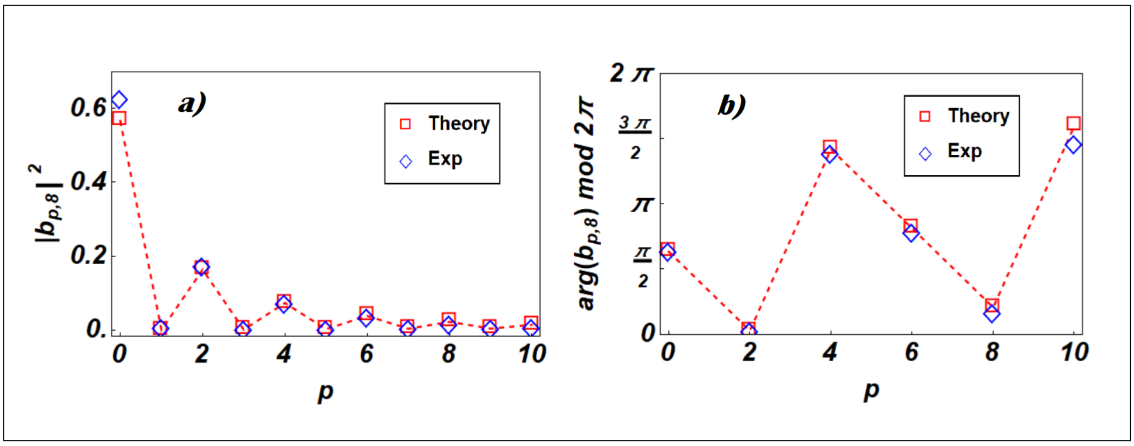

FIGURE 2.3: **Complete spatial mode decomposition in terms of LG beams**. We consider the light beam emerging from a q-plate with ($q = 4$, $\delta = \pi$), described by a HyGG$_{-8,8}$ mode. We evaluate the overlap integral between the radial envelope $c_8(r)$ measured in our experiment at $z = 30$ cm and LG$_{p,8}$ modes at the same value of z and characterized by the optimal beam waist $\widetilde{w}_0 = w_0/9$ [79], where w_0 is the input beam waist. In panels **a)** and **b)** we plot the squared modulus and the phase of the resulting coefficients (blue markers), respectively, showing a good agreement with the values obtained from numerical simulations (red markers). The phases of $b_{p,8}$ with p equal to odd integers are absent in the plot since the corresponding amplitudes are vanishing (smaller than the associated error). Image taken from Ref. [40]

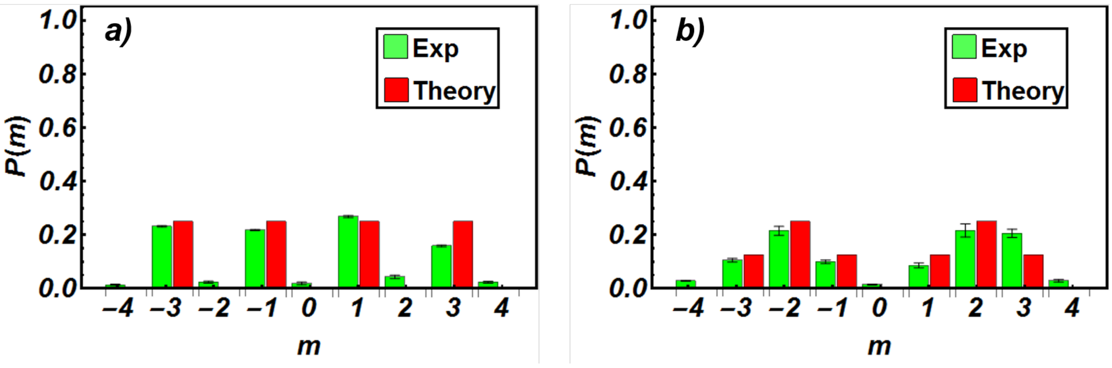

FIGURE 2.4: **Measure of shifted OAM power spectrum**. OAM probability distributions are measured for two different optical fields, obtained when shining a sequence of two q-plates with $q_1 = 1$ and $q_2 = 1/2$. A further q-plate with $q = 4$ shifts the final spectrum by $M = 8$ units. **a)** OAM spectrum for the case $\delta_1 = \pi$ and $\delta_2 = \pi$. **b)** The same data are reported for a different field, obtained when $\delta_1 = \pi$ and $\delta_2 = \pi/2$. Error bars represent the standard error multiplied by three. Image from Ref. [40]

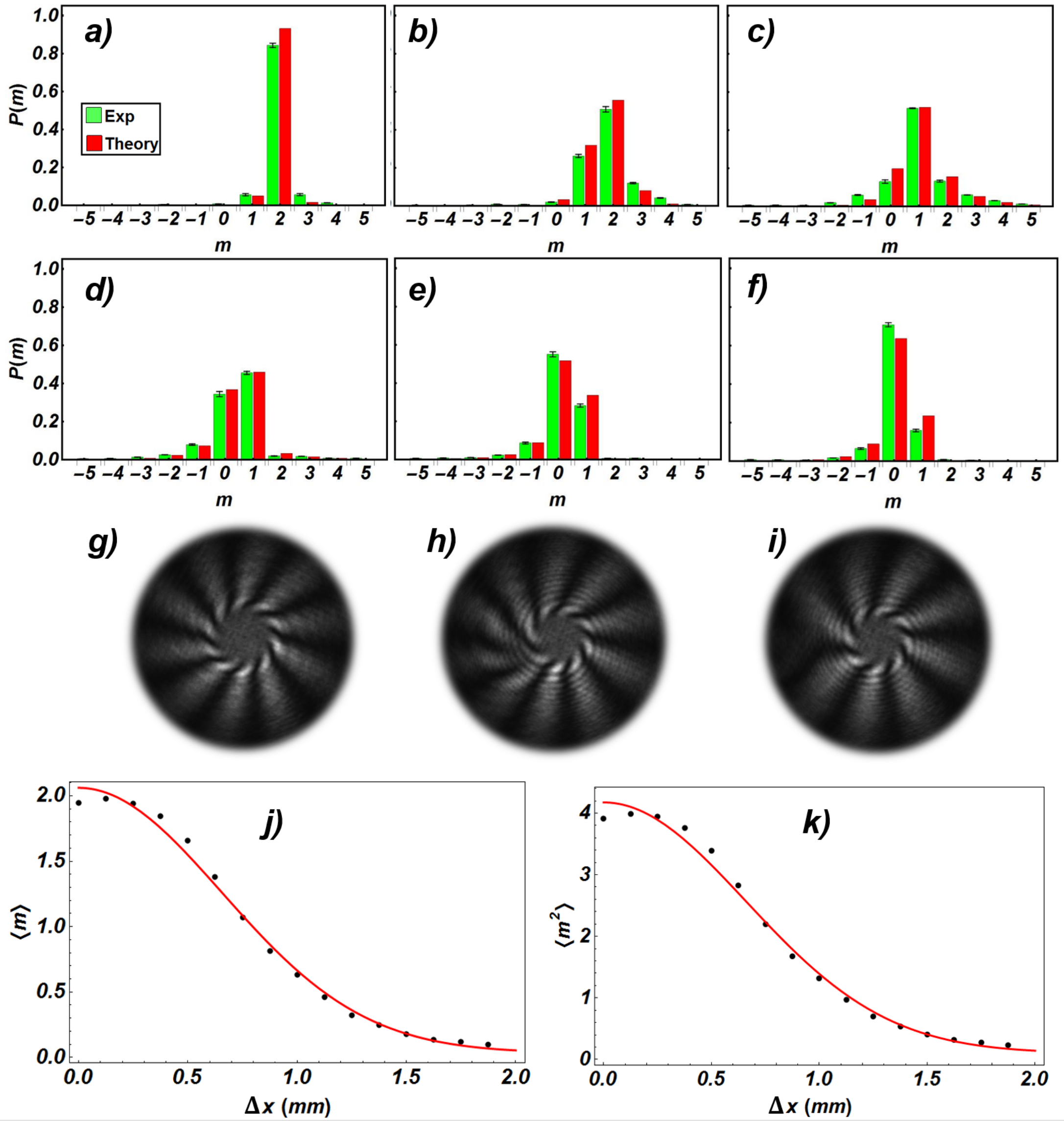

FIGURE 2.5: **OAM spectrum for a shifted q-plate**. We measure the OAM power spectrum at the exit of a q-plate ($q = 1$, $\delta = \pi$) shifted with respect to the axis of the impinging Gaussian beam, which is left-circularly polarized. The overall spectrum is shifted by $M = 8$ units since we are using a further q-plate with $q = 4$ and $\delta = \pi$. However, we plot the original OAM distribution associated with the signal field. **a-f)** Experimental (green) and simulated (red) OAM power spectra when the lateral shift is equal to $a\Delta x$, with $a = 1, 3, 6, 9, 12, 15$ and Δx =0,125 mm, respectively. Error bars represent the standard error multiplied by three. **g-i)** Examples of the experimental intensity pattern I_0 used for determining the power spectra reported in panels a,c,e. The number of azimuthal fringes reveals that the OAM spectrum has been shifted. **j- k)** First and second moment ($\langle m \rangle$ and $\langle m^2 \rangle$) measured as a function of the lateral displacement. Error bars are not visible because smaller than the experimental points. Image from Ref. [40]

Chapter 3

Topology and dynamics of polarization singularities in optical beams

3.1 Introduction

[1] Quantum Walks with structured light are processes that generate complex light fields. As we have mentioned in the introduction of the previous chapter, they give rise to superpositions of multiple helical modes. Moreover these processes are implemented introducing spatially dependent transformations of the polarization state. As a consequence the resulting light beam exhibits a polarization state that changes spatially. The resulting polarization patterns can present interesting features, like polarization singularities, that can be investigated in the future to better understand the topological properties of Quantum Walks. Motivated by these ideas, we started to study the polarization patterns that are produced by a single q-plate, focusing on the behavior of polarization singularities when changing the optical retardation δ. The results, described in Ref. [83], showed interesting phenomena like the splitting of singularities with high topological charge and their peculiar evolution along the propagation direction.

Light beams showing an inhomogeneous polarization distribution, commonly referred to as vector beams (VBs), represent a precious resource in an increasing number of photonic applications [84]: astronomy [85], microscopy [86, 87], optomechanics [88, 89], materials structuring [90], nanophotonics [91, 92] and quantum sciences [16, 93–95] are some remarkable examples. Uniformly polarized beams can be easily converted into such

---

[1] Some paragraphs and sentences of this section are adapted or copied verbatim from the work [83] which I coauthored

spatially structured fields by coupling the vector and the spatial degrees of freedom of light [84, 96], as recently demonstrated in a variety of photonic architectures [97–106]. The fine structure of VBs polarization may show several typologies of singular points [107–111], in close analogy to other inhomogeneous systems (fingerprint, tidal heights across the oceans, etc.).

This chapter is dedicated to the study of polarization singularities. We will first introduce some generalities on how light beams with spatially varying polarization can be generated and controlled using devices, like the q-plates, that realize spin-orbit coupling effects. Then we will review the classification of topological singularities that can be observed in paraxial beams. Point-like singularities, like C-points and V-points can be characterized in terms of an index that is an integer or semi-integer number. These indexes will represent a first simple example of topological invariants, a mathematical concept that will be of fundamental importance in Chapter 5. Polarization singularities can evolve and transform under the constraint of index conservation, i.e. the sum of the indexes of all the singularities present in a given region can change only if some of these singular points flow out of this region. On the other hand there is no constraint on the conservation of the "character" of a singularity, e.g. a V-point can transform and evolve into C-points. Finally, by reviewing the results in Ref. [83], we will give examples of these effects by considering the consequences of perturbing a radially or azimuthally polarized beam with an uniformly polarized one.

3.2 Paraxial beams with spatially varying polarization

We are used to read in standard optics textbooks about uniformly polarized electromagnetic waves. However one can consider also beams with spatially varying polarization where at each position in space the electric field rotates in a different fashion. These kinds of beams are becoming of great interest for their applications in classical and quantum optics.

A paraxial light beam is inhomogeneously polarized when the electric field can be written in the form:

$$\mathbf{E}(x,y,z) = A_L(x,y,z)\mathbf{e}_L + A_R(x,y,z)\mathbf{e}_R. \tag{3.1}$$

This equation can be understood as the superposition of two different spatial modes of light, A_L and A_R, with orthogonal polarizations, $\mathbf{e}_L$ and $\mathbf{e}_R$. At each point in space Eq. 3.1 describes a different point on the Poincaré sphere. Light beams of this kind are known as Vector Beams (VB).

Among the most known and important examples there are the so called Vector Vortex Beams (VVB) obtained by coherently superimposing beams which are orthogonally polarized and carry opposite Orbital Angular Momentum:

$$|VVB\rangle_m = f(r,z)\left(c_L|L\rangle\, e^{-i\,m\,\phi} + c_R|R\rangle\, e^{i\,m\,\phi}\right), \tag{3.2}$$

where $c_{L/R}$ are complex coefficients and $f(r,z)$ takes into account the radial envelope. In particular the VVB often considered in literature are of the form:

$$|l,\alpha\rangle = \frac{|l\rangle \otimes |L\rangle + \mathrm{e}^{i\alpha}|-l\rangle \otimes |R\rangle}{\sqrt{2}}, \tag{3.3}$$

Here we used the Dirac notation to highlight that these states of the electromagnetic field are characterized by a non-separability between the SAM and OAM. In this sense they can be regarded as a realization of entanglement between two degrees of freedom that are distinct because corresponding to different observables and not because belonging to different particles. As a consequence, the term *classical entanglement* [112] was coined (however the debate around this terminology is still open [94, 113]). This idea has become of interest since one can increase the effective number of qubits in a quantum system adding degrees of freedom rather than particles: we cite, for example, the recent realization of a 18 qubit state using 6 photons and 3 degrees of freedom [114].
Eq. 3.3 describes a beam with annular shaped intensity and everywhere linearly polarized with a spatially varying orientation of the polarization ellipse. In particular, the polarization pattern is singular on the beam axis, where the electric field itself is zero. Indeed the name Vector Vortex Beams comes from the nonzero vorticity of the electric field orientation. In the particular case $l = 1$ and $\alpha = 0, \pi/2$ one obtains respectively, a radially or azimuthally polarized beam (showed in Fig. [**?**]). These two kinds of VVBs are of interest in a large variety of applications: from focusing by high numerical apertures [86], microscopy [87] etc... Moreover the set $|l,0\rangle, |l,\pi/2\rangle$, with l fixed, constitutes a basis of a 2-dimensional Hilbert space, i.e. VVBs can be used as qubit states for quantum computation and communication. In particular they have been suggested for performing alignment free quantum communications [16], and have been recently exploited for intra-city high dimensional Quantum Cryptography [115].

Another interesting class of VBs is given by the so called *Full Poincaré Beams* (FP beams), introduced in Ref. [100]. They are optical beams that cover the entire Poincarè sphere, i.e. they realize a stereographic projection in real space of the sphere. One example is given by the superposition of a Gaussian and an $\mathrm{LG}_{0\,1}$ mode, where each mode has a polarization orthogonal to the other:

$$\mathbf{E}_{FP}(\mathbf{r},\theta) = \cos(\theta)\mathrm{LG}_{0\,0}(\mathbf{r})\mathbf{e}_1 + \sin(\theta)\mathrm{LG}_{0\,1}(\mathbf{r})\mathbf{e}_2. \tag{3.4}$$

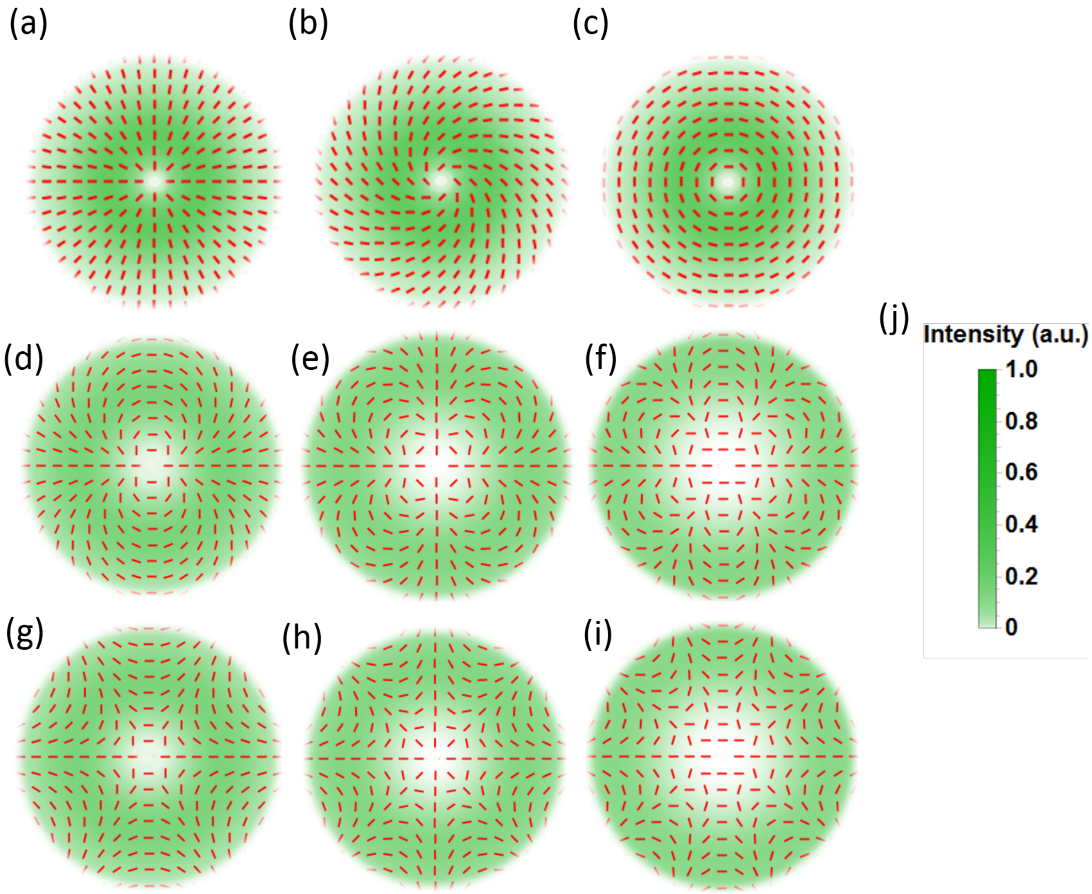

FIGURE 3.1: **Polarization patterns of VVBs** Some polarization patterns of Vector Vortex Beams are shown for different values of l. Panels **a-c** correspond to $l = 1$ and $\alpha = 0, \pi/2, \pi$ for,respectively, radial, (a), spiral, (b), and azimuthal, (c), polarization patterns. In panels (d-f) the polarization patterns for $l = 2, 3, 4$ ($\alpha = 0$) are displayed showing the characteristic flower-like shape. Web-like patterns can be obtained for $l < 1$. Panels (g-i) show examples for $l = -2, -3, -4$. In all the figures the background color corresponds to the local intensity, assuming a LG radial mode, whose colour scale is shown in panel (j).

where $\mathbf{e}_{1,2}$ are orthogonal vectors. Using the explicit expressions of $\mathrm{LG}_{0\,m}$ modes, this equation can be rewritten as:

$$\mathbf{E}_{FP}(\mathbf{r}, \theta) \propto \big(\mathbf{e}_1 + e^{i(\phi - \arctan(z/z_0))}\sqrt{2}\frac{r}{w(z)}\tan(\theta)\mathbf{e}_2\big)\cos(\theta)e^{-r^2/w^2}. \tag{3.5}$$

From this expression one can easily see that in the transverse plane there is any possible polarization state. The factor $\sqrt{2}\frac{r}{w(z)}\tan(\theta)$ determines at every point in space the ratio between the polarizations $\mathbf{e}_1$ and $\mathbf{e}_2$. In particular the polarization state is switched from $\mathbf{e}_1$ to $\mathbf{e}_2$ when going from the origin, $r = 0$, to infinity. At fixed radius the azimuthal phase term realizes all the possible relative phases between the two polarizations.

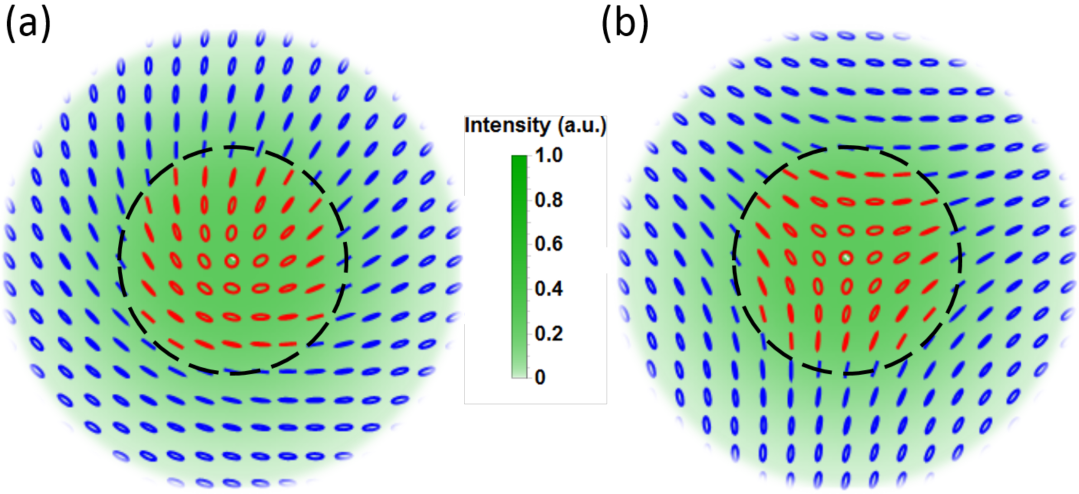

FIGURE 3.2: **Polarization patterns of FP beams.** In(a) a FP beam obtained superposing orthogonally polarized $\mathrm{LG}_{0,0}$ and $\mathrm{LG}_{0,1}$ modes is shown. The colors of the polarization ellipses correspond to their handedness (red for left-handed ellipses and blue for right-handed). In (b) we show the pattern that results from replacing the $\mathrm{LG}_{0,1}$ mode with a $\mathrm{LG}_{0,-1}$. In both cases one obtains a stereographic projection of the Poincarè sphere (right circular polarization is actually located at infinity). The dashed black circle indicates the presence of an L-line, i.e. a line where the polarization is everywhere linear. As we will see in the next section, the difference between panels (a) and (b) is in the topological charge associated to the point of circular polarization, called C-point.

Both the space variant polarization patterns described above can be obtained using q-plates, playing with the input polarization and the optical retardation [17, 101]. Indeed the action of a q-plate with $\delta = \pi$ on an input linearly polarized beam is:

$$|L\rangle + e^{i\gamma}|R\rangle \overset{q-\text{plate}\,\delta=\pi}{\longrightarrow} e^{i2(\alpha_0+q\phi)}|L\rangle + e^{-i2(\alpha_0+q\phi)+i\gamma}|R\rangle. \tag{3.6}$$

For $q = 1/2$, the resulting polarization pattern is radial, azimuthal or spiral-like, depending on the value of $2\alpha_0 - \gamma$. For higher values of the topological charge q one obtains the flower-like patterns shown in Fig. 3.1. Similarly one can obtain web-like patterns using q-plates with negative q.

Poincarè beams can instead be realized by sending a circularly polarized light into a q-plate with $\delta < \pi$. For example, an input L polarized beam with Gaussian amplitude becomes:

$$\cos\left(\frac{\delta}{2}\right)\mathrm{HyGG}_{0,0}(r,z)|L\rangle + i\sin\left(\frac{\delta}{2}\right)e^{i2(\alpha_0+q\phi)}\mathrm{HyGG}_{-|2q|,|2q|}(r,z)|R\rangle. \tag{3.7}$$

where in the expression of the HyGG mode we considered only the dependence on the r and z coordinates and made explicit the dependence on the azimuthal angle. The fact that this is indeed a Full Poincarè beam can be understood by comparing the radial shapes of the $\mathrm{HyGG}_{0,0}$ (Gaussian mode) and the $\mathrm{HyGG}_{-|2q|,|2q|}$ mode. Indeed, the

HyGG$_{-|2q|,|2q|}$ mode diverges more rapidly than the Gaussian one. Hence at any plane $z > 0$ the $|R\rangle$ polarization becomes dominant for $r \to \infty$. This is strictly true in the far field. In the near field the ripples in the radial structure of HyGG modes give rise to multiple concentric L-lines, i.e. lines in the transverse plane where light is linearly polarized, hence there is not a one to one mapping from the Poincarè sphere to the transverse plane. However one can get rid of this by filtering out all the LG modes with $p > 0$, as was done in Ref. [104] where vector beams where generated directly from a laser cavity.

3.3 Polarization singularities in paraxial beams

Singularities are points or, more generally, sets of points, where some property of a field is ill defined. We have already met some examples of point singularities in complex scalar fields (like in the amplitude of a scalar beam carrying OAM) and line fields (like in the liquid crystals orientations in q-plates or in the polarization patterns showed in the previous section). Here we briefly review the definition and characterization of these kind of singularities focusing on fields defined in two dimensions. First let us consider a complex scalar field $f(\mathbf{r})$, with $\mathbf{r} = (x, y)$, that can be written as:

$$f(\mathbf{r}) = \rho(\mathbf{r}) \exp(i\psi(\mathbf{r})) = \xi(\mathbf{r}) + i\eta(\mathbf{r}).$$

One will have a *phase singularity* at the zeros of f, i.e. the points for which $f(\mathbf{r}) = 0$. Indeed at these points the value of the phase is undefined. As an example, we have seen that an optical beam whose local amplitude is approximated by: $A(x, y) = (x + iy)^m = r \exp(im\phi)$, has a phase singularity at the origin, where the amplitude is zero. The integer m determines the "strength" of the singularity. It can be associated to the number of times the phase of the field goes from 0 to 2π in a path around the singularity. More precisely, one can define the integral:

$$s = \frac{1}{2\pi} \oint_C d\psi = \frac{1}{2\pi} \oint_C \nabla\psi(\mathbf{r}) \cdot d\mathbf{r}, \tag{3.8}$$

where C is any smooth closed path oriented in the counterclockwise direction over which the field f is well defined and different from zero. Since the phase is defined modulo 2π, this integral is an integer number and cannot be changed by smooth deformations. Hence the value of s, when C encloses the singularity, can be ascribed to the singularity itself. One refers to s as the *topological charge*, or *winding number*, of the singularity.

Similar ideas can be introduced for vector fields in two dimensions. A vector field $\mathbf{V}(\mathbf{r}) = \big(V_x(\mathbf{r}), V_y(\mathbf{r})\big)$ has an undefined direction when both its components vanish: $\mathbf{V}(\mathbf{r}) = 0$. Still, one can define for this singularity a topological charge, known as *Poincarè Index*.

This is done defining the modulus V and direction θ of the vector field. As in Eq. 3.8 one defines:

$$I_P = \frac{1}{2\pi}\oint_C d\theta.$$

In this chapter we will be more interested in line fields, or fields of ”headless vectors”. Here the direction θ is defined only modulo π (rather than 2π). As a consequence the Poincarè index can also be a semi-integer. We have already seen an example of semi-integer topological charges in q-plates. Indeed the liquid crystal pattern can be regarded as a line field specifying the local orientation of the molecular director. The charge q is the Poincarè index of this line field.

When dealing with singularities in polarization patterns we must consider ellipse fields. An ellipse can be defined by two parameters: the eccentricity ϵ and the orientation θ. Like in line and vector fields, we can look for points where the orientation θ is ill defined. These are points where the ellipse becomes a circle. Hence, in polarization patterns, points of circular polarization, like the ones appearing in Poincarè beams, are singular points, called *C-points*. In a polarization pattern one should append to any ellipse some additional property: the handedness and the intensity of the electric field. In this case the orientation is ill defined not only where the polarization is circular, but also at points of zero intensity. Indeed this is the case that we observe in Vector Vortex Beams where the polarization has a vortex-like structure around the beam axis. In this case the singularity in the polarization pattern is called V-point. The sign of the topological charge of a V-point determines the polarization pattern surrounding it. For positive charges the polarization realizes a *flower-like* pattern, while for negative charges one has *web-like* patterns (see Fig. 3.1). The V-point is actually a singularity in the electric field and can have only integer topological charges. One can have also line singularities which are lines where the polarization is linear at each point. These so called *L-lines* appear for example in Poincarè Beams as shown in the previous section.

While the winding number of a V-point can be only an integer, the C-points can carry also semi-integer topological charges. Indeed the simplest C-points are the ones with $I_P = \pm 1/2$. These C-points can be further distinguished by the patterns of the ellipses orientations surrounding them. In particular one looks at the number of radial lines, i.e. lines starting from the singularity where the orientation θ of the polarization ellipse is radial ($\theta = \phi$, where ϕ is the azimuthal angle). Thus there are three kinds of C-points [116] called: lemon, star and monstar. The lemon has a topological charge $+1/2$ and only one radial line, an example is shown in Fig. 3.2a. The star has topological charge $-1/2$ and three radial lines (like in Fig. 3.2b). The monstar, however, has positive topological charge $I_P = +1/2$ and three radial lines. Lemon and star patterns can be realized using q-plates [17], while, for realizing monstars with space variant birefringent optics, it has been recently showed that one needs an elliptically-symmetric q-plate [117].

Topological singularities can split, merge and modify their nature. There are some general principles that allow to understand their dynamics. These principles are discussed in Ref. [118]. The first is the *conservation of total topological charge*: due to the continuity of the wave field, during free propagation the total topological charge in the field cannot change. As a consequence, point singularities can only appear and disappear as twins with opposite charge. This result is known as the *twin principle*. This principle does not necessarily holds in the presence of boundaries where the wave field changes abruptly. Thus discontinuities induced in the wave field can change its topology. The twin principle does not completely determines the features of singularities in a wave field for the signs of the two twin singularities cannot be determined from it. Another principle, the proof of which can be found in Ref. [118], allows to solve this ambiguity. The *sign principle*, indeed states that: adjacent vortices on any given zero crossing must have opposite sign. Zero crossing are defined as lines where the real, or the imaginary part, of a scalar complex field is zero. Indeed vortexes always lie on the intersections of zero crossings. We cite some corollaries of the sign principle: the sign of any single vortex fixes the sign of all the remaining vortexes in the wave field. As a consequence, flipping this sign changes the signs of all the other vortexes. Moreover, the sign of the first vortex generated during the evolution of a wave field fixes the sign of all future generations of vortexes.

We have stated the sign principle in terms of scalar fields. However it also holds for singularities in polarization patterns. Indeed, both V-points and C-points can be regarded as singularities of the scalar field:

$$\sigma_{12} = S_1 + iS_2. \tag{3.9}$$

Where S_1 and S_2 are the first and second reduced Stokes parameters. Indeed the argument of this field is proportional to the orientation of the polarization ellipse. It is also evident that the zeros of this field correspond to $S_3 = \pm 1$, in the case of C-points, or $S_3 = 0$ where the field intensity itself is zero, which is the case of a V-point singularity.

3.4 Topological features of vector vortex beams perturbed with uniformly polarized light

[2] In this section we will report the results of Ref. [83], where we investigated the properties of polarization singularities by exploiting the tunability of q-plates.

---

[2] Some paragraphs and sentences of this section are adapted or copied verbatim from the work [83] which I coauthored

We consider those spatial regions where there is no preferred direction for the oscillations of the electric field [107, 108, 111], with the most relevant case being represented by the so called C-points, that is points where the polarization is circular. Their formation and dynamical evolution has been investigated in the complex polarization pattern characterizing several structured fields, such as for instance speckle fields [119], random superposition of vector waves [108], light passing through inhomogeneous anisotropic media [17, 100], photonic crystals [120, 121]. Independently of the specific system, the electric field around a polarization singularity is oriented according to the value of the associated topological charge η. Besides its connection with the surrounding polarization distribution [122], the value of this charge is particularly important in determining the singularity robustness, since only the lowest order C-points with $\eta = \pm 1/2$ are stable with respect to small deformations of the optical system [107, 116, 121, 123, 124]. This is analogous to the case of high-order optical vortexes in scalar field, which have been observed to split into elementary vortexes as soon as a tiny perturbation is introduced [125–130]. The instability of higher-order polarization singularities, with the role of C-points played by points of unpolarized light, can be beautifully observed in the skylight polarization pattern; here the original two singular points ($\eta = 1$), positioned at the Sun and the anti-Sun, split into four ($\eta = 1/2$) because of the contribution from multiple Rayleigh scattering of sunlight in the atmosphere [131].

Inspired by these phenomena, here we investigate the formation of lowest order C-points at the center of vector vortex beams (VVBs) [132, 133] characterized by a polarization singularity typically referred to as V-point [124]; differently from the case of a C-point, here the instantaneous oscillation direction of the electric field is undefined (at any time). The lowest topological charge admitted for V-points is ± 1, since these are singularities of a field of vectors (the instantaneous electric field), while C-points refer to a field of ellipses (the trajectory described by the vector in a temporal cycle). Here we show that a small perturbation changes the nature of the vector field characterizing pure VVBs, whose local polarization states acquire a tiny ellipticity. As in such a field Maxwell's equations allows for polarization singularities with a lower charge (C-points), even the lowest order V-point becomes unstable and unfolds into a pair of equally charged C-points [124]. We investigate experimentally this mechanism by perturbing a radial and azimuthal VVB ($\eta = 1$) with a uniformly polarized beam, and complete the analysis with an example of higher order VVB ($\eta = 2$). This kind of perturbation acts as a coherent background, whose role has been investigated in the decay of optical vortexes at the center of beams carrying OAM [129]. Recently a similar study of V-point unfolding was proposed theoretically in Ref. [134], although the analysis is focused on V-point and C-point dynamics during the beam propagation, rather than the instability of V-points. By controlling the amplitude of the two fields, we report the progressive formation of C-points (that originate from the central V-point), whose separation increases as the

Gaussian term gets higher. Importantly, the polarization pattern modification is always accompanied by a deformation of the original intensity pattern. Interesting features arise when increasing the intensity of the perturbing term, in particular when this becomes equal or higher than the original VVB and the polarization pattern may lose its non-trivial topological features (at least in the region where almost all the field energy is enclosed).

V-point instability at the center of a vector vortex beam

In the case of an ideal VVB, a V-point with charge $\eta = m$ is present at the center of the beam, at any plane transverse to the propagation direction. In order to show a possible mechanism that leads to the V-point decay, let us consider the specific case $m = 1$ and $c_L = c_R = 1$, corresponding to a radially polarized beam. At a fixed transverse plane and very close to the beam center, that is at r much smaller than the typical beam dimensions, Eq. 3.2 has a simpler expression:

$$|VVB\rangle_1^{rad} \simeq A\, r \left(|L\rangle\; e^{-i\,\phi} + |R\rangle\, e^{i\,\phi} \right), \tag{3.10}$$

where A is a real constant defining the field intensity. We add to Eq. 3.10 a linearly polarized term with uniform amplitude $\epsilon\, e^{i\,\alpha_\epsilon}$ (ϵ and α_ϵ are real constants), whose electric field is oriented at an angle θ with respect to the horizontal direction. In the representation of circular polarizations, this perturbation can be written as $|\epsilon, \theta\rangle = \epsilon/\sqrt{2}\, e^{i\,\alpha_\epsilon} \left(e^{-i\,\theta}\, |L\rangle + e^{i\,\theta}\, |R\rangle\right)$; when added to the original VVB, Eq. 3.10 becomes

$$\begin{aligned} |VVB\rangle_1^{rad} \to\, & |VVB\rangle_1^{rad} + |\epsilon, \theta\rangle \simeq \\ & \simeq (A\, r\, e^{-i\,\phi} + \epsilon\, e^{i\,(\alpha_\epsilon - \theta)})|L\rangle + \\ & + (A\, r\, e^{i\,\phi} + \epsilon\, e^{i\,(\alpha_\epsilon + \theta)})|R\rangle. \end{aligned} \tag{3.11}$$

Left and right C-points are located at positions (r_L, ϕ_L) and (r_R, ϕ_R) where the right and left circular components of the field are vanishing, respectively. It is straightforward to see that

$$r_L = r_R = \epsilon/A; \quad \phi_R = \theta - \alpha_\epsilon - \pi; \quad \phi_L = \theta + \alpha_\epsilon + \pi. \tag{3.12}$$

In general $\phi_L \neq \phi_R$ and two C-points with opposite handedness but with equal charge $\eta = 1/2$ generate from the original V-point. Using the same approach it is possible to show that V-points of order m unfold into $2m$ C-points, with the sign of their charge being equal to that of the original singularity.

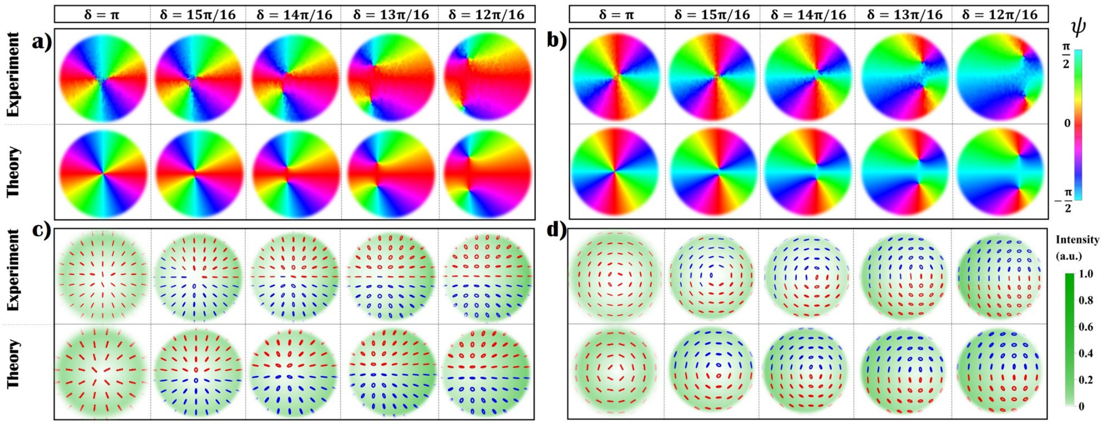

FIGURE 3.3: **Instability of polarization singularities at the center of a VVB.** The instability of a V-point with topological charge $\eta = 1$ is investigated experimentally by changing the q-plate retardation with respect to the optimal condition $\delta = \pi$. In panels a-b we plot the quantity $\psi = \frac{1}{2} Arg(S_1 + i\,S_2)$, that represents the orientation of polarization ellipses, for a radial (panel a) and an azimuthal (panel b) VVB. Colors associated with different values of ψ are shown in the figure legend. As visible in the figure labels, plots are obtained when varying δ in the range $\{12\pi/16, \pi\}$ with steps of $\pi/16$. Importantly, C-points and V-points appear here as vortexes of the scalar field $S_1 + i\,S_2$; as we decrease δ, two C-points clearly appears in place of the V-point. As discussed in the main text, we are considering only a small area (of the order of $w^2/4$, where w is the beam width) at the center of the beam, where the singularity transformation is taking place. In c-d, we show the corresponding experimental and theoretical polarization patterns associated with these fields. Here, red and blue colored ellipses are associated with left ($S_3 > 1$) and right handed ($S_3 < 1$) polarization states, respectively. Image from Ref. [83]

Generation and perturbation of a VVB in electrically tunable q-plates

These results can be easily simulated experimentally by exploiting the same approach reported in [101] for the generation of pure VVBs. The preparation and the controlled alteration of a VVB is obtained by exploiting tunable q-plates [33, 135]. When passing through a q-plate placed at the beam waist, a TEM$_{00}$ Gaussian beam with uniform left or right circular polarization is transformed as follows [136]:

$$\begin{aligned}\hat{Q}_\delta\,\mathrm{TEM}_{0,0}\,|L\rangle &= \cos\left(\frac{\delta}{2}\right)\mathrm{TEM}_{0,0}\,|L\rangle + \\ &\quad i\sin\left(\frac{\delta}{2}\right)\mathrm{HyGG}_{-|2q|,2q}\,e^{i\,2(q\,\phi+\alpha_0)}\,|R\rangle, \\ \hat{Q}_\delta\,\mathrm{TEM}_{0,0}\,|R\rangle &= \cos\left(\frac{\delta}{2}\right)\mathrm{TEM}_{0,0}\,|R\rangle + \\ &\quad i\sin\left(\frac{\delta}{2}\right)\mathrm{HyGG}_{-|2q|,-2q}\,e^{-i\,2(q\,\phi+\alpha_0)}\,|L\rangle, \end{aligned} \tag{3.13}$$

where α_0 is the angle of the liquid crystals optic axis at $\phi = 0$. The previous equation shows that left and right circular polarizations are partially converted into helical modes of order $\pm 2q$, respectively, with the amount of converted light depending on the value of δ ($\delta = \pi$ corresponds to a full conversion). Helical modes generated by a q-plate are described by the so-called HyperGeometric-Gaussian modes (HyGG$_{p,m}$) [**?**], corresponding to a specific class of light beams carrying OAM [137], analogously to Laguerre-Gauss or Bessel beams. Two indices (p, m) specify the mode properties, where m is associated with the OAM content while p determines the radial distribution of the field. Eq. 3.13 clearly shows that, if $\delta = \pi$, a linearly polarized Gaussian beam is fully converted into a VVB, showing a V-point with charge $\eta = 2q$ at its center. In particular, azimuthally and radially polarized beams are obtained when the input polarization is vertical (V) and horizontal (H), respectively, the plate charge is $q = 1/2$ and $\alpha_0 = 0$ (see Fig. 3.3) :

$$\begin{aligned}\hat{Q}_\pi \,\mathrm{TEM}_{0,0}\,|H\rangle &= i\,|VVB\rangle_1^{rad},\\ \hat{Q}_\pi \,\mathrm{TEM}_{0,0}\,|V\rangle &= i\,|VVB\rangle_1^{az}.\end{aligned} \tag{3.14}$$

where kets $|H\rangle$ and $|V\rangle$ represent H and V polarizations states. When changing the value of the retardation to $\delta = \pi + \varepsilon$, with $\varepsilon \ll \pi$, a fraction ε of the input beam is added to the pure VVB:

$$\begin{aligned}\hat{Q}_{\pi+\varepsilon}\,\mathrm{TEM}_{0,0}\,|H\rangle = i\,\sin\left[(\pi+\varepsilon)/2\right]|VVB\rangle_1^{rad} &+\\ +\cos\left[(\pi+\varepsilon)/2\right]\mathrm{TEM}_{0,0}\,|H\rangle &\simeq\\ \simeq i\left(|VVB\rangle_1^{rad} + i\,\varepsilon\,\mathrm{TEM}_{0,0}\,|H\rangle\right)&.\end{aligned} \tag{3.15}$$

A similar expression holds for an azimuthal VVB. In close analogy to Eq. 3.11, the latter equations show that a small variation of δ can be treated as a perturbation to the original VVB. In Fig. 3.3 we show a simulation of the polarization distribution of perturbed radial and azimuthal VBs (Eq. 3.15). In particular in the upper part of panels **a-b** we plot a 2D map of the orientation angle ψ of the local polarization ellipse, calculated in terms of the reduced Stokes parameters; here the two C-points are clearly visible as vortexes of this scalar field (the ellipse orientation), with their separation changing with the value of δ.

Experimental results

To confirm the theoretical predictions discussed in the previous section, we implemented the setup shown in Fig. 3.4. The output of a Ti:Sa laser (λ=800 nm) is coupled into a single-mode fiber (SMF), used as a spatial filter in order to produce a pure TEM$_{00}$ Gaussian mode at the input of the setup. At the exit of the SMF, the beam (uniform) polarization is prepared into vertical or horizontal states by means of a linear polarizer

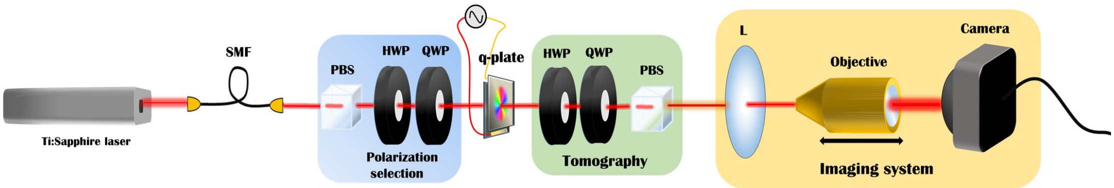

FIGURE 3.4: **Experimental apparatus**. A TEM_{00} beam is obtained by filtering the output of a Ti:Sapphire laser through a single mode fiber (SMF). The initial polarization state is selected by using a polarizing beam splitter (PBS), a half-wave plate (HWP) and a quarter-wave plate (QWP). Then the beam passes through an electrically tunable q-plate, whose optical retardation is controlled by applying an adjustable electric field. When exiting the q-plate the beam has acquired an inhomogeneous polarization pattern that can be experimentally reconstructed by employing a point by point Stokes polarimetry, as discussed in the main text. The projection over the six polarization states H, V, A, D, L, R is implemented through a QWP and a HWP followed by a PBS. The intensity of the analyzed field component is recorded on a CMOS camera. A lens (focal length $f = 10$ cm) and a 20X microscope objective placed on a translation stage are used to study the polarization pattern at different distances z from the q-plate. Image from Ref. [83]

followed by a half-wave plate (HWP). A q-plate (q=1/2) with optical retardation δ, whose value is controlled through a tunable electric field applied to the outer faces of the cell, transforms the beam into the VB reported in Eq. 3.15. In order to reconstruct the 2D polarization pattern in a transverse plane we implemented a point-by-point polarization analysis, similar to that reported in Ref. [101]. For each beam configuration, on a CMOS camera (1280x1024 pixels) we recorded the intensity profile of the field components associated with $\{H, V\}$, $\{L, R\}$ and diagonal and anti-diagonal ($\{D, A\}$) polarization states. These components are selected by rotating suitably a set of waveplates, followed by a linear polarizer. By using a dedicated software, Stokes parameters are calculated point-by-point according to the definitions $S_0 = I_H + I_V$, $S_1 = I_H - I_V$, $S_2 = I_D - I_A$, $S_3 = I_R - I_L$; here I_j represent the measured intensities of the six polarization components, with $j \in \{H, V, D, A, L, R\}$. To take into account small fluctuations of the beam position with respect to the camera the field intensities are averaged over arrays of 3x3 pixels. An imaging system made of a lens (focal length = 10 cm) followed by a microscope objective is used to determine the polarization pattern at different positions along the propagation axis z.

By introducing a tiny alteration of the q-plate voltage with respect to the optimal condition $\delta = \pi$, we investigated the instability of a V-point singularity that transforms into a pair of C-points. When $\delta = \pi$, the polarization is linear in every point of the transverse plane and has a radial or azimuthal pattern, depending on the input polarization. If we introduce a small detuning, that is $\delta \to \pi - \epsilon$, a uniform polarized Gaussian beam is added coherently to the original VVB. As previously discussed, 2η C-points are expected to form in place of the original singularity with topological charge η. In Fig. 3.3

we show the experimental results that confirm these predictions. In order to unveil the formation of C-points pairs, that occurs very close to the beam center, we used a single lens to image this small portion of the beam on the camera sensor. We imaged on the camera the beam at $z = 0.22\, z_R$ and considered only the region $r < 0.58\, w_0$, where z_R and w_0 are the Rayleigh range and the beam waist, respectively. The measured Stokes parameters are used to determine the polarization pattern and, as a consequence, the orientation angle ψ of the local polarization ellipses, calculated as $\psi = \frac{1}{2} \arg (S_1 + i\, S_2)$. In good agreement with the theoretical predictions (see Fig. 3.3c-d), we observe the original V-point splitting into two C-points with opposite handedness, whose spatial separation grows as ϵ is increased, in agreement with Eq. 3.12. The topological charge of such C-points is 1/2, hence the total charge is conserved.
The same phenomenon can be observed for V-points with higher topological charge, obtained using q-plates with $|q| > 1/2$. In Fig. 3.5 we plot the polarization pattern and the orientation angle of ψ measured for a q-plate with $q = 1$ and $\alpha_0 = 3\pi/4$. Here a V-point with charge $\eta = 2$ is observed to split into four C-points. For each circular component, the central vortex has a charge ± 2; being unstable, it decays into two equally charged vortexes [127, 129], and this process is much faster (with respect to a variation of δ) with respect to the V-point decay discussed previously (see Fig. 3.3). Two C-point pairs move away from the beam center as δ decreases, although in each of them the distance between the two singularities is small and the system resolution does not allow for a clear detection.

By changing the voltage applied to the q-plate we can tune the device retardation to any value in the range $(0, 2\pi)$, thus we can explore what happens when the Gaussian term becomes comparable with the VVB amplitude. In Fig. 3.6 we show the polarization and intensity patterns measured in the near field of the beam (compared with theoretical predictions), obtained when varying δ between 0 and π with steps of $\pi/8$. Theoretical simulations are added here for comparison. At a glance, decreasing δ C-points are observed to move away from the beam center and seem to disappear when $\delta < \pi/2$. Accordingly, the topological features of the polarization pattern change abruptly when the amplitude of the Gaussian term becomes higher than the original VVB. This is not surprising, as we are exploring an intermediate regime between the extreme cases $\delta = 0$ (a Gaussian beam with no polarization singularities) and $\delta = \pi$ (VVB beam with a $\eta = 1$ V-point), which have different topological features. In general, we expect that a well defined threshold at $\delta = \delta^*$ should separate these two regimes; when $\delta < \delta^*$, the beam topological features should be those of the uniformly polarized Gaussian beam, while when $\delta > \delta^*$ they should be similar to the radial or azimuthal patterns, with pairs of C-points in place of the original V-point. However, as the VVB and the perturbing term diffract differently, these features (and the value of δ^*) are expected to change when the beam propagates, making the situation much more complex. We investigate

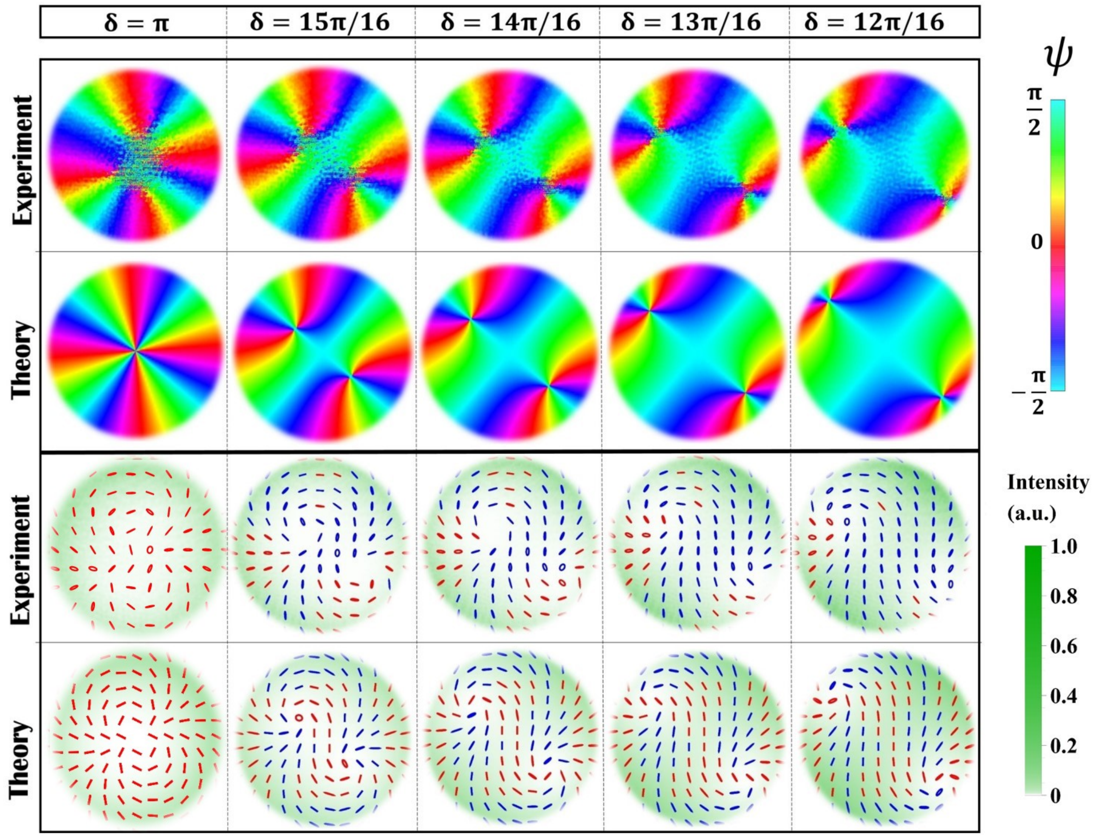

FIGURE 3.5: Instability of a higher-order V-point in VVB with $\eta = 2$ generated by a q-plate with $q = 1$ and $\alpha_0 = 2.121$, acting on a $\text{TEM}_{0,0}$ vertically polarized beam. a-b) We plot the orientation angle ψ of the measured polarization ellipses, and the corresponding theoretical predictions, when varying δ between $\delta = \pi$ and $\delta = 3\pi/4$ with steps of $\pi/16$. Simulations show that the original V-point splits into two pairs of C-point; similarly to the previous case, in each pair the two singularities have opposite handedness. In the experimental data, the formation of these two pairs can be observed clearly: as discussed in the main text, this is associated with the decay of the high-order phase vortex in each of the two circular components. Nevertheless, for each pair the system solution does not allow to distinguish two different C-points, at least for small deviations from the ideal case. In c-d, we show the correpsonding experimental and theoretical polarization patterns associated with these fields. Here, red and blue colored ellipses are associated with left ($S_3 > 1$) and right handed ($S_3 < 1$) polarization states, respectively. Image from Ref. [83].

this behavior by considering the expression of the beam generated by a q-plate when shined with a H or V polarized Gaussian beam:

$$\begin{aligned}|OUT\rangle =&\Big(\text{TEM}_{00}(\rho,\zeta)\cos(\delta/2)+\\&+i\text{HyGG}_{-|m|,|m|}(\rho,\zeta)e^{im\phi}\sin(\delta/2)\Big)|R\rangle\pm\\&\pm\Big(\text{TEM}_{00}(\rho,\zeta)\cos(\delta/2)+\\&+i\text{HyGG}_{-|m|,|m|}(\rho,\zeta)e^{-im\phi}\sin(\delta/2)\Big)|L\rangle,\end{aligned}$$

where the ± sign stands for H or V input polarization, respectively, and $m = 2q$. Adimensional units are introduced here, where the distance from the q-plate z and the radial coordinate r are normalized with respect to the Rayleigh range z_R and the waist w_0 of the beam, respectively ($\zeta = z/z_R$, $\rho = r/w_0$). C-points positions are calculated by solving the equations $C_{L/R}(\rho, \phi, \zeta) = 0$, where left and circular components $C_{L/R}$ are those reported in Eq. 3.16 (details on this analysis are reported in Appendix B). In Fig. 3.7 we plot the position of left-handed C-points with respect to the coordinate ζ. For small values of ζ, multiple rings characterize the radial distribution of HyperGeometric-Gaussian modes and many C-points may appear at given transverse plane. We can note that for any value of δ and ζ there exist at least a left-handed C-point (and its right-handed partner), although it might be positioned in the peripheral regions of the beam where the field intensity is negligible. On the other hand, we can note that as we approach the near field, striking differences manifest when the q-plate retardation is higher or lower than $\pi/2$. In the latter case singularities move away at infinite distances, while in the former case L and R C-points merge at the beam center (forming a single V-point), since the width of the central dip in HyGG_{pm} modes with $m \neq 0$ vanishes as $\zeta \to 0$. For high values of ζ (far field), numerical simulations show that the distance between C-point positions and the beam axis is proportional to the coordinate ζ. In this configuration, we can evaluate if these singularities can be still considered within the beam; in particular, for different values of δ we can compute the fraction of the beam intensity contained in the circular region delimited by the C-point radial position. In Fig. 3.7b we plot the relative encircled intensity of the beam, which is observed to increase as the Gaussian contribution becomes stronger. When $\delta < \pi/8$, for example, more than the 99% of the beam intensity is contained in the radius defined by the C-point position, i.e. the singularities can be considered as lying outside the beam. These different features are a consequence of the irregular behavior of $\text{HyGG}_{|m|,m}$ modes in the limit $\zeta \to 0$. As discussed in the following subsection indeed C-points can form at the intersections between the Gaussian and $\text{HyGG}_{|m|,m}$ envelopes; when $\delta > \pi/2$, these envelopes cross in the region of the central dip characterizing $\text{HyGG}_{|m|,m}$ modes, at a specific radial distance that depends on δ. However, since the dip width vanishes when approaching the near field, independently of δ all C-points merge at the center. When $\delta < \pi/2$, singularities do not form in the HyGG dip but rather at the intersection of the tails of both Gaussian and HyGG modes; such intersections exist since the latter have a larger radial profile, for finite values of ζ. But as $\zeta \to 0$, the HyGGs envelope converges to that of the Gaussian beam, and clearly two Gaussian profiles with different amplitudes cannot have intersection points, so that all C-points are expelled from the beam. Below, we will repeat this analysis for the simpler case in which Laguerre-Gauss modes are taken in the place of HyGG modes.

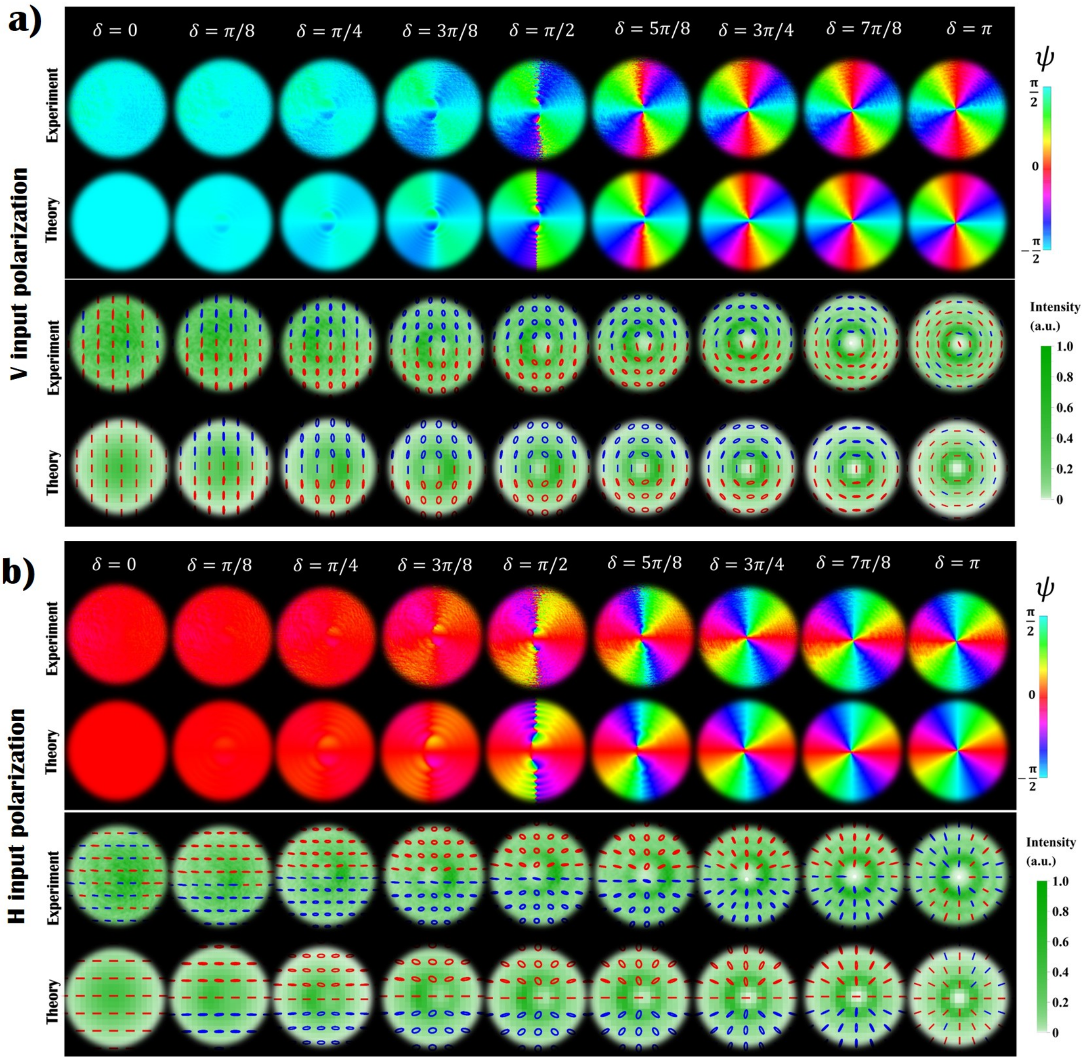

Figure 3.6: Transition from a trivial to a topologically non-trivial polarization pattern. In panels a-b we report the experimental and theoretical intensity and polarization distribution of the near field ($\zeta = 0.01$) for both radial and azimuthal VVB, respectively. We observe no polarization singularities (actually, C-points exist in a region where the beam intensity is too low, as shown in Fig. 3.7) when $\delta < \pi/2$. At $\delta = \pi/2$ an undefined number of C-point dipoles appears, in proximity of the nodes of the HyGG$_{-1,1}$ modes. When δ is increased, a pair of C-points with $\eta = 1/2$ appears in the polarization pattern, with the distance between these points getting smaller as $\delta \to \pi$. The topological charge associated with a path enclosing both singularities is $\eta = 1$. Here, red and blue colored ellipses are associated with left ($S_3 > 1$) and right handed ($S_3 < 1$) polarization states, respectively. Image from Ref. [83].

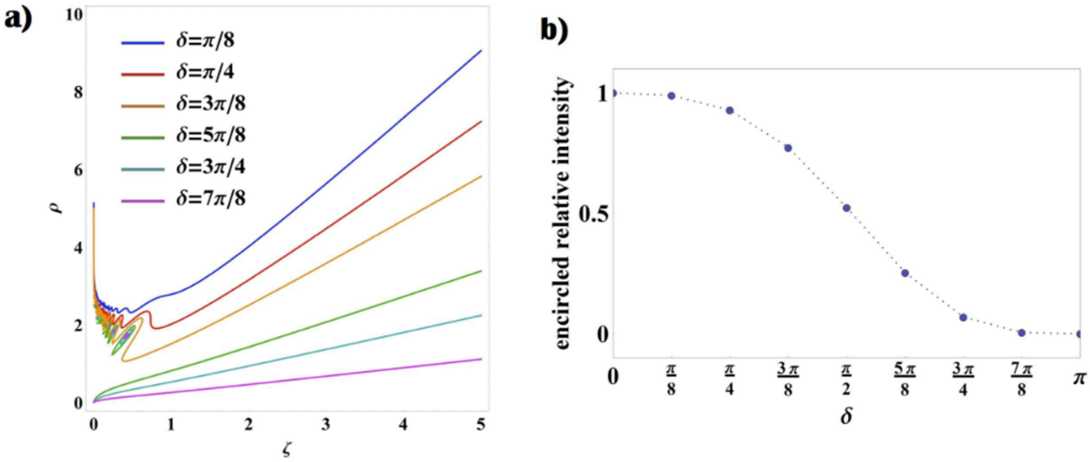

FIGURE 3.7: **Dynamical evolution of C-points during propagation and associated enclosed energy**. (a) We plot the radial coordinate ρ of the position of left handed C-points vs the longitudinal coordinate ζ, for different values of δ (the latter are encoded in the color of the curve, as displayed in the figure legend). Two regimes can be distinguished: for $\pi/2 < \delta < \pi$ C-points merge at the beam center ($\rho = 0$) as $\zeta \to 0$, hence making the polarization pattern topology non-trivial. In the same regime, additional closed loops indicate the existence of C-point dipoles appearing and disappearing as the beam propagates, as a consequence of the dynamical evolution of the radial ripples characterizing HyGG modes. For $0 < \delta < \pi/2$, instead, the C-point radius increases indefinitely as we approach the beam near field. (b) For the same values of δ as in panel a, we plot here the fraction of the beam intensity contained in a circular region with a radius given by the C-point radial coordinate, in the far field limit. These results, in particular, are obtained when considering $\zeta = 15$, but in the limit of largeζ, they remain essentially constant. Image adapted from Ref. [83].

As shown in Fig. 3.7, VBs obtained when $\delta < \pi/2$ may show C-points only after a definite value of ζ. We confirm experimentally this effect by investigating the dynamical formation of such singular points in the polarization pattern of a beam obtained when $\delta = 6.7\pi/16$. In Fig. 3.8 we report the experimental data and the associated theoretical predictions. Although no C-points are observed in the near field (see Fig. 3.6), they appear as we increase the propagation distance ζ, in agreement with our previous discussion (see Fig. 3.7(a)). In particular, at $\zeta = 0.2$ we can observe a double pair of singularities, as a consequence of the VVB amplitude profile at the first radial node of the corresponding HyGG mode.

The formation and dynamical evolution of C-points singularities in VBs reported in Eq. 3.16 have simpler features when considering Laguerre-Gauss modes in place of HyGG modes, since their radial distribution is less complex. LG beams are characterized by a pair of indexes (p, m), where m is an integer fixing the OAM content of the mode, while p is a positive integer determining the radial distribution. Specific architectures, such as for instance a q-plate placed inside a laser cavity [104], can produce VVBs whose radial distribution is that of LG modes with the lowest radial index $p = 0$. Differently from the HyGG case, these have no radial nodes and the light is confined inside a single ring.

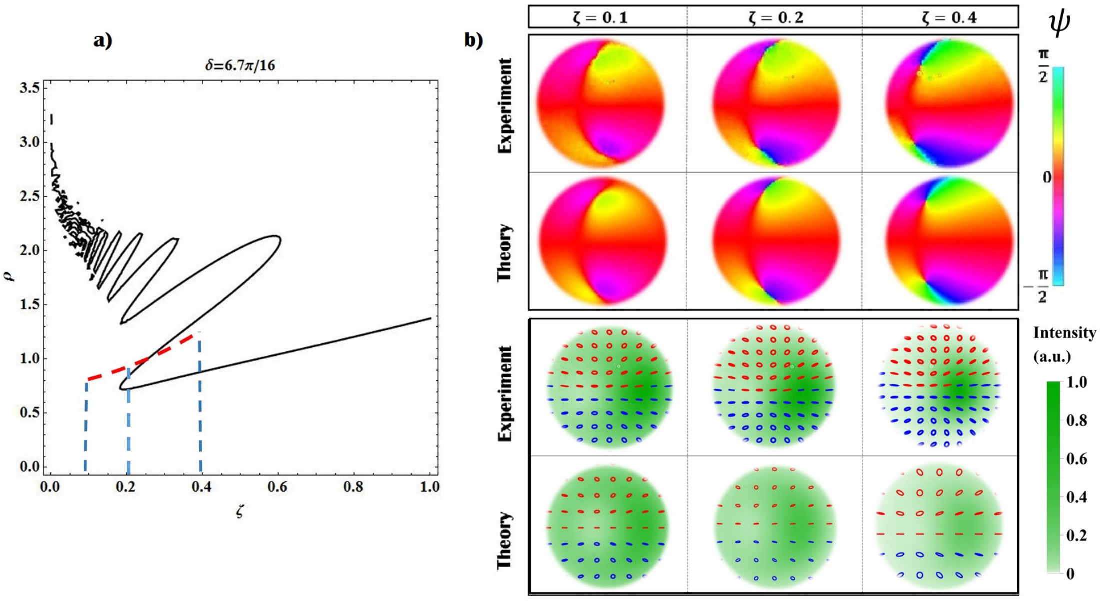

FIGURE 3.8: **Dynamical formation of C-points**. Here we show that for $\delta < \pi/2$ C-points (absent in the near field) appear during propagation. In panel a) we report the C-point position versus the longitudinal coordinate ζ in the case $\delta = 6.7\pi/16$, for a H polarized input beam. The red line indicates the dimension of the regions investigated in the experiment while blue dashed lines show the corresponding values of ζ. In panel b), we report the plot of the orientation angle ψ and the polarization pattern of the associated beam; here, theoretical simulations are added for comparison. Data refers to three different propagation distances, as reported in the plot: when $\zeta = 0.1$, no singularities are visible in the polarization pattern; at $\zeta = 0.2$, two C-point dipoles are clearly emerging, and a single pair is observed at $\zeta = 0.4$. In the polarization plots, red and blue colored ellipses are associated with left ($S_3 > 1$) and right handed ($S_3 < 1$) polarization states, respectively. Image from Ref. [83].

As a consequence, only one pair of C-points manifests in the VB polarization pattern, independently of the longitudinal coordinate ζ. As we will show in the following, the positions of C-points for LG beams can be analytically calculated and can be compared with the beam width. In particular, it results that they are both proportional to the quantity $\sqrt{1+\zeta^2}$, with a different proportionality constant that depends on δ. Hence, when δ is lower than a given threshold, no C-points can be found in the far field and the polarization pattern is trivial.

3.5 Conclusions

[3] In this chapter we investigated the topological features of vector vortex beams and the robustness of the associated singularities when introducing a perturbation to the field. Polarization singularities manifesting at the center of such beams are unstable

---

[3] Some paragraphs and sentences of this section are adapted or copied verbatim from the work [83] which I coauthored

and transform into multiple C-points with equal topological charge $\pm 1/2$, the lowest order singularities of fully polarized light. Here we perturbed a VVB by adding coherently a tunable amount of a linearly polarized Gaussian beam and demonstrated experimentally a possible mechanism that leads to the unfolding of the central singularity, in analogy to similar phenomena observed in the skylight polarization [131] or in high-order optical vortexes [111]. On one hand this realization provides a simple example of transformations between different polarization singularities [123, 124, 134, 138]; on the other, it allows for a detailed investigation of phenomena that may affect optical systems exploiting VVBs, where the presence of the fundamental TEM_{00} mode can result from different types of misalignments [125, 126, 128], scattering [129] or from turbulence in the medium where light propagates [139]. Investigating the stability of VVBs can be of interest for all photonic applications involving these structured beams, since a modification of the intensity pattern always accompanies the singularity decay. As discussed before, similar alterations of a VVB can occur as a consequence of experimental imperfections, and the beam distortion caused by the V-point splitting may play a role in a variety of applications, as for example in material shaping [140]. Reversing the current approach, as a prospect it could be possible to tune the q-plate optical retardation in order to compensate the effect of experimental imperfections and reduce such deformations of the beam profile [141]. Finally, these results may find application in the context of singularimetry; weak fields can indeed be measured by letting them perturb unstable optical fields, and features of materials that have interacted with such beams can be extracted from the pattern formed by split singularities [142]. In addition, since perturbations can be introduced by imperfections in the optical setup, the unfolding of the central V-points can be used to assess the quality of the VVB generation system [129]. We conclude observing that the technique used in this work for generating vortex beams superimposed with uniformly polarized light has been applied in Ref. [143] to extend the possible surface patterns that can be obtained with laser ablation.

Chapter 4

Photonic quantum walks employing light's spatial degrees of freedom

4.1 Introduction

Quantum walks were first introduced in 1993 by Aharonov et al. [144] to study a quantum counterpart of the classical random walk. The latter is a process where a classical particle moves on a lattice or a graph, choosing randomly the motion direction at every time-step, independently from its previous path. The simplest picture considers a particle on a one dimensional lattice. At every step, the particle moves right or left depending on the outcome of a random process, often depicted as a coin toss. In the quantum version of this process the particle is in a quantum state with two degrees of freedom: one spatial, which is infinite dimensional, and one ”internal”, which is finite dimensional and is often identified with the spin. The internal degree of freedom is necessary to introduce the quantum version of ”coin tossing”. Indeed, the quantum walk introduced in Ref. [144] consists in the repetition of two elementary steps. A translation on the lattice conditioned by the internal state, followed by a trasformation on the internal state itself, that mimics the classical coin tossing operation.

The fact that the “quantum” coin tossing allows the particle to be not only in a finite number of possible internal states, but also in a coherent superpositions of them, is the essential feature that distinguishes the quantum walk from the classical one. This results in a completely different dynamics of the quantum walk with respect to its classical counterpart. While the classical quantum walk is characterized by a diffusive spreading of the particle probability distribution in position space (i.e. in one dimension, the variance of the distribution grows linearly with the number of steps) the quantum walk presents an asymptotic distribution with ballistic features (in one dimension the variance of the probability distribution grows as n^2, where n is the number of steps), which results from quantum interference effects occurring during the process. This feature has lead to the idea of using quantum walks for the speed up of search algorithms [145–147]. Moreover, contrary to the classical case, the probability distribution of the quantum walk is dependent on the initial coin state.

After the work of Aharonov et al. quantum walks have become of great interest as tools for quantum simulation and for quantum computation. Indeed it has been shown that quantum walks can be used for universal quantum computation [148, 149], as a fundamental process for realizing quantum search algorithms [145, 146] and Boson Sampling [150, 151]. Quantum walks have revealed themselves as a powerful tool for simulating quantum systems, like topological states of matter [152] multiparticle statistics [153], Anderson localization and other disorder related phenomena [154, 155], multiparticle interactions [156] and even for modeling energy transfer in photosynthesis [157]. This broad range of applications came out from new proposals of more complex quantum walk protocols and their experimental realizations.

This chapter focuses on the experimental realizations of the quantum walks employed in this Thesis. After a brief description of the general features of Quantum Walk processes and a review of the most important photonic implementations realized so far, we will give a detailed description of specific quantum walk protocols that can be implemented exploiting the OAM space and the transverse momentum space of light. The q-plates and g-plates, together with ordinary wave-plates, will be shown to be the fundamental tools for the realization of these experiments. We will also show how these implementations allow to mimic the dynamic of a charged particle in a periodic potential under an external electric field. In the next chapter we will show how these platforms allow to investigate interesting topological phenomena

4.2 General features of quantum walks

The Quantum Walk (QW) is a process evolving in an Hilbert space given by the tensor product $\mathcal{H}_{QW} = \mathcal{H}_w \otimes \mathcal{H}_c$. The space $\mathcal{H}_w$, called *walker space*, is infinite dimensional and is spanned by the set of position eigenstates $\{|\mathbf{j}\rangle\}_{\mathbf{j}\in\mathcal{X}}$, where $\mathcal{X}$ is a lattice or a graph of arbitrary dimensionality. Instead, the *coin space*, $\mathcal{H}_c$, is a finite dimensional space (often chosen two or four dimensional). The QW is defined by a set of unitary operators applied to an initial state in $\mathcal{H}_{QW}$. These operators are of two kinds: *rotation* or *coin operators* which act only on the coin space, and *shift operators* acting on the whole space $\mathcal{H}_{QW}$. Shift operators change the position on $\mathcal{X}$ in a way that is conditioned by the coin state.

The simplest example of such a process is the QW introduced by Aharonov et al. [144], that we will call *standard Quantum Walk*. In this case $\mathcal{X} = \mathbb{Z}$, i.e. the walker space is a one dimensional lattice, and the coin space is two dimensional, i.e. spanned by the vectors: $\{|\uparrow\rangle, |\downarrow\rangle\}$. The shift operator $\hat{S}$ is defined as:

$$\hat{S} = \sum_j \big(|\uparrow\rangle\langle\uparrow| \otimes |j+1\rangle\langle j| + |\downarrow\rangle\langle\downarrow| \otimes |j-1\rangle\langle j|\big), \tag{4.1}$$

where $j \in \mathbb{Z}$. The shift operation is such that, if the internal state is, say, $|\uparrow\rangle$, then the particle will move right, while, if it is $|\downarrow\rangle$ the particle will move left. If it is a superposition $c_\uparrow|\uparrow\rangle + c_\downarrow|\downarrow\rangle$, then it will move right or left with probabilities given by $|c_\uparrow|^2$ and $|c_\downarrow|^2$. Between two successive traslations, the "coin operation" changes the internal quantum state. The coin operator, $\hat{C}$, can be a generic unitary 2×2 matrix. For example one can use the Hadamard matrix:

$$\hat{C}_{Had} = \frac{1}{\sqrt{2}} \begin{pmatrix} 1 & -1 \\ -1 & 1 \end{pmatrix}$$

or a more generic rotation around the y axis of the Bloch sphere:

$$\hat{C}(\theta) = e^{-i\theta\sigma_y/2}.$$

The single step operator is thus:

$$\hat{U} = \hat{S}\hat{C}.$$

Its action is illustrated in Fig. 4.1(a). A N step QW is realized applying the operator $\hat{U}^N$ on a generic initial state $|\psi(0)\rangle$. Often one chooses an initial state localized in a given position. Examples of probability distributions arising form the standard QW are shown in Fig. 4.1(b).

When the QW is unitary one can define an effective Hamiltonian $\hat{H}_{eff}$ from the identity (here and hereafter we pose the Planck constant $\hbar = 1$):

$$\hat{U} = \exp(-i\hat{H}_{eff}\Delta T), \tag{4.2}$$

where ΔT represents the conventional time interval between two steps. From now on we will choose $\Delta T = 1$. The basic idea of using QWs for quantum simulations is to engineer H_{eff} in order for it to have properties (e.g symmetries, spectrum...) shared with some system of interest. Hence it is desirable to have at disposal an experimental platform with many controllable parameters allowing to simulate a broad class of Hamiltonians. The QW considered here is a time periodic process, hence it should be described by a

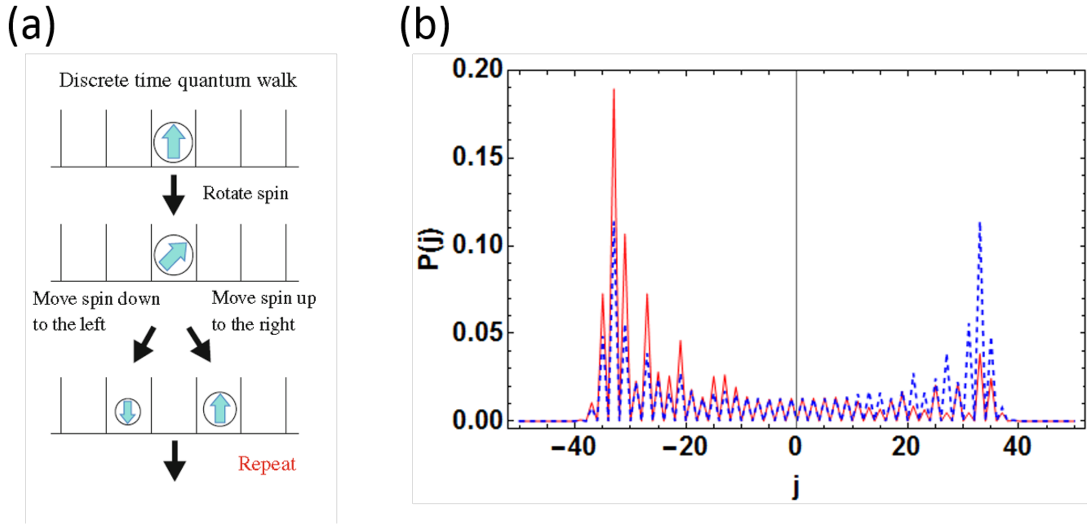

FIGURE 4.1: **Standard Quantum Walk.** In **a** the single step of the standard QW is schematically illustrated (adapted from [152]). In **b** two probabilities distributions after 50 steps are plotted. They differ from the choice of the initial coin state. The red distribution was obtained choosing the state $|\uparrow\rangle$ giving rise to an asymmetrical envelope. A symmetric distribution is instead obtained for the initial coin state: $(|\uparrow\rangle + |\downarrow\rangle)/\sqrt{2}$ (blue dashed line). In both cases the ballistic spreading is evident.

time dependent Hamiltonian:

$$H(t) = H(t + \Delta T)$$

. In the case $H(t)$ commutes with itself at different times we can write H_{eff} in the closed form:

$$H_{eff} = \int_t^{t+\Delta T} H(t')\frac{dt'}{\Delta T}.$$

The effective Hamiltonian differs from a truly static Hamiltonian since it is defined only as the exponent of the single step unitary operator. Hence adding to H_{eff} an integer multiple of 2π will not alter the description of the system. Therefore the eigenvalues of H_{eff}, called *quasi-energies*, are defined modulo 2π. This result arises from the the discrete time translational symmetry, in analogy with the more familiar case of invariance under discrete space traslations which results in the definition of quasi-momentum.

We point out that we are considering here the so called Discrete Time Quantum Walks (DTQW). There is however also interest in Continuous Time Quantum Walks (CTQWs), where no coin degree of freedom is introduced. A tipical example of experimental CTQW is given by arrays of optical waveguides in which light propagates following a Schroedinger-like equation, where the Hamiltonian resembles a tight binding model [158].

Symmetry under discrete traslations, or *lattice symmetry*, is another fundamental property of QWs on regular lattices since it allows to define quasi-energy bands, in analogy with Solid State systems. Eigenstates of the quantum walk operator can in general be written as $|q\rangle \otimes |s(q)\rangle$, where:

$$|q\rangle = \sum_j e^{ijq}|j\rangle \tag{4.3}$$

is a state uniformly distributed on the lattice with quasi-momentum q, defined in the Brillouin zone (corresponding to the set $BZ = [-\pi, \pi)$ in one dimension), and $|s(q)\rangle$ is a coin state to be determined solving the eigenvalue equation for $\hat{H}_{eff}$. To this aim one writes the effective Hamiltonian in the quasi-momentum basis:

$$\hat{H}_{eff} = \int_{BZ} \frac{dq}{(2\pi)^d} \{E(q)\mathbf{n}(q) \cdot \sigma\} \otimes |q\rangle\langle q|, \tag{4.4}$$

where $E(q)$ is the quasi-energy, $\mathbf{n}(q)$ the vector representing $|s(q)\rangle$ on the Bloch sphere and d the system dimensionality.

The quasi-momentum representation allows to calculate easly the asymptotic distribution of a quantum walker starting at the origin, $j = 0$ [159]. Let $P(X)$ be the probability distribution written as function of $X = j/n$, where n is the number of steps, one obtains, for large n:

$$P(X) = \int_{-\pi}^{\pi} \frac{dq}{2\pi} \Bigg\{ \frac{1}{2}(1 + \langle \mathbf{n}(q) \cdot \sigma \rangle)\delta(X + v(q)) \tag{4.5}$$

$$+ \frac{1}{2}(1 - \langle \mathbf{n}(q) \cdot \sigma \rangle)\delta(X - v(q)) \Bigg\}, \tag{4.6}$$

where $v(q) = dE(q)/dq$ is the group velocity associated to the eigenstate $|q\rangle$ and the brackets $\langle \ldots \rangle$ represent the mean over the final state. This result clearly shows the ballistic feature of the particle propagation in a quantum walk: asymptotically the initial state propagates with speed $\pm v(q)$ where the sign depends on the projection over the two quasi-energy bands. As already stated in the introduction the ballistic, rather than diffusive, features of QWs have suggested their use for efficient quantum search algorithms [145, 147]. It is interesting to note that the diffusive behavior can be restored by introducing decoherence effects [160]. This is a simple example of transition from quantum to classical phenomena as an effect of the introduction of random phases.

4.3 Review of photonic realizations of quantum walks

Several platforms have been developed for realizing quantum walks and studying their properties. Here we give a brief account of the most important ones. Quantum Walks have been implemented in a broad range of physical platforms. Different physical realizations allow for different controls of the system. Some platforms can have an easier access to the lattice space allowing to implement, for example, spatial dependent coins, boundaries and impurities. Others can have a large variety of tunable parameters, useful

for exploring the QW dynamics of different effective Hamiltonians. Still, the number of steps achievable can vary strongly from one platform to the other.
One of the first QW was realized with cold atoms by Karsky et al. [161]. Here Cesium (Ce) atoms where used encoding the coin degree of freedom in two hyperfine states and the walker space was realized by trapping the atoms in an optical lattice. The rotation operator was implemented through the application of resonant microwave radiation between the two hyperfine states, while the shift operator was realized by adiabatic traslation of the optical lattice. Nowadays, neutral atoms in optical lattices still represent a competitive physical platform for QWs (see e.g. Refs: [162, 163]). In this architecture, the QW lattice space coincides with the real space in the laboratory. However one can exploit any degree of freedom associated to an infinite dimensional space. As an example, in Ref. [164], the QW was realized in the phase space of trapped ions. Recently QW walks have been encoded using superconducting qubits in a microwave cavity [165]. There the transmon qubit encodes the internal degree of freedom while the lattice is implemented in the cavity phase space. The shift operator arises from the interaction between the qubit and the coherent cavity mode.

Let us focus now on the photonic implementations. The coin degree of freedom can be naturally encoded in the polarization of the photon. This is indeed what is done in the majority of platforms. Coin operations can be easly realized using ordinary waveplates. Photonic QWs mostly differ for the choice of the degree of freedom (d.o.f.) to be used as walker space. The most straightforward realization is probably the encoding of the lattice space in the optical path of the photon: a different transverse position is associated to a different lattice site. If the polarization is chosen as the coin, then the shift operator can be implemented by a birefringent device, for example a calcite crystal thick enough to spatially separate two orthogonal polarizations. This idea was realized by Broome et al. [160] where the QW consisted in alternating calcite crystals with half wave plates (rotated in order to act as the Hadamard coin). By introducing a small misalignment between calcite crystals, so as to simulate the effects of decoherence, it was also possible to show the transition from a ballistic to a diffusive behavior. This kind of architecture has been also used to explore topological phases [152, 167, 168], QWs with time dependent coins [169], and foundations of quantum mechanics [114].
Another interesting implementation of QW in the space of transverse modes is an array of Mach-Zender interferometers. Here the polarization does not play any role, but the coin can be associated to the entrance door of the Beam Splitters in each interferometer. Such an architecture can be regarded as the optical analogue of the Galton board. Realizing this system with bulk optics would be challenging due to necessity of controlling the stability of a large number of interferometers. Indeed, this architecture has been realized using integrated photonics circuits [153], where the laser written waveguides

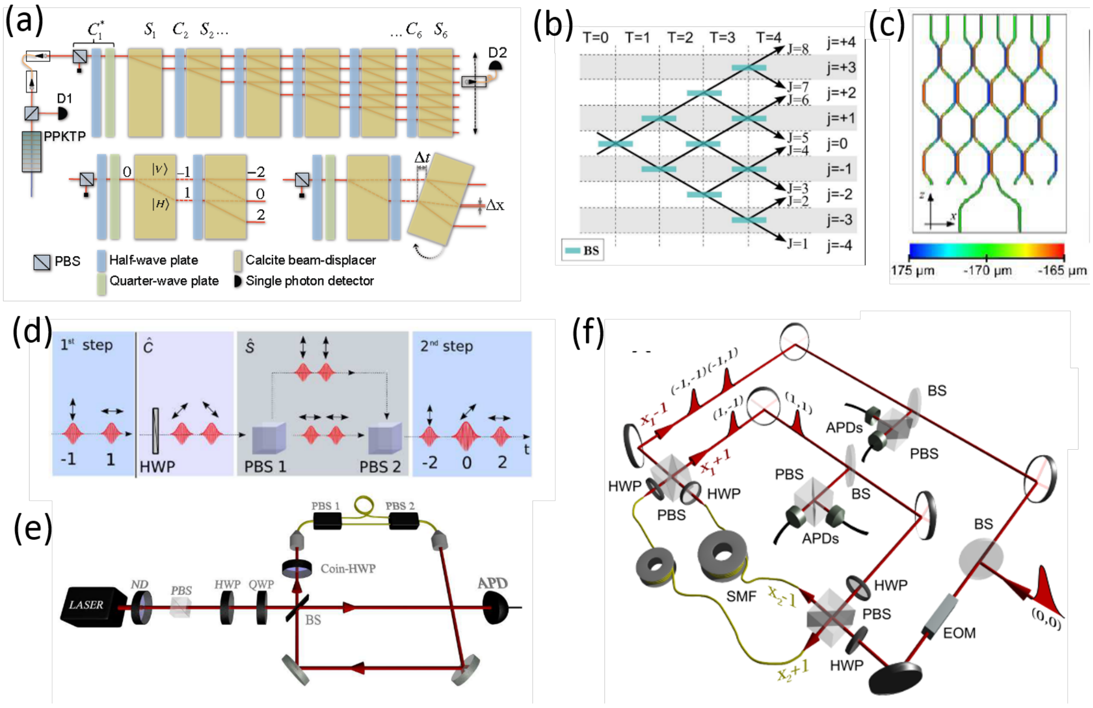

FIGURE 4.2: **Examples of photonic quantum walks.** (a) Illustration of a QW realized alternating calcite crystals with wave-plates [160]. Decoherence effects can be simulated by misalignment the crystals. (b) A photonic quantum walk can, in principle, be realized within a series of beam splitters. The actual implementations, (c), which avoids stability issues, consists into arrays of integrated Mach-Zender interferometers (pictures adapted from [153]). (d) Illustration of the single step of a QW in the time domain [166]. Panel (e) shows a sketch [166] of the corresponding experimental apparatus. This system can be modified for simulating two dimensional QWs by introducing additional optical paths, as illustrated in (f)[156].

were tailored in order to not alter the polarization state of the crossing photons. Hence it was possible to inject entangled photon pairs in a state $(|H,H\rangle + e^{i\alpha}|V,V\rangle)/\sqrt{2}$ in order to investigate bosonic, fermionic and anyonic statistics. In Ref. [154] the interplay between particle statistics and spatial disorder was studied by adding controllable phase shifters in the circuit.

Waveguides arrays have also been used as platforms for CTQWs [158]. In particular, using arrays of coupled evanescent waveguides, two photon correlations have been explored [170]. Very recently, a two dimensional CTQW has been demonstrated [171].

Hitherto we have considered photonic quantum walks in which the lattice was realized in real space. However we have seen in Chapter 1 that light has multiple infinite dimensional degrees of freedom. Before discussing the QW implementations using the OAM and the transverse wavevector spaces, we briefly mention another platform where the lattice space was encoded by the arrival time of light pulses. The system presented in Ref. [166] was able to overcome scalability and flexibility issues present in previous platforms. It was based on a loop architecture that allowed to keep constant the number of optical elements with the increasing number of steps. In this kind of setup, the coin is again identified with the photon polarization, while the lattice position is mapped in the arrival time of a photon (or a coherent light pulse) at the detector. The coin dependent shift in lattice space can be easily realized sending the pulses into a Polarizing Beam Splitter in such a way that H polarized photons will follow an optical path shorter than the one followed by V polarized photons. Recombining coherently the two paths, one will have that V polarized photons have been delayed in time, hence displaced in the lattice step, with respect to H polarized photons. The QW is realized alternating this interferometric setup with a waveplate performing the coin operation. In Ref. [166] this system was inserted in an optical feedback loop allowing for an higher stability and for a number of devices indipendent from the required number of steps. In Ref. [155] the setup was improved using a fast Electrooptic Modulator (EOM) for performing the coin operation. The optical retardation of this device can be switched fast enough to apply a different operator for each arriving pulse. Therefore a spatially (and temporally) varying coin operation could be implemented for studying static and dynamic disorder effects. By introducing two additional paths in the experiment [156] it was possible to demonstrate a Quantum Walk on a plane with a 4-dimensional coin, where the sites on the square lattice were carefully mapped into the arrival times of the light pulses. In this kind of setup the 2D single particle QW could be mapped into a 1D Quantum Walk of two interacting particles, an ingenious method for study multi-particle interactions with light.

Multi-dimensional quantum walks are still a challenge from the experimental point of view. The DTQW in Ref. [156] is the only setup realized so far. We also mention a recent implementation of a 2D Continuous Time QW [171] realized with laser written waveguides. However, in this chapter we will present a novel platform where 2D-DTQWs can be performed. There, instead of using the trick of mapping a one dimensional d.o.f. (the arrival time) into a two dimensional one, we will use a space that is intrinsically two dimensional.

4.4 Quantum Walks in the OAM space of light

We have seen in Chapter 1 that the Orbital Angular Momentum of light is an infinite dimensional and discrete degree of freedom that can be exploited in quantum applications in high-dimensional spaces. As such, the OAM space, $\mathcal{H}_o$, represents a candidate space over which performing QW experiments. This idea was first proposed by Zhang et al. [172] in 2010, where the q-plate was suggested as the fundamental element for performing the shift operation. A similar scheme was discussed in Ref. [173] considering the possibility of inserting a q-plate and a quarter wave plate into an optical feedback

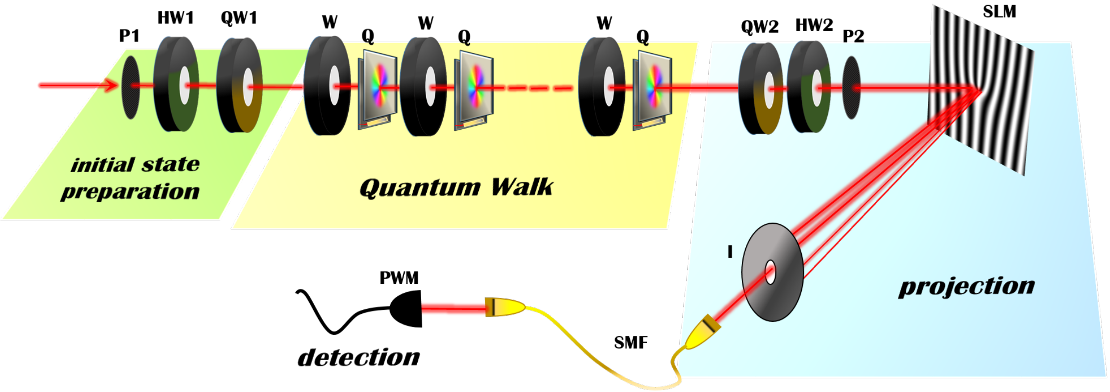

FIGURE 4.3: **Experimental setup for QWs with OAM.** We show a sketch of the experimental setup used for performing QWs in the OAM space of light. The initial coin state of a photon (or a coherent laser beam, depending on the source that we want to use) is prepared with a polarizer ($P1$), an half wave plate ($HW1$) and a quarter wave plate ($QW1$). Then the beam crosses the QW setup, consisting in alternate q-plates, Q, and quarter wave plates, W. In order to detect the final probability distribution we use a programmable liquid crystal based SLM that, coupled with a single mode fiber SMF allows to measure the relative intensity of the desired OAM mode. The other diffraction orders are blocked with an iris (I). Since the pattern displayed on the SLM is seen by a specific linear polarization, say H, we require that the beam impinging on it is always H polarized. Thus, in order to measure the total probability distribution, we first project over two orthogonal polarization states (both transformed in H) and then send the beam to the SLM. We do this by means of a set of wave-plates ($QW2$ AND $HW2$) and a polarizer $P2$. The light intensity filtered by the SMF is then measured by a powermeter (PWM).

loop. In 2015 Cardano et al. [174] made the first experiments with this platform exploring also wavepacket motions and two photon QWs. In this Thesis the same setup has been employed to detect the topological invariants of the system, as we will see in detail in the next chapter [175]. In this section we proceed to illustrate the details of this experimental scheme. We want to implement a QW where the lattice is encoded in the OAM space of a light beam (or of a single photon) and, as in other experiments, the coin corresponds to the polarization. While the coin operation can be obtained by means of standard wave-plates, we need a device that realizes the shift operator, i.e. that changes the OAM state in a way that is conditioned by the polarization. The q-plate does exactly the job. Let us firs consider a q-plate with $\delta = \pi$ (half-wave retardation). If we limit ourselves to the near field, where the radial profile of the beam is not sensibly altered, the action of the q-plate on the SAM-OAM space is given by the operator:

$$\hat{Q} = \sum_m \big(|m+1\rangle\langle m| \otimes |R\rangle\langle L| + |m-1\rangle\langle m| \otimes |L\rangle\langle R| \big), \tag{4.7}$$

where we considered $q = 1/2$, $\alpha_0 = 0$ and the ket $|m\rangle$ correspond to a mode with amplitude proportional to $\exp(im\phi)$. Eq. 4.7 strongly resembles the shift operator (Eq.4.1). The only difference is that, in this case, when the "particle" changes position also its coin state changes, i.e. the polarization handedness is flipped. In principle one can obtain exactly the operator $\hat{S}$ of Eq.4.1 adding an half wave plate after the q-plate. However, having exactly the operator $\hat{S}$ is not important for our purposes. The main features of the standard QW can be obtained alternating a q-plate with a quarter wave plate.

We can go even beyond the "standard" QW by considering other values of the q-plate optical retardation. For arbitrary δ the q-plate action is:

$$\hat{Q}|L,m\rangle = \cos\left(\frac{\delta}{2}\right)|L,m\rangle + i\sin\left(\frac{\delta}{2}\right)|R,m+1\rangle \tag{4.8}$$

$$\hat{Q}|R,m\rangle = \cos\left(\frac{\delta}{2}\right)|R,m\rangle + i\sin\left(\frac{\delta}{2}\right)|L,m-1\rangle. \tag{4.9}$$

Hence a term whose action is proportional to the identity operator is added. This means introducing the possibility that, between one step and the other, the walker stays in its position instead of changing site. In general the probability that the walker jumps from one site to the other will be $\sin(\delta/2)^2$. If we depict the term proportional to the identity as an inertial contribution it is easy to expect that for smaller δ the probability distributions will have a smaller width (even is always increasing linearly with the number of steps). We will consider a QW described by the single step operator:

$$\hat{U}(\delta) = \hat{Q}(\delta)\cdot\hat{W}, \tag{4.10}$$

where W is a quarter wave plate. The experimental setup is sketched in Fig. 4.3. We prepare the initial coin state with a set of wave-plates and a polarizer. Then we perform the QW alternating electrically controlled q-plates and quarter wave-plates. The resulting probability distribution is measured coupling an SLM with a single mode fiber, as explained in Chapter 2. Since the SLM works on a specific input polarization, an additional set of wave-plates and polarizer before the OAM projection system is needed. If we desire to reconstruct the total probability distribution $P(m)$, we need first to measure the distributions relative to two orthogonal polarizations, say H and V, given by $P_H(m) = |\langle H,m|\psi(n)\rangle|^2$ and $P_V(m) = |\langle V,m|\psi(n)\rangle|^2$, where $|\psi(n)\rangle$ is the state after n steps of the QW. The distribution $P(m)$ is then obtained summing $P_H(m)$ and $P_V(m)$.

4.4.1 Spectral features

To understand better the dynamical properties of the QW defined by Eq. 4.10 we will look now at the Fourier transform of $\hat{U}$. From Eq. 4.3 we can write the OAM eigenstates as:

$$|m\rangle = \int_{-\pi}^{\pi} \frac{dq}{2\pi} e^{-imq} |q\rangle. \tag{4.11}$$

Then the q-plate operator takes the form:

$$\hat{Q}(\delta) = \int_{-\pi}^{\pi} \frac{dq}{2\pi} \left\{ \cos\left(\frac{\delta}{2}\right) \sigma_0 + i \sin\left(\frac{\delta}{2}\right) (\cos(q)\sigma_x + \sin(q)\sigma_y) \right\} \otimes |q\rangle\langle q|, \tag{4.12}$$

where σ_0 is the identity in the coin space and $\hat{\boldsymbol{\sigma}} = (\sigma_x, \sigma_y, \sigma_z)$ the Pauli matrices. The expression in curly brackets is the representation of the q-plate operator in Fourier space. It coincides with the Jones matrix of the q-plate where q is identified with the azimuthal angle ϕ. Hence, since in our platform the lattice space is associated with the Orbital Angular Momentum, the quasi-momentum q is encoded in the azimuthal angle ϕ. Similarly, the quarter wave plate, considered oriented at an angle θ, is expressed by the operator:

$$\hat{W}(\theta) = \frac{\sigma_0 + i\cos(2\theta)\sigma_x + i\sin(2\theta)\sigma_y}{\sqrt{2}} \otimes \hat{I}_w, \tag{4.13}$$

where $\hat{I}_w$ is the identity matrix in the walker space. We will label as $\mathcal{W}(\theta)$ and $\mathcal{Q}(q,\delta)$ the Jones matrices of the quarter wave plate and the q-plate, respectively. The single step operator is:

$$\hat{U}(\delta,\theta) = \int_{-\pi}^{\pi} \frac{dq}{2\pi} \mathcal{U}(q,\delta,\theta) \otimes |q\rangle\langle q|, \tag{4.14}$$

where $\mathcal{U}(q,\delta,\theta)$ is:

$$\begin{aligned} \mathcal{U}(q,\delta,\theta) &= \mathcal{Q}(q,\delta) \cdot \mathcal{W}(\theta) & (4.15)\\ &= \exp(iE(q,\delta,\theta)\mathbf{n}(q,\delta,\theta) \cdot \hat{\boldsymbol{\sigma}}) & (4.16) \end{aligned}$$

where we have defined the quasi-energy eigenvalues, $E(q,\delta,\theta)$, and the eigenvectors of $\mathcal{U}$ are represented on the Bloch sphere by the unit vector: $\mathbf{n}(q,\delta,\theta)$. Their explicit expression can be found from straightforward calculations. The quasi-energies are:

$$E(q,\delta,\theta) = \pm \arccos\left[\frac{\cos(\delta/2) - \sin(\delta/2)\cos(q-2\theta)}{\sqrt{2}}\right], \tag{4.17}$$

where the signs are associated to the two possible eigenstates of the systems, represented by $\pm\mathbf{n}(q,\delta,\theta)$ (whose explicit expression will be investigated in the next chapter). From this result it is evident that the effect of the angle θ is to shift the energy bands along the q direction. We will work in the following considering the case $\theta = 0$. The quasi-energy dispersion relations are shown in Fig. 4.4 (a). They are analog to the energy bands of a one dimensional insulator. Changing the value of δ we can tune the energy bands and thus study different effective Hamiltonians. In particular there are two values of δ where the energy gap is zero (modulo 2π). We remind that, since this is a periodic system,

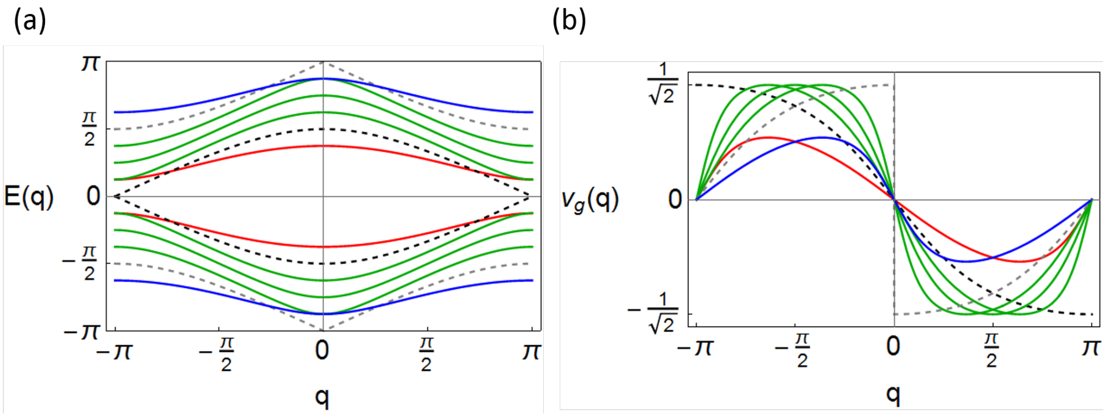

FIGURE 4.4: **Energy bands and group velocity of 1D QW.** We plot the dispersion curves of the, **a**, quasi-energies $E(q,\delta)$ and, **b**, group velocities $v_g(q,\delta) = dE(q,\delta)/dq$ for different values of δ. Red curves are for $\delta = \pi/4$. Green curves are for $\delta = 3\pi/4, \pi, 5\pi/4$ and the blue ones for $\delta = 7\pi/4$. The energy gap closes at $E = 0$ for $\delta = \pi/2$ (black dashed curve) and at $E = \pm\pi$ for $\delta = 3\pi/2$ (gray dashed curve). The gap closing manifests itself in jumps of the group velocity dispersion. The different colors have been chosen to differentiate with respect to the different topological phases, as we will see in Chapter 5. Dashed curves correspond to points where topological phase transition occurs.

one can have gap closure at $E = 0$ but also at $E = \pi$, since the values $E = \pi, -\pi$ are identified. To find the values of δ where the gap closes it suffices to solve the equation:

$$\frac{\cos(\delta/2) - \sin(\delta/2)\cos(q)}{\sqrt{2}} = \pm 1.$$

Hence one finds that the energy gap closes at $E = 0$ in $q = \pi$ when $\delta = \pi/2$, and at $E = \pi$ in $q = 0$ when $\delta = 3\pi/2$. In these regions the dispersion relation presents a discontiuity which is evident when looking at the plots of the group velocity $v_g(q,\delta) = dE(q,\delta)/dq$ (Fig. 4.4 (b)). Indeed, in correspondence of the gap closing, the group velocity has a jump discontinuity.

Gap closing points, where the energy dispersion is linear, also called *Dirac points*, are signatures of intriguing physics. Indeed the existence of Dirac points in graphene is at the origin of many of its innovative properties. Moreover, as we will see in Chapter 5, the closing of a gap when varying some parameter is often associated to a topological phase transition. This suggest that our system can have different topological phases and hence can be an useful platform for studying these phenomena.

4.5 Quantum Walks in the transverse wavevector space

QWs implemented in the OAM space have been demonstrated as a powerful tool to investigate wavepacket dynamics, two photon correlations and topological phases [95, 174, 175]. However they are limited to a one-dimensional space. To realize QWs on higher dimensional lattices would require a different scheme. In principle one can think about increasing the dimensionality of the QW introduced in the previous section by considering the radial degree of freedom. We have seen that this is indeed another infinite dimensional degree of freedom, indexed, in the case of LG$_{p,m}$ modes, by a positive integer p which could be associated to a coordinate in another 1D lattice. A 2D QW could be realized introducing shift operators that change both the indexes m and p. However, a device able to perform such a task is still unknown.

Here we propose another approach that allows to realize the QW presented in the previous section with a simpler detection scheme and an higher versatility, and can be easily extended to two dimensional scheme [38]. The lattice will be encoded by the transverse projection of the light wavevector. The g-plates, introduced in Chapter 1, will be used to implement shift operators. Again, the coin d.o.f. will be identified with the polarization. In the following subsections we will describe the platform, discussing the detection scheme, and then we will show how to simulate a QW with an external applied force. Finally we will present some experimental results. In Appendix C we consider in detail the possible deviations from the ideal QW evolution in our setup. In Chapter 5 we will look in more detail at the 2D platform, focusing on its topological properties.

4.5.1 Description of the platform

We have seen in Chapter 1 how the transverse wavevector space of the photon can be used to encode states defined on one and two dimensional lattices. These states are superpositions of plane waves whose wavevector has a transverse component smaller than the longitudinal one k_z. The transverse wavevector $\mathbf{k}_t$ is given by:

$$\mathbf{k}_t = p(n\mathbf{x} + m\mathbf{y}), \tag{4.18}$$

where $\mathbf{x}$ and $\mathbf{y}$ are orthogonal unit vectors lying along the x and y axis, respectively. The plane wave is associated to a quantum state on a two dimensional lattice defined by the two integers n and m. The constant p, which has the dimensions of an inverse length, defines the lattice step. To perform a QW in this space, with the polarization chosen as the coin d.o.f., we use uniform wave-plates and g-plates. The latter have been introduced in Chapter 1. They are characterized by an optic axis pattern which is a linear function of a Cartesian coordinate. If $|n,m\rangle \otimes |c\rangle$ is the state encoded by the plane wave $\exp(ip(nx+my)+ik_z z)\mathbf{c}$, where $\mathbf{c}$ is the direction of the electric field associated to the coin state $|c\rangle$, the action of a g-plate patterned, say, along the direction x is described by the operator:

$$\hat{T}_x(\delta,\alpha_0) = \cos\left(\frac{\delta}{2}\right)\hat{I} \tag{4.19}$$

$$+\, i\sin\left(\frac{\delta}{2}\right)\sum_n (\mathrm{e}^{i2\alpha_0}\hat{\mathcal{L}}_{x,+}\otimes|R\rangle\langle L| + \mathrm{e}^{-i2\alpha_0}\hat{\mathcal{L}}_{x,-}\otimes|L\rangle\langle R|), \tag{4.20}$$

where $\hat{\mathcal{L}}_{x,\pm} = |n\pm 1, m\rangle\langle n, m|$. Here we included explicitly the parameter α_0 that will reveal important for simulating an external force. This is exactly the same action of a q-plate in the OAM space. However, this new implementation allows access to an additional dimension by including in the Quantum Walk g-plates patterned along y, whose associated operator, $\hat{T}_y$, has an expression that can be obtained by replacing x with y in Eq. 4.20. Hence, with g-plates and wave-plates we can simulate both the 1D protocol, described in the previous section, and a 2D QW. In this thesis we will consider the two following protocols:

$$\hat{U}_{1D}(\delta) = \hat{T}_x(\delta)\cdot\hat{W} \tag{4.21}$$

$$\hat{U}_{2D}(\delta) = \hat{T}_y(\delta)\cdot\hat{T}_x(\delta)\cdot\hat{W}. \tag{4.22}$$

Here W is again a quarter wave plate, but protocols with different coin operators can be realized: in our setup the g-plates and the uniform wave-plates are both Liquid Crystal based devices with electrically tunable optical retardation. Hence we can modify, on demand, both the coin and shift operators. We have chosen to investigate in particular the protocols in Eqs: 4.21 and 4.22 for their interesting topological features, as we will see in the next chapter. Another protocol of interest would be the Grover walk with a two dimensional coin [176] that can be realized with the single step operator $\hat{T}_y\cdot\hat{W}\cdot\hat{T}_x\cdot\hat{W}$. This is a fundamental element for implementing the Grover search algorithm.

The experimental setup for the protocol $\hat{U}_{2D}$ is sketched in Fig. 4.5. The measurement of the probability distribution $P(n,m)$ is remarkably easy. Indeed we want to detect the intensity distribution in the transverse wavevector space $I(k_x,k_y)$ which can be obtained by Fourier transforming the field exiting the QW. This can be done in an all-optical way: the distribution $I(k_x,k_y)$ can indeed be observed in the focal plane of a converging lens. In the actual experiment the laser beam is spatially limited in the transverse plane. Hence it cannot be described by plane waves but rather by Gaussian modes. The ket $|n,m\rangle$ is therefore encoded by:

$$|n,m\rangle = G(x,y,z)\mathrm{e}^{ip(nx+my)+ik_z z},$$

where $G(x,y,z)$ is the Gaussian beam amplitude. In this case, the Fourier transformed field will show an intensity pattern consisting of regularly distributed Gaussian spots,

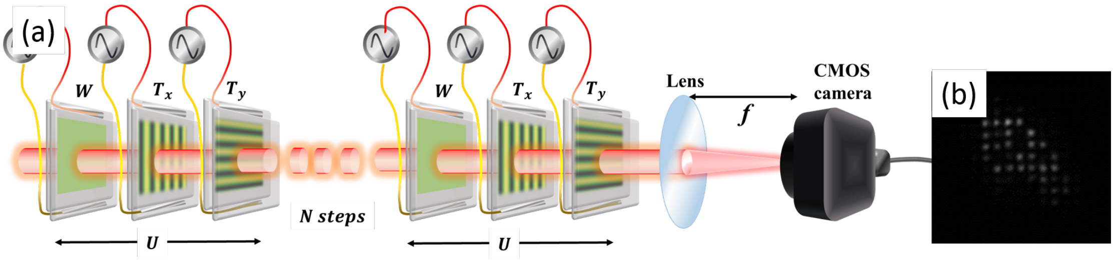

Figure 4.5: **Experimental setup for 2D QW.** The protocol $\hat{U}_{2D}$ is realized alternating a waveplate $\hat{W}$ with an g-plate patterned along the x direction, $\hat{T}_x$, and one patterned along y, $\hat{T}_y$ (panel (a)). The final probability distribution can be observed sending the outgoing beam through a converging lens. In its focal plane the Fourier transform of the beam transverse amplitude can be observed (b). The intensity pattern on this plane corresponds indeed to the desired probability distribution. Panel (b) is adapted from Ref. [38]

as shown for instance in Fig. 4.5 (b). If we place a converging lens at the end of the quantum walk, the field distribution $\tilde{G}$ in its focal plane, will correspond to the distribution of the transverse wavevector, that is:

$$\tilde{G}(X,Y;n,m) \propto \int_{\Omega} G(x,y,d)\mathrm{e}^{ip(nx+my)+ik_z z}\mathrm{e}^{i\frac{k}{f}(Xx+Yy)}dxdy, \tag{4.23}$$

where Ω is the transverse plane, d the distance of the lens from the beam waist (located at $z=0$), f the focal length of the lens, and (X,Y) the spatial coordinates in the focal plane of the lens. The intensity of the focused Gaussian beam will be:

$$\left|\tilde{G}(X,Y;n,m)\right|^2 \propto \exp\left(-2\frac{(pn-kX/f)^2+(pm-kY/f)^2}{\omega_k^2}\right), \tag{4.24}$$

with $\omega_k = 2/w_0$. Thus ω_k is a measure of the radius of the spots that appear in the focal plane. The overlap between different spots can be considered small if $p \geq 2\omega_k$. In our experiment we used g-plates with pitch $\Lambda = 5$mm and an input beam waist of the same order of magnitude: $w_0 \approx 5$mm. The overlap of adjacent modes is around 0.8%.

Extraction of the probability distributions from the intensity pattern. With the description given until now, one expects to see the result of the QW as a pattern of different Gaussian spots arranged on a regular lattice. The probability distribution of the associated quantum walk can be extracted from the relative amount of light around the lattice sites, i.e. the probability $P(n,m)$ of finding the particle on site (n,m) can be calculated normalizing the total intensity around a circular region, centered on the given site and with radius given by the spot waist. In principle, the positions on the camera corresponding to the lattice can be extracted as follows: first, all the g-plates are set at $\delta = 0$, so that a single spot appears on the camera. The spot position corresponds to the lattice origin. Then, knowing the equivalent in pixel of the lattice step size, one can

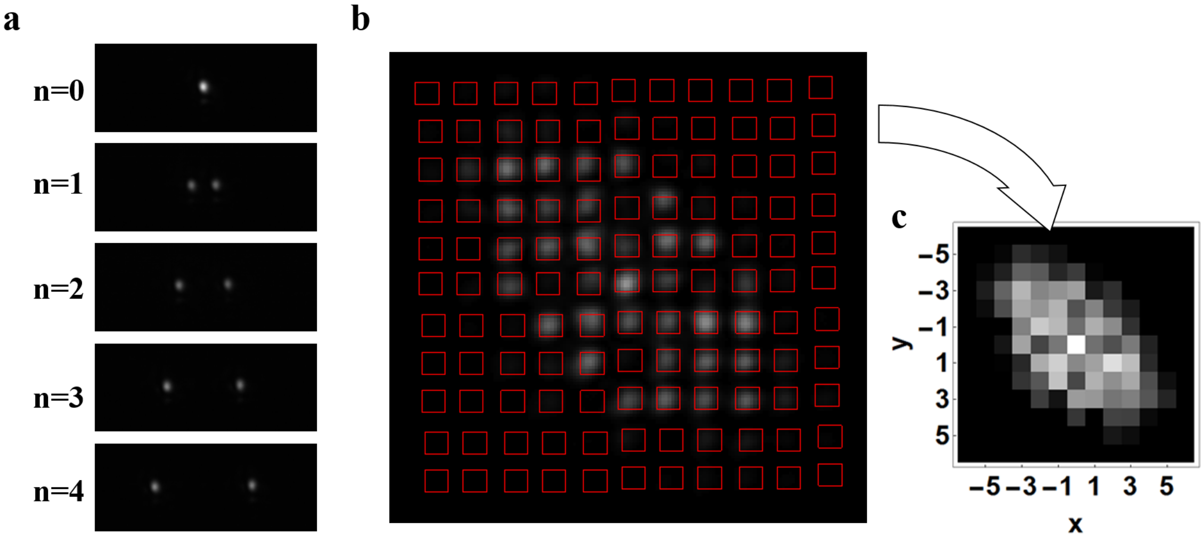

FIGURE 4.6: **Extraction of the probability distributions from the recorded intensity patterns.** **a**: Examples of the intensity patterns obtained with the "spin-momentum locking" protocol $\hat{U} = \hat{T}_x(\pi) \cdot \hat{H}_{wp}$. An input linearly polarized state is split into two spots with opposite circular polarizations. At each step these spots are shifted by a quantity corresponding to the lattice cell size. This process can be used to identify the coordinates of the lattice sites on the camera, getting rid of the experimental imperfections explained in the text. Insets **b** and **c** show the procedure used to extract the probability distributions from the intensity patterns. The red squares in **b** represent the regions over which we calculate the total intensities associated to specific lattice sites (since the single spots occupy a small number of pixels there is no substantial difference in using square or circular integration regions). Normalizing to 1 the sum of all these intensities we obtain the probability distribution (**c**).

calculate the positions of all the sites.

In practice, however, each spot can be displaced with respect to the position calculated with the above method. This can be due to a series of small experimental imperfections. One contribution can be ascribed to undesired modulations in the g-plates patterns, that can be modeled by the following local optic axis angle: $\alpha(x, y) = \alpha_0 + p/2x + \epsilon(x, y)$, where $\epsilon(x, y)$ is a small in magnitude, but unknown, function. Another cause can be a small tilt in the polarization gratings, so that the coordinate x in $\alpha(x)$ should be replaced by $x' = \cos(\theta)x + \sin(\theta)y$ (with θ small, and different for each grating). We can get rid of these effects by following a different procedure in which we measure the center of each spot and assign to it the corresponding lattice site. This procedure is simplified by employing the following quantum walk protocol. Let us first consider the 1D setup defined by the single step operator $\hat{U} = \hat{T}_x(\delta = \pi) \cdot \hat{H}_{wp}$, where $\hat{H}_{wp}$ is an half waveplate (that can be described by the operator σ_x). This protocol simulates a recently proposed system where a spin momentum locking effect has been predicted [177]. The particle dynamics, shown in Fig. 4.6 **a**, is indeed very simple: at each step the L polarized component of the state is shifted by one site along one direction (say on the left), while the R polarized component is shifted on the right. If we start with a linearly polarized input beam, in the successive steps we will see two separate spots (with opposite circular polarizations), that will be located, at the step t, on the effective positions corresponding to sites t and $-t$. In this way we reconstruct the coordinates of each site by performing Gaussian fits for the two spots. The generalization to the 2D case is straightforward, since the same protocol (performed along one transverse direction, e.g. x) can be obtained turning off ($\delta = 0$) the g-plates patterned along the perpendicular direction (e.g. y). In this way, by first turning off the T_x operators, and then operators T_y, one can obtain the coordinates of the sites $(n, 0)$ and $(0, m)$ (with n and m integers). The remaining sites can be easily found taking, for example, the set of lattice coordinates of the sites $(n, 0)$ and shifting them by quantities given by the coordinates of the sites $(0, n)$. In Fig. 4.6 **b** and **c** it is shown the result of this procedure.

4.5.2 Quantum walks with an applied external force

Until now we have considered Quantum Walks as the result of repeated applications of a fixed unitary operator over some initial state. It is however natural to ask what kind of phenomena can be observed when considering step-dependent operations. Among the most interesting effects are deviations from the ballistic behavior that can even reduce to the revival of the probability distribution or of the full quantum state [169, 178, 179]. Quantum Walks with step dependent operators can be considered as means to simulate a quantum system under the effect of a time dependent perturbation. In particular one can think of mimicking the action of an external force. These processes are named "Electric Quantum Walks" [178]. The effect of a constant force is to drive an eigenstate of the effective Hamiltonian of the unperturbed system along the Brillouin zone. Hence, after a given time, if the force is small enough to prevent interband transitions and if only one band is occupied from the beginning of the process, the system will return to its initial state. This phenomenon is known as Bloch oscillation. Revivals in QWs can be interpreted as resulting from Bloch oscillations [165]. In general, when multiple bands are occupied, Bloch oscillations can be observed only in some particular cases where the dynamical phase acquired in one cycle is a multiple of π. However refocusing can be destroyed when the applied force induces energy transfers comparable with the energy gap, resulting in interband transitions. In particular, when the energy gap becomes zero, the transition from one band to the other when crossing the Dirac point occurs with maximum probability as demonstrated by the Landau-Zener theory [180].

Applying an external force to a periodically driven system can produce phenomena that do not occur when doing the same on static systems. Remarkably, the dynamics is strongly conditioned by the force being a rational or irrational multiple of 2π (here considered as an adimensional quantity), as shown in the work of Cedzich et al. [181]. For example, localization effects, rather than pure refocusing, have been observed experimentally when applying an irrational force [178]. In our first experiments we considered rational values of the force, however we can implement any arbitrary value, as we will show below.

We can turn an ordinary QW, described by the single step unitary $\hat{U}$, into an electric one, U_E, by adding the extra operation: $\hat{F}_E = \exp(-iF\hat{x}\Delta T)$. Here $\hat{x}$ is the lattice position operator (expressed in adimensional units) and ΔT the time duration of a single step, that we conventionally put equal to 1. The parameter F is the force in adimensional units. It can be associated to an electric field E acting on an electron (whit charge e) using the formal definition $F = eE/\hbar$. Thus the electric quantum walk is described by the process:

$$\hat{U}_E = \hat{F}_E \hat{U}. \tag{4.25}$$

We can rewrite Eq. 4.25 in the quasimomentum space representation by using the property: $\hat{x} = -i\partial/\partial k$. Indeed this implies that the action of $\hat{F}_E$ on a quasimomentum eigenstate $|q\rangle$ is a translation by an amount F in the Brillouin zone: $\hat{F}_E|q\rangle = |q - F\rangle$. Thus Eq. 4.25 reads:

$$\hat{U}_E = \int_{BZ} \frac{dq}{2\pi} \mathcal{U}(q + F) \otimes |q\rangle\langle q|, \tag{4.26}$$

where $\mathcal{U}$ is the action of $\hat{U}$ in Fourier space. Hence the external driving force acts, at every step, as a traslation by F of $\mathcal{U}$: $\mathcal{U}(q) \to \mathcal{U}(q + F)$. The Fourier space unitary corresponding to an N-step electric QW is: $\mathcal{U}(q + NF) \ldots \mathcal{U}(q + F)$.

We now show how refocusing effects can arise in electric quantum walks. We consider a two level system in order to understand also which are the contributions leading to interband transitions. Let $|u_\pm(q)\rangle$ be the eigenstates of the effective Hamiltonian in absence of the external force, with corresponding energies $E_\pm(q)$. The initial state can be written in the general form:

$$|\psi_0\rangle = \int_{-\pi}^{\pi} \frac{dq}{2\pi} \big(c_+(q)|u_+(q)\rangle + c_-(q)|u_-(q)\rangle\big) \otimes |q\rangle. \tag{4.27}$$

Depending on the explicit expression of $c_\pm(q)$ one can have localized or delocalized states. We now consider the action of $\mathcal{U}(q + F)$ on $|u_\pm(q)\rangle$ for small values of F. Expanding up to the first order around $q+F$ we have:

$$\begin{aligned}\mathcal{U}(q+F)|u_\pm(q)\rangle \approx\, & \mathrm{e}^{-iE_\pm(q+F)}|u_\pm(q+F)\rangle \\ & - F\mathrm{e}^{-iE_\pm(q+F)}\langle u_\pm(q+F)|\partial_q u_\pm(q+F)\rangle|u_\pm(q+F)\rangle \\ & - F\mathrm{e}^{-iE_\mp(q+F)}\langle u_\mp(q+F)|\partial_q u_\pm(q+F)\rangle|u_\mp(q+F)\rangle. \end{aligned} \tag{4.28}$$

The first line represents the adiabatic contribution. The second and third line are non-adiabatic terms. The second line in a non-adiabatic contribution that is related to the rapidity of variation of the eigenstates along the Brillouin zone. This contribution does not induces a transition to the other band. The third line, instead, takes into account the interband transitions. Next we neglect the non-adiabatic terms retaining only the first line of Eq. 4.28. In this approximation, after the the first step, we obtain the state:

$$|\psi_1\rangle = \hat{U}_E|\psi_0\rangle = \int_{-\pi}^{\pi}\frac{dq}{2\pi}\big(c_+(q)e^{-iE_+(q+F)}|u_+(q+F)\rangle + c_-(q)e^{-iE_-(q+F)}|u_-(q+F)\rangle\big)\otimes|q\rangle. \tag{4.29}$$

Suppose now that after N steps we have $q+NF = q\,\mathrm{mod}2\pi$, i.e. the BZ has been traversed by the particle eigenstates in N steps. In the adiabatic approximation we have:

$$|\psi_N\rangle = \hat{U}_E|\psi_0\rangle = \int_{-\pi}^{\pi}\frac{dq}{2\pi}\big(c_+(q)e^{-i\gamma_+}|u_+(q)\rangle + c_-(q)e^{-i\gamma_-}|u_-(q)\rangle\big)\otimes|q\rangle. \tag{4.30}$$

where

$$\gamma_\pm = \sum_{j=0}^{(2\pi/F-1)} E_\pm(q+jF), \tag{4.31}$$

are the dynamical phases acquired by the system eigenstates when traversing the whole Brillouin zone. These phases are independent of k, hence they can be factored out from the integrals. Therefore, in case one single band has been occupied from the beginning, the final state is coincident with the initial one, apart from a global phase factor. In this case the QW consists in a dynamical process where every N steps we find the same quantum state. When the system is prepared in a state that occupies both bands, refocusing can be observed only in some cases, when the difference between the dynamical phases is a multiple of 2π. In general the final state will be different because of the additional relative phase acquired by the states over the two bands. In particular, when $\gamma_+ - \gamma_- = \pi$, the final state is orthogonal to the initial one. Non-adiabatic effects have consequences on the long time dynamics. Indeed, for rational values of F one can consider the N-step process as a single step of a quantum walk without external force. This QW will show ballistic dynamics on the long time scale arising from the accumulation of the small non-adiabatic contributions [181] In Eq. 4.30 we have also ignored the effects of the geometric phase acquired during the cycle. Geometric phases appear as an additional contribution to the global phase acquired by a system after a cyclic adiabatic evolution as a consequence of some global feature of the system. We will consider them in more detail in the next chapter due to their fundamental importance for the study of topological phenomena. Actually, Bloch oscillations can be used as a tool to measure the geometric phase of a quantum system, as showed in Refs: [165, 182].

Experimental implementation of electric Quantum Walks We can easily realize electric QWs in the two photonic implementations presented in this chapter. As we now show, there is not even need to add any optical device to the ones required in the case without force. We will explicitly refer to the quantum walk implementation in transverse momentum space, although the results for the QW in OAM space are the same.

The transverse plane of the physical space where the QW is performed actually encodes the quasi-momentum space of the abstract protocol that we want to simulate. Hence a traslation on this plane must be interpreted as a shift in the Brillouin zone: the transformation $\mathcal{U}(q) \to \mathcal{U}(q+F)$ where q is identified with, say, the x coordinate, correspond to translating along x the g-plate of an amount proportional to F (obviously, the quarter-wave-plates, being uniform, can be left in their original position). We have seen that the transverse translation of a single g-plates correspond to a redefinition of the origin of the reference frame, or, equivalently, to a change in the value of α_0. Indeed, as shown in Ref. [38], it is easy to verify that:

$$\mathcal{U}(q+jF) = \mathcal{T}_x(\delta, \alpha_0 + jF/2) \cdot \mathcal{W}, \tag{4.32}$$

where $\mathcal{T}_x$ and $\mathcal{W}$ are the Jones matrices of the g-plate and the quarter-wave plate. A similar result holds for the 2D protocol where, by shifting independently the positions of $\mathcal{T}_x$ and $\mathcal{T}_y$ one can mimic external fields of arbitrary strength and direction.

Our ability to tune the energy band dispersions allows us to consider different regimes and to explore the interplay between Bloch oscillations and Landau-Zener transitions. We considered in particular the protocol $U_{1D}(\delta)$, where, when $\delta = \pi$, we have indeed that, if $F = 2\pi/2l$, with l integer, (i.e. the Brillouin zone is fully explored in a even number of steps), $\gamma_+ - \gamma_- = 2\pi$. If, otherwise, $F = 2\pi/(2l+1)$, then $\gamma_+ - \gamma_- = \pi$. Hence in both cases, if adiabatic theory holds, we expect a revival of the probability distributions. When $F = 2\pi/2l$ the revival corresponds to a full refocusing of the quantum state, i.e. the polarization of the final state is the same of the polarization of the initial state. On the other hand, if $F = 2\pi/(2l+1)$, after a full cycle (that is a number of steps $N = 2\pi/F$) the particle will be in a state orthogonal to the initial one, i.e. with the same probability distribution of the initial state but with opposite polarization. Moreover this result should be independent from the initial state. When we consider, instead, $\delta = \pi/2$, Bloch oscillations are suppressed due to the closing of the energy gap at $q = \pi$. This implies that, when the initial state is prepared in an eigenstate of the unperturbed ($F = 0$) Hamiltonian, it experiences a Landau-Zener transition to the other band when crossing the Dirac point. Thus after one cycle we will not have the same state, but one lying on the other band. Interestingly, if a second cycle is performed, the particle will again cross the Dirac point and turn back on the initial energy band. As a consequence we expect a refocusing after a number of steps $N = 4\pi/F$. In Fig. 4.7 we validate these predictions by carrying some computer simulations. These consideration are based on the assumption that adiabatic approximation holds, at least in points of the BZ away from the gap closing. However deviation from perfect refocusing at $\delta = \pi$ are still observed due to the discrete time nature of the process. A stronger force means that the refocusing should happen in a smaller number of steps. But this implies that the discreteness of time becomes more relevant in this cases. To show this we carried simulations for decreasing values of the force. In particular, as shown in Fig. 4.8 we calculated the refocusing fidelity, $RF = |\langle\psi_0|\psi_N\rangle|^2$, as a function of the number of cycles for the different values of the force. Fig. 4.8 (a) clearly shows that the smaller the force the higher is the RF.

4.5.3 Experimental results

In this section we show some experimental results for the protocols $\hat{U}_{1D}$ and $\hat{U}_{2D}$, showing the evolution of initially localized states. We then show how to prepare initial states which are delocalized, and how to use them to probe the group velocity dispersion.

1D Protocol. We realized a 1D QW of 10 steps, carrying experiments for $\delta = \pi$ and $\pi/2$ with and without an external force $F = \pi/5$. The value of F has been chosen in order to observe a single Bloch oscillation after 10 steps. In Fig. 4.9 we present our data when the initial state is $|H, n = 0\rangle = (|R, 0\rangle + |L, 0\rangle)/\sqrt{2}$. The effect of a constant force in the x direction is simulated by shifting the g-plate at the time-step t of the amount $\Delta x_t = t\,\Lambda/10$. In panel (a) and (c) we show the data for a walk with no force, when $\delta = \pi/2$ and $\delta = \pi$, respectively. Panel (b) and (d) contain the walker distribution for the same configuration of δ, when $F = \pi/5$. All data are in good agreement with numerical predictions. Here and in the following, we quantify the overlap between experimental and numerical results by computing the similarity $\mathcal{S} \in [0, 1]$ of the two distributions, which is maximum for two identical distributions and diminishes when differences increase. Let $E(n)$ and $Th(n)$ be the experimental and theoretical

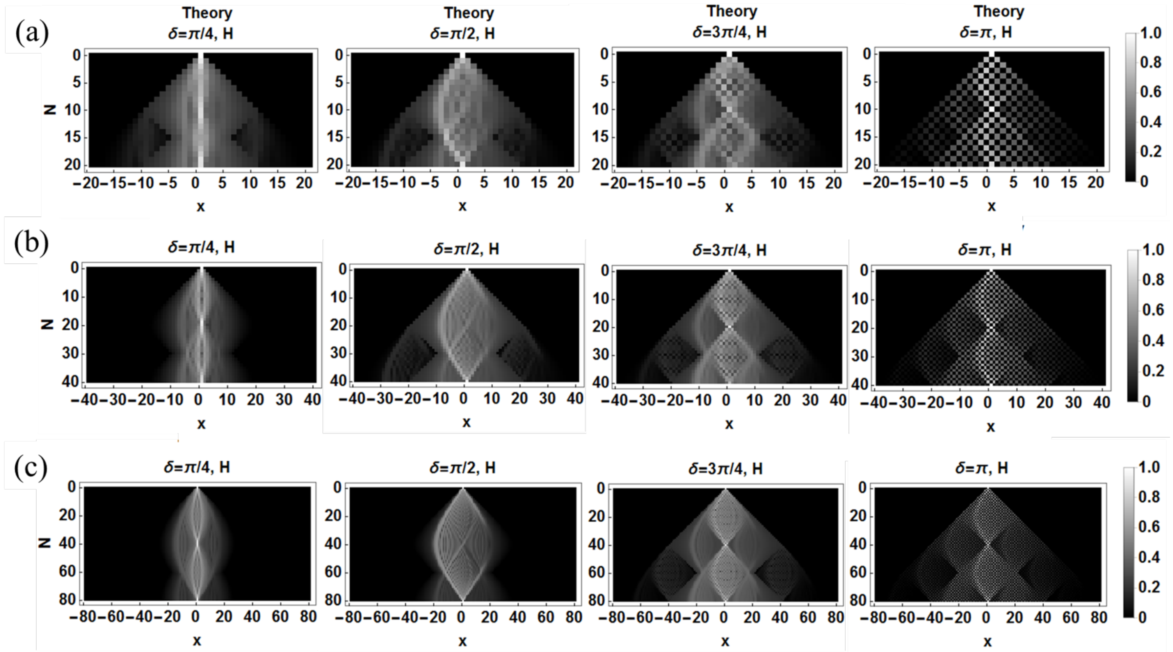

FIGURE 4.7: **Simulations of electric quantum walks for different δs and with decreasing force strength.** Here we show theoretical simulations of forced quantum walks with: (a), $F = \pi/5$, (b), $F = \pi/10$, (c), $F = \pi/20$. The simulations are carried for a number of steps given by $4\pi/F$ at different values of δ (which corresponds to an eigenstate spanning two times the Brillouin zone). The qualitative behavior looks independent on the ratio between force strength and step number, only at $\delta = \pi/2$ we can notice a suppression of the distribution tails when F becomes smaller. In general we can observe oscillating behavior on two characteristic periods. At $\delta = \pi$ and $\delta \leq \pi/4$ there is approximate refocusing every $2\pi/F$ steps, which is the expected period of Bloch oscillations. At $\delta = \pi/2$ the period of oscillations is doubled. In this situation the energy gap closes at $q = 0$ which implies a probability equal to one of Landau-Zener transitions (in the adiabatic limit, e.g. the limit $F \rightarrow 0$). Notice that in the observed period ($4\pi/F$) a particle prepared into an eigenstate of $H_{eff}(q)$ explores two times the Brillouin zone, thus experiencing a double Landau-Zener transition. At intermediate δs (for example $\delta = 3\pi/4$) both contribution are present, as it appears in the figures.

distributions, respectively. The Similarity is defined as:

$$\mathcal{S} = \frac{\sum_n E(n)Th(n)}{\sqrt{\sum_n E(n)^2}\sqrt{\sum_n T(n)^2}}. \tag{4.33}$$

We observe an almost complete refocusing of the quantum state only when $\delta = \pi$ (panel (d)), independently of the initial polarization (results for different input states are shown in Figs. 4.10,4.11). The existence of small contributions from other lattice sites is caused by non-adiabatic effects, as discussed before. Besides being mostly localized at $x = 0$, the final state is expected to have the same polarization of the input beam. In the experiment we were able to measure the refocusing fidelity after 10 steps for the case $F = \pi/5$ and $\delta = \pi$. Even if we did not reconstruct the full quantum state of the final step (since measuring the relative phases would require more complex interferometric

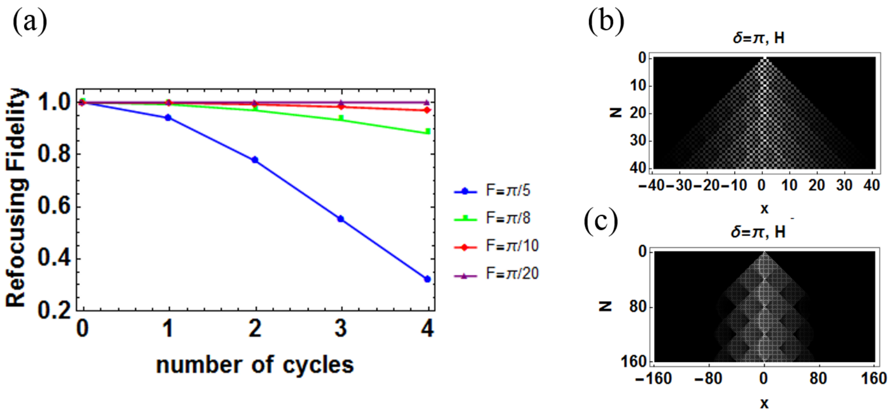

FIGURE 4.8: **Refocusing fidelity after more cycles.** Here we show that by decreasing F the refocusing of the quantum state after several cycles for $\delta = \pi$ (one cycle correspond to $2\pi/F$ steps) is actually enhanced. In panel (a), we show how the refocusing fidelity RF scales after four cycles for different values of F. We observe that, as expected, the refocusing is higher for smaller values of F. This should be a consequence of the suppression of non-adiabatic effects. Panels (c) and (d) show the probability distributions for, respectively, $F = \pi/5$ and $F = \pi/20$. While in panel **c** the Bloch oscillations are rapidly destroyed after few cycles, they persist in the other case (**d**).

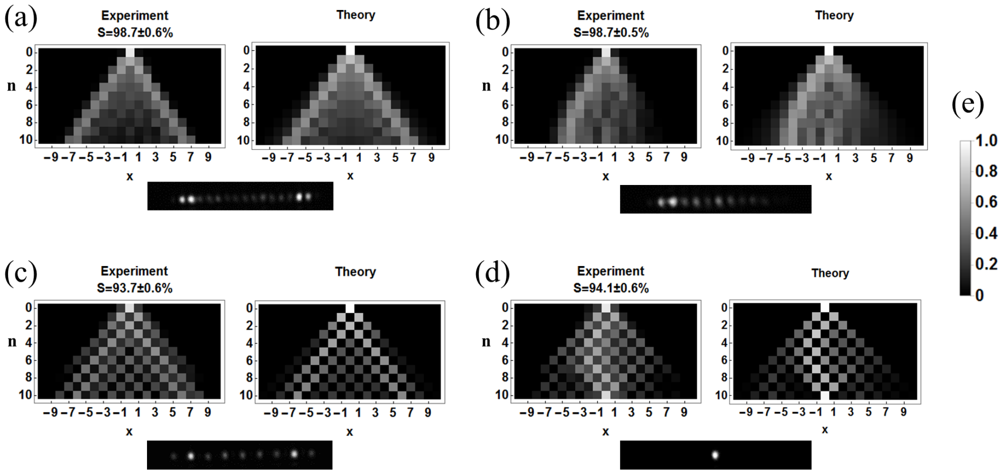

FIGURE 4.9: **Quantum walks on a line with and without a constant force.** We show the experimental and numerical probability distributions of 10 steps quantum walks with an input state $|H, 0\rangle$. (a-b), distributions at $\delta = \pi/2$ with (a) $F = 0$ and (b) $F = \pi/5$. (c-d), distributions at $\delta = \pi$ with (c) $F = 0$ and (d) $F = \pi/5$. Panel (e) shows the color scale used in all the plots. In panel (d) an almost complete refocusing of the initial state is observed, while this does not happen at $\delta = \pi/2$ due to Landau-Zener transitions. All the insets show the experimental intensity patterns on the focal plane after the 10-nth step. For each step we calculated the similarity between the theoretical and experimental distribution. In the figure we report the average similarities over all the steps. All experiments are repeated four times, after re-aligning all plates to take into account possible errors associated with this procedure. Uncertainties represent the standard errors.

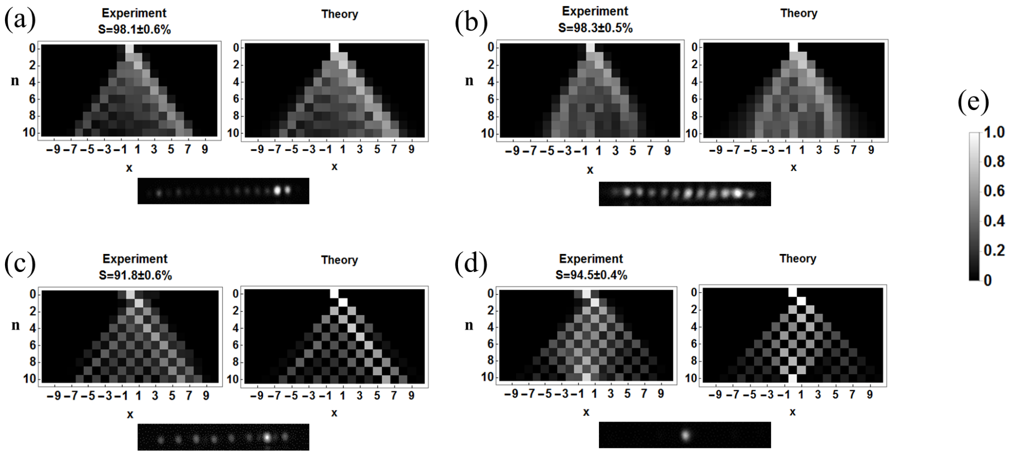

FIGURE 4.10: **1D DTQW for input polarization $|A\rangle$.** Calculated and measured probability distributions of 10 steps quantum walks with an input state $|A,0\rangle = (|R,0\rangle + i|L,0\rangle)/\sqrt{2}$. (a-b), Distributions at $\delta = \pi/2$ with (a) $F = 0$ and (b) $F = \pi/5$. **c-d**, Distributions at $\delta = \pi$ with (c) $F = 0$ and (d) $F = \pi/5$.

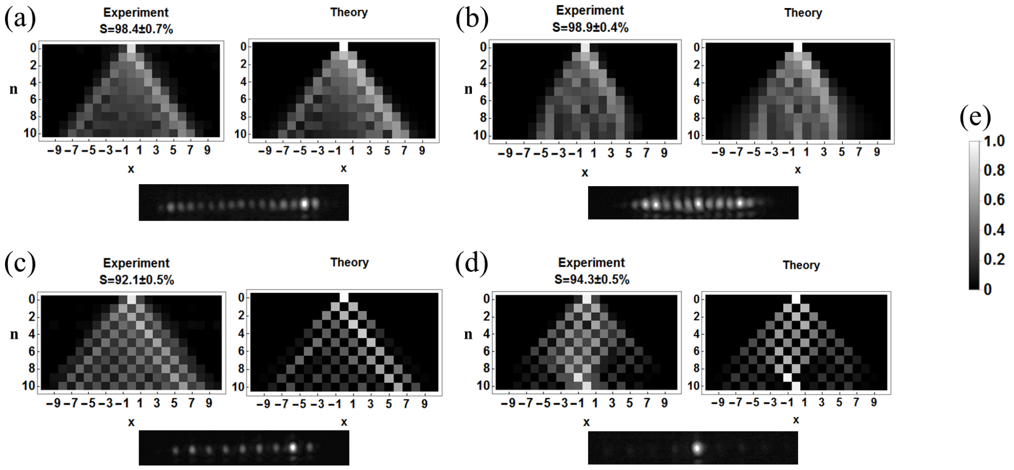

FIGURE 4.11: **1D DTQW for input polarization $|L\rangle$.** Calculated and measured probability distributions of 10 steps quantum walks with an input state $|L,0\rangle$. (a-b), Distributions at $\delta = \pi/2$ with (a) $F = 0$ and (b) $F = \pi/5$. (c-d), Distributions at $\delta = \pi$ with (c) $F = 0$ and (d) $F = \pi/5$.

setups), this is not needed to measure the fidelity with a reference state localized in a single lattice site. Indeed, let $|\psi_0\rangle = |\phi_0, n = 0\rangle$ be the initial state (with ϕ_0 representing the polarization state) and $|\psi_f\rangle = \sum_n c_n |\phi_{f,n}, n\rangle$ the general form of the final state. The fidelity between the two states is:

$$RF = |\langle\psi_0|\psi_f\rangle|^2 = |c_0\langle\phi_0|\phi_{f,0}\rangle|^2 = P_f(0)R_{pol}, \tag{4.34}$$

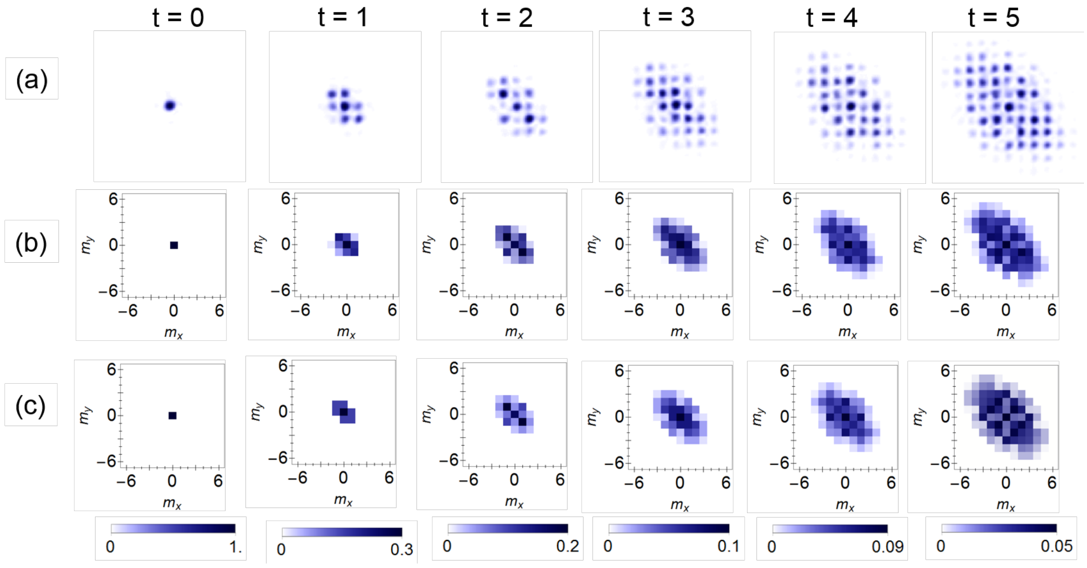

FIGURE 4.12: **2D Quantum Walk on a square lattice.** We implemented a 5 steps of the process $\hat{U}_{2D}$ with $\delta = \pi/2$ and input state $|H, 0, 0\rangle$. All experiments are repeated four times, after re-aligning all plates to take into account possible errors associated with this procedure. Uncertainties represent the standard errors. In (a), we show examples of the intensity patterns on the focal plane. The probability distributions (b) are obtained from these images measuring the relative intensity of the single spots. In (c) we show the theoretical results. Picture adapted from Ref. [38].

where $P_f(0) = |c_0|^2$ is the probability to find the particle in site $m = 0$ in any polarization state, and $R_{pol} = |\langle\phi_0|\phi_{f,0}\rangle|^2$ the probability that the central spot has the same polarization of the initial state. We obtained experimentally $RF = 83 \pm 2.6\%$ while the theoretical refocusing is 93%. The discrepancy is due to experimental imperfections, however we point out that the polarization of the central spot is the same of the initial state since $R_{pol} = 99.1 \pm 0.01\%$ in agreement with the theory. At $\delta = \pi/2$, no refocusing is observed. In this case, the quasi-energy spectrum of the effective Hamiltonian exhibits a gap closing at the center of the Brillouin zone. This gives rise to interband Landau Zener transitions that destroy the refocusing effect (Fig.4.9(b)).

2D protocol: localized initial state. By exploiting the possibility of moving the walker along both x and y directions of the transverse wave-vector space, we demonstrate a discrete time QW on 2D squared lattice, with a 2-level coin.

Our 2D protocol consists in the step operator U_{2D} of Eq. 4.22, made of a quarter-wave plate W, and two g-plates T_x and T_y, characterized by the same retardation δ. In Fig. 4.12 we show representative data regarding the dynamical evolution of a localized input state, up to 5 timesteps. Starting from the first steps, the walker distribution remains concentrated along the diagonal $x = -y$, as a consequence of the absence of the coin rotation between T_x and T_y. Distributions obtained for different choices of the coin input state are reported in Figs. 4.13,4.14.

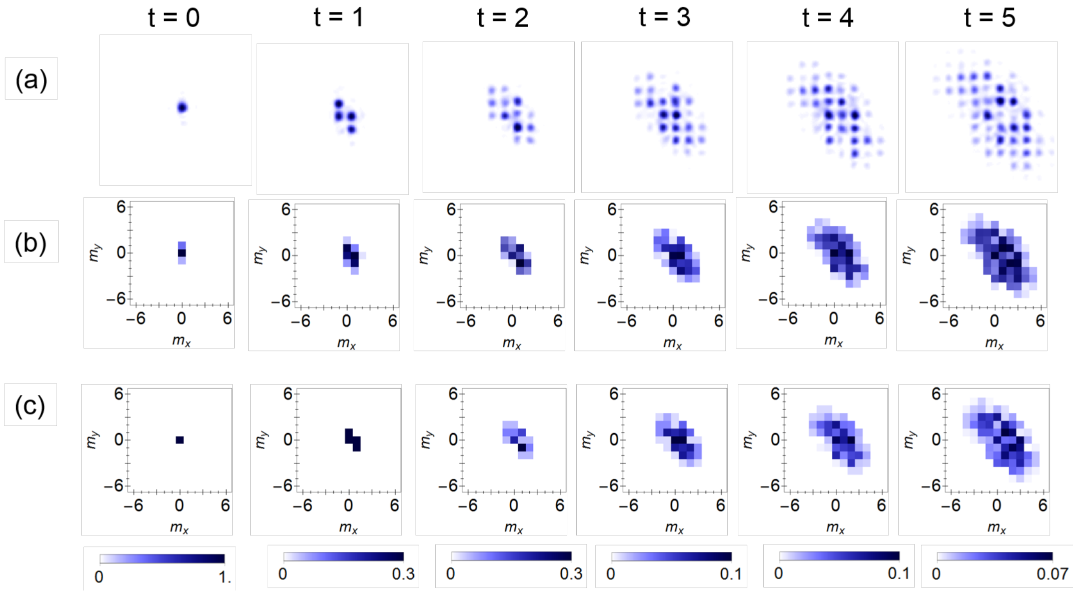

FIGURE 4.13: **2D DTQW for input polarization $|A\rangle$.** We show the theoretical and experimental probability distributions of the 2D quantum walk protocol introduced in the main text. We implemented a 5 steps process with $\delta = \pi/2$ and input state $|A, 0, 0\rangle$. In (a), we show examples of the intensity patterns on the focal plane. The probability distributions (b) are obtained from these images measuring the relative intensity of the single spots. In (c) we show the theoretical results. Picture adapted from Ref. [38].

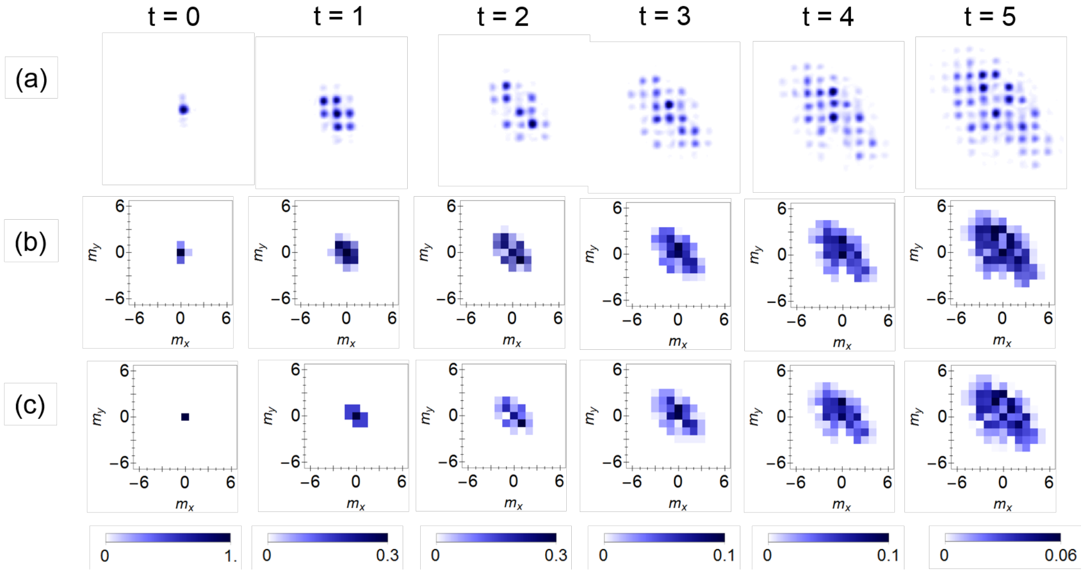

FIGURE 4.14: **2D DTQW for input polarization $|R\rangle$.** We show the theoretical and experimental probability distributions of the 2D quantum walk protocol introduced in the main text. We implemented a 5 steps process with $\delta = \pi/2$ and input state $|R, 0, 0\rangle$. In (a), we show examples of the intensity patterns on the focal plane. The probability distributions (b) are obtained from these images measuring the relative intensity of the single spots. In (c) we show the theoretical results. Picture adapted from Ref. [38].

Preparing Gaussian wavepackets By adjusting the shape of the input beam we can easily prepare initial states that are spread over many lattice sites. An important example is that of Gaussian wavepackets that are sharply peaked around a specific quasi-momentum $\mathbf{q}$, with a polarization state $|\phi_s(\mathbf{q})\rangle$. In the following we refer to these states as $|\tilde{q}_s\rangle = |G(\mathbf{q}), \phi_s(\mathbf{q})\rangle$, where $s \in \{1, 2\}$ is the band index. These provide good approximations of the system eigenstates $|\mathbf{q}, \phi_s(\mathbf{q})\rangle$, whose spatial part is a plane wave with quasi-momentum $\mathbf{q}$, and are expected to propagate by preserving their Gaussian envelope, with a dynamics dictated by the group velocity dispersion [84].

A Gaussian wavepacket of width w, peaked around the quasi-momentum $\mathbf{q}_0$ and with uniform polarization corresponding to the coin eigenstate in $\mathbf{q}_0$, $|\phi_s(\mathbf{q}_0)\rangle$, has the explicit expression:

$$|G(\mathbf{q}_0), \phi_s(\mathbf{q}_0)\rangle = \mathcal{N} \int_{BZ} \frac{d^2\mathbf{q}}{4\pi^2} \mathrm{e}^{\left(-\frac{(\mathbf{q}-\mathbf{q}_0)^2}{w}\right)} |\mathbf{q}, \phi_s(\mathbf{q}_0)\rangle, \tag{4.35}$$

where $\mathcal{N}$ is a normalization factor and $BZ = \{-\pi < q_x < \pi, -\pi < q_y < \pi\}$ is the Brillouin zone. In lattice space the above expression reads:

$$|G(\mathbf{q}_0), \phi_s(\mathbf{q}_0)\rangle = \mathcal{N}_1 \sum_{n,m} \mathrm{e}^{-w^2(n^2+m^2)/4+i(q_{0x}n+q_{0y}m)} |n, m, \phi_s(\mathbf{q}_0)\rangle. \tag{4.36}$$

Where n, m are integers denoting the position in lattice space. In our implementation we can obtain a good approximation of such a state as follows. We recall that the physical transverse space in which the QW is experimentally realized corresponds to the space of the quasi-momentum $\mathbf{q}$. Hence the input beam waist determines which region in the $\mathbf{q}$-space is occupied by the initial state. If all the $\mathbf{q} \in BZ$ are occupied, i.e. if the beam has a waist diameter of order Λ, this will correspond to a localized state. Therefore, decreasing the beam waist only a subset of the BZ, given approximately by $2w_0/\Lambda$, will be occupied. Now it remains to determine experimentally the value of $\mathbf{q}_0$. This can be simply done displacing the beam axis in a position corresponding to $(q_x, q_y) \bmod \Lambda$. We remark that, in order to do this, the value of α_0 in the QW protocol should be set a-priori (which can always be done redefining the origin of the reference frame). Then, the coin state $|\phi_s(\mathbf{q}_0)\rangle$ is selected with a standard set of wave plates.

With this approach we prepare a state whose Fourier transform is still a single Gaussian that, even if overlapping with Eq. 4.36, occupies points in space which do not correspond to any site in the walker space. However this does not alter the results presented in the main text. Indeed the modes of the initial state with wavevectors that do not belong to the lattice will never superimpose with the ones belonging to it, since the quantum walk modifies transverse wavevectors by quantities which are multiple of the lattice step p. See also the discussion about QW with non-orthogonal states in Ref. [183].

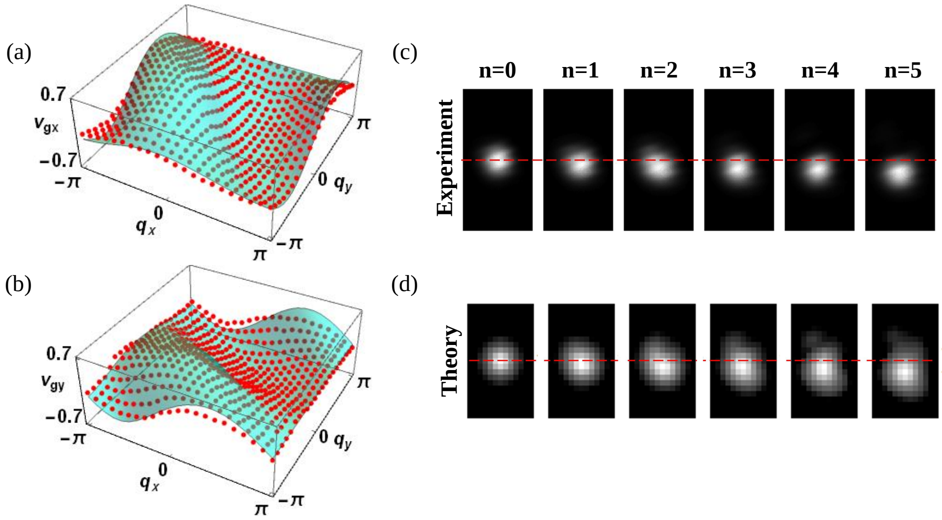

FIGURE 4.15: **Detection of the group velocity dispersion of U_{2D}.** We report the detected group velocity components, v_{gx} (a) and v_{gy} (b), for 22×22 values of the quasi-momentum in the 2D Brillouin zone, measured with a linear fit of the center of mass displacement of the corresponding wavepackets $\widetilde{q}_1$. Red points are the experimental data, whose size corresponds to the average standard error extracted from the linear fits. Cyan surfaces represent the theoretical plots. (c) Representative trajectories for wavepackets with $\mathbf{q} = (\pi/2, \pi)$ where the coin eigenstate is circularly polarized (here we chose the right circular polarization). Data are from Ref. [38]

In the experiment we realize such states by preparing an input beam whose waist is small (compared to the period Λ), and aligning it so that its central position is $\mathbf{r} = \mathbf{q}\Lambda/2\pi$. The sequence of plates yielding the QW evolution is mounted on a x-y translation stage, synchronized with motors that rotate the wave-plates at the walk entrance, so that the central position of the wavepackets (that is their momentum) and their overall polarization can be changed dynamically.

Following the dynamical evolution of Gaussian wavepackets provides a convenient approach for the detection of the system group velocity dispersion, as already demonstrated in 1D in Ref. [174]. In Fig. 4.15(a), we report the group velocity of the lower band of our QW, for 22 values of q_x and q_y (244 states in total) uniformly distributed in the entire Brillouin zone. This has been measured by detecting the displacement of the center of mass $\langle \mathbf{r} \rangle(t)$ of each wavepacket as a function of the time-step t (up to t=5), which is expected to follow the simple law of motion $\langle \mathbf{r} \rangle(t) = \mathbf{v_g}(\mathbf{q})t$. Plotted values are determined after a linear fit of the detected displacements. Some examples of measured trajectories are reported in Fig. 4.15(b).

Chapter 5

Exploring topological phases with structured light

5.1 Introduction

Topology is the study of mathematical properties that are invariant under smooth deformations [184]. This abstract mathematical topic has revealed itself as a powerful tool to understand many physical phenomena. In particular, topological methods have been employed to study phases of matter that could not be described by the traditional Landau-Ginzburg theory [185]. The latter proved itself as a successful theory for understanding phase transitions associated with symmetry breaking in systems described by *local* order parameters. However, the discovery of the integer and fractional Hall effects provided examples of phases of matter that could not be described by a local order parameter but characterized by a more general *global* feature. Topological phases of matter have been identified in strongly interacting systems, like Fractional Quantum Hall (FQH) systems [186], but also, surprisingly, in non interacting insulators. Indeed topology has played in the past decades a fundamental role in reformulating the band theory of crystals [187]. The pioneering works of Thouless, Kohmoto, Nightingale and den Nijs [188] showed that the Hall conductance in the Quantum Hall Effect (QHE), which is quantized as a multiple of the quantum of conductance, is proportional to the Chern number of the occupied energy bands. The Chern number is an example of a topological invariant, a mathematical object that can be used to classify different topological phases. The phenomenon of conductance quantization was discovered experimentally by von Kiltzing in 1980 [189] and used to determine with high accuracy the fine structure constant. Moreover, the discovery of QHE paved the way for the study of other crystalline structures exhibiting non-trivial topological phases. The research was motivated by the observation that topological insulators should host robust edge states, i.e. states confined at the boundary of the system and that cannot be moved into the bulk by smooth perturbations (at least without destroying the possible symmetries defining the topological phase). Hence one can have intriguing phenomena like solitons in 1D polyacetylene chains [190], edge charge and spin currents circulating without dissipation [191–193], electric polarization induced by magnetic fields (demonstrated in 3D topological insulators) [193, 194] and Majorana fermions in topological superconductors [187, 193]. The existence of protected edge modes has suggested their use for quantum computation, for these modes should be resilient against external disturbances and decoherence effects. This idea has given birth to the new field of *topological quantum computation* [195, 196].

Remarkably, the topological band theory developed for crystalline insulators can be equally applied to periodically structures where the “wave particle” is not an electron but, for example, a photon or a phonon. Hence, thanks to the increasing capabilities in material structuring, in recent years there have been growing efforts in developing topological photonic and phononic crystals, i.e. systems with a spatial periodicity in the refractive index, or in the sound speed, where the associated frequency bands exhibit nontrivial topology [197–200]. These systems can be useful in a variety of applications, since they allow for guiding light or acoustic waves without back-scattering. Topological phases have also been observed in superconductors [201], atoms [202] and even mechanical systems [203].

Turning back to crystalline topological insulators, it has emerged that finding materials exhibiting non-trivial topology is not an easy task. In Ref: [204] a new method was suggested for obtaining topological insulators by perturbing a trivial system (a graphene layer) with an external field periodic in time. Indeed periodically driven systems, also called Floquet systems, can exhibit richer topological features as a consequence of the fact that the energy becomes a periodic quantity (the *quasi-energy*). These results stimulated researchers for a deeper understanding of the theory of these systems, in particular for the definition of more general topological invariants [205, 206] and for the search of new experimental platforms [207]. Discrete Time Quantum Walks are a paradigmatic example of Floquet systems and, indeed, an ideal platform where to study the connections between topology, dynamics and non-equilibrium physics [95, 114, 159, 175].

In this chapter we will introduce some fundamentals of the theory of topological insulators, in both the static and periodically driven frameworks, and investigate the topological properties of the quantum walk protocols $\hat{U}_{1D}$ and $\hat{U}_{2D}$ introduced in Chapter 4. For the 1D case we will introduce a new observable, called *chiral displacement*, that allows to distinguish, by means of bulk measurements, between different topological phases and to infer the value of the corresponding topological invariant. We will show the experimental results obtained with the platform employing the OAM of light.

We will then explore the topological phase diagram of the 2D case. The effect of the nontrivial topology on the dynamics of the particle subjected to an external force will be investigated. Therefore, we will report the experimental observation of a drift of the average position of the ground state in the direction perpendicular to the applied force, an effect that can be directly ascribed to the non-trivial Chern number of the system.

5.2 Topological Invariants and Geometric Phases

Topology can be regarded as a generalization of Euclideian geometry where different geometrical structures can be considered equivalent, if they can be continuously deformed into one another [184]. As such, topology can be regarded as the study of continuity. Objects that can transform continuously into one another form equivalence classes that can be distinguished in terms of a mathematical object, called *topological invariant*. The nature of a topological invariant depends on the problem of interest: it can be an integer, as the number of holes in a closed surface, or can be a specific property of a topological space, like compactness, or even an entire mathematical structure, such as an homotopy group [184]. Indeed, a topological invariant is any feature that remains unchanged under smooth infinitesimal transformations.

We give a mathematical example to better clarify the idea. Consider the set of all closed curves defined on $\mathcal{P} = \mathbb{R}^2 - \{(0,0)\}$, i.e. a plane with an hole in the origin. Then we can distinguish the closed curves on $\mathcal{P}$ in various equivalence classes: there are loops that do not enclose the origin and loops that enclose the origin one time, or an integer number of times (this is possible because we can consider also self intersecting curves). Curves belonging to the first class can be continuously shrunk to a point, while curves enclosing the origin cannot. A curve that does not contain the origin cannot be smoothly deformed into one containing it. Each equivalence class can be identified by an integer number, that is the number of times the curve wraps around the origin. This number is a topological invariant, called *winding number*. We have already used the concept of winding number in the first chapters of this Thesis. For example, the winding number associated to a polarization singularity was defined as the number of times that the orientation θ of the polarization ellipse changes by 2π in a loop around the singularity (see Chapter 3). If, instead, θ is the phase of a scalar optical beam, then the winding number gives the amount of OAM in units of $\hbar$ (Chapter 1). Still, in this chapter we will introduce a winding number associated to the eigenstates of a topological insulator. In the study of topological insulators there is another object playing a fundamental role, that is indeed of fundamental importance for defining some topological invariants. This object, called *Berry phase* was introduced investigating cyclic adiabatic evolution in quantum systems. Next we proceed to a description of this concept that will be of fundamental importance as we go on through the Chapter.

In 1984, M.V. Berry [208] demonstrated that when a quantum system is subjected to a cyclic adiabatic evolution it will acquire a global phase that, in general, is not only given by the dynamical phase, but also by an additional geometric contribution. The latter, known as Berry phase or geometric phase, is of physical importance since it cannot be deleted by a suitable gauge transformation. Indeed, some intriguing physical phenomena, like the Aharonov-Bohm effect, can be understood in terms of the Berry phase [208]. Later it turned out that some of the assumptions that led to the discovery of geometric phases were not necessary. The geometric phase concept was anticipated by Pancharatnam in 1956 under more general hypotheses [209]. Pancharatnam proposed an operational criterion to establish when two polarized beams can be considered "in phase". In doing this he actually found that a geometric phase appears even when considering processes which are not adiabatic, nor unitary or cyclic.

Here we derive the Berry phase in the specific framework of quantum systems which are symmetric under discrete translations. For these systems, Bloch theorem states that the eigenstates, $|\psi_{i,\mathbf{q}}(\mathbf{r})\rangle$, of the Hamiltonian, $\hat{H}$, are plane waves with momentum $\mathbf{q}$ modulated by functions which are spatially periodic, with a period given by the lattice translation vector $\mathbf{R}$:

$$|\psi_{i,\mathbf{q}}(\mathbf{r})\rangle = \mathrm{e}^{i\mathbf{q}\cdot\mathbf{r}}|u_i(\mathbf{q},\mathbf{r})\rangle, \tag{5.1}$$

$$|u_i(\mathbf{q},\mathbf{r})\rangle = |u_i(\mathbf{q},\mathbf{r}+\mathbf{R})\rangle, \tag{5.2}$$

where the index i takes into account the presence of other degrees of freedom (like spin). Since $\mathbf{q}$ is a good quantum number, the Hamiltonian can be written in the block diagonal form:

$$\hat{H} = \sum_{\mathbf{q},i,j} \mathcal{H}_{i,j}(\mathbf{q})|u_i(\mathbf{q})\rangle\langle u_j(\mathbf{q})| \tag{5.3}$$

where $\mathcal{H}_{i,j}(\mathbf{q})$ are matrix elements of the so called Bloch Hamiltonian, which acts on the "internal" degrees of freedom, labeled by the indexes i and j. It can be diagonalized by a suitable unitary transformation: $|\mathbf{q},s\rangle = V_{s,i}|u_i(\mathbf{q})\rangle$ for which:

$$\mathcal{H}(\mathbf{q})|\mathbf{q},s\rangle = E_s(\mathbf{q})|\mathbf{q},s\rangle. \tag{5.4}$$

The eigenenergies of the system, $E_s(\mathbf{q})$, are thus parametrized by the quasi-momentum $\mathbf{q}$, and thus represented by functions on the reciprocal space called *energy bands*. We recall that $\mathbf{q}$ is defined up to a translation vector $\mathbf{G}$ in the reciprocal lattice space [210], for this reason it is called *quasi-momentum*.

Let us consider a curve C in the quasi-momentum space. We want to study the evolution of the eigenvectors $|\mathbf{q},s\rangle$ along C. If there are no degeneracies, i.e. level crossings, on

C we can consider a single energy band and thus fix the label s. We consider the phase $\arg\langle \mathbf{q}, s|\mathbf{q}+d\mathbf{q}, s\rangle$, where the infinitesimal displacement is along C. This phase can be rewritten as:

$$\arg\langle \mathbf{q}, s|\mathbf{q}+d\mathbf{q}, s\rangle \approx \arg(1+\langle \mathbf{q}, s|\text{grad}_{\mathbf{q}}|\mathbf{q}, s\rangle d\mathbf{q}). \tag{5.5}$$

The quantity $\langle \mathbf{q}, s|\text{grad}_{\mathbf{q}}|\mathbf{q}, s\rangle$ is purely imaginary. Hence the total phase acquired during the evolution along C is:

$$\gamma_s(C) = -i\int_C \langle \mathbf{q}, s|\text{grad}_{\mathbf{q}}|\mathbf{q}, s\rangle d\mathbf{q} \equiv \int_C \mathbf{A}(\mathbf{q})\cdot d\mathbf{q}. \tag{5.6}$$

Now we observe that this phase is in general gauge dependent. Indeed given the transformation:

$$|\mathbf{q}, s\rangle \to \mathrm{e}^{i\alpha(\mathbf{q})}|\mathbf{q}, s\rangle, \tag{5.7}$$

we have that:

$$\mathbf{A}(\mathbf{q}) \to \mathbf{A}(\mathbf{q}) + \text{grad}_{\mathbf{q}}\alpha(\mathbf{q}) \tag{5.8}$$

$$\gamma_s(C) \to \gamma_s(C) + \alpha(\mathbf{q}_2) - \alpha(\mathbf{q}_1), \tag{5.9}$$

where $\mathbf{q}_1$ and $\mathbf{q}_2$ are the extremes of the curve C. The field $\mathbf{A}$ behaves as the electromagnetic vector potential under gauge transformations. For this reason it is usually called *Berry vector potential*. Often one also uses the name *Berry connection*, referring to the language of differential geometry.

Consider the case in which C is a closed curve. Hence the points $\mathbf{q}_2$ and $\mathbf{q}_1$ coincide. Single valuedness of the Bloch wavefunctions $|\mathbf{q}\rangle$ implies that: $\alpha(\mathbf{q}_2) - \alpha(\mathbf{q}_1) = 2m\pi$, where m is an integer. It follows that $\gamma_s(C)$ is a meaningful quantity, defined modulo 2π, which cannot be removed by a suitable gauge choice. $\gamma_s(C)$ is known as *Berry phase*. This quantity is dependent only on the path chosen in the parameter space and not on the path parameter. In this sense it has a geometric nature.

It has been shown that the Berry phase can be associated to an important physical quantity that can be observed in a crystal: the electric polarization P. This result, together with the derivation of the Berry phase in Bloch bands, was first obtained by Zak [211]. When the Berry phase is evaluated over the entire Brillouin zone in a one dimensional system, it is called *Zak's phase*. Detection of the Berry phase has been realized first in optical systems [212], but is also of interest in condensed matter due to its relation with topological invariants [165, 182, 213–215].

If some additional symmetry is included in the system, the Zak phase can be quantized and therefore regarded as a topological invariant. The first example was given by Zak itself, which showed that if the system presents inversion symmetry then $\gamma = 0, \pi$ [216]. Here we are interested in another symmetry, called *chiral symmetry* [217]. A quantum system, described by the Hamiltonian $\hat{H}$, possess chiral symmetry if there exist a unitary operator $\hat{\Gamma}$, called *chiral operator*, such that:

$$\hat{\Gamma}\hat{H}\hat{\Gamma}^{-1} = -\hat{H}. \tag{5.10}$$

It immediately follows that $\hat{\Gamma}^2 = 1$, hence eigenstates of the chiral operator have eigenvalues ± 1. Moreover, chiral symmetry implies that, given any eigenstate $|\psi\rangle$ of $\hat{H}$ with energy E, then there exist another eigenstate of $\hat{H}$ with energy $-E$. This state is: $\hat{\Gamma}|\psi\rangle$, as can be seen by direct calculation. This result has a consequence on the general form of the Bloch Hamiltonian $\mathcal{H}(q)$. First, it is evident that chiral symmetry can exist only if the internal degrees of freedom are even-dimensional, i.e. $s \in \{1, \ldots, 2N\}$ (N integer). Second, with a proper choice of the zero of the energy, $\mathcal{H}(q)$ has the block off-diagonal form:

$$\mathcal{H}(q) = \begin{pmatrix} 0 & h(q) \\ h^\dagger(q) & 0 \end{pmatrix}, \tag{5.11}$$

where $h(q)$ and its Hermitian conjugate, $h^\dagger(q)$, are $N \times N$ dimensional matrices. Let us focus on the simplest case $N = 1$, where the internal degree of freedom is two-dimensional. In this case we can write the chiral operator in the form:

$$\hat{\Gamma} = \exp(-i\pi \mathbf{v}_\Gamma \cdot \hat{\boldsymbol{\sigma}}/2). \tag{5.12}$$

Hence $\hat{\Gamma}$ rotates a vector in the Bloch sphere orthogonal to $\mathbf{v}_\Gamma$ by an angle π. Indeed the eigenstates of $\mathcal{H}(q)$ are represented by vectors on the Bloch sphere, $\mathbf{n}(q)$, lying in a plane perpendicular to $\mathbf{v}_\Gamma$. This is consistent with the fact that the chiral operator transforms $\mathbf{n}(q)$ in $-\mathbf{n}(q)$. If we rotate the system in a basis where $\mathbf{v}_\Gamma = (0, 0, 1)^T$, the Bloch Hamiltonian will have the form:

$$\mathcal{H}(q) = E(q)(n_x(q)\sigma_x + n_y(q)\sigma_y). \tag{5.13}$$

The fact that $\mathbf{n}(q)$ lies on a fixed plane for every value of q allows to define a topological invariant. Imagine to follow the direction of $\mathbf{n}(q)$ as q changes from $-\pi$ to π. Because the Brillouin zone is a circle (the points $q = -\pi$ and $q = \pi$ are identified), we will have $\mathbf{n}(-\pi) = \mathbf{n}(\pi)$. Hence $\mathbf{n}(q)$ can rotate by an angle $\theta(q) < 2\pi$ and turn back to its original position, or it can cover the entire circle a finite number of times. The number of times that $\mathbf{n}(q)$ covers the equatorial plane is an integer and, as such, it cannot be changed by smooth deformation. We will call it the *winding number*. Defining

$$\theta(q) = \mathbf{n}(q) \cdot \mathbf{n}(-\pi) = \arctan \frac{n_y(q)}{n_x(q)}, \tag{5.14}$$

we can write the explicit expression of the winding number ν:

$$\begin{aligned}\nu = \frac{\theta(\pi)-\theta(-\pi)}{2\pi} &= \int_{-\pi}^{\pi} \frac{d}{dq}\theta(q)dq \\ &= \int_{-\pi}^{\pi} \left(n_x(q)\frac{d}{dq}n_y(q) - n_y(q)\frac{d}{dq}n_x(q) \right) \frac{dq}{2\pi}.\end{aligned} \tag{5.15}$$

It turns out that this expression is also proportional to the Zak phase. Indeed, by inserting the spinor representation of the Bloch eigenstates,

$$|\mathbf{n}(q)\rangle = \frac{1}{\sqrt{2}} \begin{pmatrix} n_x(q) - i n_y(q) \\ 1 \end{pmatrix}, \tag{5.16}$$

into the Zak phase formula:

$$\gamma_{Zak} = -i \int_{-\pi}^{\pi} \langle \mathbf{n}(q) | \partial_q \mathbf{n}(q) \rangle dq, \tag{5.17}$$

we obtain:

$$\gamma_{Zak} = \pi\nu. \tag{5.18}$$

Therefore, in chiral systems, the Zak phase is quantized and can be regarded as a topological invariant. However the winding number is a more appropriate quantity for distinguishing topological phases. Indeed the values $\nu = 2$ and $\nu = 0$ represent two different topological phases even if they are associated to equivalent Zak phases (2π and 0, respectively).

5.3 A 1D model of chiral topological insulator: the SSH model

We proceed to illustrate one of the most celebrated models on 1D chiral topological insulators: the Su-Schrieffer-Heeger (SSH) model [190]. This is a nearest neighbor tight binding model for a one dimensional lattice with two atoms per unit cell. Once the unit cell has been defined one can consider the hopping amplitudes *inside* the single cells, the hoppings and between one cell and the other. We label A and B the two possible sites in a unit cell and thus define the creation operators $c^{\dagger}_{A,i}$ ($c^{\dagger}_{B,i}$) that create a particle on site $A(B)$ belonging to the cell i. Thus, by defining the *intracell* hopping $(t+\delta t)$ and the *intercell* hopping $(t-\delta t)$, where δt can be positive or negative, we write the SSH Hamiltonian as:

$$H_{SSH} = \sum_i (t+\delta t)c^{\dagger}_{A,i}c_{B,i} + (t-\delta t)c^{\dagger}_{A,i+1}c_{B,i} + h.c. \tag{5.19}$$

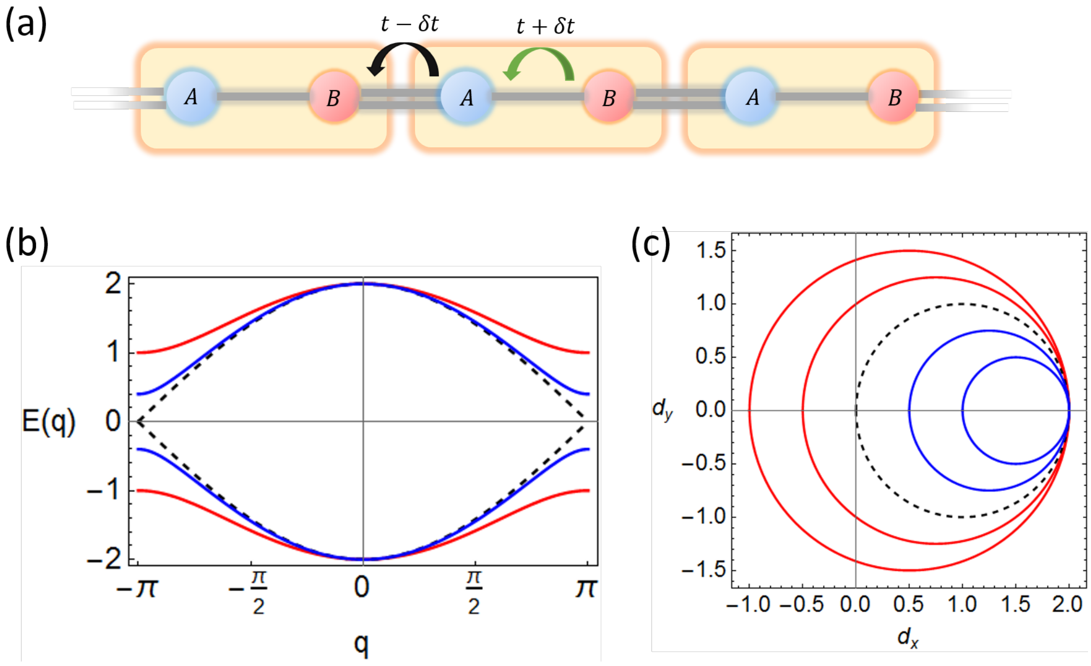

FIGURE 5.1: **SSH model.** (a) Schematic of the SSH model. A single cell is composed by two lattice sites A and B coupled by an hopping amplitude $t+\delta t$, schematized by a single bond. The intercell hopping, $t-\delta t$ is indicated by a double bond. (b) Energy spectrum for different values of δt (we set $t=1$). The red plot is for $\delta t=-0.5$, the blue is for $\delta t=0.2$. For $\delta t=0$ (dashed black plot) the gap closes at $q=\pm\pi$. (c) Parametric plot of the curve $D=(d_x(q),d_y(q))$, with $q\in[-\pi,\pi)$, for different values of δt. For positive δt (here we show the cases $\delta t=0.25,0.5$ represented by blue curves) the curve D does not contain the origin, indicating a zero winding number. At $\delta t=0$ (dashed black curve), D touches the origin, therefore the winding number is ill defined. A non trivial winding number is obtained for $\delta t<0$ (red curves) here shown for $\delta t=-0.25,-0.5$.

This system is illustrated in Fig. 5.1 (a). By Fourier transforming H_{SSH} we obtain the Bloch Hamiltonian:

$$\mathcal{H}_{SSH}(q)=d_x(q)\sigma_x+d_y(q)\sigma_y, \tag{5.20}$$

$$d_x(q)=(t+\delta t)+\cos(q)(t-\delta t), \tag{5.21}$$

$$d_y(q)=\sin(q)(t-\delta t). \tag{5.22}$$

Where the distance between two cells is: $a=1$. The energy eigenvalues are given by:

$$E(q)=\pm|\mathbf{d}(q)|=\pm\sqrt{2\left[(t^2+\delta t^2)+\cos(k)(t^2-\delta t^2)\right]}. \tag{5.23}$$

This is a simple model of a one dimensional insulator, whose energy band structure is illustrated in Fig. 5.1 (b). Notice that the energy gap at $q=\pi$ is zero for $\delta t=0$, i.e. when the intracell and intercell hoppings are equal. In this case the system becomes a simple one dimensional crystal with one atom per unit cell. When the energy gap is closed the corresponding eigenstates are degenerate. This implies that the winding number is ill defined for $\delta t = 0$. Indeed, if we consider the curve $D = (d_x(q), d_y(q))$, we can identify the winding number as the number of times D encircles the origin (see Fig. 5.1 (c)). At $\delta t = 0$ the origin is a point of D, thus we cannot determine the winding number, i.e. we cannot say if the origin belongs or not to the interior of D. When $\delta t > 0$ the winding number is $\nu = 0$ (blue curves in Fig. 5.1 (c)). However, for $\delta t < 0$ the winding number is $\nu = 1$ (the curve D must be considered as oriented counterclockwise), hence we have a nontrivial topological phase. This is a first example of how a transition from one topological phase to another can happen in correspondence of a zero gap phase. In general a topological invariant can be changed by crossing regions of the parameter space where the topological invariant itself is ill defined.

This idea allows to get some intuition about the origin of topologically robust edge states. These are states with energy lying in the gap of the bulk Hamiltonian whose wavefunction is localized on the boundary of the system. Let us consider the boundary between a topologically nontrivial system and a trivial one. By trivial, we mean a system which can be smoothly transformed into the vacuum, without ever closing the spectral gap. The boundary can be seen as a spatial transformation of the system parameter, e.g. δt in the SSH case, from values corresponding to a trivial topology to values corresponding to a non trivial one. In our case we can consider a function $\delta t(x)$ which is negative in $x < 0$ and positive for $x > 0$. If this function is smooth enough, i.e. slowly changing on the atomic scale, we can consider any small interval dx as a bulk system, where we can still define, with good approximation, the quasi-momentum, q, and an energy spectrum given by Eq: 5.23. Therefore we can say that the energy dispersion is given by $E(q, x)$ and exhibits the gap closing in $x = 0$. Hence a zero energy state exists around $x = 0$. This state is topologically protected in the sense that any perturbation that does not destroy the topological features of the system in $x < 0$ cannot remove this state. We can also remove the restriction of $\delta t(x)$ being a smooth function, provided that we change it to a function jumping abruptly from negative to positive values, with a transformation that has no influence on the topology. These considerations can be confirmed by numerical calculations of the spectrum of a finite system. The general result is that a zero point energy eigenvalue appears inside the energy gap (which still exists for finite systems even if the energy bands cannot be expressed as functions of the quasi-momentum q).

The result that a bulk property, the topological invariant of the system, tells us what will happen on the edge of the system, is known as *bulk-edge correspondence* [187]. More precisely, the bulk-edge correspondence allows to *count* the number of eigenstates by simply knowing the value of the topological invariant. We will see some examples in the following sections.

We conclude showing another method that allows to explicitly construct zero modes by analytical calculations. We illustrate it in the specific case of the SSH model. Let the system parameter $\delta t(x)$ be a function positive in $x > 0$ and negative in $x < 0$. Since the system is finite we will have to replace the quasi-momentum q with its operatorial representation $q \to -i\partial_x$. Since we are interested to low energy solutions, that in the bulk case lie around $q = \pi$, we expand the Bloch Hamiltonian around this point obtaining, at first order, the Dirac-like equation:

$$[2\delta t\sigma_x + (t - \delta t)\sigma_y(-i\partial_x)]\psi(x) = E\psi(x). \tag{5.24}$$

Then we look for a square integrable solution with $E = 0$. Multiplying for σ_y the two sides of Eq: 5.24 we obtain, for $E = 0$:

$$[-2i\delta t\sigma_z + (t - \delta t)(i\partial_x)]\psi(x) = 0. \tag{5.25}$$

Defining $m(x) = 2\delta t(x)/(t - \delta t(x))$, which is negative for $x < 0$, we can write a bounded solution:

$$\psi(x) = \begin{pmatrix} 1 \\ 0 \end{pmatrix} \exp\left(-\int_{x<0} |m(x)|\, dx\right), \tag{5.26}$$

which is a state peaked on the boundary decaying exponentially in the $x < 0$ (non-trivial) region. The topological protection can be understood by noticing that this solution is valid for any deformation of the function $m(x)$ that does not change its sign [218].

5.4 Simulating topological phases with Quantum Walks

[1] As we have seen in the previous Chapter, Quantum Walks are ideal platforms where to investigate spatially periodic systems with various band structures. The idea to use Quantum Walks to study topological phases was introduced by Kitagawa [159, 219]. A generalization of the standard quantum walk was proposed, the *split-step QW*, and implemented in photonic systems where it was possible to show the existence of protected bound states [152].

In this section we investigate the topological properties of the 1D protocol proposed in Chapter 4, $\hat{U}_{1D}(\delta)$. We will show that this protocol is a chiral symmetric system that can exhibit non-zero Zak phase for some values of the parameter δ. Therefore we will investigate the edge states appearing in this system and study how topology affects the dynamics of the Quantum Walk. In a previous work [95] it was showed that the topological phase transition is associated to discontinuities in the first and second moments of the QW probability distribution. Here we will also show that the Zak phase is actually contained in the expression of the first moment of the probability distribution.

---

[1] Some paragraphs and sentences of this section are adapted or copied verbatim from the work [175] which I coauthored.

Its contribution can be isolated by defining a new observable, the *chiral displacement*, that allows to directly certify the topological phase of the system.
The protocol we are interested in is: $\hat{U}_{1D}(\delta) = \hat{Q}(\delta)\cdot\hat{W}$, where $\hat{Q}(\delta)$ is a q-plate operator with optical retardation δ and W a quarter wave plate. We have seen that $\hat{U}_{1D}(\delta)$ is described by an effective Hamiltonian, whose expression in the Fourier space is of the form: $\mathcal{H}_{eff}(q) = E(q)\mathbf{n}(q,\delta)\cdot\hat{\boldsymbol{\sigma}}$, where $E(q)$ are the energy bands, already described in Chapter 4, and $\mathbf{n}(q,\delta)$ is the Bloch sphere representation of the eigenstates of the system, whose components are:

$$n_x(q,\delta) = -\frac{\cos(\delta/2)+\cos(q)\sin(\delta/2)}{\sqrt{2}\,c(q,\delta)}, \tag{5.27}$$

$$n_y(q,\delta) = -\frac{\sin(q)\sin(\delta/2)}{\sqrt{2}\,c(q,\delta)}, \tag{5.28}$$

$$n_z(q,\delta) = n_y(q,\delta), \tag{5.29}$$

where: $c(q,\delta) = \sin(E(q,\delta))$. It is straightforward to see that this system exhibits chiral symmetry. Indeed since $n_z(q,\delta) = n_y(q,\delta)$, the vector $\mathbf{n}(q,\delta)$ is always perpendicular to the constant vector $\mathbf{v}_\Gamma = (0,1,-1)^T$ for every q and δ. This defines the chiral symmetry operator $\hat{\Gamma} = \mathbf{v}_\Gamma\cdot\hat{\boldsymbol{\sigma}}$. We can therefore ask if there are some values of the system parameter, δ, where the Zak phase, or equivalently the winding number, has a nonzero value.
To simplify calculations it is convenient to analyze the system in a basis where $\mathbf{v}_\Gamma = (0,0,1)^T$. This is obtained by applying the transformation:

$$\hat{U}_{1D}(\delta) \to \sqrt{\hat{W}}\hat{U}_{1D}(\delta)\sqrt{\hat{W}}^{-1} = \sqrt{\hat{W}}\hat{Q}(\delta)\sqrt{\hat{W}}, \tag{5.30}$$

where $\sqrt{\hat{W}}$ is an operator describing an uniform waveplate with optical retardation $\delta = \pi/4$ (see also Eq: 5.44). In this new reference frame the energy band dispersion remains unaltered, while the vector $\mathbf{n}(q,\delta)$ has components:

$$n_x(q,\delta) = -\frac{\cos(\delta/2)+\cos(q)\sin(\delta/2)}{\sqrt{2}\,c(q,\delta)}, \tag{5.31}$$

$$n_y(q,\delta) = -\frac{\sin(q)\sin(\delta/2)}{c(q,\delta)}, \tag{5.32}$$

$$n_z(q,\delta) = 0. \tag{5.33}$$

As it can be seen in Fig. 5.9 we have a nontrivial topological phase for $\pi/2 < \delta < 3\pi/2$, where the winding number of the curve $D = (d_x(q), d_y(q)) \equiv E(q)\,(n_x(q), n_y(q))$ is $\nu = 1$, corresponding to a value of the Zak phase $\gamma_{Zak} = \pi$. As we will see below, even the phase $\delta > 3\pi/2$ is topologically non trivial, despite exhibiting zero winding number. This is a consequence of the fact that we are considering a periodically driven system, that

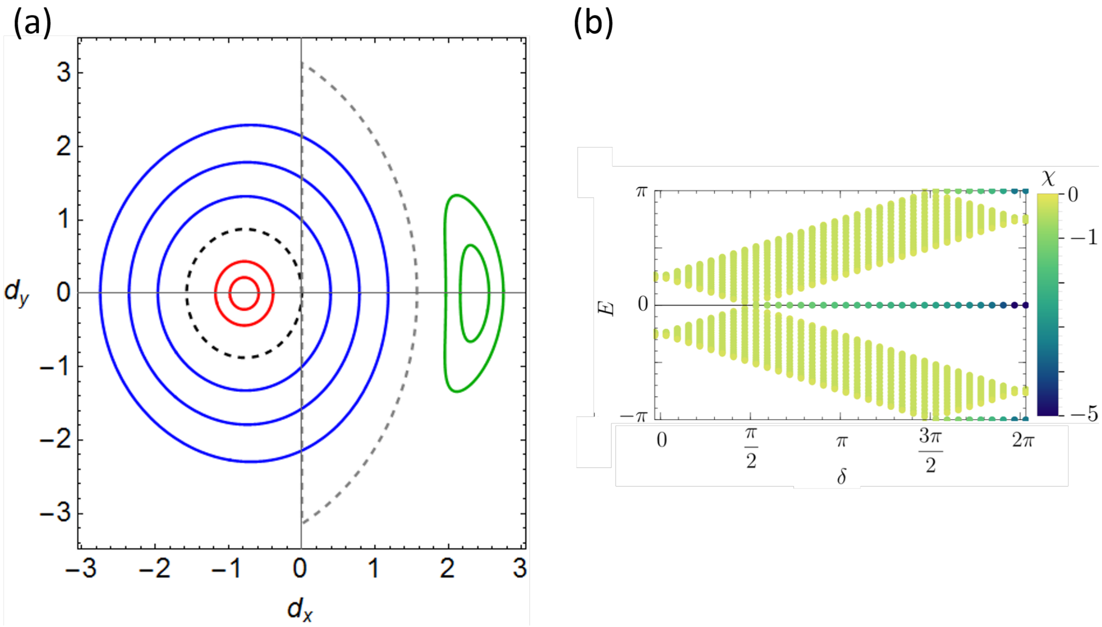

FIGURE 5.2: **Topological invariants and edge states of the protocol $\hat{U}_{1D}$.** (a) Parametric plots of the curve $D = (d_x(q), d_y(q)) \equiv E(q)\,(n_x(q), n_y(q))$, for different values of $\delta \in [0, 2\pi)$. Red curves are for $\delta < \pi/2$ ($\delta = \pi/8, \pi/4$) and show a zero winding number (trivial topology), blue curves correspond to $\pi/2 < \delta < \pi/2$ ($\delta = 3\pi/4, \pi, 5\pi/4$) a winding number $\nu = 1$, since they enclose the origin, while, again, for $\delta > 3\pi/2$ (green curves, shown for $\delta = 7\pi/4, 15\pi/8$) the winding number is again trivial. Dashed curves correspond to $\delta = \pi/2$ (black) and $\delta = 3\pi/2$ (gray), where the winding number is ill defined. (b) Energy spectrum of a finite system (made of $2L = 20$ lattice sites) described by the protocol $\hat{U}_{1D}$. The plot shows zero energy states for $\pi/2 < \delta < 3\pi/2$, while no states are observed in the gap for $\delta < \pi/2$. Surprisingly, edge states are still present for $\delta > 3\pi/2$. In this case we have edge states at $E = 0$ and at $E = \pi$. The winding number is zero because it actually counts the difference between the number of states at $E = 0$ and the number of states at $E = \pi$. The parameter $\chi = \log_{10}(1 - \langle|m|\rangle)$ indicates the degree of localization of the eigenstates ($\langle|m|\rangle$ is the average absolute value of the position in the lattice space). Panel (b) is adapted from Ref: [175]

can exhibit richer topological features. As expected, the topological phase transitions happen in correspondence of gap closing points, like at $\delta = \pi/2$, where the gap closes at $E = 0$, and at $\delta = 3\pi/2$ where the gap closes at $E = \pi$ (by adding edge modes with $E = \pi$, without destroying the edge modes with zero energy).

These result are confirmed by numerical calculations of the eigenstates and eigenvalues for a finite lattice, shown in Fig. 5.9 (b), where the presence of edge states is confirmed by their degree of localization: $\chi = \log_{10}(1 - \langle|m|\rangle)$ ($\langle|m|\rangle$ is the average absolute value of the position in the lattice space). At $\pi/2 < \delta < 3\pi/2$, there is an edge mode with energy $E = 0$, while for $\delta > 3\pi/2$ an additional edge state with $E = \pi$ appears.

Until now we have seen how topology influences the boundary between two different phases. However, since the topological phase of a system is defined by a bulk property (notice that we have expressed topological invariants in terms of Bloch wavefunctions), we can ask if there is some observation that can be made in the system bulk that allow to distinguish between a topological phase and the other.

Quantum Walk experiments often focus on measuring the probability distribution after t steps of evolution of an initially localized state. Therefore one can study the behavior of the moments of the resulting distributions as the system parameter, in our case δ, is changed. The $k-$th order moment, at step t, $M_k(\delta, t)$ is defined as:

$$M_k(\delta, t) = \langle \psi(t)|\hat{m}^k|\psi(t)\rangle = \int_{-\pi}^{\pi} \frac{dq}{2\pi} \langle \mathcal{U}(q,\delta)^{-t}(-i\partial_q)^k \mathcal{U}(q,\delta)^t\rangle_{\psi_0}, \tag{5.34}$$

where $\langle \ldots \rangle_{\psi_0}$ indicates the average over an initial localized state $|\psi(0)\rangle$, and $\hat{m} = -i\partial_q$. From this equation, in Ref: [95], the first and second order moments have been evaluated to the leading order in t. The results showed that, in the asymptotic limit, $t \to \infty$, these moments exhibit slope discontinuities at the values of δ where a topological phase transition occurs. Although a general proof is still missing, it was showed that this phenomenon appears also in other systems, like the SSH model, the p-wave superconductor and also 1D QWs without chiral symmetry.

In Ref: [175] we focused on the first order moment, looking for the complete expression comprising the subleading contributions. Consider the evolution of a state $|\psi_0\rangle$ initially localized at site $m = 0$, and let its polarization be characterized by the expectation values of the three Pauli operators: $\mathbf{s} = \langle \boldsymbol{\sigma}\rangle_{\psi_0} \equiv \langle \psi_0|\boldsymbol{\sigma}|\psi_0\rangle$. The evolution operator in the coin space is, for t time-steps: $\mathcal{U}^t = (Q.W)^t = \mathrm{e}^{-iEt\mathbf{n}\cdot\boldsymbol{\sigma}} = \cos(Et)\sigma_0 - i\sin(Et)\mathbf{n}\cdot\boldsymbol{\sigma}$. Using of the standard identity $(\mathbf{a}\cdot\boldsymbol{\sigma})(\mathbf{b}\cdot\boldsymbol{\sigma}) = (\mathbf{a}\cdot\mathbf{b})\sigma_0 + i(\mathbf{a}\times\mathbf{b})\boldsymbol{\sigma}$ (valid for arbitrary vectors $\mathbf{a}$ and $\mathbf{b}$), it is straightforward to show that the mean displacement of the wavepacket reads:

$$\begin{aligned}\langle \hat{m}(t)\rangle = \langle \psi(t)|m|\psi(t)\rangle &= \int_{-\pi}^{\pi} \frac{dq}{2\pi} \left\langle \mathcal{U}^{-t}(i\partial_q)\mathcal{U}^t\right\rangle_{\psi_0} \\ &= \int_{-\pi}^{\pi} \frac{dq}{2\pi} \langle [\cos(Et)\sigma_0 + i\sin(Et)\mathbf{n}\cdot\boldsymbol{\sigma}]\,(-i\partial_q)\,[\cos(Et)\sigma_0 - i\sin(Et)\mathbf{n}\cdot\boldsymbol{\sigma}]\rangle_{\psi_0} \\ &= \int_{-\pi}^{\pi} \frac{dq}{2\pi} \left[\left(-t\frac{\partial E}{\partial q} + \frac{\partial}{\partial q}\frac{\sin(2Et)}{2}\right)\mathbf{n} + \sin(Et)^2\left(\mathbf{n}\times\frac{\partial \mathbf{n}}{\partial q}\right)\right]\cdot\mathbf{s}\,.\end{aligned} \tag{5.35}$$

In the above expression we suppressed the dependence of $E, \mathbf{n}$ and $\mathcal{U}$ on q and δ. When a protocol possesses chiral symmetry, the unit vector $\mathbf{n}$ of the corresponding effective Hamiltonian is bound to rotate in the plane orthogonal to the vector $\mathbf{v}_\Gamma = \mathrm{tr}(\Gamma\boldsymbol{\sigma})/2$ associated to its chiral operator $\hat{\Gamma}$. In turn, this means that $(\mathbf{n}\times\partial_k\mathbf{n})$ is parallel to $\mathbf{v}_\Gamma$. We arrive then to the expression:

$$\langle m(t)\rangle = [L(t) + S(t)] + \langle \hat{\Gamma}\rangle_{\psi_0} S_\Gamma(t). \tag{5.36}$$

The terms in square brackets are proportional to $\langle\hat{\Gamma}\rangle_{\psi_0}$, i.e. the projetcion of the initial state along a vector orthogonal to $\mathbf{v}_\Gamma$. Their explicit expression is:

$$L(t) = -\,t\int_{-\pi}^{\pi}\frac{dq}{2\pi}\frac{\partial E}{\partial q}\mathbf{n}\cdot\mathbf{s}, \tag{5.37}$$

$$S(t) = \int_{-\pi}^{\pi}\frac{dq}{2\pi}\frac{\partial}{\partial q}\left(\frac{\sin(2Et)}{2}\right)\mathbf{n}\cdot\mathbf{s}. \tag{5.38}$$

$L(t)$ is a term that grows linearly with time and becomes dominant on the subleading term $S(t)$ in the long time limit. Of particular interest is the term:

$$S_\Gamma(t) = \int_{-\pi}^{\pi}\sin(Et)^2\left|\mathbf{n}\times\frac{\partial\mathbf{n}}{\partial q}\right|\frac{dq}{2\pi}, \tag{5.39}$$

called the *chiral subleading term*. By noticing that $(\mathbf{n}\times\partial_k\mathbf{n})\cdot\mathbf{s}$ is proportional to the Berry connection, we can write:

$$S_\Gamma(t) = \frac{\gamma_{Zak}}{2\pi} - \int_{-\pi}^{\pi}\cos(2Et)\left|\mathbf{n}\times\frac{\partial\mathbf{n}}{\partial q}\right|\frac{dq}{2\pi}. \tag{5.40}$$

The above analysis shows that information on the Zak phase is contained in the mean displacement of the walker, and it may be extracted by fitting $\langle m\rangle$ at long times, isolating in turn the second term of Eq: 5.36. However, this measurement would not be robust. Indeed, even if one prepared the initial polarization in an eigenstate of the chiral operator $\hat{\Gamma}$, so that $\langle\Gamma_\perp\rangle_{\psi_0} = 0$, disorder during the propagation of the beam would introduce polarization components orthogonal to $\mathbf{v}_\Gamma$. These would give rise to ballistic contributions, which in the long time limit would dramatically affect the result. A related result for the case of a non-Hermitian quantum walk initialized on a chiral eigenstate (i.e., an initial condition such that $\langle\Gamma_\perp\rangle_{\psi_0} = 0$) was demonstrated theoretically in Ref: [220], and verified experimentally in Ref: [221].

We introduced an alternative and more convenient approach, that consists in measuring the *mean chiral displacement*:

$$\mathcal{C}(t) \equiv -\langle\Gamma\hat{m}(t)\rangle_{\psi_0} = S_\Gamma(t), \tag{5.41}$$

which quantifies the relative shift between the two projections of the state onto the eigenstates of the chiral operator. Importantly, the result contained in Eq: 5.41 is (i) independent of the initial polarization and (ii) robust against disorder. The chiral displacement becomes proportional to the Zak phase in the limit $t\to\infty$. Indeed the additional term appearing in $S_\Gamma(t)$ is an oscillating contribution (as a function of δ) whose amplitude, in the asymptotic limit, goes to zero as $1/\sqrt{t}$, as can be easily seen by evaluating the integral with the method of stationary phase.

We derive here the result of Eq: 5.41 choosing the reference frame in the polarization

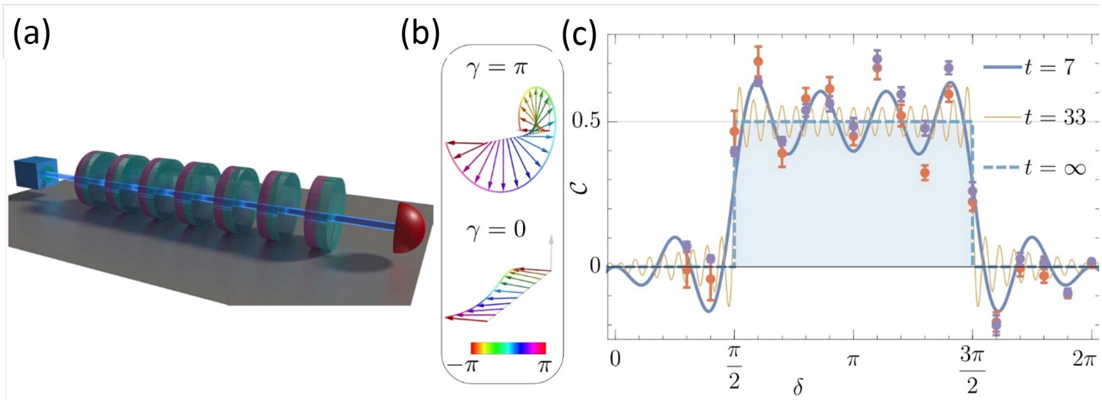

FIGURE 5.3: **Zak phase detection through the mean chiral displacement.** (a) Sketch of the setup implementing the protocol $U = Q \cdot W$. A light beam, exiting a single mode fiber depicted on the left, performs a QW by propagating through a sequence of quarter-wave plates (purple disks) and q-plates (turquoise disks). (b) The unit vector $\mathbf{n}(k)$ winds either 1 or 0 times around the chiral axis, as k traverses the whole Brillouin zone, depending on the value of the optical retardation δ. (c) Mean chiral displacement $\mathcal{C}$ after a 7-steps QW of protocol U, vs. the optical retardation δ. Each datapoint is an average over ten different measurements (error bars are the associated standard errors). Purple and red dots refer, respectively, to different input polarizations, $|L\rangle$ and $(|L\rangle + |R\rangle)/\sqrt{2}$. The lines represent the function $S_\Gamma(t)$ given in equation 5.40, for different values of the time t. In the long time limit, $S_\Gamma(t)$ converges to (a multiple of) the Zak phase γ of protocol U. Image adapted from Ref: [175].

space such that: $\hat{\Gamma} = \sigma_z$. One finds:

$$\begin{aligned}
\tilde{\mathcal{C}}(t) =& \langle \tilde{\Gamma} m(t) \rangle = \int_{-\pi}^{\pi} \frac{dq}{2\pi} \left\langle \mathcal{U}^{-t} \sigma_z (-i\partial_q) \mathcal{U}^t \right\rangle_{\psi_0} \\
&= \int_{-\pi}^{\pi} \frac{dq}{2\pi} \Big\langle \sin(Et)^2 \Big[\left(\mathbf{n} \times \partial_q \mathbf{n}\right)_z \sigma_0 - \frac{i}{2} \partial_q |\mathbf{n}|^2 \sigma_z \Big] \\
&\quad + i\partial_q \Big[\cos(Et)\sin(Et)(n_x\sigma_y - n_y\sigma_x) - \sin(Et)^2 \sigma_z \Big]_{\psi_0} \\
&= \int_{-\pi}^{\pi} \frac{dq}{2\pi} \sin(Et)^2 \left(\mathbf{n} \times \frac{\partial \mathbf{n}}{\partial q} \right)_z = S_\Gamma(t).
\end{aligned} \tag{5.42}$$

In the second line of Eq: 5.42, all terms preceded by an imaginary unit i integrate to zero: the first because $\mathbf{n}$ is a vector of unit norm for all k, and the second because it is the integral of a total derivative over a closed path. The final result is purely real, in agreement with the fact that the chiral displacement is the expectation value of an Hermitian operator.

After deriving the above result, we probed the chiral displacement in our OAM-based platform (see Chapter 4), by performing a 7-step quantum walk of the protocol $\hat{U}_{1D}$, as depicted in Fig. 5.3(a) [175]. The chiral eigenstates correspond to two specific orthogonal polarization states, which depend explicitly on the protocol, and which we detect at the end of the quantum walk.

At the end of the walk we can select any polarization component of the final state by a combination of a quarter-wave and a half-wave plate, followed by a linear polarizer, and we measure its OAM content by diffraction on a spatial light modulator coupled to a SMF and a power meter, which records the light intensity. Since we are interested in analyzing the OAM spectrum of chiral components of the final wavepacket, waveplates orientations are selected so as to implement polarization projections onto chiral states $|\uparrow\rangle$ and $|\downarrow\rangle$. The chiral operator for $\hat{U}_{1D}$ is $(\sigma_y + \sigma_z)/\sqrt{2}$, so it is straightforward to see that $|\uparrow\rangle_U = \cos{(\pi/8)}|L\rangle + i\,\sin{(\pi/8)}|R\rangle$ and $|\downarrow\rangle_U = \sin{(\pi/8)}|L\rangle - i\,\cos{(\pi/8)}|R\rangle$. The combination of polarization and OAM projections allows for determining the probabilities $P_{i,m}$, with $i = \{\uparrow, \downarrow\}$, that the system is in the chiral state $|i\rangle$ and in the OAM state $|m\rangle$. Given the probability distributions $P_{i,m}$, the chiral displacement is simply given by: $\sum_m m\,(P_{\uparrow,m} - P_{\downarrow,m})$.

In Fig. 5.3(c), we report the measured values of $\mathcal{C}$ for two different initial polarization states. Experimental points closely follow the theory curve for 7 time steps (blue solid line), and no significant differences can be observed between the two different initial states, proving that this measurement is insensitive to the choice of the polarization of the photons. For completeness we also show results predicted for 33 steps, and the asymptotic long-time limit, which coincides with the Zak phase (over 2π). We note here that, although both theory and data oscillate, as few as 7 steps are enough to distinguish clearly between the two topological phases.

In the experiment we could also test the stability of the quantization of the mean chiral displacement against dynamical disorder. In particular, we introduced dynamical disorder by offsetting the optical retardation δ_j $(1 \leq j \leq 7)$ of each q-plate by a small random amount $|\epsilon_j| < \Delta$ around their common mean value $\bar{\delta}$. In our experiment, we set $\Delta = \pi/10$ and $\pi/5$.

We note that this disorder is dynamic, in the sense that it affects independently the various q-plates crossed by the beam, but crucially it respects chiral symmetry. This can be simply understood by noting that the vector $\mathbf{v}_\Gamma$, defining the chiral operator, does not depend on δ.

As shown in Fig. 5.4, in single realizations the mean chiral displacement presents oscillations featuring higher amplitude for increasing disorder, but an ensemble average over independent realizations smoothly converges to the expected theoretical result, which in the infinite time limit gives the bulk value of the Zak phase. Here we performed measurements on protocol $\hat{U}_{1D}$, but similar robustness of the chiral displacement shall hold for every 1D QW chiral protocol, and more generally every 1D chiral system, as long of course as the disorder does not break chiral symmetry and its strength is small compared to the gap size to prevent inter-band transitions. As an example, in Ref: [175] we showed that the mean chiral displacement is an equally robust topological marker for the SSH model.

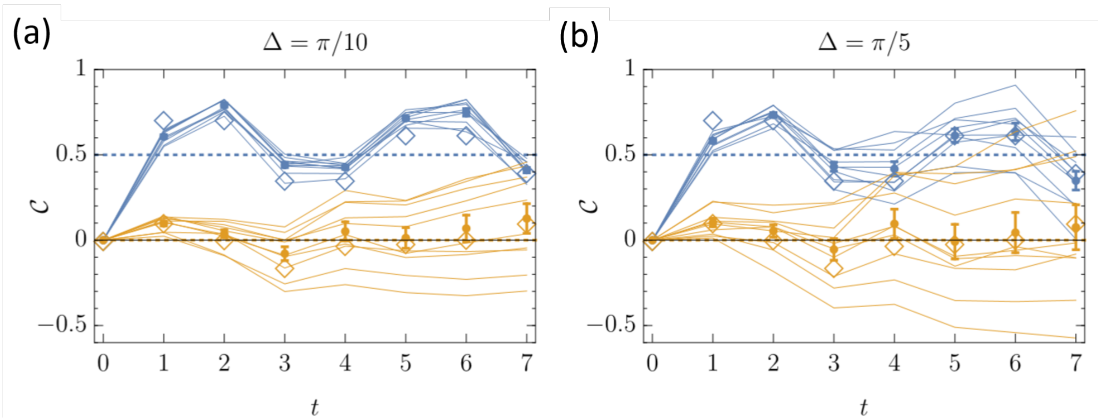

FIGURE 5.4: **Robustness to dynamical disorder.** Measurement of the mean chiral displacement $\mathcal{C}$ for a localized input state in presence of dynamical disorder. For the orange (blue) lines, we choose a mean value of the q-plate optical retardation $\bar{\delta} = 7\pi/4$ ($\bar{\delta} = \pi$), expected to yield a Zak phases of $\gamma/2\pi = 0$ ($\gamma/2\pi = 1/2$), and we add at each time step a small random retardation $|\epsilon| < \Delta$, with $\Delta = \pi/10$ (left) and $\pi/5$ (right). Thin solid lines display the measurements of single realizations, and their average is shown as filled circles (error bars are the standard error of the mean). In all plots, empty diamonds represent theoretical simulation calculated for the ideal case $\Delta = 0$, and dotted lines the expected result for $t \to \infty$. Image from Ref: [175].

5.4.1 Full topological characterization of our 1D protocol

[2]The detection of the chiral displacement showed that our protocol exhibits a winding number equal to $\nu = 1$ for $\pi/2 < \delta < 3\pi/2$, while it is zero for the other values of $\delta \in (0, 2\pi]$. However we have also seen that the phase $\delta > 3\pi/2$ is actually non-trivial, since edge modes at energy $E = 0$ and $E = \pi$ are present. We will call these modes 0-mode and π-mode, respectively. Hence, the winding number alone, fails to predict the topological features of the phase $\delta > 3\pi/2$. Moreover, one single integer cannot give a complete topological classification of a system that exhibits two kinds of edge modes. In such a case we would need to count the number of 0-modes *and* the number of π-modes. Therefore we expect that our system must be characterized by two integers.

An approach for a full topological characterization of one dimensional chiral systems which are periodic in time has been developed by J.Asboth and H.Obuse [222] by introducing the concept of *time frames*. Another way to experimentally measure all the topological invariants of a DTQW has been demonstrated in Ref: [223]. Here we will employ the first approach.

We have considered the protocol $\hat{Q}\hat{W}$, but we could also define the protocol $\hat{W}\hat{Q}$, which is actually the same quantum walk where we start with a q-plate rather than with a wave-plate, i.e we consider a different starting time. Indeed, in any time-periodic system we can introduce the effective Hamiltonian in multiple ways, by considering different

---

[2] Some paragraphs and sentences of this section are adapted or copied verbatim from the work [175] which I coauthored

starting times. The resulting effective Hamiltonian will have the same energy spectrum but, in general, different eigenvectors. In particular, as noted in Ref: [222], changing time-frame can break the chiral symmetry of the system. This has suggested the authors to define as *chiral*, any periodically driven system that presents at least one time frame where the effective Hamiltonian exhibits chiral symmetry (CS). It turns out that, if a time frame with CS exists, then one can find a second time frame that still presents chiral symmetry. Indeed, imagine to split the unitary process that starts at time τ, into two operators: $\hat{U}'(\tau) = \hat{G}\hat{F}$. If $\hat{U}'$ is a time frame with CS, then we can write $\hat{G} = \hat{\Gamma}\hat{F}^{-1}\hat{\Gamma}$. Then it is straightforward to show that also the time frame $\hat{U}'' = \hat{F}\hat{G}$ possess chiral symmetry. In general two time frames will have the same energy band dispersions but different eigenstates. Hence it is possible to observe in $\hat{U}''$ a winding number different from the one in $\hat{U}'$.

Let us turn to the specific case of our implementation. We consider the protocol $\hat{U}(\delta)$ in the basis where $\hat{\Gamma} = \sigma_z$:

$$\hat{U}_1(\delta) = \sqrt{\hat{W}}\hat{Q}(\delta)\sqrt{\hat{W}}. \tag{5.43}$$

We have already seen that this time frame exhibit CS, and the measurement of the corresponding winding number has been shown in the previous section. More precisely we measured the topological invariants of the protocol $\hat{U} = \hat{Q}\hat{W}$, which is actually another time frame (still chiral symmetric), but since $\hat{U}_1$ is equivalent to a rotation in the coin space of $\hat{U}$, there can be no difference in the winding numbers of the two systems.

In the following we will make use of the relation (valid for any waveplate $\hat{L}$ with optical retardation δ):

$$\hat{L}^k(\delta) = \hat{L}(k\delta), \tag{5.44}$$

which can be proved by verifying that $\hat{L}^k(\delta) \cdot \hat{L}^{1-k}(\delta) = \hat{L}(\delta)$.

Let us define $\hat{U}_1 = \hat{G}\hat{F}$, with $\hat{F} = \sqrt{\hat{Q}(\delta)}\sqrt{\hat{W}}$, and $\hat{G} = \hat{\Gamma}\hat{F}^{-1}\hat{\Gamma} = \sqrt{\hat{W}}\sqrt{\hat{Q}(\delta)}$. We can thus built the second chiral time frame, $\hat{\hat{U}}(\delta) = \hat{F}\hat{G}$, which explicitly reads:

$$\hat{\hat{U}}(\delta) = \sqrt{\hat{Q}(\delta)}\hat{W}\sqrt{\hat{Q}(\delta)}. \tag{5.45}$$

The effective Hamiltonian of this protocol exhibits a winding number given by:

$$\begin{aligned} \nu &= 0, \quad 0 < \delta < \pi/2, \\ \nu &= 1, \quad \pi/2 < \delta < 3\pi/2, \\ \nu &= 2, \quad 3\pi/2 < \delta < 2\pi, \end{aligned} \tag{5.46}$$

as it is also shown in Fig. 5.5. Hence looking also at the winding number of a second chiral symmetric time frame allows to obtain a full topological characterization of our

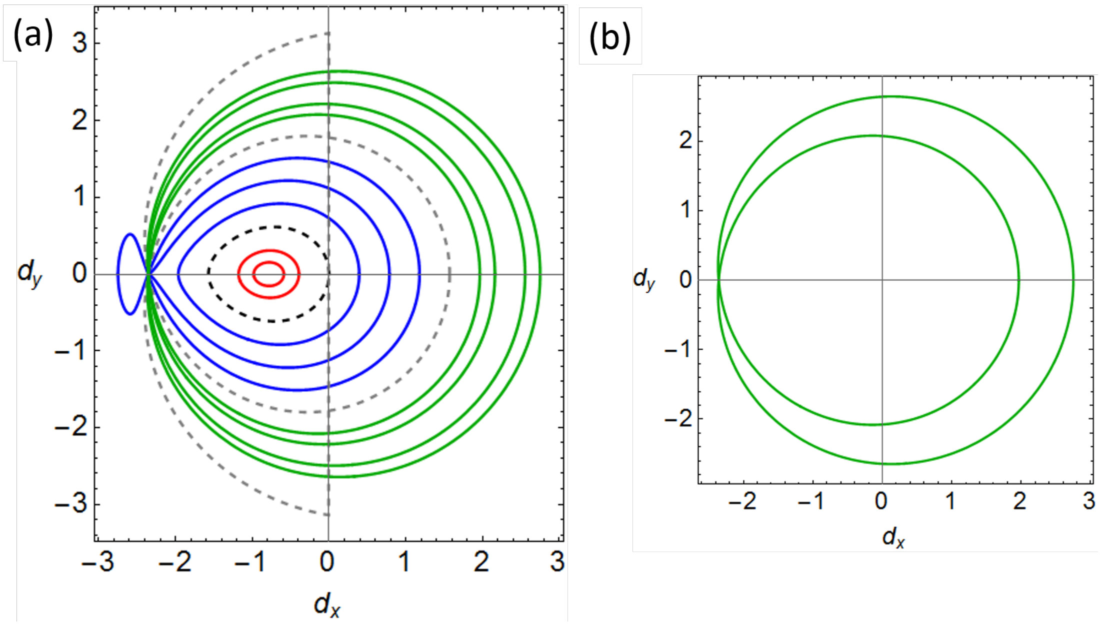

FIGURE 5.5: **Topological invariants and edge states of the protocol $\tilde{\hat{U}}$.** (a) Parametric plots of the curve $D = (d_x(q), d_y(q)) \equiv E(q)\,(n_x(q), n_y(q))$, for different values of $\delta \in [0, 2\pi)$. Red curves are for $\delta < \pi/2$ ($\delta = \pi/8, \pi/4$) and show a zero winding number (trivial topology), blue curves correspond to $\pi/2 < \delta < \pi/2$ ($\delta = 3\pi/4, \pi, 5\pi/4$) and winding number $\nu = 1$, since they enclose the origin one time, while, for $\delta > 3\pi/2$ (green curves shown for $\delta = 7\pi/4, 15\pi/8$) the winding number is $\nu = 2$, as can be better appreciated in panel (b), showing the case $\delta = 7\pi/4$. Dashed curves correspond to $\delta = \pi/2$ (black) and $\delta = 3\pi/2$ (gray), where the winding number is ill defined.

system.

From Eq: 5.44 it is evident that we can physically implement the protocol $\tilde{\hat{U}}$ by reordering the waveplates in our setup. We realize experimentally protocol $\tilde{\hat{U}}$ by the setup shown schematically in Fig. 5.6 (b). Using the relation $\sqrt{\hat{Q}(\delta)} = \hat{Q}(\delta/2)$, it is straightforward to see that $\tilde{U}^t = \sqrt{Q}WQW...QW\sqrt{Q}$. Hence, we realize the operator $\tilde{\hat{U}}^t$ by placing q-plates yielding an optical retardation $\delta/2$ ($\sqrt{Q}$) at the beginning and end of the optical path, while in the bulk of the walk we adopt the same sequence reported in Fig. 5.3 (a) (with the last q-plate removed). Overall, our quantum walk implements 7 steps of protocol $\tilde{\hat{U}}$ by means of a total of eight q-plates, six with retardation δ, two tuned at $\delta/2$ (first and last plates), separated by quarter-wave plates. In Fig. 5.6(d), we report the measure of the mean chiral displacement $\tilde{\mathcal{C}}$ generated by the single step operator $\tilde{\hat{U}}$. As in the case of protocol $\hat{U}_1$, this quantity accurately follows the theory prediction, providing an unambiguous detection of the Zak phase $\tilde{\gamma}$ of the infinite system after just 7 steps.

The bulk-edge correspondence in these driven systems requires two invariants C_0 and C_π, yielding respectively the number of 0- and π-energy edge states. As shown in Ref: [222], the complete topological classification of 1D chiral systems may be obtained by

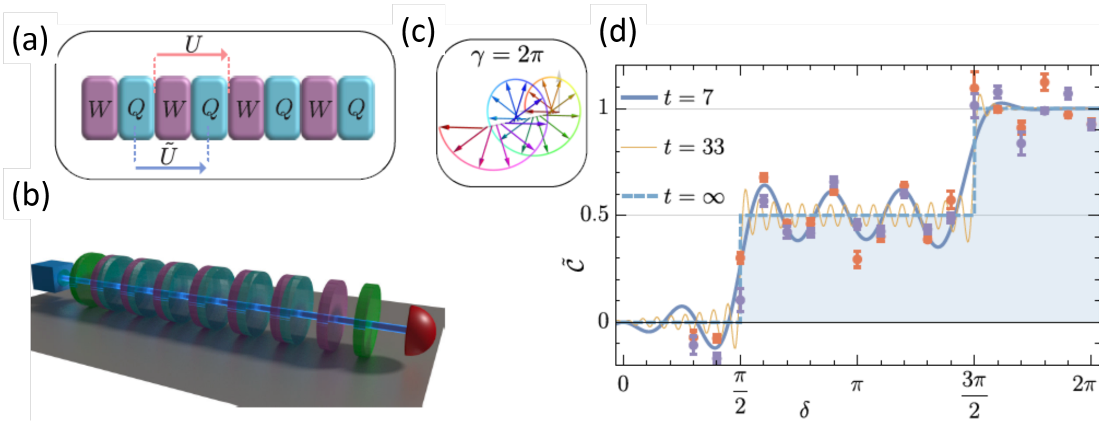

FIGURE 5.6: **Zak phase in the complementary time frame.** (a) Different choices of the origin of the periodic cycle lead to different protocols. (b) Sketch of the setup implementing protocol $\tilde{U} = \sqrt{Q} \cdot W \cdot \sqrt{Q}$. The two q-plates at the beginning and end of the optical path (shown in bright green) yield an optical retardation $\delta/2$, where δ is the optical retardation characterizing bulk q-plates (turquoise). (c) The unit vector $\tilde{\mathbf{n}}(k)$ associated to the operator $\tilde{U}$, for optical retardation $3\pi/2 < \delta < 2\pi$, winds twice around the chiral axis as k spans the whole Brillouin zone. (d) Mean chiral displacement $\tilde{\mathcal{C}}$ after a 7-steps QW with protocol $\tilde{U}$. The data-points are averages of ten experimental measurements, and error bars are the associated standard errors. Purple and orange colors refer, respectively, to input polarizations $|L\rangle$ and $(|L\rangle + i\,|R\rangle)/\sqrt{2}$. The lines display $S_\Gamma(t)$, for different values of the time t. At long times, S_Γ converges to the Zak phase $\tilde{\gamma}$. Image from Ref: [175].

means of the two quantities

$$C_0 = \frac{\tilde{\mathcal{C}} + \mathcal{C}}{2\pi} \quad \text{and} \quad C_\pi = \frac{\tilde{\mathcal{C}} - \mathcal{C}}{2\pi}, \tag{5.47}$$

which converge in the long time limit, respectively, to the number of 0- and π-energy edge states. By combining our measurements of the mean chiral displacements measured in the nonequivalent time frames we are now able to compute the invariants C_0 and C_π and detect the complete phase diagram of this system: the result is shown in Fig. 5.7. Once again, our measurements show a remarkably fast convergence towards the asymptotic limit.

Although here we investigated experimentally a specific quantum walk, our results are not restricted to QWs, nor to Floquet systems. Indeed, the mean chiral displacement provides a robust topological characterization of arbitrary spin-1/2 1D chiral systems, either static or periodically-driven. These may nowadays be realized in a variety of platforms, ranging from ultra-cold atoms in optical lattices to photonic waveguides, and from semiconductor quantum wells to optomechanical systems. While formerly known methods for detection of topological properties require a uniform filling of the band of interest, external forces, loss mechanisms, or fine-tuning so that only edge states are populated, the method proposed here quite remarkably achieves this goal by observing the free evolution of a single particle, initially localized on a single site in the bulk.

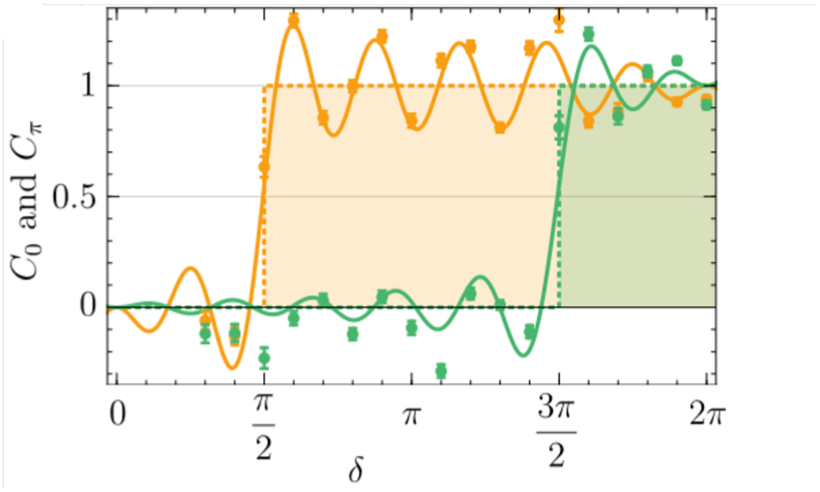

Figure 5.7: **Complete topological characterization of the QW protocol.** Topological invariants C_0 and C_π, obtained by combining the measurements of the mean chiral displacements $\mathcal{C}$ and $\tilde{\mathcal{C}}$ of protocols $\hat{U}$ and $\hat{\tilde{U}}$, and averaging the results obtained from the two initial states (error bars are the propagated standard errors). The dashed lines show the long-time limit of the topological indices C_0 and C_π, yielding respectively the number of edge states at 0- and π-energy. Image from Ref: [175].

This aspect may be specially beneficial for systems where filling a band is intrinsically challenging, such as bosonic condensates or phononic and photonic ensembles. Indeed, after this work, the measurement of the chiral displacement has been employed in other systems. For example, it has been recently used in in Ref: [168], and in the first observation of a topological Anderson insulator [224]. Moreover the results showed here for the particular case of a two dimensional coin, have been generalized for chiral systems with more than two internal states [225].

5.5 2D topological systems

Topology started to have a key role in solid state physics with the discovery of the Quantum Hall Effect (QHE), in 1980. This phenomenon was observed in a two dimensional electron gas [189] subjected to strong magnetic fields (of the order of few Tesla). At low temperatures, the Hall conductance, σ_{xy}, related to the current traveling in the direction perpendicular to an applied (in plane) electric field, behaves as a step-like function, rather than growing linearly with the magnetic field B. Interestingly, the jumps between one plateau and the other were shown to be integer multiples of the conductance quantum e^2/h. Moreover, the longitudinal conductance, related to Ohmic losses, is negligible in correspondence of the plateaus, while it exhibits peaks at the values of B where σ_{xy} is (in the zero temperature limit) discontinuous. This suggested that the quantized Hall conductance was associated to a non-dissipative charge transport. Many theoretical efforts have been employed to explain this phenomenon. In 1982, Thouless, Komoto, Nightale and Niu [188] calculated the Hall conductance for a two dimensional crystal discovering that it was proportional to a topological invariant, today called TKNN invariant, related to the sum of the Chern numbers of the occupied bands. This work allowed to understand that the quantization of the Hall conductance was related to the topological properties of the spectrum of the system. Moreover it became clear that the non-trivial Chern numbers where due to the breaking of time reversal symmetry (TRS), as a consequence of the applied magnetic field. This suggested that, to observe a quantum Hall effect, there is no need of strong magnetic fields if other ways of breaking TRS are found. Systems that exhibits non zero Chern numbers in absence of external magnetic fields are known as Anomalous Chern insulators [187]. Various models of Chern insulators without magnetic fields have been proposed: we cite the Haldane model of an honeycomb lattice with a zero net magnetic flux per unit cell [226], and the Bernevig Huges Zhang model [227] which can be used as a qualitative description of HgTe quantum wells with magnetic impurities [193]. In this section we will see how the 2D quantum walk protocol introduced in Chapter 4 describes a periodically driven Chern insulator. For completeness we mention that topological insulators with TRS do actually exist. We cite the two dimensional spin Hall insulators (theoretically proposed in graphene [228] but realized with HgTe quantum wells [229]) and the three dimensional topological insulators [230].

Let us proceed to introduce the Chern number. Our aim is to construct a topological invariant for a two dimensional system (here we follow Ref: [187]). We start by considering the Berry phase acquired on a closed loop ∂R, which is the boundary of a region R, in the 2D Brillouin zone:

$$\oint_{\partial R} \mathbf{A}(\mathbf{q}(\mathbf{s})) \cdot d\mathbf{q}(\mathbf{s}), \tag{5.48}$$

where s is the curve parameter. This equation can be written, by using the Stokes theorem, as:

$$\int_R \mathrm{curl}\mathbf{A}(\mathbf{q}) \cdot \mathbf{m}(\mathbf{q}) dS, \tag{5.49}$$

where $\mathbf{m}(\mathbf{q})$ is the normal to the surface D and dS the infinitesimal area over the surface. The vector field $\Omega(\mathbf{q}) = \mathrm{curl}\mathbf{A}(\mathbf{q})$ is known as *Berry curvature*. Often one also defines the *Berry curvature tensor* $\Omega_{ij} = \partial_i A_j - \partial_j A_i$, in terms of which Eq: 5.49 reads:

$$\int_R \epsilon_{ij} \Omega_{ij}(\mathbf{q}) d^2\mathbf{q}, \tag{5.50}$$

where ϵ_{ij} is the Levi-Civita symbol. Let us consider what happens when R is extended to the whole Brillouin zone. In this case $R = BZ$ is a closed surface, i.e. the boundary

∂R collapses to a set of measure zero. The integral:

$$\nu = \int_{BZ} \epsilon_{ij}\Omega_{i,j}(\mathbf{q})\frac{d^2\mathbf{q}}{2\pi}, \tag{5.51}$$

is known as *Chern number*. Notice that if the Stokes theorem can be applied, in order to turn back to a curvilinear integral, then the result would be zero since the Brillouin zone has no boundary. Hence, in order to have a non-zero Chern number, there must be a point in the Brillouin zone where the Berry connection is singular. This happens when it is not possible to find a smooth gauge over the whole space. For example, suppose to choose a gauge, $f(\mathbf{q})$, such that the first component of the Bloch wavefunction, denoted by $\psi(\mathbf{q})_1$, is real, i.e. to multiply $|\psi(\mathbf{q})\rangle$ by $\exp(if(\mathbf{q})) = |\psi(\mathbf{q})_1|/\psi(\mathbf{q})_1$. However, if at some points $\mathbf{q}_0$ this component vanishes, we cannot prolong our gauge choice to these points. Therefore one is constrained to make different gauge choices in separate patches of the Brillouin zone. For example, by defining the gauge: $\exp(ig(\mathbf{q})) = |\psi(\mathbf{q})_2|/\psi(\mathbf{q})_2$, one can require that in a closed region around $\mathbf{q}_0$ the second component of the Bloch wavefunction is real. At the boundary ∂P between two patches, P_1 and $P_2 = BZ - P_1$, the wavefunctions must be related by a gauge transformation, i.e. they must be equal except for a global phase $\chi(\mathbf{q})$. Let $\mathbf{A}_1$ be the Berry connection in P_1, and $\mathbf{A}_2$ the Berry connection in P_2. At the boundary ∂P these two fields are related by $\mathbf{A}_1(\mathbf{q}) = \mathbf{A}_2(\mathbf{q}) + \operatorname{grad}\chi(\mathbf{q})$. We can split the integral defining the Chern number as:

$$\nu = \int_{P_1} \operatorname{curl}\mathbf{A}_1(\mathbf{q})\cdot\mathbf{m}(\mathbf{q})\frac{dS}{2\pi} + \int_{P_2} \operatorname{curl}\mathbf{A}_2(\mathbf{q})\cdot\mathbf{m}(\mathbf{q})\frac{dS}{2\pi}. \tag{5.52}$$

The two integrals are on open surfaces, hence we can use Stokes theorem:

$$\begin{aligned}
\nu &= \int_{\partial P_1} \mathbf{A}_1(\mathbf{q})\cdot\frac{d\mathbf{q}}{2\pi} + \int_{\partial P_2} \mathbf{A}_2(\mathbf{q})\cdot\frac{\mathbf{q}}{2\pi} & (5.53)\\
&= \int_{\partial P_1} (\mathbf{A}_1(\mathbf{q}) - \mathbf{A}_2(\mathbf{q}))\cdot\frac{d\mathbf{q}}{2\pi} & (5.54)\\
&= \int_{\partial P_1} \operatorname{grad}\chi(\mathbf{q})\cdot\frac{d\mathbf{q}}{2\pi}. & (5.55)
\end{aligned}$$

Since $\chi(\mathbf{q})$ is a phase, it can change along a closed curve only by a multiple of 2π. hence the above integral is an integer number [187].

We thus showed that the Chern number can be treated as a topological invariant for 2D systems. Its value is different from zero in the case there is an obstruction in defining a smooth gauge over the whole Brillouin zone. The Chern number can be also seen as an extension of the winding number concept to two dimensions. Indeed in the case of a two level system described by the Hamiltonian: $\mathcal{H}(\mathbf{q}) = E(\mathbf{q})\mathbf{n}(\mathbf{q})\cdot\hat{\boldsymbol{\sigma}}$, the Chern number can be written as:

$$\nu = \int_{BZ} \frac{dq_x dq_y}{4\pi} \mathbf{n}(\mathbf{q}) \cdot \left(\partial_{q_x} \mathbf{n}(\mathbf{q}) \times \partial_{q_y} \mathbf{n}(\mathbf{q})\right). \tag{5.56}$$

The integrand is a map from an infinitesimal area on the Brillouin zone to an infinitesimal area of the Bloch sphere. This map wraps around the Bloch sphere an integer number of times, given by ν, due to the periodic boundary conditions of the Brillouin zone.
Due to the symmetry properties of the Berry curvature, the Chern number is zero if time reversal symmetry holds [187]. A system exhibiting a nontrivial Chern number, where time reversal symmetry was broken in absence of external magnetic fields, was realized experimentally for the first time in Ref: [231] by introducing ferromagnetic order in time reversal invariant topological insulators. In 2011, Lindner et al. [232] proposed the realization of topological Floquet insulators introducing a periodic driving on a trivial insulator. Floquet insulators with non-trivial Chern numbers have been recently realized in various systems, see e.g. Refs: [233, 234]. In the next section we investigate the topological properties of the 2D Quantum Walk introduced in the previous chapter showing that it can exhibit non-trivial Chern numbers.

5.6 Topological features of the protocol $\hat{U}_{2D}$

Let us turn back to the 2D quantum walk defined by the single step operator:

$$\hat{U}_{2D}(\delta) = \hat{T}_y(\delta) \cdot \hat{T}_x(\delta) \cdot \hat{W}, \tag{5.57}$$

where we remind that $\hat{T}_{x,y}(\delta)$ are shift operators implemented by g-plates with optical retardation δ. This operator realizes a quantum walk on a square lattice [38]. The Brillouin zone for this kind of lattices is again a square defined by the set $BZ = \{-\pi \leq q_x \leq \pi, -\pi \leq q_y \leq \pi\}$. In Fig. 5.8 (a) we show the Brillouin zone togheter with the high symmetry points Γ, M, R. The essential features of the quasienergy spectrum can be analyzed by looking at the quasienergy dispersion along the path joining these points, shown in Fig. 5.8 (a). The results are plotted in Fig. 5.8 (b) for various values of $\delta \in [0, \pi]$ (the results for $\delta \in [\pi, 2\pi]$ are specularly symmetric with respect to the case showed here). By changing δ the energy gap closes at $E = 0$, for $\delta = \pi/4$, and at $E = \pi$ for $\delta = 3\pi/4$. Hence we can expect a topological phase trasition in correspondence of these points. Interestingly, the gap closing at the Γ point, for $\delta = 3\pi/4$, suggests that in this system time reversal symmetry must be broken. Indeed, a general theorem, known as the *fermion doubling* theorem, states that, in a system where time reversal symmetry holds true, there cannot be an odd number of Dirac cones [218]. The violation of this result allows for the possibility of observing non trivial Chern numbers. Indeed

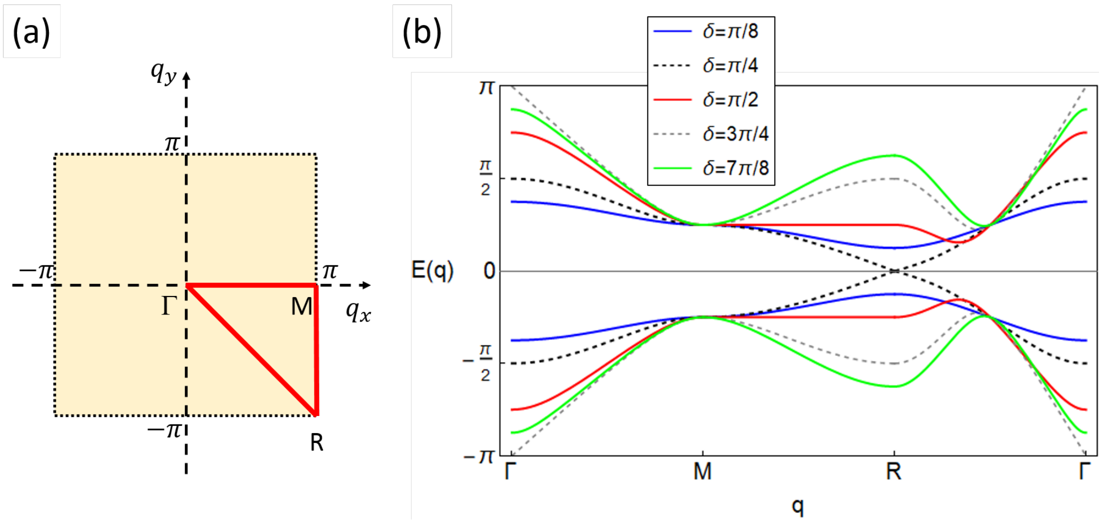

FIGURE 5.8: **Energy band dispersion for the protocol $\hat{U}_2 D$.** (a) The Brillouin zone is a square set. Here it is showed with the path (in red) joining the high symmetry points Γ, M, R. In (b) we plot the quasienergies along this path. Gap closing is observed at $E = 0$, for $\delta = \pi/4$ (dashed black line), and at $E = \pi$ for $\delta = 3\pi/4$ (dashed gray line).

we calculated the Chern number for different values of $\delta \in [0, \pi]$, obtaining a Chern number $\nu = 1$ for $\pi/4 < \delta < 3\pi/4$, and $\nu = 0$ otherwise. Moreover, by following the line of reasoning already used in the 1D case, we expect that the phase $3\pi/4 < \delta < 5\pi/4$ is topologically not trivial, with both 0- and π- edge modes. This can be confirmed by the calculation of generalized topological invariants, W_0 and W_π, that count the number of 0- and π- edge states (Fig.. 5.9 (a)). These invariants have been introduced in Ref. [206] to obtain a complete classification of Floquet Chern insulators. Their difference gives the Chern number. These result are confirmed by numerical calculations of the energy spectra for a finite system. For a 2D system one can consider an open boundary along the x direction, while keeping periodic boundary conditions along y. In such a case the y component of the quasi-momentum, q_y, is still a good quantum number. The Hamiltonian can thus be written in the form: $\hat{H} = \sum_{x,q_y} \mathcal{H}_x(q_y)$. The eigenvalues of $\mathcal{H}_x(q_y)$, for x fixed, form energy bands along the q_y direction. For the values of x near the boundary, if the topological phase of the finite system is not trivial, the bands will cross the values $E = 0$ and/or $E = \pi$. Thus edge states will appear with a finite group velocity $v_g(q_y)$ along the y direction. These states are modes confined at the edge of the system that propagate without dissipation or backscattering along the boundary. The energy spectra for our QW protocol are shown in Fig. 5.9 (b).

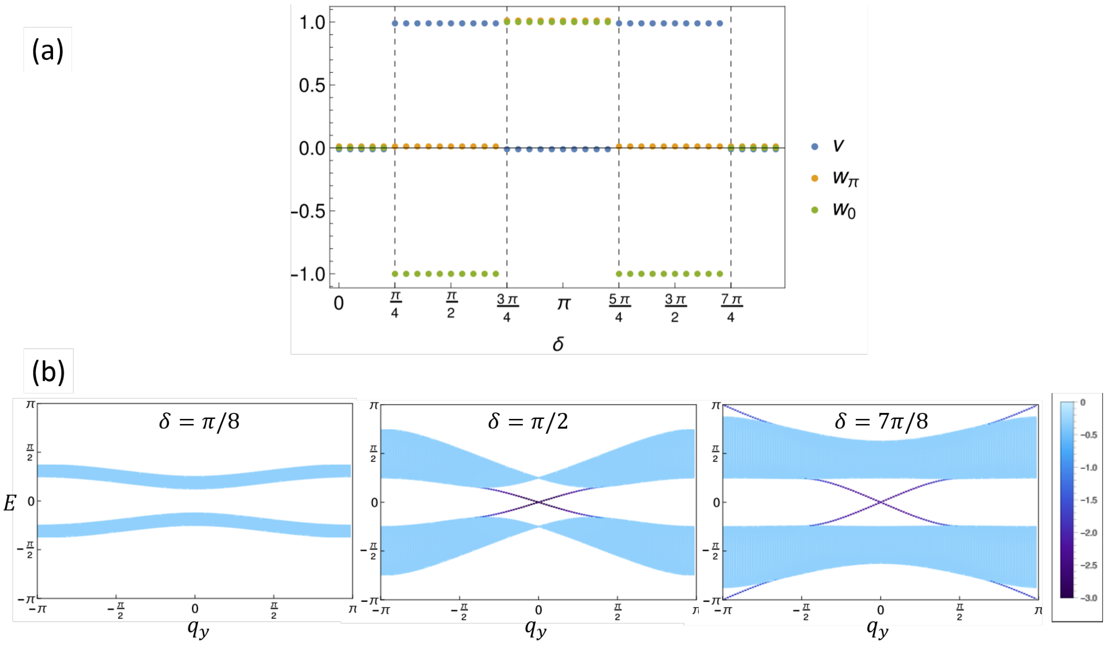

FIGURE 5.9: **Topological phases of $\hat{U}_2 D$.** (a) Phase diagram of our QW protocol in terms of the topological invariants $\mathcal{W}_0$, $\mathcal{W}_\pi$ defined in Ref. [206] and $\nu = \mathcal{W}_0 - \mathcal{W}_\pi$. These invariants provide the bulk-edge correspondence expected in topological systems, as clear from the quasi-energy spectra, (b), computed within cylindrical boundary conditions for $\delta = \pi/8$, $\delta = \pi/2$ and $\delta = 7\pi/8$. The color coding of the spectrum indicates the degree of localization on the two edges $m = -N$ (dark blue) and $m = N$ (red). As degree of localization of each state ψ we take the function $\log_{10}(1 - \langle \hat{x} \rangle_\psi)/N)$.

5.7 Experimental study of anomalous velocity effects in 2D quantum walks

[3] In order to experimentally ascertain the existence of a non-trivial Chern number in our system, we investigated the propagation in 5 steps of the ground state subjected to a force along the x direction. As we will briefly discuss now, the effect of an external field is to give rise to a displacement of the center of mass of the ground state in the direction perpendicular to the force. The amount of this displacement is indeed proportional to the Chern number multiplied by the force strength.

Let us consider a constant force F^x acting on a translational symmetric 2D system of Hamiltonian H. We can write a Bloch Hamiltonian $H(\mathbf{q})$ for each value of the quasi-momentum $\mathbf{q} = (q_x, q_y)$ in the Brillouin torus. Let us assume to be in adiabatic regime, namely that the momentum variation $\Delta q_x(t) = F^x t$ is slow with respect to the frequency associated to the energy gaps $|E^{(s\pm1)} - E^{(s)}|$, with s being the index of the band where the dynamics is starting from. As derived in Refs. [235, 236], in adiabatic approximation, the semi-classical equations of motion for a wave-packet $|\Psi_g(\mathbf{q}_0, s)\rangle$ sharply centered

---

[3] Some paragraphs and sentences of this section are adapted or copied verbatim from Ref. [38] which I coauthored

around an energy eigenstate $e^{i\mathbf{q}_0\mathbf{r}_0}|u_s(\mathbf{q}_0)\rangle$ read:

$$\begin{aligned}\dot{r}_i &= \partial_{q_i}E^{(s)}(\mathbf{q}) - \dot{q}_j\Omega^{(s)}_{ij}(\mathbf{q}), \\ \dot{q}_i &= F_i,\end{aligned} \tag{5.58}$$

where i and $j \in \{x, y\}$, and $\Omega^{(s)}_{ij}$ is the Berry curvature of the s-th band. Hence the wave-packet's velocity reads

$$\dot{r}_i = \partial_{q_i}E^{(s)}(\mathbf{q}) - F^j\Omega^{(s)}_{ij}(\mathbf{q}) = v^{(s)}_i(\mathbf{q}) - F^j\Omega^{(s)}_{ij}(\mathbf{q}), \tag{5.59}$$

where $\mathbf{v}^{(s)}$ is the standard group velocity of the s-th band and $-F^j\Omega^{(s)}_{ij}$ is its anomalous velocity. The wave-packet's displacements in adiabatic approximation are simply:

$$\langle\Delta x(t)\rangle_{\Psi_g} = v^{(s)}_x(\mathbf{q})t \tag{5.60}$$

$$\langle\Delta y(t)\rangle_{\Psi_g} = v^{(s)}_y(\mathbf{q})t + F^x\Omega^{(s)}_{xy}(\mathbf{q})t, \tag{5.61}$$

where we used the antisymmetry of the Berry curvature tensor: $\Omega^{(s)}_{yx}(\mathbf{q}) = -\Omega^{(s)}_{xy}(\mathbf{q})$. Eq. [**?**] shows that a non-zero Berry curvature gives rise to an additional term for the displacement in the direction perpendicular to the applied force. It comes straightforwardly that if the system's state is an homogeneous superposition of all the band's eigenstates the overall mean displacements is given by the integrals over the Brillouin zone of the single wave-packets displacements:

$$\langle\Delta y(t)\rangle_s = \frac{1}{2\pi}tF\nu^{(s)}, \tag{5.62}$$

$$\langle\Delta x(t)\rangle_s = 0. \tag{5.63}$$

The total displacement along the direction of the force is zero, as the integrals of both components of the standard group velocity over the Brillouin zone vanish. However, the integral of the anomalous displacement is proportional to the Chern number, $\nu^{(s)}$. Hence, this topological invariant can be measured by looking at the center of mass displacement of a state that fills completely the energy band of interest, under the application of an external field.

Going beyond the adiabatic regime will change the above result, due to effects caused by interband transitions. However one can still retrieve informations about the Chern number of the system even in this case. Let us consider a general two band system described by the unitary operator $\hat{U}$. Imagine now to fill one single band, say the lowest, i.e to prepare a mixed state, described by a density operator $\hat{\rho}$, that is an incoherent superposition of the band eigenstates. Under the application of an external force the system evolution will partially be subjected to the effects of the Berry curvature, and

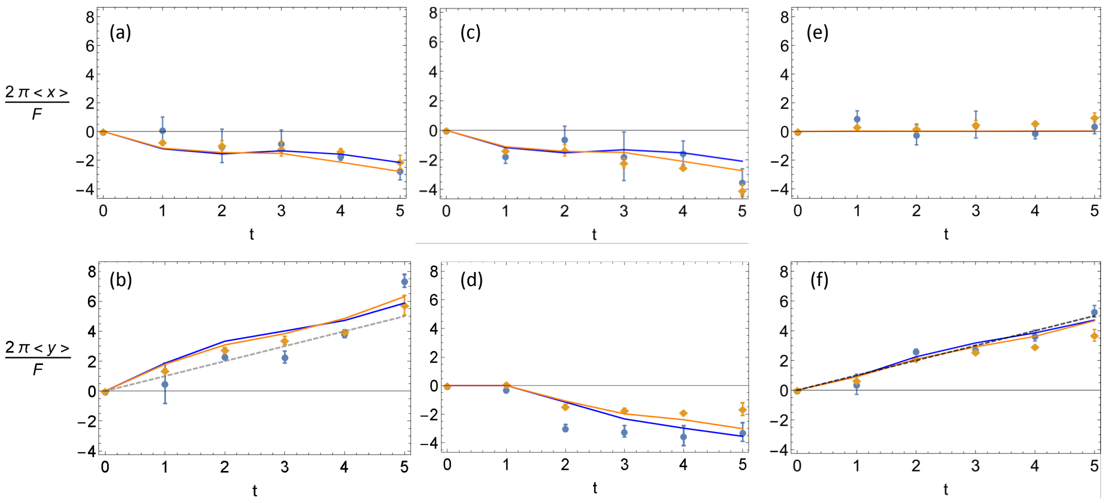

Figure 5.10: **Averaged anomalous velocity in non-trivial topological phase.** (a-b) Average displacements in the (a) x and (b) y directions for the direct protocol, divided by $F/2\pi$. We show results for $F = \pi/10, \pi/5$ (represented, respectively, by blue and orange plots). Points are experimental data, the continuous lines are the results of numerical simulations. Similar results where obtained for the inverse protocol (c-d). In (e-f) we show the difference (divided by two) for the results for the protocols U and U^{-1} in order to get rid of non-adiabatic effects. Indeed, in (f) we can appreciate that the difference between anomalous displacements is in agreement with the "Chern lines" (shown as dashed lines), while it can be seen (e) that the longitudinal displacement are the same in the two protocols. All experiments are repeated four times, after re-aligning all plates to take into account possible errors associated with this procedure. The calculation of uncertainties is detailed in Appendix D. Data are from Ref. [38]

partially to the interband transitions and band dispersion effects. Now, if we consider the inverted protocol, $\hat{U}^{-1}$, by preparing the same state of before (that now will be eigenstate of the *upper* band), the evolution under $\hat{U}^{-1}$ will be conditioned in the same way as before by interband transitions and band dispersion, but the displacements due to the Berry curvature will change sign (since the Berry curvature of the upper band has the opposite sign with respect to the lowest). Thus, by subtracting the center of mass displacements obtained by evolving the same initial state, $\hat{\rho}$, once with $\hat{U}$ and another with $\hat{U}^{-1}$, and dividing by two, one will obtain again the results in Eq. 5.62 and Eq. 5.63.

These considerations allow us to detect the effect of the Chern number, even in a quantum walk with few steps. We can indeed implement both the protocols $\hat{U}_{2D}(\delta)$ and $\hat{U}_{2D}^{-1}(\delta)$ and mimic an external force, with the same technique explained in Chapter 4 for the 1D case. The inverse protocol $\hat{U}_{2D}^{-1}(\delta)$ can be realized by suitably changing the ordering of the waveplates and their retardation. Indeed, using Eq. 5.44 and $\hat{W} =$

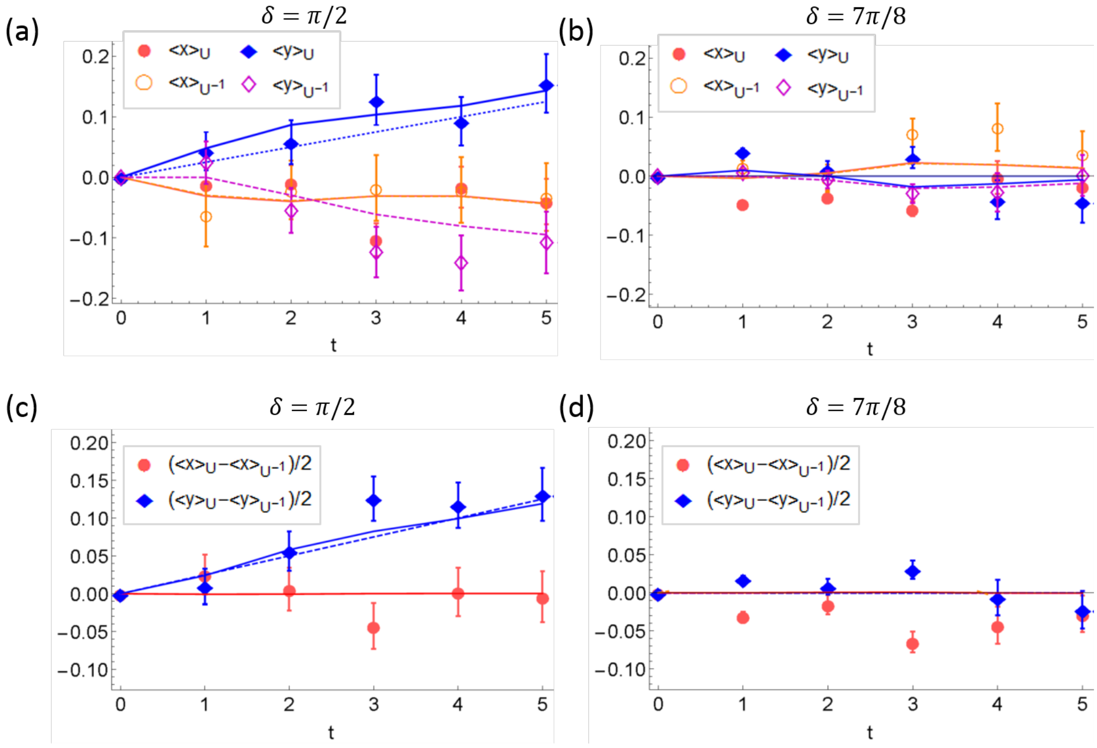

FIGURE 5.11: **Anomalous displacement in two different topological phases.** Here we show data for a smaller force, $F = \pi/20$ for $\delta = \pi/2$, (a) and (c), corresponding to the non-trivial topological phase with $\nu = 1$, and for $\delta = 7\pi/8$, (b) and (d), where $\nu = 0$. In (a) and (b) we show the average displacements, together with theoretical simulations, for the individual protocols $\hat{U}_{2D}$ (continuous lines) and $\hat{U}_{2D}^{-1}$(dashed lines). In (c-d) we show how subtracting the displacements for the two protocols we can suppress the non-adiabatic effects and recover, for the y-displacement, a contribution proportional to the Chern number. The calculation of uncertainties is detailed in Appendix D. Data are from Ref. [38]

$\hat{L}(\pi/2)$, we have that:

$$\begin{aligned}
\hat{U}_{2D}^{-1}(\delta) &= \left(\hat{T}_y(\delta)\cdot\hat{T}_x(\delta)\cdot\hat{L}(\pi/2)\right)^{-1} \\
&= \hat{L}^{-1}(\pi/2)\cdot\hat{T}_x^{-1}(\delta)\cdot\hat{T}_y^{-1}(\delta) \\
&= \hat{L}(3\pi/2)\cdot\hat{T}_x(2\pi-\delta)\cdot\hat{T}_y(2\pi-\delta). \qquad (5.64)
\end{aligned}$$

As initial states we prepared different Gaussian wavepackets $|\Psi(\mathbf{q})\rangle$, each centered around a given quasi-momentum $\mathbf{q}$, and with uniform polarization corresponding to the coin eigenstate, $\mathbf{n}(\mathbf{q})$, of $\hat{U}_{2D}(\delta)$. These states are good approximations of the system eigenstates: $|\mathbf{q}, \mathbf{n}(\mathbf{q})\rangle$ (as we have already seen in Chapter 4 when probing the group velocity dispersion). Choosing a set of uniformly distributed quasi-momentum values in the Brillouin zone $\{\mathbf{q}_{i,j}\}_{i,j=1\ldots M}$, we performed 5 steps of electric quantum walks for each wavepacket: $|\Psi(\mathbf{q}_{i,j})\rangle$. At each step we measured the mean displacement: $\langle\Delta\mathbf{r}(t)\rangle_{\Psi(\mathbf{q}_{i,j})}$.

Then, by summing over all the $\{\mathbf{q}_{i,j}\}$, we obtained an approximation of the integral:

$$\langle \Delta\mathbf{r}(t)\rangle = \int_{BZ} \langle \Delta\mathbf{r}(t)\rangle_{\Psi(\mathbf{q})} d\mathbf{q}^2/(4\pi^2).$$

We have chosen $M = 11$, i.e. we ran the experiment over 11×11 points of the BZ, after checking by numerical simulations that these give a good approximations of the above integral. This procedure was followed for both the protocols $\hat{U}_{2D}(\delta)$ and $\hat{U}_{2D}^{-1}(\delta)$.

Both the simulations and the experiments show that, for the individual protocols, a nonzero longitudinal displacement appears (see Fig. 5.10). Moreover, the anomalous displacement presents some, small, deviations from the predictions of the adiabatic theory, Eq. 5.62. All these contributions, unexpected from the adiabatic theory, can be eliminated by subtracting the results of the two protocols, as already explained above.

We performed the experiment for the cases $\delta = \pi/2$ where the Chern number is $\nu = 1$, repeating it for different values of the force: $F = \pi/5, \pi/10$. Fig. 5.10 (a-d) shows the results of the longitudinal and anomalous displacements for the individual protocols. Fig. 5.10 (e-f) shows that the subtraction of the results, divided by 2, gives rise to a behavior of the mean displacement in agreement with the predictions of Eqs: 5.62 and 5.63.

Moreover we studied the same problem for a smaller force $F = \pi/20$ considering two different topological phases. In particular we explored the cases $\delta = \pi/2$, where the Chern number (for the upper band) is $\nu = 1$, and $\delta = 7\pi/8$ where $\nu = 0$. As shown in Fig. 5.11 it is possible to appreciate the fact that, while for $\delta = \pi/2$ the anomalous displacement increases linearly with time, for $\delta = 7\pi/8$ it is zero (within the experimental errors).

In conclusion we have demonstrated the experimental realization of a 2D DTQW that simulates a periodically driven Chern insulator. The effect of the non-trivial topology in this system has been investigated by the analysis of anomalous displacement in the motion of wavepackets subjected to an external force. We also observed the effect of non-adiabatic contributions that are still not completely understood and will be the subject of future investigations. The exploration of the properties of this new protocol is still in its infancy. Future work will be devoted to generalizations of the presented protocols to different lattice geometries (for example triangular lattices), and the study of dynamical topological phase transitions [237] in 2D quantum walks. If transforming the platform into a loop architecture, it will be possible to realize other interesting experiments and significantly increase the number of steps. Moreover, a Fourier transform at each step would in principle allow direct access to the lattice space, opening for the possibility of implementing boundaries between different topological phases and position dependent operations. This would be ideal for observing edge modes and study more complex dynamics. Finally, going in the single photon regime would be interesting for studying multi-particle correlations and quantum statistics in 2D QWs, or performing

Boson Sampling experiments.

Conclusions

Light is a natural phenomenon with a rich variety of features that can be controlled with current technologies. Among these, we considered those degrees of freedom which are infinite-dimensional, motivated by the possibility of employing these features in the simulation of quantum phenomena occurring in large Hilbert spaces. In particular we focused on two degrees of freedom: the Orbital Angular Momentum, and the transverse wavevector component (that can be associated with the *linear* momentum). Using special devices developed in our lab, named q-plates and g-plates, respectively, we implemented quantum walk processes on one and two dimensional lattices.

In particular, our 1D platform allowed us to give a complete topological characterization of the protocol by measuring the topological invariant in two independent chiral time frames.

This measurement required the reconstruction of the probability distribution of the state at each step. In this setup this means to measure the OAM power spectrum of the beam, a task that is typically done by means of many projective measurements. This procedure can become prohibitive for high numbers of modes to be detected. This has motivated us to develop an interferometric technique which allows one to reconstruct the OAM distribution by digital analysis of few image recordings. With an additional measurement, we showed that it is even possible to reconstruct the full electric field. Indeed we used this technique to determine with high precision the amplitude and phase shape of the modes produced by a q-plate.

In the transverse momentum based QW, we demonstrated the possibility to simulate the action of an external force and we employed this feature to detect anomalous displacement effects related to non-trivial Chern numbers in the 2D protocol. In the near future we plan to generalize this protocol considering the possibility of changing the retardation of the uniform waveplates (until now we have used them only as quarter waveplates) and considering the case in which the operators $\hat{T}_x$ and $\hat{T}_y$ have different optical retardation. The technique described in the last chapter can then be used to reconstruct the topological phase diagram of this generalized protocol. However we have also seen that there are topological phases that host protected edge states even if the

Chern number is zero. The non-triviality of these phases cannot be ascertained by the measurement of center of mass displacements but will require a different technique. A possible approach can be the observation of dynamical topological phase transitions, which will require the reconstruction of the full quantum state, a task that can be performed in our architecture by making the final state interfere with the initial one. More insights on the topological features of our system can be obtained exploring the formation of complex polarization patterns in the Brillouin zone, i.e. at the exit of the QW. Hence we can extend the approach of Chapter 3 to more complex systems of tunable anisotropic devices and study the topology and evolution of polarization singularities.

In the future we aim to further develop the 2D platform for studying more complex protocols, eventually also on triangular lattices. Including an additional coin operator we can realize the 2D Grover quantum walk, a fundamental element for the realization of the Grover search algorithm. More possibilities can emerge if our architecture is inserted into an optical feedback loop, allowing to easily increase the number of steps and, in principle, to compensate for the undesired phase shifts described in Chapter 4. Moreover, inserting at every step a $4f$ system would allow to switch to the lattice space, where spatially dependent operations can be performed.

The transverse wavevector as a degree of freedom for quantum application is a resource largely unexplored. The use of g-plates, and the possibility to switch to the more usual path encoding (by ordinary optical Fourier transform), would pave the way for new interesting applications.

Appendix A

Limitations on the set of detectable spatial modes.

[1] In this Appendix we consider the limitation in the number of spatial modes detectable with the technique introduced in Chapter 2. The finite size of the detector area and the finite dimension of sensor pixels impose certain restrictions on the features of the helical modes that can be resolved in our setup. Let us consider the simple case wherein we want to decompose the signal field in terms of $\mathrm{LG}_{p,m}$ modes, and we want to evaluate the p, m-bandwidth of detectable modes. We consider only the case $m > 0$, since only the absolute value $|m|$ is relevant to our discussion. Consider a camera with $N \times N$ pixels, with pixel dimensions $d \times d$ (in our setup $N = 576$ and $d = 9$ μm). We define the following quantities:

$$r_{\max} = d * N/2, \tag{A.1}$$

$$r_{\min} = md/\pi, \tag{A.2}$$

$$r_1 = w(z)\left\{\frac{2p+m-2-[1+4(p-1)(p+m-1)]^{1/2}}{2}\right\}^{1/2}, \tag{A.3}$$

$$r_p = w(z)\left\{\frac{2p+m-2+[1+4(p-1)(p+m-1)]^{1/2}}{2}\right\}^{1/2}, \tag{A.4}$$

$$\tilde{r}_p = w(z)\left\{2p+m+1\right\}^{1/2}. \tag{A.5}$$

Here $r_{\max}$ is the maximum radius available on the sensor; $r_{\min}$ is the minimum radial distance where azimuthal oscillation associated with the OAM content of the $\mathrm{LG}_{p,m}$ mode can be detected, before facing aliasing issues; r_1 is a lower bound for the first root of the Laguerre polynomials contained in the expression of LG modes; similarly, r_p is the

---

[1] This appendix is adapted from the work [40] which I coauthored

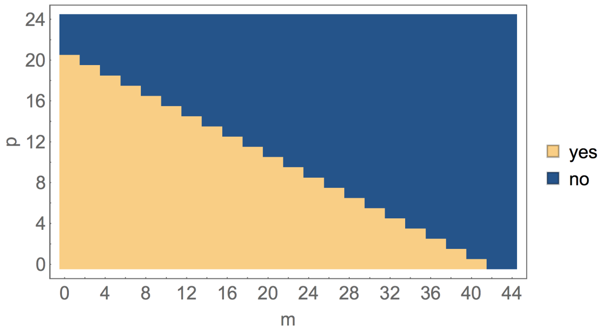

FIGURE A.1: **Detectable LG modes**. Different colors, as reported in the legend, indicate whether a specific $\mathrm{LG}_{p,m}$, in a transverse plane $z = 30$ cm and with a beam waist $w_0 = 0.16$ mm [$w(z = 30 \text{ cm}) \to 0.4$ mm] can be resolved in our setup. These parameters correspond to the ones used for the complete spatial decomposition of the HyGG beam generated by a q-plate ($q = 4, \delta = \pi$) in terms of LG beams. Image taken from Ref. [40]

upper bound for the $p-$th root, while $\tilde{r}_p$, with $r_p < \tilde{r}_p$, delimits the oscillatory region of the Laguerre polynomials [238, 239]. Interestingly, the spatial region $r_1 < r < \tilde{r}_p$ well approximates the area containing all the power associated with the mode. At the same time, the quantity $\Lambda = (r_p - r_1)/p$ well describes the average distance between consecutive nodes of the LG mode, defining the periodicity of their radial oscillations. A given $\mathrm{LG}_{p,m}$ mode is then "detectable" (or properly "resolvable") if all the following conditions are satisfied:

$$\begin{cases} r_{\min} < r_1 & \text{(i)} \\ r_p < r_{\max} & \text{(ii)} \\ \Lambda > 2d & \text{(iii)} \end{cases} \tag{A.6}$$

Indeed, we are requiring that (i) the field is vanishing below the azimuthal aliasing threshold given by $r_{\min}$, that (ii) all the power associated with the mode is contained in the sensor area and (iii) that the field radial oscillations have a spatial period such that at least two pixels are contained in a single period, respectively (radial aliasing limit). It is easy to check that in our configuration, where the beam waist is $w(z) = 0.4$ mm, conditions (i) and (iii) are always satisfied for the values of $\{p, m\}$ that are solution of (ii), i.e. the limiting factor is only the dimension of the sensor area. By solving such inequality, we get the relation

$$p < \left(\frac{N^2 d^2}{4w^2(z)} - m - 1 \right) /2 \tag{A.7}$$

In Fig. A.1 we plot a color map for a rapid visualization of detectable modes. If we apply this analysis to the case of Fig. 2.3, in which a beam with $m = 8$ is studied, we obtain that only radial modes with $p < 16$ can be detected. In general, for smaller values of $w(z)$ the determination of detectable LG mode is more complex and requires the complete resolution of the system of inequalities system given in (A.6).

Appendix B

Determination of C-points position

[1] Here we give a detailed description of the derivation of the C-points position (see Fig. 3.7). We recall here the general expression describing a beam generated by a q-plate when shined by a H or V polarized Gaussian beam:

$$
\begin{aligned}
|OUT\rangle = C_R(\rho,\zeta,\phi;\delta)|R\rangle \pm C_L(\rho,\zeta,\phi;\delta)|L\rangle = \\
\Big(\mathrm{TEM}_{00}(\rho,\zeta)\cos(\delta/2) + i f_{|m|}(\rho,\zeta)e^{-im\phi}\sin(\delta/2)\Big)|R\rangle \\
\pm\Big(\mathrm{TEM}_{00}(\rho,\zeta)\cos(\delta/2) + i f_{|m|}(\rho,\zeta)e^{im\phi}\sin(\delta/2)\Big)|L\rangle.
\end{aligned}
\tag{B.1}
$$

where the plus or minus sign is for H and V input polarizations, respectively, $\zeta = z/z_R$ is the propagation distance normalized with respect to the Rayleigh range z_R, and $m = 2q$. In our experiment the function $f_{|m|}$ is given by Hypergeometric Gaussian mode $\mathrm{HyGG}_{-|m|,|m|}$. It is worth noting that specific architectures allow using the q-plate to generate helical modes with a different radial profile; as an example, recently a q-plate placed inside a laser cavity has been exploited for the generation of high quality Laguerre-Gauss VBs [104] with $p = 0$. For this reason, we consider here also the case $f_{|m|} = LG_{0,m}$. As we will show in the following, the C-points positions can be deduced analytically in this case.

The C-point position at a given δ and ζ can be obtained simply by solving the implicit equation $C_{L,R}(\rho,\zeta,\phi;\delta) = 0$ (see Eq. B.1). We limit ourselves to searching for the distance of C-points from the center, which can be found by solving the simplified equation

---

[1] Some paragraphs and sentences of this appendix are adapted or copied verbatim from the work [83] which I coauthored

$|C_{L,R}(\rho,\zeta,\phi;\delta)|^2 = 0$. Explicitly, this reads:

$$\begin{aligned}&\cos^2(\delta/2)|\mathrm{TEM}_{00}(\rho,\zeta)|^2 + \sin^2(\delta/2)|f_{|m|}(\rho,\zeta)|^2 + \\ &2\cos(\delta/2)\sin(\delta/2)Re\{ie^{-im\phi}\mathrm{TEM}^*_{0,0}(\rho,\zeta)f_{|m|}(\rho,\zeta)\} = 0.\end{aligned} \tag{B.2}$$

A solution for such equation exists only if the following condition holds

$$\cos^2(\delta/2)|\mathrm{TEM}_{00}(\rho,\zeta)|^2 = \sin^2(\delta/2)|f_{|m|}(\rho,\zeta)|^2; \tag{B.3}$$

hence, by solving jointly Eq. B.2-B.3 we are left with an implicit equation for ρ as function of ζ. If needed, then the solution can be inserted into Eq. B.2 to find the azimuthal coordinates of the singularities.

The case $f_{|m|} = \mathrm{HyGG}_{-|m|,|m|}$ can be solved only numerically. Some solutions are shown in Fig. 3.7 and discussed in the main text. Here we focus on the case $f_{|m|} = LG_{0,m}$ where we can find an analytical expression for C-points positions as a function of ζ. In this case Eq. B.3 reads:

$$\left|\frac{LG_{0,m}(\rho,\zeta)}{TEM_{0,0}(\rho,\zeta)}\tan(\delta/2)\right|^2 = \frac{2^{|m|}}{m!}\frac{\rho^{2|m|}}{(1+\zeta^2)^{|m|}}\tan^2(\delta/2) = 1. \tag{B.4}$$

It follows that the distance of C-points from the beam center $\rho_C(\zeta)$ is given by:

$$\rho_C(\zeta) = \left[\sqrt{\frac{m!}{2^{|m|}}}\cot^2(\delta/2)\right]^{1/2|m|}\sqrt{1+\zeta^2}. \tag{B.5}$$

In order to evaluate if such singularities are contained in the beam or not, it is interesting to compare this result with the expression of the beam radius, defined as [22]:

$$\sigma^2(\zeta) = \int I(\rho,\zeta,\phi)\rho^3 d\rho d\phi, \tag{B.6}$$

where $I(\rho,\zeta,\phi)$ is the beam intensity. From Eq. B.1 with $f_{|m|} = LG_{0,m}$ we obtain:

$$\sigma(\zeta) = \sqrt{\frac{1+|m|\sin^2(\delta/2)}{2}}\sqrt{1+\zeta^2}. \tag{B.7}$$

The corresponding beam divergence is simply:

$$\theta_{rms}(\delta,|m|) = \sqrt{[1+|m|\sin^2(\delta/2)]/2}, \tag{B.8}$$

where r.m.s. stands for root-mean-square. By comparing Eq. B.7 and Eq. B.5 we can observe that the beam radius has the same functional form as the C-point position. The divergence of the latter is:

$$\theta_c(\delta, |m|) = \left[\sqrt{\frac{m!}{2^{|m|}}}\cot^2(\delta/2)\right]^{1/2|m|}. \tag{B.9}$$

In conclusion, for LG beams, C-points can diverge more or less rapidly than the beam radius depending on the value of δ. Thus, there exists a critical value of δ above which C-points are expelled from the beam and the polarization pattern has a non trivial topology. This critical value can be found by solving the equation $\theta_c(\delta, |m|) = \theta_{rms}(\delta, |m|)$. However, we observe that our analysis aims to show only qualitative features: quantitative results are ambiguous as multiple definition of the beam divergence can be given (for instance the quantity $\sqrt{2}\theta_{rms}$ is often used). In conclusion, we point out that the same analysis cannot be done for HyGG beams since their r.m.s divergence is not well defined [22].

Appendix C

Possible deviations from the ideal QW evolution in the transverse linear momentum based platform

During propagation through the QW set-up, effects related to free space propagation of modes $|\mathbf{m}_{x,y}\rangle$ can act as perturbations to the ideal QW dynamics. In this Appendix

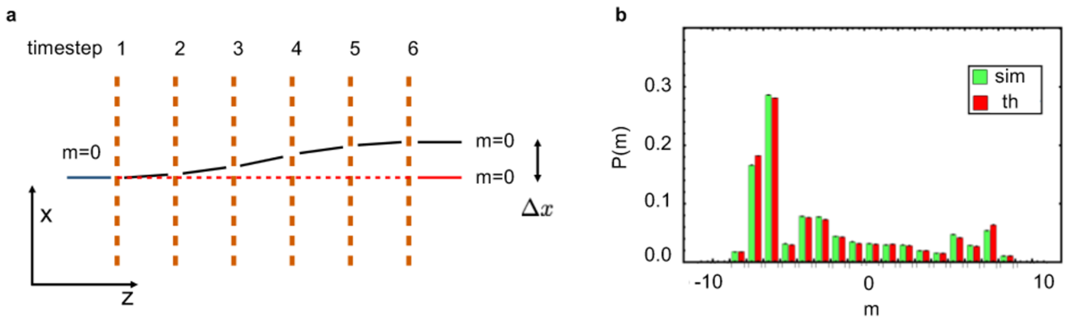

Figure C.1: **Deviations from the perfect simulation of a QW process.** **a**, at the input of the 1D QW, we have a single beam with $\mathbf{k}_\perp = 0$, localized at the lattice site $m = 0$. At the exit of a 6-steps QW, we consider two contributions at the final wavefunction at site $m = 0$. One is resulting from the part of the input state that has been left unchanged (red). The second has gained Δk transverse momentum at the first three steps, and then has acquired opposite momentum at steps 4 to 6 (black). At the exit of the walk, also this component corresponds to the lattice site $m = 0$. However, the associated beams have some differences, which represent deviations from the ideal QW; being related to the same lattice site, they should be identical. First, they exit the walk laterally displaced by Δx, and the lack of overlap may ruin the interference, similarly to a decoherence effect. Second, the upper beam suffered a longer optical path, hence it accumulated a relative phase with respect to the central one. Finally, at each g-plate, the effective value of α_0 changes at each step for the deflected beam. **b**, we show the results of a numerical simulation of a 1D walk with protocol $U = T_x W$, for $\delta = \pi/2$ and for an input state $|0, R\rangle$, compared to a simulation of the ideal QW dynamics. After 10 steps differences are minimal. Figure adapted from Ref. [38]

we describe the main phenomena that can take place in our walk, and investigate their effect with the help of a numerical analysis. For simplicity, we will refer to a 1D QW, where modes $|\mathbf{m}_{x,y}\rangle$ are characterized by a single integer $m_x = m$.
There are essentially two "undesired" effects that arise when considering the tilt in propagation direction *inside* the quantum walk:

1. At the end of the quantum walk, to each value of $\mathbf{k}_\perp$ will correspond the superposition of waves that have followed different paths in the wavevector space, as illustrated in Fig. C.1. These trajectories are actually associated with different optical paths, which give rise to additional relative phases. The latter are absent in the ideal QW dynamics and can modify the interference of the wavefunction components associated with these paths. To simulate such effect, the final amplitude of each mode $|\mathbf{m}_{x,y}\rangle$ should be calculated as the sum of all components related to these optical paths, multiplied by their relative phase. When propagating between two consecutive timesteps, mode $|0\rangle$ and different mode $|s\rangle$ accumulate a phase delay $\Delta\phi_1 = (\pi\lambda d s^2)/(\Lambda^2)$, where d is the distance between consecutive steps.

2. The two beams considered in point 1) have an imperfect overlap that makes them distinguishable, since they are propagating along axes that are parallel but laterally displaced. These modes have a finite extension, and the absence of perfect spatial overlap results in a reduction of the interference visibility, similarly to a decoherence effect. Referring to the case presented above, the two modes accumulate a lateral shift $|\Delta x| = d\lambda s/\Lambda$.

3. A tilted beam hits two consecutive g-plates at points that have a relative shift. For instance, in Fig. C.1 we observe a mode $|1\rangle$ that at the second timestep is laterally displaced by Δx. The action of a g-plate, as described in Eq. 4.20, is derived by considering a Gaussian beam that hits the plate with its central position at $(x, y) = (0, 0)$. If the beam center is displaced by Δx, Eq. 4.20 keeps holding if replacing α_0 with $\alpha_0' = \alpha_0 + \Delta x\pi/\Lambda$, which represent the effective LC orientation at the beam central position. By looking at Eq. 4.20, we can observe that this effect results in additional phases accumulated by modes $|m\rangle$ during propagation, which have to be added to the phases associated with the different path lengths (see the previous point 1).

In Fig. C.1, we provide a comparison between an ideal QW evolution and the simulation of the real beam propagation through our set-up, by taking into account effects described in points 1-3) and using the real system parameters. After 10 steps of a 1D walk, we observe no significant deviations. This guarantees that also 5 steps of a 2D would not suffer any deviations. Indeed, such effects strongly depends on the order of the modes that are excited in the walk. In the first case, if starting from a localized input, the highest-order mode that can be excited is $|m = \pm 10\rangle$. In the 2D case, these modes would be those with $|\mathbf{m}_{xy}| = 5$. When increasing the number of steps, we expect these systematic errors to become more relevant. These issues could be tackled by (i) changing the system parameters, in particular by reducing Λ and decreasing the step distance d, or (ii) by adopting a loop architecture combined with an imaging system. Indeed, by imaging the output of each step to the input of the following one, all the effects discussed above are canceled.

Appendix D

Extimation of errors in the measurement of the anomalous velocity

In Chapter 5, Figs. 5.10 and 5.11, we have presented experimental results for the longitudinal and anomalous displacement of the ground state in ad 2D QW with an applied external force [38]. Results were averages over 4 different measurements. However, a more careful estimate of statistical errors should take into account the imperfection of the system. In particular we considered the fact that, in our current setup, we cannot control with extreme precision the α_0 angles of the $\hat{T}_y$ operators. Hence the relative value of these angles is determined during the mounting procedure. We have measured a standard deviation around the value $\alpha_0 = 0$ of $\sigma = 5$ degrees. In order to take account these effects we ran multiple simulations of the QW choosing each time s a different sequence of values $\{\alpha_{0,i}^{(s)}\}_{i=1,\ldots,N}$, extracted randomly from a Gaussian distribution, centered around $\alpha_0 = 0$ and with width σ. The simulations were performed 500 times and the resulting average displacement $\langle \mathbf{r}^{(s)} \rangle$ for each event was extracted. We then took the standard deviation $\sigma_{\mathbf{r}}$ of the set $\{\langle \mathbf{r}^{(s)} \rangle\}_{s=0,\ldots,500}$. Considering also the standard errors of the mean, $\Sigma_{\mathbf{r}}$, obtained from the 4 repeated experimental measurements, we calculated the errors in Figs. 5.10 and 5.11 by summing in quadrature $\sigma_{\mathbf{r}}$ and $\Sigma_{\mathbf{r}}$.

Bibliography

[1] Jackson, J. D. *Classical electrodynamics* (Wiley, New York, NY, 1999), 3rd ed. edn. URL `http://cdsweb.cern.ch/record/490457`.

[2] Enk, S. J. V. & Nienhuis, G. Rules and Eigenvalues of Spin and Orbital Angular Momentum of Radiation Fields. *Journal of Modern Optics Commutation* **41**, 963–977 (1994).

[3] Barnett, S. M. Rotation of electromagnetic fields and the nature of optical angular momentum. *Journal of Modern Optics* **57**, 1339–1343 (2010).

[4] Barnett, S. M. *et al.* On the natures of the spin and orbital parts of optical angular momentum Energy conservation and the constitutive relations in chiral and non-reciprocal media 1–4 (2016).

[5] Siegman, A. *Lasers* (University Science Books, 1986). URL `https://books.google.it/books?id=1BZVwUZLTkAC`.

[6] Saleh, B. E. A. & Teich, M. C. *Fundamentals of photonics; 2nd ed.* Wiley series in pure and applied optics (Wiley, New York, NY, 2007). URL `https://cds.cern.ch/record/1084451`.

[7] Yariv, A. *Quantum electronics* (Wiley, 1989). URL `https://books.google.it/books?id=UTWg1VIkNuMC`.

[8] van Enk, S. & Nienhuis, G. Eigenfunction description of laser beams and orbital angular momentum of light. *Optics Communications* **94**, 147 – 158 (1992). URL `http://www.sciencedirect.com/science/article/pii/003040189290424P`.

[9] Beth, R. A. Mechanical detection and measurement of the angular momentum of light. *Phys. Rev.* **50**, 115–125 (1936). URL `https://link.aps.org/doi/10.1103/PhysRev.50.115`.

[10] Bandres, M. A. & Gutiérrez-Vega, J. C. Circular beams. *Opt. Lett.* **33**, 177–179 (2008). URL `http://ol.osa.org/abstract.cfm?URI=ol-33-2-177`.

[11] Padgett, M. & Bowman, R. Tweezers with a twist. *Nature Photonics* **5**, 343–348 (2011).

[12] Molina-Terriza, G., Vaziri, A., Rehacek, J., Hradil, Z. & Zeilinger, A. Triggered qutrits for quantum communication protocols. *Physical Review Letters* **92**, 167903–1 (2004). `0401183`.

[13] Nagali, E. *et al.* Optimal quantum cloning of orbital angular momentum photon qubits through Hong–Ou–Mandel coalescence. *Nature Photonics* **3**, 720–723 (2009). URL `http://dx.doi.org/10.1038/nphoton.2009.214`. `1010.5214`.

[14] Mirhosseini, M. *et al.* High-dimensional quantum cryptography with twisted light. *New Journal of Physics* **17**, 1–12 (2015). `1402.7113`.

[15] Vallone, G. *et al.* Free-space quantum key distribution by rotation-invariant twisted photons. *Physical Review Letters* **113**, 1–8 (2014). `1402.2932`.

[16] D'Ambrosio, V. *et al.* Complete experimental toolbox for alignment-free quantum communication. *Nature Communications* **3**, 961 (2012). URL `http://www.nature.com/doifinder/10.1038/ncomms1951{%}5Cnhttp://dx.doi.org/10.1038/ncomms1951`. `1203.6417`.

[17] Cardano, F., Karimi, E., Marrucci, L., De Lisio, C. & Santamato, E. Violation of Leggett-type inequalities in the spin-orbit degrees of freedom of a single photon. *Physical Review A - Atomic, Molecular, and Optical Physics* **88**, 1–5 (2013). `arXiv:1304.1738v1`.

[18] Karimi, E. *et al.* Hardy's paradox tested in the spin-orbit Hilbert space of single photons. *Physical Review A - Atomic, Molecular, and Optical Physics* **89**, 1–7 (2014). `arXiv:1403.5681v1`.

[19] Erhard, M., Fickler, R., Krenn, M. & Zeilinger, A. Twisted photons: New quantum perspectives in high dimensions. *Light: Science and Applications* **7**, 17111–17146 (2018). URL `http://dx.doi.org/10.1038/lsa.2017.146`. `1708.06101`.

[20] Zucker, H. Optical Resonators With Variable Reflectivity Mirrors. *Bell System Technical Journal* **49**, 2349–2376 (1970). URL `http://ieeexplore.ieee.org/lpdocs/epic03/wrapper.htm?arnumber=6772781`.

[21] Allen, L., Beijersbergen, M. W., Spreeuw, R. J. C. & Woerdman, J. P. Orbital angular momentum of light and the transformation of Laguerre-Gaussian laser modes. *Physical Review A* **45**, 8185–8189 (1992).

[22] Vallone, G. *et al.* General theorem on the divergence of vortex beams. *Phys. Rev. A* **94**, 023802 (2016). URL `https://link.aps.org/doi/10.1103/PhysRevA.94.023802`.

[23] Abramowitz, M. & Stegun, I. A. *Handbook of Mathematical Functions with Formulas, Graphs, and Mathematical Tables* (Dover, New York, 1964), ninth dover printing, tenth gpo printing edn.

[24] Karimi, E., Zito, G., Piccirillo, B., Marrucci, L. & Santamato, E. Hypergeometric-gaussian modes. *Opt. Lett.* **32**, 3053–3055 (2007). URL `http://ol.osa.org/abstract.cfm?URI=ol-32-21-3053`.

[25] Bechmann-Pasquinucci, H. & Tittel, W. Quantum cryptography using larger alphabets. *Phys. Rev. A* **61**, 062308 (2000). URL `https://link.aps.org/doi/10.1103/PhysRevA.61.062308`.

[26] Zhou, Y. *et al.* Sorting laguerre-gaussian modes by radial quantum number. In *Conference on Lasers and Electro-Optics*, JTh2A.4 (Optical Society of America, 2018). URL `http://www.osapublishing.org/abstract.cfm?URI=CLEO_SI-2018-JTh2A.4`.

[27] Gu, X., Krenn, M., Erhard, M. & Zeilinger, A. Gouy Phase Radial Mode Sorter for Light: Concepts and Experiments. *Physical Review Letters* **120**, 103601 (2017). URL `https://link.aps.org/doi/10.1103/PhysRevLett.120.103601http://arxiv.org/abs/1712.02892http://dx.doi.org/10.1103/PhysRevLett.120.103601`. `1712.02892`.

[28] Forbes, A., Dudley, A. & McLaren, M. Creation and detection of optical modes with spatial light modulators. *Advances in Optics and Photonics* **8**, 200–227 (2016). URL `https://www.osapublishing.org/abstract.cfm?URI=aop-8-2-200`.

[29] Bolduc, E., Bent, N., Santamato, E., Karimi, E. & Boyd, R. W. Exact solution to simultaneous intensity and phase encryption with a single phase-only hologram. *Optics Letters* **38**, 3546 (2013). URL `https://www.osapublishing.org/abstract.cfm?URI=ol-38-18-3546`.

[30] Turtaev, S. *et al.* Comparison of nematic liquid-crystal and DMD based spatial light modulation in complex photonics. *Optics Express* **25**, 29874 (2017). URL `https://www.osapublishing.org/abstract.cfm?URI=oe-25-24-29874`.

[31] Spilman, A. K. & Brown, T. G. Stress birefringent, space-variant wave plates for vortex illumination. *Applied Optics* **46**, 61 (2007).

URL http://ao.osa.org/abstract.cfm?URI=ao-46-1-61https://www.osapublishing.org/abstract.cfm?URI=ao-46-1-61.

[32] Vella, A., Dourdent, H., Novotny, L. & Alonso, M. A. Birefringent masks that are optimal for generating bottle fields. *Opt. Express* **25**, 9318–9332 (2017). URL http://www.opticsexpress.org/abstract.cfm?URI=oe-25-8-9318.

[33] Marrucci, L., Manzo, C. & Paparo, D. Optical spin-to-orbital angular momentum conversion in inhomogeneous anisotropic media. *Phys. Rev. Lett.* **96**, 163905 (2006). URL https://link.aps.org/doi/10.1103/PhysRevLett.96.163905.

[34] Slussarenko, S. *et al.* Tunable liquid crystal q-plates with arbitrary topological charge. *Opt. Express* **19**, 4085–4090 (2011). URL http://www.opticsexpress.org/abstract.cfm?URI=oe-19-5-4085.

[35] Karimi, E., Piccirillo, B., Nagali, E., Marrucci, L. & Santamato, E. Efficient generation and sorting of orbital angular momentum eigenmodes of light by thermally tuned q -plates. *Applied Physics Letters* **94**, 4–7 (2009). 0905.0562.

[36] Piccirillo, B., D'Ambrosio, V., Slussarenko, S., Marrucci, L. & Santamato, E. Photon spin-to-orbital angular momentum conversion via an electrically tunable q-plate. *Applied Physics Letters* **97**, 4085–4090 (2010). URL http://arxiv.org/abs/1010.4473http://dx.doi.org/10.1063/1.3527083. 1010.4473.

[37] Lodahl, P. *et al.* Chiral quantum optics. *Nature* **541**, 473–480 (2017). URL http://arxiv.org/abs/1608.00446http://dx.doi.org/10.1038/nature21037http://www.nature.com/articles/nature21037. 1608.00446.

[38] D'Errico, A. *et al.* Two-dimensional topological quantum walks in the momentum space of structured light (2018). URL http://arxiv.org/abs/1811.04001. 1811.04001.

[39] Piccirillo, B., Slussarenko, S., Marrucci, L. & Santamato, E. The orbital angular momentum of light: Genesis and evolution of the concept and of the associated photonic technology. *Rivista del Nuovo Cimento* **36**, 501–555 (2013).

[40] D'Errico, A., D'Amelio, R., Piccirillo, B., Cardano, F. & Marrucci, L. Measuring the complex orbital angular momentum spectrum and spatial mode decomposition of structured light beams. *Optica* **4**, 1350–1357 (2017). URL http://www.osapublishing.org/optica/abstract.cfm?URI=optica-4-11-1350.

[41] Sztul, H. I. & Alfano, R. R. Double-slit interference with Laguerre-Gaussian beams. *Optics Letters* **31**, 999 (2006). URL https://www.osapublishing.org/abstract.cfm?URI=ol-31-7-999.

[42] Hickmann, J. M., Fonseca, E. J. S., Soares, W. C. & Chávez-Cerda, S. Unveiling a Truncated Optical Lattice Associated with a Triangular Aperture Using Light's Orbital Angular Momentum. *Physical Review Letters* **105**, 053904 (2010). URL http://link.aps.org/doi/10.1103/PhysRevLett.105.053904.

[43] Ferreira, Q. S., Jesus-Silva, A. J., Fonseca, E. J. S. & Hickmann, J. M. Fraunhofer diffraction of light with orbital angular momentum by a slit. *Optics Letters* **36**, 3106 (2011). URL https://www.osapublishing.org/abstract.cfm?URI=ol-36-16-3106.

[44] Mourka, A., Baumgartl, J., Shanor, C., Dholakia, K. & Wright, E. M. Visualization of the birth of an optical vortex using diffraction from a triangular aperture. *Optics Express* **19**, 5760 (2011). URL https://www.osapublishing.org/abstract.cfm?URI=oe-19-7-5760.

[45] Mazilu, M., Mourka, A., Vettenburg, T., Wright, E. M. & Dholakia, K. Simultaneous determination of the constituent azimuthal and radial mode indices for light fields possessing orbital angular momentum. *Applied Physics Letters* **100**, 231115 (2012). URL http://aip.scitation.org/doi/10.1063/1.4728111.

[46] Berkhout, G. C. G. & Beijersbergen, M. W. Method for Probing the Orbital Angular Momentum of Optical Vortices in Electromagnetic Waves from Astronomical Objects. *Physical Review Letters* **101**, 100801 (2008). URL http://link.aps.org/doi/10.1103/PhysRevLett.101.100801.

[47] Harris, M., Hill, C. A., Tapster, P. R. & Vaughan, J. M. Laser modes with helical wave fronts. *Physical Review A* **49**, 3119–3122 (1994). URL http://link.aps.org/doi/10.1103/PhysRevA.49.3119.

[48] Padgett, M., Arlt, J., Simpson, N. & Allen, L. An experiment to observe the intensity and phase structure of Laguerre–Gaussian laser modes. *American Journal of Physics* **64**, 77–82 (1996). URL http://aapt.scitation.org/doi/10.1119/1.18283.

[49] Leach, J., Padgett, M. J., Barnett, S. M., Franke-Arnold, S. & Courtial, J. Measuring the Orbital Angular Momentum of a Single Photon. *Physical Review Letters* **88**, 257901 (2002). URL http://link.aps.org/doi/10.1103/PhysRevLett.88.257901.

[50] Slussarenko, S., D'Ambrosio, V., Piccirillo, B., Marrucci, L. & Santamato, E. The Polarizing Sagnac Interferometer: a tool for light orbital angular momentum sorting and spin-orbit photon processing. *Optics Express* **18**, 27205 (2010). URL https://www.osapublishing.org/oe/abstract.cfm?uri=oe-18-26-27205.

[51] Lavery, M. P. J., Dudley, A., Forbes, A., Courtial, J. & Padgett, M. J. Robust interferometer for the routing of light beams carrying orbital angular momentum. *New Journal of Physics* **13**, 093014 (2011). URL `http://stacks.iop.org/1367-2630/13/i=9/a=093014?key=crossref.1ab6ce8fee960ad78d07919baf356044`.

[52] Courtial, J., Robertson, D. A., Dholakia, K., Allen, L. & Padgett, M. J. Rotational Frequency Shift of a Light Beam. *Physical Review Letters* **81**, 4828–4830 (1998). URL `http://link.aps.org/doi/10.1103/PhysRevLett.81.4828`.

[53] Vasnetsov, M. V., Torres, J. P., Petrov, D. V. & Torner, L. Observation of the orbital angular momentum spectrum of a light beam. *Optics Letters* **28**, 2285 (2003). URL `https://www.osapublishing.org/abstract.cfm?URI=ol-28-23-2285`.

[54] Mair, A., Vaziri, A., Weihs, G. & Zeilinger, A. Entanglement of the orbital angular momentum states of photons. *Nature* **412**, 313–316 (2001). URL `http://www.nature.com/doifinder/10.1038/35085529`. `0104070`.

[55] Kaiser, T., Flamm, D., Schröter, S. & Duparré, M. Complete modal decomposition for optical fibers using CGH-based correlation filters. *Optics Express* **17**, 9347 (2009). URL `http://www.osapublishing.org/viewmedia.cfm?uri=oe-17-11-9347{&}seq=0{&}html=true`.

[56] Schulze, C., Dudley, A., Flamm, D., Duparré, M. & Forbes, A. Measurement of the orbital angular momentum density of light by modal decomposition. *New Journal of Physics* **15** (2013).

[57] Karimi, E., Piccirillo, B., Nagali, E., Marrucci, L. & Santamato, E. Efficient generation and sorting of orbital angular momentum eigenmodes of light by thermally tuned q-plates. *Applied Physics Letters* **94**, 231124 (2009). URL `http://aip.scitation.org/doi/10.1063/1.3154549`. `0905.0562`.

[58] Karimi, E., Marrucci, L., de Lisio, C. & Santamato, E. Time-division multiplexing of the orbital angular momentum of light. *Optics Letters* **37**, 127 (2012). URL `https://www.osapublishing.org/abstract.cfm?URI=ol-37-2-127`. `arXiv:1202.0559v1`.

[59] Bierdz, P., Kwon, M., Roncaioli, C. & Deng, H. High fidelity detection of the orbital angular momentum of light by time mapping. *New Journal of Physics* **15**, 113062 (2013). URL `http://stacks.iop.org/1367-2630/15/i=11/a=113062?key=crossref.9b1f6b50ce783333e463e161b5c04a7c`. `arXiv:1309.2980v1`.

[60] Gruneisen, M. T., Dymale, R. C., Stoltenberg, K. E. & Steinhoff, N. Optical vortex discrimination with a transmission volume hologram. *New Journal of*

Physics **13**, 083030 (2011). URL `http://stacks.iop.org/1367-2630/13/i=8/a=083030?key=crossref.99260cccf02390616353f28b004e7dcb`.

[61] Berkhout, G. C. G., Lavery, M. P. J., Courtial, J., Beijersbergen, M. W. & Padgett, M. J. Efficient Sorting of Orbital Angular Momentum States of Light. *Physical Review Letters* **105**, 153601 (2010). URL `http://link.aps.org/doi/10.1103/PhysRevLett.105.153601`.

[62] Mirhosseini, M., Malik, M., Shi, Z. & Boyd, R. W. Efficient separation of the orbital angular momentum eigenstates of light. *Nature Communications* **4**, 1–6 (2013). URL `http://arxiv.org/abs/1306.0849http://www.nature.com/doifinder/10.1038/ncomms3781`. `1306.0849`.

[63] Malik, M. *et al.* Direct measurement of a 27-dimensional orbital-angular-momentum state vector. *Nature communications* **5**, 3115 (2014). URL `http://www.ncbi.nlm.nih.gov/pubmed/24445503`. `arXiv:1306.0619v2`.

[64] Forbes, A., Dudley, A. & McLaren, M. Creation and detection of optical modes with spatial light modulators. *Advances in Optics and Photonics* **8**, 200 (2016). URL `https://www.osapublishing.org/abstract.cfm?URI=aop-8-2-200`.

[65] Berkhout, G. C. G., Lavery, M. P. J., Padgett, M. J. & Beijersbergen, M. W. Measuring orbital angular momentum superpositions of light by mode transformation. *Optics Letters* **36**, 1863 (2011). URL `https://www.osapublishing.org/abstract.cfm?URI=ol-36-10-1863`.

[66] Mirhosseini, M., Magaña-Loaiza, O. S., Omar S., Chen, C., Hashemi Rafsanjani, S. M. & Boyd, R. W. Wigner distribution of twisted photons. *Physical Review Letters* **116**, 1–6 (2016). `1512.01577`.

[67] Schulze, C., Ngcobo, S., Duparré, M. & Forbes, A. Modal decomposition without a priori scale information. *Optics Express* **20**, 27866 (2012). URL `http://www.ncbi.nlm.nih.gov/pubmed/23262731https://www.osapublishing.org/oe/abstract.cfm?uri=oe-20-25-27866`.

[68] Langford, N. K. *et al.* Measuring entangled qutrits and their use for quantum bit commitment. *Physical Review Letters* **93**, 1–4 (2004). `0312072`.

[69] Agnew, M., Leach, J., Mclaren, M., Roux, F. S. & Boyd, R. W. Tomography of the quantum state of photons entangled in high dimensions. *Physical Review A - Atomic, Molecular, and Optical Physics* **84**, 3–8 (2011).

[70] Qassim, H. *et al.* Limitations to the determination of a Laguerre–Gauss spectrum via projective, phase-flattening measurement. *Journal of the Optical Society of America B* **31**, A20 (2014). URL

http://www.opticsinfobase.org/abstract.cfm?URI=josab-31-6-A20https://www.osapublishing.org/josab/abstract.cfm?uri=josab-31-6-A20. arXiv:1401.3512v2.

[71] Hossack, W. J., Darling, A. M. & Dahdouh, A. Coordinate transformations with multiple computer-generated optical elements. *Journal of Modern Optics* **34**, 1235–1250 (1987).

[72] Lavery, M. P. J. *et al.* Refractive elements for the measurement of the orbital angular momentum of a single photon. *Optics Express* **20**, 2110 (2012). URL https://www.osapublishing.org/oe/abstract.cfm?uri=oe-20-3-2110.

[73] O'Sullivan, M. N., Mirhosseini, M., Malik, M. & Boyd, R. W. Near-perfect sorting of orbital angular momentum and angular position states of light. *Optics Express* **20**, 24444 (2012). URL http://www.osapublishing.org/viewmedia.cfm?uri=oe-20-22-24444{&}seq=0{&}html=true. 1208.2891.

[74] Lavery, M. P. J. *et al.* Efficient measurement of an optical orbital-angular-momentum spectrum comprising more than 50 states. *New Journal of Physics* **15**, 013024 (2013). URL http://stacks.iop.org/1367-2630/15/i=1/a=013024?key=crossref.74649d4fdc7b8cfe3a03e23e5d1171a6.

[75] Abouraddy, A. F., Yarnall, T. M. & Saleh, B. E. A. Angular and radial mode analyzer for optical beams. *Opt. Lett.* **36**, 4683–4685 (2011). URL http://ol.osa.org/abstract.cfm?URI=ol-36-23-4683.

[76] Zhou, H. L. *et al.* Orbital angular momentum complex spectrum analyzer for vortex light based on the rotational Doppler effect. *Light: Science and Applications* **6** (2017). 1505.07884.

[77] Grillo, V. *et al.* Holographic generation of highly twisted electron beams. *Phys. Rev. Lett.* **114**, 034801 (2015). URL https://link.aps.org/doi/10.1103/PhysRevLett.114.034801.

[78] Yao, A. M. & Padgett, M. J. Orbital angular momentum: origins, behavior and applications. *Advances in Optics and Photonics* **3**, 161 (2011). URL http://aop.osa.org/abstract.cfm?URI=aop-3-2-161https://www.osapublishing.org/aop/abstract.cfm?uri=aop-3-2-161.

[79] Vallone, G. Role of beam waist in laguerre–gauss expansion of vortex beams. *Opt. Lett.* **42**, 1097–1100 (2017). URL http://ol.osa.org/abstract.cfm?URI=ol-42-6-1097.

[80] Piccirillo, B., Slussarenko, S., Marrucci, L. & Santamato, E. Directly measuring mean and variance of infinite-spectrum observables such as the photon orbital angular momentum. *Nature Communications* **6**, 8606 (2015). URL `http://www.nature.com/doifinder/10.1038/ncomms9606`.

[81] Takeda, M., Ina, H. & Kobayashi, S. Fourier-transform method of fringe-pattern analysis for computer-based topography and interferometry. *J. Opt. Soc. Am.* **72**, 156–160 (1982). URL `http://www.osapublishing.org/abstract.cfm?URI=josa-72-1-156`.

[82] Yamaguchi, I. & Zhang, T. Phase-shifting digital holography. *Opt. Lett.* **22**, 1268–1270 (1997). URL `http://ol.osa.org/abstract.cfm?URI=ol-22-16-1268`.

[83] D'Errico, A. *et al.* Topological features of vector vortex beams perturbed with uniformly polarized light. *Scientific Reports* **7**, 1–11 (2017). URL `http://dx.doi.org/10.1038/srep40195`. `1609.05553`.

[84] Cardano, F. & Marrucci, L. Spin–orbit photonics. *Nat. Photon.* **9**, 776–778 (2015). URL `http://www.nature.com/doifinder/10.1038/nphoton.2015.232`.

[85] Mawet, D. *et al.* the Vector Vortex Coronagraph: Laboratory Results and First Light At Palomar Observatory. *Astrophys J.* **709**, 53 (2010). URL `http://arxiv.org/abs/0912.2287$\delimiter"026E30F$nhttp://stacks.iop.org/0004-637X/709/i=1/a=53?key=crossref.bc8109a0db5052ee4255a1761ffbccbb`. `0912.2287`.

[86] Dorn, R., Quabis, S. & Leuchs, G. Sharper Focus for a Radially Polarized Light Beam. *Phys. Rev. Lett.* **91**, 233901 (2003). URL `http://link.aps.org/doi/10.1103/PhysRevLett.91.233901`.

[87] Abouraddy, A. F. & Toussaint, K. C. Three-dimensional polarization control in microscopy. *Phys. Rev. Lett.* **96**, 1–4 (2006).

[88] Shvedov, V., Davoyan, A. R., Hnatovsky, C., Engheta, N. & Krolikowski, W. A long-range polarization-controlled optical tractor beam. *Nat. Photon.* **8**, 846–850 (2014). URL `http://www.nature.com/doifinder/10.1038/nphoton.2014.242`.

[89] Rui, G., Wang, X., Gu, B., Zhan, Q. & Cui, Y. Manipulation metallic nanoparticle at resonant wavelength using engineered azimuthally polarized optical field. *Opt. Express* **24**, 7212 (2016). URL `https://www.osapublishing.org/abstract.cfm?URI=oe-24-7-7212`.

[90] Anoop, K. K. *et al.* Femtosecond laser surface structuring of silicon using optical vortex beams generated by a q-plate. *Appl. Phys. Lett.* **104**, 241604

(2014). URL http://scitation.aip.org/content/aip/journal/apl/104/24/10.1063/1.4884116.

[91] Li, X., Lan, T.-H., Tien, C.-H. & Gu, M. Three-dimensional orientation-unlimited polarization encryption by a single optically configured vectorial beam. *Nat. Commun.* **3**, 998 (2012). URL http://www.ncbi.nlm.nih.gov/pubmed/22893122.

[92] Neugebauer, M., Bauer, T., Banzer, P. & Leuchs, G. Polarization tailored light driven directional optical nanobeacon. *Nano Lett.* **14**, 2546–2551 (2014).

[93] Fickler, R., Lapkiewicz, R., Ramelow, S. & Zeilinger, A. Quantum entanglement of complex photon polarization patterns in vector beams. *Phys. Rev. A* **89**, 1–5 (2014). 1312.1306.

[94] Aiello, A., Töppel, F., Marquardt, C., Giacobino, E. & Leuchs, G. Classical entanglement: Oxymoron or resource? *arxiv.org/abs/1409.0213* 1–9 (2014). URL http://arxiv.org/abs/1409.0213. 1409.0213.

[95] Cardano, F. *et al.* Dynamical moments reveal a topological quantum transition in a photonic quantum walk. *Nature Communications* **7**, 11439 (2015). URL http://www.nature.com/ncomms/2016/160422/ncomms11439/full/ncomms11439.htmlhttp://www.nature.com/doifinder/10.1038/ncomms11439http://arxiv.org/abs/1507.01785http://dx.doi.org/10.1038/ncomms11439. 1507.01785.

[96] Bliokh, K. Y., Rodríguez-Fortuño, F. J., Nori, F. & Zayats, A. V. Spin–orbit interactions of light. *Nat. Photon.* **9**, 796–808 (2015). URL http://arxiv.org/abs/1505.02864http://www.nature.com/doifinder/10.1038/nphoton.2015.201. 1505.02864.

[97] Oron, R. *et al.* The formation of laser beams with pure azimuthal or radial polarization. *Appl. Phys. Lett.* **77**, 3322 (2000). URL http://link.aip.org/link/APPLAB/v77/i21/p3322/s1{&}Agg=doi.

[98] Niv, A., Biener, G., Kleiner, V. & Hasman, E. Rotating vectorial vortices produced by space-variant subwavelength gratings. *Opt. Lett.* **30**, 2933–2935 (2005).

[99] Maurer, C., Jesacher, A., Fürhapter, S., Bernet, S. & Ritsch-Marte, M. Tailoring of arbitrary optical vector beams. *New J. Phys.* **9**, 78 (2007).

[100] Beckley, A. M., Brown, T. G. & Alonso, M. A. Full Poincaré beams. *Opt. Express* **18**, 10777–10785 (2010).

[101] Cardano, F. *et al.* Polarization pattern of vector vortex beams generated by q-plates with different topological charges. *Appl. Opt.* **51**, C1 (2012). 1201.2646.

[102] Gong, L. *et al.* Generation of cylindrically polarized vector vortex beams with digital micromirror device. *J. Appl. Phys.* **116** (2014). URL `http://dx.doi.org/10.1063/1.4901574`.

[103] Bouchard, F., Mand, H., Mirhosseini, M., Karimi, E. & Boyd, R. W. Achromatic orbital angular momentum generator. *New J. Phys.* **16**, 123006 (2014). URL `http://dx.doi.org/10.1088/1367-2630/16/12/123006`. `arXiv:1407.0065v1`.

[104] Naidoo, D. *et al.* Controlled generation of higher-order Poincaré sphere beams from a laser. *Nat. Photon.* **10**, 327–332 (2016). URL `http://arxiv.org/abs/1505.02256http://www.nature.com/doifinder/10.1038/nphoton.2016.37`. `1505.02256`.

[105] Chille, V. *et al.* Experimental generation of amplitude squeezed vector beams. *Opt. Express* **24**, 12385 (2016). URL `http://arxiv.org/abs/1602.08387https://www.osapublishing.org/abstract.cfm?URI=oe-24-11-12385`. `1602.08387`.

[106] Radwell, N., Hawley, R. D., Götte, J. B. & Franke-Arnold, S. Achromatic vector vortex beams from a glass cone. *Nat. Commun.* **7**, 10564 (2016). URL `http://www.nature.com/doifinder/10.1038/ncomms10564`.

[107] Nye, J. F. & Hajnal, J. V. The Wave Structure of Monochromatic Electromagnetic Radiation. *Proc. R. Soc. A* **409**, 21–36 (1987). URL `http://rspa.royalsocietypublishing.org/content/409/1836/21.short`.

[108] Berry, M. V. & Dennis, M. R. Polarization singularities in isotropic random vector waves. *Proc. R. Soc. A* **457**, 141–155 (2001). URL `http://dx.doi.org/10.1098/rspa.2000.0660$\delimiter"026E30F$nhttp://rspa.royalsocietypublishing.org/cgi/doi/10.1098/rspa.2000.0660`.

[109] Freund, I., Mokhun, A. I., Soskin, M. S., Angelsky, O. V. & Mokhun, I. I. Stokes singularity relations. *Opt. Lett.* **27**, 545 (2002). URL `http://www.osapublishing.org/viewmedia.cfm?uri=ol-27-7-545{&}seq=0{&}html=true`.

[110] Soskin, M. S., Denisenko, V. & Freund, I. Optical polarization singularities and elliptic stationary points. *Opt. Lett.* **28**, 1475 (2003). URL `http://www.osapublishing.org/viewmedia.cfm?uri=ol-28-16-1475{&}seq=0{&}html=true`.

[111] Dennis, M., O'Holleran, K. & Padgett, M. Singular Optics- Optical Vortices and Polarization Singularities. *Prog. Optics* **53**, 293–363 (2009). URL `http://www.sciencedirect.com/science/article/pii/S0079663808002059/`

pdf?md5=2f4f9d9d126ab63eab9e341ce57cb214{&}pid=1-s2.0-S0079663808002059-main.pdf{&}{_}valck=1$\delimiter"026E30F$nhttp://dx.doi.org/10.1016/S0079-6638(08)00205-9.

[112] Spreeuw, R. J. A Classical Analogy of Entanglement. *Foundations of Physics* **28**, 361–374 (1998).

[113] Karimi, B. E. & Boyd, R. W. Classical entanglement? *Science* **350**, 1172–1173 (2015).

[114] Wang, X.-l. *et al.* 18-Qubit Entanglement With Photon'S Three Degrees of Freedom. *arXiv* **260502**, 1–5 (2018). URL http://arxiv.org/abs/1801.04043. 1801.04043.

[115] Sit, A. *et al.* High-Dimensional Intra-City Quantum Cryptography with Structured Photons **4** (2016). URL http://arxiv.org/abs/1612.05195. 1612.05195.

[116] Dennis, M. R. Polarization singularities in paraxial vector fields: Morphology and statistics. *Opt. Commun.* **213**, 201–221 (2002).

[117] Cvarch, B. A. *et al.* Monstar polarization singularities with elliptically-symmetric q-plates. *Opt. Express* **25**, 14935–14943 (2017). URL http://www.opticsexpress.org/abstract.cfm?URI=oe-25-13-14935.

[118] Freund, I. & Shvartsman, N. Wave-field phase singularities: The sign principle. *Physical Review A* **50**, 5164–5172 (1994).

[119] Flossmann, F., O'Holleran, K., Dennis, M. R. & Padgett, M. J. Polarization singularities in 2D and 3D speckle fields. *Phys. Rev. Lett.* **100**, 2–5 (2008).

[120] Burresi, M. *et al.* Observation of polarization singularities at the nanoscale. *Phys. Rev. Lett.* **102**, 033902 (2009).

[121] Lang, B., Beggs, D. M., Young, A. B., Rarity, J. G. & Oulton, R. Stability of polarization singularities in disordered photonic crystal waveguides. *Phys. Rev. A* **92**, 063819 (2015). URL http://link.aps.org/doi/10.1103/PhysRevA.92.063819.

[122] Freund, I. Polarization flowers. *Opt. Commun.* **199**, 47–63 (2001).

[123] Bliokh, K. Y., Niv, A., Kleiner, V. & Hasman, E. Singular polarimetry: evolution of polarization singularities in electromagnetic waves propagating in a weakly anisotropic medium. *Opt. Express* **16**, 695–709 (2008). 0710.4804.

[124] Freund, I. Polarization singularity indices in Gaussian laser beams. *Opt. Commun.* **201**, 251–270 (2002). URL http://dx.doi.org/10.1016.

[125] Bekshaev, A. Y., Soskin, M. & Vasnetsov, M. Transformation of higher-order optical vortices upon focusing by an astigmatic lens. *Opt. Commun.* **241**, 237–247 (2004). URL `http://linkinghub.elsevier.com/retrieve/pii/S0030401804007424`.

[126] Dennis, M. R. Rows of optical vortices from elliptically perturbing a high-order beam. *Opt. Lett.* **31**, 1325 (2006). URL `https://www.osapublishing.org/abstract.cfm?URI=ol-31-9-1325`. `0602066`.

[127] Freund, I. Critical point explosions in two-dimensional wave fields. *Opt. Commun.* **159**, 99–117 (1999). URL `http://www.sciencedirect.com/science/article/pii/S0030401898005914http://linkinghub.elsevier.com/retrieve/pii/S0030401898005914`.

[128] Kumar, A., Vaity, P. & Singh, R. P. Crafting the core asymmetry to lift the degeneracy of optical vortices. *Opt. Express* **19**, 6182 (2011). URL `https://www.osapublishing.org/oe/abstract.cfm?uri=oe-19-7-6182`.

[129] Ricci, F., Löffler, W. & van Exter, M. Instability of higher-order optical vortices analyzed with a multi-pinhole interferometer. *Opt. Express* **20**, 22961 (2012). URL `https://www.osapublishing.org/oe/abstract.cfm?uri=oe-22-8-9920https://www.osapublishing.org/oe/abstract.cfm?uri=oe-20-20-22961`. `arXiv:1205.6457v1`.

[130] Soskin, M. S., Gorshkov, V. N., Vasnetsov, M. V., Malos, J. T. & Heckenberg, N. R. Topological charge and angular momentum of light beams carrying optical vortices. *Phys. Rev. A* **56**, 4064–4075 (1997). URL `http://link.aps.org/doi/10.1103/PhysRevA.56.4064`.

[131] Berry, M. V., Dennis, M. R. & Lee, R. L. Polarization singularities in the clear sky. *New J. Phys.* **6**, 162 (2004).

[132] Niv, A., Biener, G., Kleiner, V. & Hasman, E. Manipulation of the Pancharatnam phase in vectorial vortices. *Opt. Express* **14**, 4208 (2006). URL `http://www.osapublishing.org/viewmedia.cfm?uri=oe-14-10-4208{&}seq=0{&}html=true`.

[133] Holleczek, A., Aiello, A., Gabriel, C., Marquardt, C. & Leuchs, G. Classical and quantum properties of cylindrically polarized states of light. *Opt. Express* **19**, 9714 (2010). URL `https://www.osapublishing.org/oe/abstract.cfm?uri=oe-19-10-9714$\delimiter"026E30F$nhttp://libra.msra.cn/Publication/27618331/classical-and-quantum-properties-of-cylindrically-polarized-states-of-light$\`

delimiter"026E30F$nhttp://arxiv.org/abs/1012.4578$\ delimiter"026E30F$nhttp://dx.doi.org/10.1364/OE.19.009714. 1012.4578.

[134] Vyas, S., Kozawa, Y., Sato, S. & Miyamoto, Y. Unfolding of optical singularities in vector laguerre-gaussian beams. In *2015 CLEOPR*, 28F2_1 (Optical Society of America, 2015). URL http://www.osapublishing.org/abstract.cfm?URI=CLEOPR-2015-28F2_1.

[135] Marrucci, L. *et al.* Spin-to-orbital conversion of the angular momentum of light and its classical and quantum applications. *J. Opt.* **13**, 064001 (2011).

[136] Karimi, E., Piccirillo, B., Marrucci, L. & Santamato, E. Light propagation in a birefringent plate with topological charge. *Opt. Lett.* **34**, 1225–1227 (2009). arXiv:0809.4220v2.

[137] Vallone, G. On the properties of circular beams: normalization, Laguerre-Gauss expansion, and free-space divergence. *Opt. Lett.* **40**, 1717–20 (2015). URL http://www.osapublishing.org/viewmedia.cfm?uri=ol-40-8-1717{&}seq=0{&}html=true.

[138] Flossmann, F., Schwarz, U. T., Maier, M. & Dennis, M. R. Polarization singularities from unfolding an optical vortex through a birefringent crystal. *Phys. Rev. Lett.* **95**, 253901 (2005).

[139] Cheng, W., Haus, J. W. & Zhan, Q. Propagation of vector vortex beams through a turbulent atmosphere. *Opt. Express* **17**, 17829–17836 (2009).

[140] Nivas, J. J. J. *et al.* Laser ablation of silicon induced by a femtosecond optical vortex beam. *Opt. Lett.* **40**, 4611–4 (2015). URL http://www.osapublishing.org/viewmedia.cfm?uri=ol-40-20-4611{&}seq=0{&}html=true.

[141] Neo, R. *et al.* Correcting vortex splitting in higher order vortex beams. *Opt. Express* **22**, 9920 (2014). URL http://www.ncbi.nlm.nih.gov/pubmed/24787874https://www.osapublishing.org/oe/abstract.cfm?uri=oe-22-8-9920.

[142] Dennis, M. R. & Götte, J. B. Topological Aberration of Optical Vortex Beams: Determining Dielectric Interfaces by Optical Singularity Shifts. *Phys. Rev. Lett.* **109**, 183903 (2012). URL http://link.aps.org/doi/10.1103/PhysRevLett.109.183903. arXiv:1205.6457v1.

[143] Nivas, J. J. *et al.* Surface Structuring with Polarization-Singular Femtosecond Laser Beams Generated by a q-plate. *Scientific Reports* **7**, 1–10 (2017). URL http://dx.doi.org/10.1038/srep42142.

[144] Aharonov, Y., Davidovich, L. & Zagury, N. Quantum random walks. *Phys. Rev. A* **48**, 1687–1690 (1993). URL `https://link.aps.org/doi/10.1103/PhysRevA.48.1687`.

[145] Shenvi, N., Kempe, J. & Whaley, K. B. Quantum random-walk search algorithm. *Physical Review A* **67**, 052307 (2003). URL `http://arxiv.org/abs/quant-ph/0210064http://dx.doi.org/10.1103/PhysRevA.67.052307https://link.aps.org/doi/10.1103/PhysRevA.67.052307`. `0210064`.

[146] Childs, A. M. & Goldstone, J. Spatial search by quantum walk. *Physical Review A* **70**, 022314 (2004). URL `http://arxiv.org/abs/quant-ph/0306054http://dx.doi.org/10.1103/PhysRevA.70.022314https://link.aps.org/doi/10.1103/PhysRevA.70.022314`. `0306054`.

[147] Wong, T. G. Grover Search with Lackadaisical Quantum Walks. *Journal of Physics A: Mathematical and Theoretical* (2015). URL `http://arxiv.org/abs/1502.04567http://dx.doi.org/10.1088/1751-8113/48/43/435304`. `1502.04567`.

[148] Lovett, N. B., Cooper, S., Everitt, M., Trevers, M. & Kendon, V. Universal quantum computation using the discrete-time quantum walk. *Physical Review A* **81**, 042330 (2010). URL `http://arxiv.org/abs/0910.1024http://dx.doi.org/10.1103/PhysRevA.81.042330https://link.aps.org/doi/10.1103/PhysRevA.81.042330`. `0910.1024`.

[149] Childs, A. M. Universal Computation by Quantum Walk. *Physical Review Letters* **102**, 180501 (2009). URL `http://arxiv.org/abs/0806.1972http://dx.doi.org/10.1103/PhysRevLett.102.180501https://link.aps.org/doi/10.1103/PhysRevLett.102.180501`. `0806.1972`.

[150] Spring, J. B. *et al.* Boson Sampling on a Photonic Chip 1–11 (2012). URL `http://arxiv.org/abs/1212.2622http://dx.doi.org/10.1126/science.1231692`. `1212.2622`.

[151] Spagnolo, N. *et al.* Efficient experimental validation of photonic boson sampling against the uniform distribution 3–9 (2013). URL `http://arxiv.org/abs/1311.1622http://dx.doi.org/10.1038/nphoton.2014.135`. `1311.1622`.

[152] Kitagawa, T. *et al.* Observation of topologically protected bound states in photonic quantum walks. *Nature Communications* **3** (2012). `1105.5334`.

[153] Sansoni, L. *et al.* Two-Particle Bosonic-Fermionic Quantum Walk via Integrated Photonics. *Physical Review Letters* **108**, 010502 (2012). URL `http://arxiv.org/abs/1106.5713http://dx.doi.org/10.1103/PhysRevLett.108.010502https://link.aps.org/doi/10.1103/PhysRevLett.108.010502`. `1106.5713`.

[154] Crespi, A. *et al.* Anderson localization of entangled photons in an integrated quantum walk. *Nature Photonics* **7**, 322–328 (2013). URL `http://arxiv.org/abs/1304.1012http://dx.doi.org/10.1038/nphoton.2013.26http://www.nature.com/articles/nphoton.2013.26`. `1304.1012`.

[155] Schreiber, A. *et al.* Decoherence and Disorder in Quantum Walks: From Ballistic Spread to Localization. *Physical Review Letters* **106**, 180403 (2011). URL `http://arxiv.org/abs/1101.2638http://dx.doi.org/10.1103/PhysRevLett.106.180403https://link.aps.org/doi/10.1103/PhysRevLett.106.180403`. `1101.2638`.

[156] Schreiber, A. *et al.* A 2D quantum walk simulation of two-particle dynamics. *Science* **335**, 55–58 (2012). `1204.3555v1`.

[157] Mohseni, M., Rebentrost, P., Lloyd, S. & Aspuru-Guzik, A. Environment-assisted quantum walks in photosynthetic energy transfer. *The Journal of Chemical Physics* **129**, 174106 (2008). URL `http://aip.scitation.org/doi/10.1063/1.3002335`. `arXiv:0805.2741v2`.

[158] Perets, H. B. *et al.* Realization of Quantum Walks with Negligible Decoherence in Waveguide Lattices. *Physical Review Letters* **100**, 170506 (2008). URL `http://arxiv.org/abs/0707.0741http://dx.doi.org/10.1103/PhysRevLett.100.170506https://link.aps.org/doi/10.1103/PhysRevLett.100.170506`. `0707.0741`.

[159] Kitagawa, T. Topological phenomena in quantum walks: elementary introduction to the physics of topological phases. *Quantum Information Processing* **11**, 1107–1148 (2012). URL `http://link.springer.com/10.1007/s11128-012-0425-4`.

[160] Broome, M. A. *et al.* Discrete single-photon quantum walks with tunable decoherence. *Physical Review Letters* **104**, 1–5 (2010). `1002.4923`.

[161] Karski, M. *et al.* Quantum walk in position space with single optically trapped atoms. *Science* **325**, 174–177 (2009). `0907.1565`.

[162] Robens, C., Brakhane, S., Meschede, D. & Alberti, A. Quantum Walks with Neutral Atoms: Quantum Interference Effects of One and Two Particles. In *Laser Spectroscopy*, 1–15 (WORLD SCIENTIFIC, 2016). URL `http://arxiv.org/abs/1511.03569{%}0Ahttp://dx.doi.org/10.1142/9789813200616{_}0001http://www.worldscientific.com/doi/abs/10.1142/9789813200616{_}0001`. `1511.03569`.

[163] Preiss, P. M. *et al.* Strongly correlated quantum walks in optical lattices. *Science* **347**, 1229–1233 (2015). URL `http://www.sciencemag.org/cgi/doi/10.1126/science.1260364`. `1409.3100`.

[164] Zähringer, F. *et al.* Realization of a quantum walk with one and two trapped ions 1–5 (2009). URL `http://arxiv.org/abs/0911.1876http://dx.doi.org/10.1103/PhysRevLett.104.100503`. `0911.1876`.

[165] Flurin, E. *et al.* Observing topological invariants using quantum walks in superconducting circuits. *Physical Review X* **7**, 1–6 (2017). `arXiv:1610.03069v1`.

[166] Schreiber, A. *et al.* Photons walking the line: A quantum walk with adjustable coin operations. *Physical Review Letters* **104**, 3–6 (2010). `0910.2197`.

[167] Xiao, L. *et al.* Observation of topological edge states in parity–time-symmetric quantum walks. *Nature Physics* **13**, 1117 (2017). URL `http://dx.doi.org/10.1038/nphys4204http://10.0.4.14/nphys4204https://www.nature.com/articles/nphys4204{#}supplementary-information`.

[168] Wang, X. *et al.* Detecting topological invariants and revealing topological phase transitions in discrete-time photonic quantum walks. *Phys. Rev. A* **98**, 013835 (2018). URL `https://link.aps.org/doi/10.1103/PhysRevA.98.013835`.

[169] Xue, P. *et al.* Experimental quantum-walk revival with a time-dependent coin. *Physical Review Letters* **114**, 6–10 (2015). `1508.01989`.

[170] Peruzzo, A. *et al.* Quantum Walks of Correlated Photons. *Science* **329**, 1500–1503 (2010). URL `http://arxiv.org/abs/1006.4764http://dx.doi.org/10.1126/science.1193515http://www.sciencemag.org/cgi/doi/10.1126/science.1193515`. `1006.4764`.

[171] Tang, H. *et al.* Experimental two-dimensional quantum walk on a photonic chip. *Science Advances* **4**, eaat3174 (2018). URL `http://arxiv.org/abs/1704.08242http://advances.sciencemag.org/lookup/doi/10.1126/sciadv.aat3174`. `1704.08242`.

[172] Zhang, P. *et al.* Implementation of one-dimensional quantum walks on spin-orbital angular momentum space of photons. *Phys. Rev. A* **81**, 052322 (2010). URL `https://link.aps.org/doi/10.1103/PhysRevA.81.052322`.

[173] Goyal, S. K., Roux, F. S., Forbes, A. & Konrad, T. Implementing quantum walks using orbital angular momentum of classical light. *Phys. Rev. Lett.* **110**, 263602 (2013). URL `https://link.aps.org/doi/10.1103/PhysRevLett.110.263602`.

[174] Cardano, F. *et al.* Quantum walks and wavepacket dynamics on a lattice with twisted photons. *Science Advances* **1**, e1500087–e1500087 (2015). URL `http://arxiv.org/abs/1407.5424{%}5Cnhttp://advances.sciencemag.org/cgi/doi/10.1126/sciadv.1500087`. `arXiv:1407.5424v1`.

[175] Cardano, F. *et al.* Detection of Zak phases and topological invariants in a chiral quantum walk of twisted photons. *Nature Communications* **8**, 15516 (2017). URL `http://arxiv.org/abs/1610.06322http://dx.doi.org/10.1038/ncomms15516http://www.nature.com/doifinder/10.1038/ncomms15516`. `1610.06322`.

[176] Di Franco, C., Mc Gettrick, M., Machida, T. & Busch, T. Alternate two-dimensional quantum walk with a single-qubit coin. *Physical Review A* **84**, 042337 (2011). URL `https://link.aps.org/doi/10.1103/PhysRevA.84.042337`. `1107.4400`.

[177] Budich, J. C., Hu, Y. & Zoller, P. Helical floquet channels in 1d lattices. *Phys. Rev. Lett.* **118**, 105302 (2017). URL `https://link.aps.org/doi/10.1103/PhysRevLett.118.105302`.

[178] Genske, M. *et al.* Electric quantum walks with individual atoms. *Physical Review Letters* **110**, 190601 (2013). URL `https://link.aps.org/doi/10.1103/PhysRevLett.110.190601http://arxiv.org/abs/1302.2094http://dx.doi.org/10.1103/PhysRevLett.110.190601`. `1302.2094`.

[179] Wojcik, A., Luczak, T., Kurzyski, P., Grudka, A. & Bednarska, M. Quasiperiodic dynamics of a quantum walk on the line. *Physical Review Letters* **93**, 13–16 (2004).

[180] Shevchenko, S. N., Ashhab, S. & Nori, F. Landau-Zener-Stuckelberg interferometry (2009). URL `http://arxiv.org/abs/0911.1917{%}0Ahttp://dx.doi.org/10.1016/j.physrep.2010.03.002`. `0911.1917`.

[181] Cedzich, C. & Werner, R. F. Revivals in quantum walks with a quasiperiodically-time-dependent coin. *Physical Review A* **93**, 032329 (2016). URL `http://arxiv.org/abs/1510.08905https://link.aps.org/doi/10.1103/PhysRevA.93.032329`. `1510.08905`.

[182] Ramasesh, V. V., Flurin, E., Rudner, M., Siddiqi, I. & Yao, N. Y. Direct probe of topological invariants using bloch oscillating quantum walks. *Phys. Rev. Lett.* **118**, 130501 (2017). URL `https://link.aps.org/doi/10.1103/PhysRevLett.118.130501`.

[183] Matjeschk, R. *et al.* Quantum walks with nonorthogonal position states. *Physical Review Letters* **109**, 1–5 (2012). `1206.0220`.

[184] Nash, C. & Sen, S. *Topology and Geometry for Physicists* (Academic Press, 1983). URL `https://books.google.it/books?id=Lz7y9PmTdgwC`.

[185] Chaikin, P. & Lubensky, T. *Principles of Condensed Matter Physics* (Cambridge University Press, 2000). URL `https://books.google.it/books?id=P9YjNjzr9OIC`.

[186] Fradkin, E. *Field Theories of Condensed Matter Physics*. Field Theories of Condensed Matter Physics (Cambridge University Press, 2013). URL `https://books.google.it/books?id=x7_6MX4ye_wC`.

[187] Bernevig, B. & Hughes, T. *Topological Insulators and Topological Superconductors* (Princeton University Press, 2013). URL `https://books.google.it/books?id=w0n7JHSSxrsC`.

[188] Thouless, D. J., Kohmoto, M., Nightingale, M. P. & den Nijs, M. Quantized hall conductance in a two-dimensional periodic potential. *Phys. Rev. Lett.* **49**, 405–408 (1982). URL `https://link.aps.org/doi/10.1103/PhysRevLett.49.405`.

[189] Klitzing, K. v., Dorda, G. & Pepper, M. New method for high-accuracy determination of the fine-structure constant based on quantized hall resistance. *Phys. Rev. Lett.* **45**, 494–497 (1980). URL `https://link.aps.org/doi/10.1103/PhysRevLett.45.494`.

[190] Su, W. P., Schrieffer, J. R. & Heeger, A. J. Solitons in Polyacetylene. *Physical Review Letters* **42**, 1698–1701 (1979). URL `https://link.aps.org/doi/10.1103/PhysRevLett.42.1698`. `PhysRevLett.42.1698`.

[191] Qi, X.-L., Wu, Y.-S. & Zhang, S.-C. Topological quantization of the spin hall effect in two-dimensional paramagnetic semiconductors. *Phys. Rev. B* **74**, 085308 (2006). URL `https://link.aps.org/doi/10.1103/PhysRevB.74.085308`.

[192] Wunderlich, J., Kaestner, B., Sinova, J. & Jungwirth, T. Experimental observation of the spin-hall effect in a two-dimensional spin-orbit coupled semiconductor system. *Phys. Rev. Lett.* **94**, 047204 (2005). URL `https://link.aps.org/doi/10.1103/PhysRevLett.94.047204`.

[193] Qi, X.-L. & Zhang, S.-C. Topological insulators and superconductors. *Rev. Mod. Phys.* **83**, 1057–1110 (2011). URL `https://link.aps.org/doi/10.1103/RevModPhys.83.1057`.

[194] Qi, X.-L., Hughes, T. L. & Zhang, S.-C. Topological field theory of time-reversal invariant insulators. *Phys. Rev. B* **78**, 195424 (2008). URL `https://link.aps.org/doi/10.1103/PhysRevB.78.195424`.

[195] Sarma, S. D., Freedman, M. & Nayak, C. Topological quantum computation. *Physics Today* **59**, 32–38 (2006). URL `http://physicstoday.scitation.org/doi/10.1063/1.2337825`. `0101025v2`.

[196] Kitaev, A. Y. Fault-tolerant quantum computation by anyons. *Annals of Physics* **303**, 2–30 (2003). URL `http://arxiv.org/abs/quant-ph/9707021{%}0Ahttp://dx.doi.org/10.1016/S0003-4916(02)00018-0`. `9707021`.

[197] Ozawa, T. *et al.* Topological Photonics (2018). URL `http://arxiv.org/abs/1802.04173`. `1802.04173`.

[198] Yang, Z. *et al.* Topological acoustics. *Phys. Rev. Lett.* **114**, 114301 (2015). URL `https://link.aps.org/doi/10.1103/PhysRevLett.114.114301`.

[199] Fleury, R., Khanikaev, A. B. & Alù, A. Floquet topological insulators for sound. *Nature Communications* **7**, 1–11 (2016). `1511.08427`.

[200] Ozawa, T., Price, H. M., Goldman, N., Zilberberg, O. & Carusotto, I. Synthetic dimensions in integrated photonics: From optical isolation to four-dimensional quantum Hall physics. *Physical Review A* **93**, 1–17 (2016). `1510.03910`.

[201] Beenakker, C. & Kouwenhoven, L. A road to reality with topological superconductors. *Nat. Phys.* **12**, 618–621 (2016). URL `http://www.nature.com/doifinder/10.1038/nphys3778`. `arXiv:1606.09439v1`.

[202] Goldman, N., Budich, J. C. & Zoller, P. Topological quantum matter with ultracold gases in optical lattices. *Nat. Phys.* **12**, 639–645 (2016). URL `http://www.nature.com/doifinder/10.1038/nphys3803`.

[203] Huber, S. D. Topological mechanics. *Nat. Phys.* **12**, 621–623 (2016). URL `http://www.nature.com/doifinder/10.1038/nphys3801`.

[204] Oka, T. & Aoki, H. Photovoltaic hall effect in graphene. *Phys. Rev. B* **79**, 081406 (2009). URL `https://link.aps.org/doi/10.1103/PhysRevB.79.081406`.

[205] Kitagawa, T., Berg, E., Rudner, M. & Demler, E. Topological characterization of periodically driven quantum systems. *Phys. Rev. B* **82**, 235114 (2010). URL `https://link.aps.org/doi/10.1103/PhysRevB.82.235114`.

[206] Rudner, M. S., Lindner, N. H., Berg, E. & Levin, M. Anomalous edge states and the bulk-edge correspondence for periodically driven two-dimensional systems. *Physical Review X* **3**, 1–15 (2014). `1212.3324`.

[207] Cayssol, J., Dóra, B., Simon, F. & Moessner, R. Floquet topological insulators. *Physica Status Solidi - Rapid Research Letters* **7**, 101–108 (2013). `1211.5623`.

[208] Berry, M. V. Quantal Phase Factors Accompanying Adiabatic Changes. *Proceedings of the Royal Society A: Mathematical, Physical and Engineering Sciences* **392**, 45–57 (1984). URL `http://rspa.royalsocietypublishing.org/cgi/doi/10.1098/rspa.1984.0023`. `1108.0910`.

[209] Pancharatnam, B. Y. S. Generalized theory of interference and its applications 247–262 (1956).

[210] Ashcroft, N. & Mermin, N. *Solid State Physics* (Cengage Learning, 2011). URL `https://books.google.it/books?id=x_s_YAAACAAJ`.

[211] Zak, J. Berry's phase for energy bands in solids. *Phys. Rev. Lett.* **62**, 2747–2750 (1989). URL `https://link.aps.org/doi/10.1103/PhysRevLett.62.2747`.

[212] Loredo, J. C., Ortíz, O., Weingärtner, R. & De Zela, F. Measurement of Pancharatnam's phase by robust interferometric and polarimetric methods. *Physical Review A - Atomic, Molecular, and Optical Physics* **80**, 1–9 (2009). `1510.03799`.

[213] Atala, M. *et al.* Direct measurement of the Zak phase in topological Bloch bands. *Nature Physics* **9**, 795–800 (2013). URL `http://www.nature.com/articles/nphys2790`. `1212.0572`.

[214] Aidelsburger, M. *et al.* Measuring the Chern number of Hofstadter bands with ultracold bosonic atoms. *Nature Physics* **11**, 162–166 (2015). `1407.4205`.

[215] Rakovszky, T., Asbóth, J. K. & Alberti, A. Detecting topological invariants in chiral symmetric insulators via losses. *Physical Review B* **95**, 1–6 (2017). `1611.09670`.

[216] Fu, L. & Kane, C. L. Topological insulators with inversion symmetry. *Physical Review B - Condensed Matter and Materials Physics* **76**, 1–17 (2007). `0611341`.

[217] Asbóth, J., Oroszlány, L. & Pályi, A. *A Short Course on Topological Insulators: Band Structure and Edge States in One and Two Dimensions*. Lecture Notes in Physics (Springer International Publishing, 2016). URL `https://books.google.it/books?id=RWKhCwAAQBAJ`.

[218] Hasan, M. Z. & Kane, C. L. Colloquium: Topological insulators. *Reviews of Modern Physics* **82**, 3045–3067 (2010). `1002.3895`.

[219] Kitagawa, T., Rudner, M. S., Berg, E. & Demler, E. Exploring topological phases with quantum walks. *Physical Review A - Atomic, Molecular, and Optical Physics* **82** (2010). `1003.1729`.

[220] Rudner, M. S. & Levitov, L. S. Topological transition in a non-hermitian quantum walk. *Phys. Rev. Lett.* **102**, 065703 (2009). URL `http://link.aps.org/doi/10.1103/PhysRevLett.102.065703`.

[221] Zeuner, J. M. *et al.* Observation of a topological transition in the bulk of a non-hermitian system. *Phys. Rev. Lett.* **115**, 040402 (2015). URL `http://link.aps.org/doi/10.1103/PhysRevLett.115.040402`.

[222] Asbóth, J. K. & Obuse, H. Bulk-boundary correspondence for chiral symmetric quantum walks. *Phys. Rev. B* **88**, 121406 (2013). URL `http://link.aps.org/doi/10.1103/PhysRevB.88.121406`.

[223] Barkhofen, S. *et al.* Measuring topological invariants in disordered discrete-time quantum walks. *Physical Review A* **96**, 1–10 (2017). URL `http://arxiv.org/abs/1606.00299{%}0Ahttp://dx.doi.org/10.1103/PhysRevA.96.033846`. `1606.00299`.

[224] Meier, E. J. *et al.* Observation of the topological Anderson insulator in disordered atomic wires **1** (2018). URL `http://arxiv.org/abs/1802.02109`. `1802.02109`.

[225] Maffei, M., Dauphin, A., Cardano, F., Lewenstein, M. & Massignan, P. Topological characterization of chiral models through their long time dynamics. *New Journal of Physics* **20**, 1–17 (2018). `1708.02778`.

[226] Haldane, F. D. M. Model for a quantum hall effect without landau levels: Condensed-matter realization of the "parity anomaly". *Physical Review Letters* **61**, 2015–2018 (1988). `9712001`.

[227] Bernevig, B. A., Hughes, T. L. & Zhang, S. C. Quantum spin hall effect and topological phase transition in HgTe quantum wells. *Science* **314**, 1757–1761 (2006). URL `http://arxiv.org/abs/cond-mat/0611399{%}0Ahttp://dx.doi.org/10.1126/science.1133734`. `arXiv:1308.5367`.

[228] Kane, C. L. & Mele, E. J. Quantum spin hall effect in graphene. *Phys. Rev. Lett.* **95**, 226801 (2005). URL `https://link.aps.org/doi/10.1103/PhysRevLett.95.226801`.

[229] König, M. *et al.* Quantum spin hall insulator state in hgte quantum wells. *Science* **318**, 766–770 (2007). URL `http://science.sciencemag.org/content/318/5851/766`. `http://science.sciencemag.org/content/318/5851/766.full.pdf`.

[230] Chen, Y. L. *et al.* Experimental realization of a three-dimensional topological insulator, bi2te3. *Science* **325**, 178–181 (2009). URL `http://science.sciencemag.`

org/content/325/5937/178. http://science.sciencemag.org/content/325/5937/178.full.pdf.

[231] Chang, C. Z. *et al.* Experimental observation of the quantum anomalous Hall effect in a magnetic topological Insulator. *Science* **340**, 167–170 (2013). URL http://www.sciencemag.org/cgi/doi/10.1126/science.1234414. arXiv:1212.4783.

[232] Lindner, N. H., Refael, G. & Galitski, V. Floquet Topological Insulator in Semiconductor Quantum Wells 1–7 (2010). URL http://arxiv.org/abs/1008.1792{%}0Ahttp://dx.doi.org/10.1038/nphys1926. 1008.1792.

[233] Peng, Y. G. *et al.* Experimental demonstration of anomalous Floquet topological insulator for sound. *Nature Communications* **7**, 1–8 (2016). URL http://dx.doi.org/10.1038/ncomms13368. 1508.06243.

[234] Maczewsky, L. J., Zeuner, J. M., Nolte, S. & Szameit, A. Observation of photonic anomalous Floquet topological insulators. *Nature Communications* **8** (2017). 1605.03877.

[235] Gao, Y., Yang, S. A. & Niu, Q. Field induced positional shift of bloch electrons and its dynamical implications. *Phys. Rev. Lett.* **112**, 166601 (2014). URL https://link.aps.org/doi/10.1103/PhysRevLett.112.166601.

[236] Price, H. M., Zilberberg, O., Ozawa, T., Carusotto, I. & Goldman, N. Measurement of chern numbers through center-of-mass responses. *Phys. Rev. B* **93**, 245113 (2016). URL https://link.aps.org/doi/10.1103/PhysRevB.93.245113.

[237] Heyl, M. Dynamical quantum phase transitions: a review. *Reports on Progress in Physics* **81**, 054001 (2018). URL http://arxiv.org/abs/1701.08851http://stacks.iop.org/0034-4885/81/i=5/a=054001?key=crossref.023db71bd7c4add223c0ffc515a6cd09. 1701.08851.

[238] Kwon, K. H. & Lee, D. W. On the extreme zeros of orthogonal polynomials. *Journal of the Korean Mathematical Society* **36**, 489–507 (1999).

[239] Gatteschi, L. Asymptotics and bounds for the zeros of laguerre polynomials: a survey. *Journal of Computational and Applied Mathematics* **144**, 7 – 27 (2002). URL http://www.sciencedirect.com/science/article/pii/S0377042701005490. Selected papers of the Int. Symp. on Applied Mathematics, August 2000, Dalian, China.